Aus der Klinik für Strahlentherapie
Direktorin: Frau Prof. Dr. med. Rita Engenhart-Cabillic
des Fachbereichs Medizin der Philipps-Universität Marburg

Untersuchung der Modulationseigenschaften von Lungengewebe in der Strahlentherapie mit Protonen

Analyzing the modulation effects of lung tissue in proton therapy

Inaugural-Dissertation zur Erlangung des Doktorgrades
der Medizinwissenschaften (Dr. rer. med.)

dem Fachbereich Medizin der Philipps-Universität Marburg vorgelegt von

Kilian-Simon Baumann
aus München

Marburg, 2020

Angenommen vom Fachbereich Medizin der Philipps-Universität Marburg am:

21. April 2020

Gedruckt mit Genehmigung des Fachbereichs Medizin.

Dekan: Herr Prof. Dr. H. Schäfer

Referenten: Frau Prof. Dr. R. Engenhart-Cabillic und Herr Prof. Dr. K. Zink

1. Korreferent: Herr Prof. Dr. A. Schrimpf

In memory of Ian Fraser Kilmister
who was "killed by death"

Explanation of research done during this dissertation:

During this dissertation two topics were covered: in the main project the modulation effects of lung tissue in proton therapy were investigated. The results of this project as well as the corresponding publications are presented in detail in this dissertation. In a side project dosimetric problems in clinical proton beams were investigated. These results are not presented in detail but will be covered in a short manner at the end of this dissertation.

Erklärung der in dieser Dissertation bearbeiteten Projekte:

Im Laufe der Dissertation wurden neben dem Hauptthema der Untersuchung der Modulationseigenschaften von Lungengewebe in der Strahlentherapie mit Protonen noch dosimetrische Fragestellungen in der Protonentherapie behandelt. In dieser Dissertation wird vordergründig auf die Arbeiten aus dem Hauptthema eingegangen. Entsprechende Veröffentlichungen werden detailliert präsentiert und diskutiert. Die Ergebnisse aus dem Nebenprojekt werden am Ende dieser Dissertation kurz dargestellt.

Manuscripts published in Peer-Review Journals:

The present cumulative dissertation contains a compilation of the research results which were published in peer review journals. The main topic was the analysis of modulation effects of lung tissue in proton therapy. In a side project dosimetric problems in clinical proton beams were investigated. The following manuscripts were published or accepted for publication:

In Peer-Review Journalen veröffentlichte Arbeiten:

Die vorliegende kumulative Dissertation stellt eine Zusammenfassung der Forschungsergebnisse dar, die in Peer-Review Journalen veröffentlicht wurden. Neben dem Hauptthema der Modulationseigenschaften von Lungengewebe in der Protonentherapie wurden in einem Nebenprojekt dosimetrische Fragestellungen aus der Protonentherapie behandelt. Folgende Manuskripte wurden veröffentlicht bzw. zur Veröffentlichung angenommen:

Main project:

1: K.-S. Baumann, M. Witt, U. Weber, R. Engenhart-Cabillic, K. Zink, An efficient method to predict and include bragg curve degradation due to lung-equivalent materials in monte carlo codes by applying a density modulation, Physics in Medicine & Biology 62 (10) (2017) 3997-4016.

2: V. Flatten, **K.-S. Baumann**, U. Weber, R. Engenhart-Cabillic, K. Zink, Quantification of the dependencies of the bragg peak degradation due to lung tissue in proton therapy on a CT-based lung tumor phantom, Physics in Medicine & Biology 64 (15) (2019) 155005.

3: K.-S. Baumann, V. Flatten, U. Weber, S. Lautenschläger, F. Eberle, K. Zink, R. Engenhart-Cabillic, Effects of the bragg peak degradation due to lung tissue in proton therapy of lung cancer patients, Radiation Oncology 14 (183) (2019).

Side project:

4: J. Wulff, **K.-S. Baumann**, N. Verbeek, C. Bäumer, B. Timmermann, K. Zink, TOPAS/geant4 configuration for ionization chamber calculations in proton beams, Physics in Medicine & Biology 63 (11) (2018) 115013.

5: K.-S. Baumann, F. Horst, K. Zink, C. Gomà, Comparison of penh, fluka, and geant4/topas for absorbed dose calculations in air cavities representing ionization chambers in high-energy photon and proton beams, Medical Physics 46 (10) (2019) 4639-4653.

6: K.-S. Baumann, S. Kaupa, C. Bach, R. Engenhart-Cabillic, K. Zink, Monte carlo calculation of beam quality correction factors in proton beams using topas/geant4, Physics in Medicine & Biology 65 (5) (2020) 055015.

The publications are referenced in the text according to the order defined above with the numbers 1-6. Publications are printed with permission from Institute of Physics and Engineering in Medicine where necessary.

Die Publikationen werden im Text entsprechend der oben definierten Reihenfolge mit den Nummern 1-6 referenziert. Für die abgedruckten Publikationen gibt es, so erforderlich, eine Abdruckgenehmigung vom Institute of Physics and Engineering in Medicine.

Conference contributions:

During the dissertation results were presented at different conferences. The following list shows a selection of these conference contributions:

Konferenzbeiträge:

Im Laufe der Dissertationsarbeit wurden die Forschungsergebnisse auf verschiedenen Konferenzen präsentiert. Die folgende Liste zeigt eine Auswahl dieser Konferenzbeiträge:

ENLIGHT Annual Meeting 2016, Utrecht, Netherlands, poster presentation

PTCOG56, Yokohama, Japan, oral presentation

DEGRO23, Berlin, Germany, poster presentation

DGMP2017, Dresden, Germany, oral presentation

DPG-Frühjahrstagung 2018, Würzburg, Germany, oral presentation

ESTRO37, Barcelona, Spain, poster presentation

PTCOG57, Cincinnati, USA, poster presentation

DEGRO24, Leipzig, Germany, poster presentation

DGMP2018, Nuremberg, Germany, oral presentation

Third International Geant4 User Conference, Bordeaux, France, oral presentation

ESTRO38, Milan, Italy, oral presentation

PTCOG58, Manchester, United Kingdom, poster presentation

DEGRO25, Münster, Germany, poster presentation

DGMP 2019, Stuttgart, Germany, oral presentation as invited speaker

Arbeitskreistreffen des AK Monte Carlo der DGMP, Brunswick, Germany, oral presentation as invited speaker

ABSTRACT

Non-small cell lung cancer (NSCLC) is the number one cause of cancer-related deaths worldwide. Furthermore, it is predicted that the incidence and mortality will further increase due to smoking, increasing pollution of the environment, and an aging population. For patients unable to undergo surgery corresponding radiotherapy concepts are necessary. However, due to the vicinity of critical organs like the heart, esophagus, trachea, larger blood vessels, and the spinal cord a dose escalation is not always easily achievable using photon-based radiotherapy. Proton therapy (PT) has the potential to deposit a conformal dose in the target volume while better sparing surrounding normal tissue and hence could be beneficial for lung cancer patients. However, there are various challenges connected to proton therapy in general and proton therapy of lung cancer patients in particular. One of these challenges arises from the structure of the lung tissue itself: due to the microscopic density heterogeneity the proton dose distribution is degraded resulting in a broader Bragg peak and a wider distal dose fall-off. This modulation effect can significantly influence the dose distribution in patients resulting in a lower dose deposited in the target volume and higher doses deposited in distal normal tissue and organs at risk (OAR). Since the microscopic structure of the lung tissue is not fully resolved in clinical treatment-planning CT-images, a consideration of the Bragg peak degradation is not possible with current state-of-the-art treatment-planning systems (TPS).

In this dissertation, a mathematical model is used to describe the effects due to the Bragg peak degradation. The strength of the degradation is quantified using the material characteristic *modulation power*. Microscopic heterogeneous voxelized geometries are used to generate degraded dose distributions with the help of Monte Carlo (MC) simulations. Subsequently, these geometries representing human lung

tissue are replaced by clinical voxels with an edge length of 2 mm. Hence, the transition from the microscopic lung tissue as it is present in the patient to coarser clinical CT-structures that cannot resolve the fine lung structure is performed. By modulating the density of each clinical voxel the Bragg peak degradation can be reproduced. Hence, a solution is found to reproduce the lung modulation effects on clinical CT-images.

Using this technique, a CT-based phantom study was designed to estimate the effects of the Bragg peak degradation for realistic patient anatomies. Different tumor volumes located at different depths in the lung were investigated. It was shown that, if the lung modulation effects are not accounted for during the treatment-planning process, the dose deposited in the target volume is overestimated and the dose deposited in distal normal tissue is underestimated. This effect increases with an increasing depth of the tumor in lung and a decreasing extent of the tumor in beam direction.

At last, the effects were investigated for clinical treatment plans for lung cancer patients. The overestimation of the mean dose in the CTV was 5% at maximum and in the order of 2% on average. The effect on OARs distal to the target volume was negligible for all cases investigated. The investigation of treatment plans confirms that the lung modulation effects are clinically tolerable to a certain degree in the current clinical context considering the various more critical dose uncertainties due to motion and range uncertainties in proton therapy.

Nevertheless, PTV concepts were presented that could compensate for the lung modulation effects.

ZUSAMMENFASSUNG

Nicht-kleinzelliger Lungenkrebs ist weltweit die häufigste krebsbedingte Todesursache. Darüber hinaus ist anzunehmen, dass die Inzidenz und Mortalität aufgrund von Rauchen, der zunehmenden Umweltverschmutzung und der alternden Bevölkerung zunehmen wird. Für Patienten, die sich keiner Operation unterziehen können, sind entsprechende Strahlentherapiekonzepte notwendig. Aufgrund der Nähe von Risikoorganen wie dem Herzen, der Speiseröhre, der Luftröhre, größerer Blutgefäße und dem Rückenmark, ist eine Dosiseskalation im Tumor mit der photonenbasierten Strahlentherapie nicht immer möglich. Die Bestrahlung mit Protonen hat das Potenzial, eine konformale Dosis im Zielvolumen zu applizieren und gleichzeitig umliegendes Normalgewebe besser zu schonen. Es ergeben sich jedoch einige Herausforderungen im Zusammenhang mit der Protonentherapie im Allgemeinen und der Protonentherapie von Lungenkrebs im Besonderen. Eine dieser Herausforderungen ergibt sich aus der Struktur des Lungengewebes selbst: Aufgrund der mikroskopischen Dichteheterogenität kommt es zu einer Modulation der Tiefendosiskurve was einen verbreiterten Bragg Peak und einen größeren distalen Dosisabfall zur Folge hat. Dieser Modulationseffekt kann die Dosisverteilung bei Patienten signifikant beeinflussen, was potentiell zu einer niedrigeren Dosis im Zielvolumen und einer höheren Dosis im distalen Normalgewebe und Risikoorganen führen kann. Da die mikroskopische Struktur des Lungengewebes nicht vollständig in klinischen CT-Bildern aufgelöst wird, ist eine Berücksichtigung der Lungemodulationseffekte mit derzeitigen Bestrahlungsplanungssystemen nicht möglich.

In dieser Dissertation wird ein mathematisches Modell verwendet, um die Auswirkungen der Bragg-Peak-Verbreiterung zu beschreiben. Die Materialeigenschaft *Modulationsstärke* wird verwendet, um die Stärke der Lungenmodulation zu

quantifizieren. Eine heterogene, mikroskopisch voxelierte Geometrie wird verwendet, um mit Hilfe von Monte Carlo (MC) Simulationen modulierte Dosisverteilungen zu erzeugen. Anschließend werden diese voxelierten Geometrien, die menschliches Lungengewebe repräsentieren, durch gröbere Voxel klinischen Maßstabes ersetzt. Dies entspricht dem Übergang vom mikroskopischen Lungengewebe im Patienten zu den gröberen, klinischen CT-Strukturen, die das feine Lungengewebe nicht ausreichend auflösen. Durch Modulation der Dichte dieser klinischen Voxel kann die Bragg-Peak-Verbreiterung reproduziert werden. Es wurde also eine Lösung gefunden, die Lungenmodulationseffekte auf der Basis klinischer CT-Bilder zu reproduzieren.

Mit dieser Technik wurde eine CT-basierte Phantomstudie entwickelt, um die Auswirkungen der Bragg-Peak-Verbreiterung für realistische Patientenanatomien zu analysieren. Unterschiedliche Tumorvolumina in unterschiedlichen Tiefen in der Lunge wurden untersucht. Es wurde gezeigt, dass wenn die Lungenmodulation während der Bestrahlungsplanung nicht berücksichtigt wird, die Dosis im Zielvolumen überschätzt und die Dosis in distalem Normalgewebe unterschätzt wird. Dieser Effekt nimmt mit zunehmender Tiefe des Tumors in der Lunge und abnehmender Ausdehnung des Tumors in Strahlrichtung zu.

Außerdem wurden die Auswirkungen der Lungenmodulation auf klinischen Bestrahlungsplänen für Lungenkrebspatienten untersucht. Die Überschätzung der mittleren Dosis im CTV betrug maximal 5% und im Mittel ca. 2%. Für alle untersuchten Fälle war keine klinisch relevante Erhöhung der Dosis in distalen Risikoorganen zu erkennen. Die Ergebnisse zeigen, dass die Lungenmodulationseffekte im gegenwärtigen klinischen Kontext bis zu einem gewissen Grad tolerierbar sind. Insbesondere in Anbetracht der unter anderem kritischeren Dosisunsicherheiten aufgrund von Bewegung und allgemeinen Reichweiteunsicherheiten in der Protonentherapie.

Nichtsdestotrotz wurden PTV-Konzepte vorgestellt, die grundsätzlich im Stande sind, die Lungenmodulationseffekte während der Bestrahlungsplanung zu kompensieren.

Contents

List of Abbreviations

3DCRT	3-dimensional conformal radiotherapy
BED	biological equivalent dose
BERT	Bertini cascade model
BIC	Binary cascade model
CH	condensed history
CoP	Code of Practice
CPE	charged-particle equilibrium
CT	computer tomography
CTV	clinical target volume
DFW	distal fall-off width
DICOM	Digital Imaging and COmmunication in Medicine
DNA	desoxyribonucleic acid
DVH	dose-volume histogram
EM	electro-magnetic
FWHM	full-width-half-maximum
GTV	gross tumor volume
HU	Hounsfield unit
IMPT	intensity-modulated proton therapy
IMRT	intensity-modulated radiotherapy
LET	linear energy transfer
$\mathbf{LET}_{\mathrm{d}}$	dose-averaged linear energy transfer
LLN	law of large numbers
MC	Monte Carlo
MIT	Marburg Ion-Beam Therapy Center
MSC	multiple scattering
NSCLC	non-small cell lung cancer
OAR	organ at risk
P_{mod}	modulation power
PT	proton therapy
PTV	planning target volume

RBW	relative biological effectiveness
R_{CSDA}	continuous slowing down approximation range
SBRT	stereotactical body radiotherapy
SOBP	spread-out Bragg peak
TPS	treatment-planning system

List of Figures

Chapter 1

Introduction

1.1 Cancer and cancer treatment

Cancer is a serious cause of morbidity and mortality worldwide. In 2012 roughly 8.2 million cancer-related deaths were observed while in the same year approximately 12 million incidences were reported (IARC 2014). What is more, the number of incidences is expected to rise by about 70% until 2035 (IARC 2014), making cancer an increasing health issue. For men the three most common sites of cancer in 2012 were the lung (16.7% of the total), prostate (15.0%), and colorectum (10.0%). For women the three most common sites of cancer were the breast (25.2%), colorectum (9.2%), and lung (8.7%) (IARC 2014).
Cancer is commonly treated with either surgery, chemotherapy, radiotherapy or a combination of these three modalities while the therapy scheme depends individually on each patient case and tumor site. The aim of the treatment can either be curative or palliative. For the curative treatment the aim is to cure the patient while a successful curative treatment requires the removal of all tumor tissue or at least a completion of the tumor's growth and ability to spread. If that is not possible, a palliative approach is used to improve the life quality of the patient by relieving the patient of some pain and symptoms related to the disease.
Radiotherapy plays and important role in the treatment of cancer-related diseases. After surgery it is the most frequently used modality. Over 50% of all patients with localized tumors are treated with radiation (Schardt et al. 2010). The goal of radiation therapy is to damage the DNA in the cell nucleus by using ionizing radiation and hence making the tumor cell non-survivable (Lomax et al. 2013). The number of DNA damages is proportional to the energy deposited. Hence, the chance of killing the tumor cell increases with an increase in dose deposited in the tumor cells. However, cell damages in the surrounding healthy tissue must be kept low enough to avoid severe side effects. The challenge of radiotherapy is to optimize the treatment in order to deposit enough dose in the tumor region to cure the patient (for the curative treatment approach) while side effects are kept reasonable low. The ionizing radiation can be applied in two different ways: in teletherapy the ionizing radiation is applied from outside the patient's body (tele, meaning "at a distance"') while

in brachytherapy a radioactive source is inserted inside the tumor region (brachy, meaning "short distance").
Several different radiation types are clinically used for teletherapy: in the "conventional" radiotherapy ("conventional" since it was the first to be clinically applied) high-energy photons in the MeV energy range are used. For the treatment of shallow regions like skin high-energy electrons in the same energy range can be deployed due to the short range of electrons in tissue. At last, in particle therapy heavy charged particles in the ∼100 MeV/u range such as protons or heavier ions (He^{4+} or C^{12+}) are used. This work focuses on the external irradiation with protons only.

1.2 Proton therapy

Since the radiological use of fast protons has been proposed in 1946 (Wilson 1946), the significance of proton therapy (PT) as a treatment modality is continuously growing worldwide. Over 200 000 patients are treated per year (PTCOG 2019a) in almost 100 facilities (PTCOG 2019b) while many more facilities are under construction (PTCOG 2019c).
The most important advantage of PT compared to conventional radiotherapy is the more beneficial dose deposition in the patient: as shown in figure 1.1, photons develop an initial dose build-up in matter followed by an exponential decrease in dose[1] leading to a theoretically infinite range of the radiation. In contrast, the dose profile of protons consists of a low-dose plateau at small depths followed by a dose maximum, the so-called Bragg peak (Bragg and Kleeman 1905), where most of the energy is deposited. The Bragg peak is followed by a sharp dose fall-off. Distal to that fall-off almost no dose is deposited in the case of protons and only small doses for heavier ions (Kraft 2000; Schardt et al. 2010). The background for these different dose shapes lies in the kind of interactions of the particles with matter: photons are indirectly ionizing which means that in a first step, the photon's energy has to be transferred to secondary particles like electrons via collisions. Subsequently, these secondary particles in turn transfer the gained energy to the medium mostly by coulomb interactions. The initial dose build-up in photon beams is a result of the production of secondary particles. The depth of the dose maximum is approximately equal to the range of the secondary particles which is in the order of ∼1.5-3.5 cm for clinical energies (Podgorsak 2003). The exponential decrease in dose is due to the attenuation of the photon's fluence since photons are absorbed or scattered during the collisions with secondary particles.
In contrast to photons, protons are directly ionizing. On their way through matter they constantly loose energy via coulomb scattering, mostly with shell electrons of the penetrated material. Hence, the mean energy of protons decreases with depth

[1] Note that the decrease in dose is not exactly exponential but is also depending on $1/r^2$ with r being the distance to the source. However, for clinical setups the exponential part is dominant.

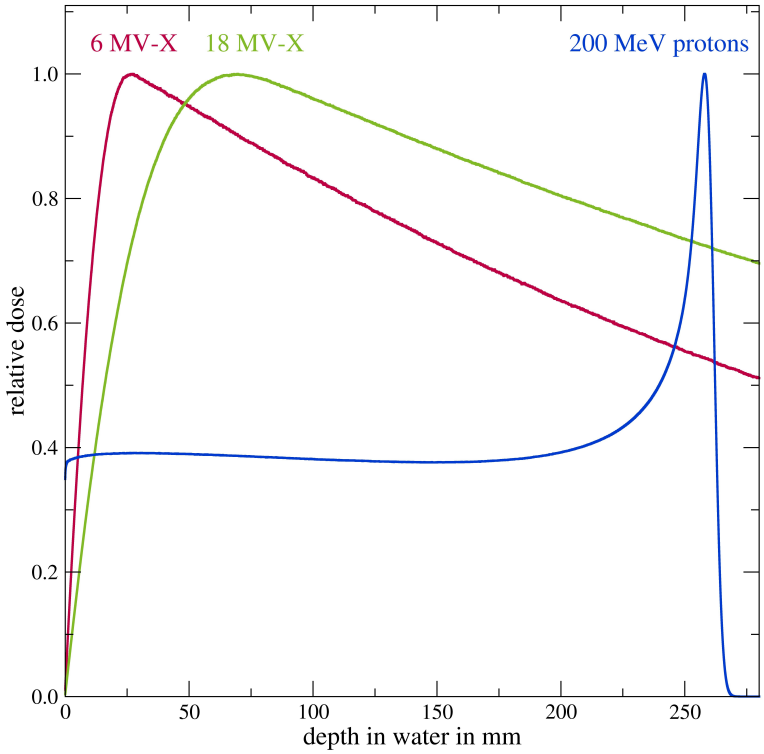

Figure 1.1: Depth-dose curves for clinical photon and proton beams in water.

in medium until they stop. The energy loss of protons is characterized by the so-called stopping power which consists of the nuclear stopping power (due to nuclear interactions) and the electronic stopping power (due to coulomb interactions with charged particles - mostly electrons). For protons with clinical energies the electronic stopping power dominates. This electronic stopping power theory is well-described by Bethe and Bloch (Bethe 1930; Bloch 1933) and several corrections for this formula exist (Ziegler 1999; Kraft 2000). The electronic stopping power $\mathrm{d}E/\mathrm{d}x$ can be calculated as follows:

$$\begin{aligned} \frac{\mathrm{d}E}{\mathrm{d}x} &= \kappa \frac{Z_P^2}{\beta^2} \frac{Z_T}{A_T} \rho \left[\frac{1}{2} \ln \left(\frac{2 m_\mathrm{e} c^2 \beta^2 \gamma^2 T_\mathrm{max}}{I} \right) - \beta^2 - \frac{\delta(\beta\gamma)}{2} \right] \\ \kappa &= \frac{4\pi}{m_\mathrm{e} c^2} \left(\frac{e^2}{4\pi\epsilon_0} \right)^2 N_A \end{aligned} \tag{1.1}$$

m_e is the electron mass, c the velocity of light in vacuum, ϵ_0 is the vacuum permittivity and N_A is the Avogadro constant. Z_P is the charge of the projectile while Z_T

and A_T are the atomic number and mass of the target material. $\beta = v/c$ is the relative velocity of the projectile and $\gamma = 1/\sqrt{1-\beta^2}$ is the Lorentz factor. The energy $T_{\max}$ is the maximum energy that can be transferred to an electron in a coulomb interaction and I is the mean ionization potential of the target material. $\delta(\beta\gamma)/2$ is the density effect correction term which becomes relevant at relativistic energies and accounts for the deformation of the electric field of the projectile.
The stopping power is proportional to $1/\beta^2$ and hence, at the end of a proton's range (where the proton's energy is smallest) the energy deposit is largest resulting in the Bragg peak. Due to the $1/\beta^2$ dependency the range of protons and thereby the position of the Bragg peak is defined by the initial energy E_0. Furthermore, the electronic stopping power depends on the target material's characteristics (namely atomic number, mass, and (electron) density). As a result, the range of protons highly depends on the patient's anatomy which leads to challenges in PT as described in section 1.4.
Since the coulomb scattering is a statistical process, fluctuations occur in the energy deposition of a proton traversing a material. Hence, the net energy loss per traveled distance has to be described by a probability distribution (Bohr 1915; Vavilov 1957; Ahlen 1980; Bichsel et al. 2000). Due to this energy loss straggling the ranges of protons of the same energy are different and their stopping positions are shifted against each other. As a result, the Bragg peak is enlarged. The width of the Bragg peak increases with an increasing depth in medium and hence an increasing initial energy.
To deliver proton beams two approaches are clinically used: passive scattering and active scanning. The passive scattering technique uses passive beam elements to model the beam in order to meet clinical requirements. Scattering foils are used to spread the beam laterally while compensators and collimators shape the beam according to the patient-specific tumor geometry. A modulator wheel is used to create a spread-out Bragg peak (SOBP) covering the tumor's extension in beam direction. Hence, a conformal dose distribution is achieved in the complete tumor volume using only one proton beam with a specific energy. Although historically motivated, the passive beam scattering technique has been replaced by the active scanning technique in most facilities. In active beam scanning systems, the dose is delivered to the tumor volume step by step using a pencil beam. The tumor is scanned laterally using dipole magnets and in depth by changing the initial energy. In general, the integral dose is lower when using the active scanning technique compared to the passive scattering technique (Schippers and Lomax 2011; Kase et al. 2011). Furthermore, with active scanning systems an intensity-modulated proton therapy (IMPT) is possible (Schippers and Lomax 2011). Additionally, except for the beam monitor system no further beam elements are used and thus, the production of undesired secondary particles, such as neutrons, is significantly lower. For passive scattering systems the dose contribution due to secondary particles is up to ten times higher compared to active scanning systems (Agosteo et al. 1998; Yan

et al. 2002).
Active scanning is more time consuming compared to the passive scattering technique. It depends on the tumor volume, the spot scan size, the Bragg peak width, and the time the accelerator needs to switch the proton energy. Using fast degraders, the energy can be switched in milliseconds at modern cyclotrons (Lomax et al. 2004; Pedroni et al. 2011). Still, this longer irradiation times make pencil beam scanning vulnerable to intrafractional motion effects as described in section 1.4.

1.3 Rationale for proton therapy of lung cancer patients

In a review by Chang *et al.* (Chang et al. 2016) the potential benefits and problems related to PT of early stage and locally advanced non-small cell lung cancer (NSCLC) patients as well as an overview of important clinical studies are presented. This chapter is in parts a summary of the most important and relevant aspects of this review. Additionally, various other relevant clinical studies and research results are being presented as well.
NSCLC is worldwide the number one cause of cancer-related deaths (Chang et al. 2016). Furthermore, it is predicted that the incidence and mortality will further increase due to smoking, increasing pollution of the environment, and an aging population (Chang et al. 2016).
For early stage lung cancer patients, anatomical resection is the standard procedure (Timmerman et al. 2010). However, patients might not be able to undergo surgery due to restrictions like emphysema, heart disease or age. For these medically inoperable lung cancer patients, conventional radiotherapy is an alternative.
Studies have shown that a dose escalation with >100 Gy (BED) delivered with photon-based radiotherapy leads to local control rates greater than 95% and increases the overall survival compared to surgery for early stage I NSCLC patients (Timmerman et al. 2010; Shirvani et al. 2014; Chang et al. 2015, 2016). However, in locally advanced NSCLC this dose escalation with photons is limited due to the vicinity of organs at risk (OAR) like the heart, trachea, and esophagus, with potential rates of severe toxicities of grade >3 of 76-79% (Chang et al. 2016). Hence, PT might be an interesting alternative for the treatment of NSCLC patients. In the clinical routine mainly two approaches for the use of PT have evolved (Chang et al. 2016): the first approach is to escalate the dose in the target volume while allowing the same dose to normal tissue and OARs compared to conventional therapy. The second possibility is to spare the normal tissue and OARs compared to conventional therapy while the same dose is applied to the target volume. The first approach is most applicable for NSCLC patients with poor local control when using conventional radiotherapy (Chang et al. 2016). In a virtual clinical study by Zhang *et al* (Zhang

et al. 2010) it was shown that it is possible to safely deliver higher doses to locally advanced NSCLC with PT than with photon-based intensity-modulated radiotherapy (IMRT), under the condition that the dose-volume constraints for normal tissues are the same for both modalities. Since the sparing of normal tissue like lung, esophagus, heart, and spinal cord is easier achieved in PT compared to IMRT, it was possible to escalate the dose from 63 Gy (RBE) to 74 Gy (Zhang et al. 2010; Chang et al. 2016).

The second approach is most applicable in difficult anatomical situations where the tumor is near to sensitive structures like heart, esophagus, trachea, large blood vessels, and the spinal cord. Several studies showed that the integral dose to normal tissue can be reduced in PT compared to conventional radiotherapy, even when compared to modern IMRT (Lomax et al. 1999; Nill et al. 2004; Macdonald et al. 2009; Hoppe et al. 2010; Register et al. 2011; Loeffler and Durante 2013). Although the integral dose to normal tissue can be reduced in PT, it was noted that the dose delivered to the skin and chest wall is slightly higher for cases where less than three proton beams were used (Macdonald et al. 2009; Chang et al. 2016). However, by using more proton beams ($\sim$4 different beam directions) (Welsh et al. 2013) or for example arc proton therapy (Seco et al. 2013), the dose to the skin and chest wall could be reduced if clinically demanded (Chang et al. 2016).

Although it can be shown in dosimetric studies that patients potentially benefit from PT in terms of improved dose-volume histograms (DVH), this does not mean that this dosimetric benefit automatically translates into an approved clinical benefit (Chang et al. 2016).

For early stage NSCLC several studies showed that 2-years local control rates of 80-100% can be achieved with PT (Shioyama et al. 2003; Nihei et al. 2006; Hata et al. 2007; Nakayama et al. 2010; Chang et al. 2016). However, since techniques like image-guidance systems increase the robustness of photon-based SBRT, similar rates can be achieved with SBRT (Sonke et al. 2009; Grutters et al. 2010; Timmerman et al. 2010; Shirvani et al. 2014; Chang et al. 2015; Harada and Murayama 2017). Additionally, most of the early stage NSCLC are small peripheral lesions that are not located in the vicinity of critical structures, hence, dose escalation is often also possible with photon-based SBRT (Chang et al. 2016).

Locally advanced (stage III) NSCLC are usually large primary tumors that are in the vicinity of critical structures (Chang et al. 2016). Additionally, locally advanced NSCLC occur together with mediastinal nodes resulting in a bad prognosis due to high local failure and metastasis (Chang et al. 2016). The current standard treatment is concurrent chemotherapy with thoracic radiotherapy (Harada and Murayama 2017). PT can spare more healthy tissue, especially OARs like the heart, compared to photon-based radiotherapy(Chang et al. 2006; Nichols et al. 2011; Ohno et al. 2015), while it is possible to deliver a comparable dose to the target volume (Chang et al. 2011; Oshiro et al. 2014; Nguyen et al. 2015; Hoppe et al. 2016; Chang et al. 2016). However, it was shown, that esophageal toxicities in high-dose PT occur

(Oshiro et al. 2014; Chang et al. 2011). Thus, the dose escalation with the use of PT stays a demanding task (Harada and Murayama 2017). In a phase II study by Chang *et al* (Chang et al. 2011), 44 patients with stage III NSCLC were treated with protons in combination with chemotherapy. A 74 Gy (radiobiologic equivalent) was applied in 37 fractions. No grade 4 or 5 toxicities were observed while some grade 3 toxicities (dermatitis, esophagitis and pneumonitis) occurred. The median survival was 29.4 months compared to 20.3 months for the regime treated with 74 Gy photons (RTOG 0617).
In conclusion, dosimetric studies show that PT can spare healthy tissue compared to photon-based radiotherapy, which is important due to the anatomical challenges in thoracic cancers, especially the vicinity of OARs. However, these dosimetric advantages do not automatically translate into clinical benefits inducing a demand for clinical studies (Chang et al. 2016).

1.4 Challenges related to proton therapy

In this section general as well as lung-specific challenges related to PT are described. The main challenge is due to the proton's finite range that strongly depends on the irradiated material. Thus, changes in the patient's anatomy that are not accounted for can affect the dose deposition and hence the treatment outcome severely. These changes can be due to weight loss, motion during irradiation, a shift in the positioning of the patient or a shrinkage of the tumor (Unkelbach et al. 2007; Hui et al. 2008; Paganetti 2012; Szeto et al. 2016). In particular, the interfractional anatomical change demands for plan adaption strategies in PT (Hoffmann et al. 2017). Szeto *et al* (Szeto et al. 2016) showed that an undercoverage of the target volume of up to 14 GyE can occur when the treatment plan is not adapted to the daily anatomy of the patient. Additional, a maximum increase of 4.7 GyE in the D_1 (dose that is received by 1% of the volume) in OARs was observed.
Furthermore, the range of protons and the dose deposition is calculated on CT-images in the current clinical practice (Arbor et al. 2015). These CT-images provide tissue attenuation coefficients that are converted to stopping powers for the calculation of proton ranges and energy loss using a stoichiometric calibration (Schneider et al. 1996). Several studies have investigated range uncertainties of protons due to such a conversion, while predicted range uncertainties ranged from 0.8% (Matsufuji et al. 1998; Chvetsov and Paige 2010) to 3% (Schaffner and Pedroni 1998; Yang et al. 2012; Arbor et al. 2015). As a result of these range uncertainties, safety margins are used to account for these range uncertainties. Different margin concepts are used clinically that enlarge the target volume by between 2.5%(of the range)+1.5 mm and 3.5%+3 mm depending on the center (Paganetti 2012). It is obvious that these margins decrease the potential of sparing normal tissue which is one of the main advantages in PT. In order to reduce the extent of the safety margins, several range

verification techniques like prompt gamma imaging (Smeets et al. 2012; Richter et al. 2016), PET imaging (Parodi and Enghardt 2000; Enghardt et al. 2004; Parodi et al. 2007; Knopf et al. 2008) or ionoacoustic detection (Assmann et al. 2015; Lehrack et al. 2017) are being developed and partly clinically implemented at the time.
Range uncertainties are also due to uncertainties in biological effectiveness models (Paganetti 2012; Carabe et al. 2012). The relative biological effectiveness (RBE) is defined as the ratio of the photon dose (as reference) and the proton dose that is necessary to cause the same effect in terms of the same clinical end point. The RBE depends on the delivered dose, end point, particle type, dose-averaged linear energy transfer ($\mathrm{LET_d}$) and tissue type (characterized by the α/β coefficient) (Paganetti 2012; Carabe et al. 2012). A constant RBE of 1.1 for protons is usually used clinically due to a lack of data that would be necessary to model the biological effectiveness more accurately (Paganetti 2012). However, it is known that the RBE strongly correlates with $\mathrm{LET_d}$. Since the $\mathrm{LET_d}$ increases at the distal end of the Bragg peak, the biological effective range reaches farther compared to the physical dose range, causing a shift of about 1-2 mm (Paganetti 2012).
Especially for the irradiation of lungs, motion plays an important role for scanned proton beams, since the motion of the lung interferes with the pencil beam (Bert et al. 2008). The resulting interplay effects lead to an inhomogeneous dose in the target and to a reduced target coverage (Bert and Durante 2011; Grassberger et al. 2013; Dowdell et al. 2013). Due to interplay effects the volume receiving 95% of the prescribed dose can decrease to 70% for one fraction (Bert et al. 2008). When applying more fractions the interplay effects might be compensated partially. However, especially for small fraction numbers motion mitigation techniques are demanded when treating moving targets with scanned proton beams (Bert et al. 2008). Current solutions include robust planning, gating, rescanning or tracking (Stuschke et al. 2012; Bert et al. 2007; Engwall et al. 2018; Lu et al. 2007; Kanehira et al. 2017).

1.5 Modulation effects of lung tissue

Another challenge in PT of lung cancer patients arises from the lung tissue itself. The lung is structured in tubular branches, the bronchi, which transport the inhaled air into the lung. These bronchi divide into smaller and smaller branches, the so-called bronchioles, which end in microscopic clusters of air sacs, the alveoli (Webpage 2019). These clusters of air sacs are surrounded by the interstitium, a layer of cells, that contains blood vessels and supports the alveoli (Webpage 2019). While the alveoli are filled with air with a low physical density of $\sim$1 mg/cm^3, the density of the interstitium is roughly 1 g/cm^3. This microscopic density heterogeneity of the lung tissue has an effect on the range of the protons traversing the lung: depending on the path of the protons through the lung, different compositions of low-density and high-density regions will lead to different energy losses resulting in variable ranges

of the protons and thus a broadened Bragg peak and a larger distal dose fall-off. This modulation of the dose distribution due to heterogeneous structures like the lung is also called degradation of the Bragg peak and has already been described in 1986 (Urie et al. 1986): dose distributions in a water phantom were measured for different heterogeneous geometries that were placed in the particle beam. The full-width-half-maximum (FWHM) of the Bragg peak as well as the distal fall-off width (DFW) were investigated demonstrating the Bragg peak degradation. In another study by Sawakuchi *et al.* (Sawakuchi et al. 2008) the Bragg peak degradation was investigated with the help of Monte Carlo (MC) studies and virtual, voxelized geometries where the voxels were either bone or air. They analyzed the change in the energy spectrum of the protons due to the different energy losses and developed a model to predict the change in the DFW in dependence of the energy spectrum.
Clinically, the degradation of the Bragg peak can significantly influence the dose distribution in lung cancer patients (España and Paganetti 2011) and lead to an underdosage of the target volume and an overdosage of distal normal tissue (Sawakuchi et al. 2008; Sell et al. 2012; Titt et al. 2015). Hence, the Bragg peak degradation should be considered during the treatment-planning process of lung cancer patients (Titt et al. 2015). However, typical CT-scanners do not fully resolve the heterogeneous structure of the lung tissue due to the restricted resolution and hence merge the microscopic structures of the lung into larger voxels (España and Paganetti 2011; Titt et al. 2015). As a result of that, a more homogeneous density distribution is predicted. Hence, it is hardly possible to consider the Bragg peak degradation based on typical CT-images. The fact that the density is averaged in CT-images can lead to differences in the Bragg peak dose of up to 11% while the distal edge degradation can be as large as 1.1 mm in water for clinical proton beams (Perles et al. 2011).
In a study by Titt *et al.* (Titt et al. 2015) the modulation effects of lung tissue were investigated using a high-resolution 3d-printed phantom as a lung substitute. The phantom was built up of microscopic voxels that consisted of plastic or air. Depth dose distributions in water downstream from that phantom were measured as well as MC simulated for a 150 MeV and 200 MeV proton beam. Additionally, proton beams penetrating CT-images of the 3d-printed phantom were simulated and compared to the measurements and simulations of the true geometry. For the simulations based on the CT-images of the phantom the distal dose fall-off was underestimated by up to 2 mm in water (corresponding to $\sim$10 mm in lung tissue), and the dose in the Bragg peak was overestimated by up to $\sim$35% (Titt et al. 2015). Additionally, a plastinated human lung was irradiated to demonstrate the Bragg peak degradation. The DFW was increased by up to 60% compared to an unperturbed pristine dose distribution. At last, the authors proposed a mathematical model to describe the degraded dose distributions: the degraded dose distribution can be estimated by shifting an unperturbed pristine dose distribution by the water-equivalent thickness of the phantom and by applying a convolution with a normal distribution.
This mathematical model was also described and further evaluated in other stud-

ies (Witt 2014; Witt et al. 2015; Ringbæk et al. 2017). By including the shift due to the water-equivalent thickness of the heterogeneous material directly into the normal distribution, the degraded dose distribution can be estimated immediately by convolving the unperturbed pristine dose distribution with that adapted normal distribution (without the need of additionally shifting the unperturbed dose distribution). From the mean value μ and standard deviation σ of the normal distribution, the material characteristic *modulation power* (P_{mod}) can be derived as $P_{\mathrm{mod}} = \sigma^2/\mu$. The modulation power has the unit length in water and is independent on the geometrical thickness of the heterogeneous material. Additionally, it can easily be determined experimentally in proton beams by measuring depth dose distributions with and without lung tissue probes in the beam. Subsequently, the parameters μ and σ of the normal distribution have to be optimized in order to minimize the difference between the degraded dose distribution and the convolution of the unperturbed dose distribution with the normal distribution.
Witt (Witt 2014) determined experimentally the modulation power of an ex-vivo porcine lung. For each measurement the position at which the lung was irradiated as well as the respiratory state of the lung were varied. The modulation powers were in the range of 300 μm to 750 μm. Since complete lungs were positioned in the beam, the so-measured modulation power corresponds to an integrated modulation power. However, the modulation power might depend on the position within the lung due to differences in the structure size of the alveoli and bronchioles. For most measurements the modulation power was in the range from 300 μm to 500 μm with an average of 450 μm. For one measurement the modulation power was 750 μm, since due to the lung's positioning a large bronchial structure was in the beam.
Additionally, high-resolution CT-images of human lung samples with a resolution of 4 μm were investigated in order to verify whether the measured modulation powers for porcine lungs are applicable for human lung tissue. The so-gained modulation powers for human lung tissue were in the range of 50 μm to 250 μm. However, the human lung tissue samples were prepared using a "critical point drying" method (Litzlbauer et al. 2006), resulting in loss of water and hence mass of up to 37%. As a consequence, the size of the structures of the lung tissue was reduced resulting in a smaller modulation power.
In conclusion, several studies have observed and described the modulation effect of lung tissue in PT and the resulting Bragg peak degradation. A mathematical model has been developed to estimate the degraded dose distribution starting from an unperturbed pristine dose distribution. The quantity modulation power P_{mod} has been introduced that quantifies the Bragg peak degradation. First measurements with ex-vivo porcine lungs and high-resolution CT-images of human lung samples suggest that the modulation power is in the range of some hundred μm water-equivalent. The main problem is that the fine structure of the lung tissue is not fully resolved in typical treatment-planning CT-images. Hence, the geometrical information is lost and it is, until now, not possible to estimate the potential effects due to the Bragg

peak degradation clinically. Especially, the potential underdosage of the target volume and overdosage of distal normal tissue cannot be approximated, yet.

1.6 The Monte Carlo code TOPAS/GEANT4

The Monte Carlo (MC) method is a technique that is widely used in the field of medical physics and is an important tool for scientific research questions connected to radiation transport. It was originally presented by Metropolis and Ulman (Metropolis and Ulam 1949) and is used to solve problems by repeating a random experiment multiple times. Following the law of large numbers (LLN), the average of the results that are obtained from a large number of randomly sampled, independent trials converges to the expected value (Dekking 2005). Concerning radiation transport applications connected to medical physics, the MC method provides a numerical solution of the Boltzmann transport equation (Bielajew 2001), while all underlying physical parameters like absorption and scattering cross-sections must be provided using corresponding formulas or data tables. Over the time many different MC codes have been developed that were designed and optimized to satisfy the specific needs of a certain research field.
One example is the multipurpose MC code GEANT4 (GEometry And Tracking) (Agostinelli et al. 2003) that was primarily designed for high-energy physics applications. It was shown that by adjusting the transport parameters, it can be used for medical physics applications and especially for dosimetric calculations in PT (Baumann et al. 2019c). For the studies in this dissertation the toolkit TOPAS (TOol for PArticle Simulation) (Perl et al. 2012) was used that is based on the MC code GEANT4. Previous studies have extensively validated TOPAS against experimental data (Perl et al. 2012; Testa et al. 2013). Since TOPAS is based on GEANT4, it uses the same physics models, processes, and interaction cross sections as GEANT4. It is capable of transporting a large variety of particles including photons, electrons, positrons, neutrons, protons, and heavy ions over a large energy range including the clinically relevant energies.
Since computing time is an important issue when using MC codes, different approaches are used to reduce the computing time. However, in general, these approaches come at the expense of the accuracy and the user has to adjust the corresponding parameters depending on the research question. In order to reduce computing time, in GEANT4 electromagnetic (EM) interactions of charged particles are grouped in the condensed history (CH) approach. The deflection at the end of a CH step is calculated using a multiple scattering (MSC) algorithm. The user can choose between various MSC theories including the Urban model (Urban 2002), the Goudsmit-Saunderson model (Goudsmit and Saunderson 1940a,b) and the WentzelVI model (Ivanchenko et al. 2010). The length of a CH step is limited by tracking limits, such as geometric boundaries and physics-related parameters such

as the parameter *dRoverR*. It determines the maximum length of one single step in relation to the residual range of the particle. Due to collisions, particles loose energy on their way through a medium and hence, the CH step length decreases until it is smaller than the *finalRange*. As soon as the CH step length gets smaller than the *finalRange*, the particle is ranged out in a single step and its residual energy is deposited locally.
The parameter controlling the production of secondary particles is given in units of length in GEANT4. Only particles with an energy high enough that the corresponding *continuous slowing down approximation range* (R_{CSDA}) is greater than or equal to the production cut range are produced. All other particles are absorbed on the spot and their energy is deposited locally.
To verify the accuracy of the CH transport algorithms implemented in a MC code, the so-called Fano cavity test can be performed, which is the most stringent test (Rogers 2006; Sterpin et al. 2014). The Fano theorem states that, as long as a medium is in charged particle equilibrium (CPE), the electron fluence is independent of the physical density as long as the cross sections ($/(\mathrm{g\,cm^{-2}})$) are independent of the physical density (Rogers 2006). For GEANT4 it was shown that the Fano cavity test is violated by less than 0.2% for clinical photon (O'Brien et al. 2016) and proton beams (Wulff et al. 2018).
Since TOPAS is developed for the clinical use in PT, it includes various features like modeling beam monitor systems or passive scattering facilities as well as performing dose calculations on patient-specific data (Perl et al. 2012). It is capable of importing CT-images via the dicom standard (Digital Imaging and COmmunication in Medicine). To convert HU values into stopping powers the conversion table by Schneider *et al.* (Schneider et al. 1996) is implemented by default - however, any desired conversion table can be used. Since TOPAS has a time feature, the dicom position and orientation as well as the beam quality can be changed within a simulation and after any amount of simulated primaries. Additionally, various physical quantities like dose, fluence or energy deposition can be scored within the dicom. Hence, the calculation of complete treatment plans is possible in TOPAS.

Chapter 2

Aim of this dissertation

The ultimate aim of this dissertation was to clinically quantify the effects of the Bragg peak degradation due to lung tissue in PT. Additionally, these effects shall be discussed in a clinical context considering the various range and dose uncertainties connected to PT of lung cancer patients as described in chapter 1.4.
The main problem remains that the fine structure of the lung tissue is not fully resolved in typical treatment-planning CT-images. Hence, the geometrical information is lost and it is hardly possible to estimate the potential effects due to the Bragg peak degradation clinically. However, with the help of measurements of ex-vivo lungs or high-resolution CT-images of human lung samples, the modulation power P_{mod} of lung tissue can be determined experimentally which quantifies the Bragg peak degradation. Based on this modulation power, a solution must be found to reproduce the Bragg peak degradation on typical treatment-planning CT-images.
In a next step, this solution shall be used to investigate the dependencies of the effects of the Bragg peak degradation on different anatomical scenarios. With the help of CT-based phantoms, the dependencies on tumor volume, tumor shape and depth of the tumor in the lung can be characterized.
At last, the effects have to be investigated for clinical treatment plans. By calculating treatment plans with and without including the Bragg peak degradation, the potential underdosage of the target volume and overdosage of distal normal tissue as well as OARs can be evaluated for different treatment scenarios for patient-specific cases.
Since MC codes provide various features and can be adjusted individually, all studies from this dissertation are MC based using the toolkit TOPAS that is based on the MC code GEANT4.

Chapter 3

Summary of the results and contributions

In this chapter the results of each published article are presented. At the end of the chapter the contributions of each author are being constituted.

3.1 Summary of results

3.1.1 Article 1

In the first article (Baumann et al. 2017), a voxelized geometry was used as a representative of human lung tissue to produce degraded dose distributions in a water phantom. The voxels consisted of either air with a physical density of $\rho_\mathrm{a} = 0.0012$ g/cm^{-3} or solid lung material with a physical density of $\rho_\mathrm{l} = 1.05$ g/cm^{-3}. The average density ρ_mean of the geometry is controlled by the fraction p_l of solid lung material voxels. For this study p_l was set to 0.25 in order to achieve an average density of 0.26 g/cm^3, which is the density of an inflated lung (Schneider et al. 1996). The probability F that the water-equivalent thickness of a random path through this voxelized geometry equals t' is described by a normal distribution:

$$F(t'|t,\sigma_t) = \frac{1}{\sqrt{2\pi\sigma_t^2}} \cdot \exp\left(-\frac{(t'-t)^2}{2\sigma_t^2}\right) \tag{3.1}$$

where t is the average water-equivalent thickness of the voxelized geometry and σ describes the strength of the degradation due to this heterogeneous geometry. The parameters are calculated as follows:

$$t = \frac{\rho_\mathrm{mean}}{\rho_{\mathrm{H_2O}}} \cdot D \quad \text{with} \quad \rho_\mathrm{mean} = p_\mathrm{l} \cdot \rho_\mathrm{l} + (1-p_\mathrm{l}) \cdot \rho_\mathrm{a} \approx \rho_\mathrm{l} \cdot p_\mathrm{l} \tag{3.2}$$

where D is the geometrical thickness of the voxelized geometry in beam direction, $\rho_{\mathrm{H_2O}} := 1$ g/cm^3, and ρ_mean is the average water-equivalent density of the geometry.

The approximation takes into account that $\rho_\mathrm{a} \ll \rho_\mathrm{l}$.
σ_t^2 is calculated as follows:

$$\sigma_t^2 = \frac{D}{d} \cdot p_\mathrm{l} \cdot (1 - p_\mathrm{l}) \cdot d^2 \cdot \left(\frac{\rho_\mathrm{l} - \rho_\mathrm{a}}{\rho_{H_2O}} \right)^2 \approx t \cdot d \cdot (1 - p_\mathrm{l}) \cdot \frac{\rho_\mathrm{l}}{\rho_{\mathrm{H_2O}}} \tag{3.3}$$

where d is the size of each voxel in beam direction. Note that the thickness D of the complete geometry is $n \cdot d$ while n is the number of voxels in beam direction. Furthermore, it is assumed that the water-equivalent density of the solid lung material is equal to its physical density, since the solid lung material consists of over 85% water.
The function $F(t'|t, \sigma_t)$ describing the voxelized geometry can also be used to estimate the degraded dose distribution due to this heterogeneous geometry as shown in figure 3.1 (this figure corresponds to figure 1 in **article 1**): when convolving an unperturbed pristine dose distribution $b_0(z)$ with $F(t'|t, \sigma_t)$, the result equals the degraded dose distribution $b_*(z)$:

$$b_*(z) = \big(F \ * \ b_0\big)(z) = \int_{-\infty}^{\infty} F(t'|t, \sigma_t) b_0(z + t') \mathrm{d}t' \tag{3.4}$$

The mean value t describes the shift of the dose distribution and σ_t describes the broadening. This concept is in agreement with other studies (Witt 2014; Witt et al. 2015; Titt et al. 2015; Ringbæk et al. 2017). Note that t describes the shift of the depth z_{p82} at which the dose of the distal fall-off is 82% of the maximum dose. The background is the energy loss straggling theory as described in chapter 1.2: the energy loss is a statistical effect that is described by a probability distribution. The maximum of this distribution corresponds to an energy loss that results in a range equal to z_{p82} (Bichsel et al. 2000).
The modulation power P_mod describing the modulation strength of the voxelized geometry can be derived from the normal distribution $F(t'|t, \sigma_t)$ using t and σ_t:

$$P_\mathrm{mod} \equiv \frac{\sigma_t^2}{t} \approx d \cdot (1 - p_\mathrm{l}) \cdot \frac{\rho_\mathrm{l}}{\rho_{\mathrm{H_2O}}} \tag{3.5}$$

The modulation power P_mod is directly proportional to the size d of the voxels in beam direction. This size of the voxels is the analogue to the size of the microscopic structures in the lung. Hence, the larger the microscopic structure of the lung the larger the modulation effect. Note that it is also possible to derive the normal distribution $F(t'|t, \sigma_t)$ from the modulation power P_mod for a geometry of thickness D via $t = \rho_\mathrm{mean}/\rho_{\mathrm{H_2O}} \cdot D$ and $\sigma_t^2 = P_\mathrm{mod} \cdot t$. Hence, the mathematical model can be used either way: for an arbitrary voxelized geometry the corresponding modulation power can be derived using the normal distribution and from the measured modulation power of an heterogeneous material the corresponding normal distribution can be derived. The mathematical model and the modulation power are a construct

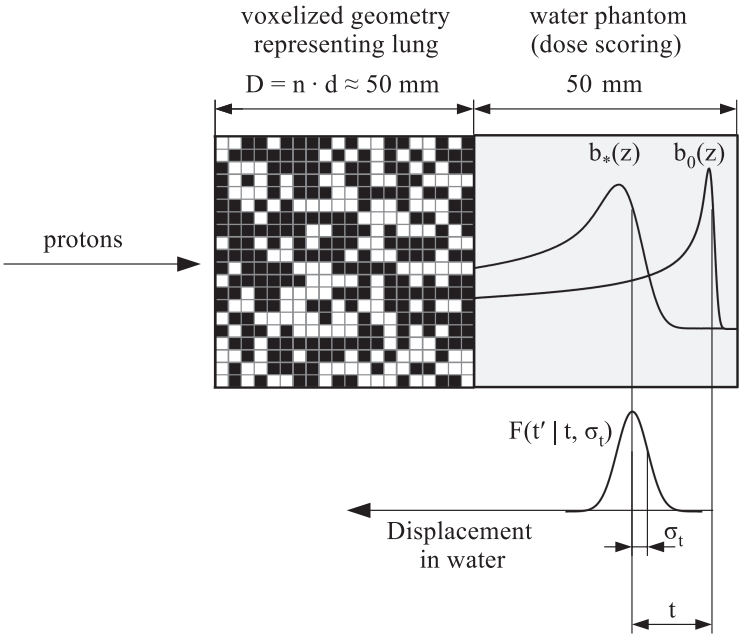

Figure 3.1: Schematic description of the mathematical model: the binary voxelized geometry consists of air (black voxels) and solid lung material (white voxels). An unperturbed reference curve $b_0(z)$ and a broadened dose distribution $b_*(z)$ are shown. The broadening and displacement of $b_*(z)$ can be described by the convolution of the reference curve with a normal distribution $F(t'|t, \sigma_t)$ giving the probability that the path a particle is taking through the voxelized geometry has a water-equivalent thickness t'. The displacement of $b_*(z)$ is given by the mean value t. The broadening is given by the value of σ_t. Figure taken from (Baumann et al. 2017).

that is based on dose distributions measured or calculated in water. Hence, t, σ_t and P_{mod} and physical densities have to be understood in water-equivalent units.
To investigate the effects due to lung modulation, different microscopic voxelized geometries with a thickness D in beam direction of $D \approx 50$ mm were created. The voxel size d was varied for each of these geometries. Values for d between $\sim$130 μm and $\sim$1000 μm were chosen in order to achieve modulation powers between 100 μm and 800 μm which is the range of determined modulation powers of human lung tissue samples and porcine lungs (Witt 2014). Using these voxelized geometries, degraded dose distributions as well as an unperturbed pristine dose distribution were

calculated in a water phantom downstream from the voxelized geometries with the MC code TOPAS/GEANT4. Subsequently, the modulation powers of the simulated voxelized geometries were determined by optimizing the parameters t and σ_t of a normal distribution in order to fulfill equation (3.4). From the parameters t and σ_t the modulation power was calculated as $P_{\mathrm{mod}} = \sigma_t^2/t$. In order to validate the mathematical model, these modulation powers from the simulations were compared to the theoretical modulation powers as calculated with equation (3.5). The maximum difference between simulated and theoretical modulation powers was 26 μm ($\hat{=}$ 3.7%). Additionally, the distal fall-off widths (DFW) from 80% to 20% of the maximum dose were investigated. For the unperturbed pristine dose distribution it was 0.9 mm, while for the degraded dose distributions it varied between 1.9 mm (for $P_{\mathrm{mod}} = 100$ μm) and 4.2 mm (for $P_{\mathrm{mod}} = 800$ μm), demonstrating the broadening of the Bragg peak due to the modulation effect of heterogeneous materials. It was shown that the depth z_{p82} was the same for all modulated dose distributions. It was shifted by 13.2 mm towards z_{p82} of the unperturbed pristine dose distribution. This shift corresponds to the prediction of the value t from the mathematical model.
Since clinical CT-scanners do not resolve the microscopic structures of the lung tissue, a solution is needed to reproduce the modulation effects of lung tissue on typical treatment-planning CTs. In order to reproduce the modulating effect, the energy loss of the single protons has to be modulated resulting in a variation of the proton's range. Following the electronic stopping power theory by Bethe and Bloch (Bethe 1930; Bloch 1933) (compare equation (1.1)), the energy loss of a particle is proportional to the geometrical thickness of the penetrated material as well as its density. Since the size of the voxels in a CT-image can hardly be altered, the solution lies in modulating the density of the voxels. A corresponding probability distribution $F(\rho'|D)$ describing the probability that a voxel of thickness D has the water-equivalent density ρ' can directly be derived from the normal distribution $F(t'|t,\sigma_t)$ by substituting the water-equivalent thickness t' with $\rho' = t'/D \cdot \rho_{\mathrm{H_2O}}$.
However, for small values of D, especially when D equals the size of CT-voxels, the normal distribution $F(t'|t,\sigma_t)$ can be positive for negative values of t' as shown in figure 3.2 (this figure corresponds to figure 2 in **article 1**). In that case the normal distribution cannot be used. Thus, a different distribution $\overline{F}(t'|D)$ has to be developed that has no negative contributions and describes the distribution of water-equivalent thicknesses t' for a thin target of thickness D, in this case a CT-voxel.
To do so, in a first step the normal distribution $F_T(t'|t,\sigma_t)$ from equation (3.1) with $t = \rho_{\mathrm{mean}}/\rho_{\mathrm{H_2O}} \cdot T$ and $\sigma_t^2 = P_{\mathrm{mod}} \cdot t$ is derived for a sufficiently thick target of thickness $T = n \cdot D$ with $n \in \mathbb{N}$, assuring that $F_T(t'|t,\sigma_t) \approx 0$ for $t' < 0$.

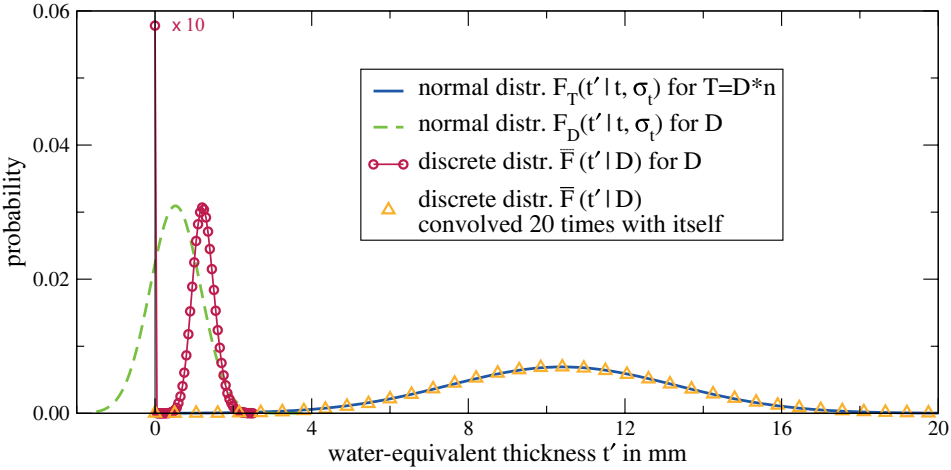

Figure 3.2: Deriving the distribution of water-equivalent thicknesses for clinical voxels of size D. In solid line the normal distribution for a target of size $T = n \cdot D$ with $n = 20$. In dashed line the normal distribution for $D = 2$ mm having non-negligible contributions for negative water-equivalent thicknesses. In circles the optimized discrete distribution consisting of a Poisson distribution and a single weight w_0 at $t' = 0$ mm. The weight w_0 is scaled with a factor of 0.1 for better visibility. The circles are connected to guide the eye. The result when convolving this distribution 20 times with itself is shown in triangles. Figure taken from (Baumann et al. 2017). © Institute of Physics and Engineering in Medicine. Reproduced with permission. All rights reserved.

In order to construct $\overline{F}(t'|D)$, the following requirements have to be fulfilled:

- $\overline{F}(t'|D)$ consists of single weights w_i based on fine steps of e.g. $\Delta = 50$ μm: $w_i = \overline{F}(t' = i \cdot \Delta|D)$ with $\sum w_i = 1$
- $\overline{F}(t'|D) = 0$ for $t' < 0$
- $\overline{F}(t'|D)$ convolved n times with itself equals the normal distribution $F_T(t'|t, \sigma_t)$:

$$\underbrace{\overline{F}(t'|D) \ * \ \overline{F}(t'|D) \ ... \ * \ \overline{F}(t'|D)}_{n \text{ times}} \approx F_T(t'|t, \sigma_t) \tag{3.6}$$

The last requirement is the most important one: it assures that n thin targets of thickness D have the same physical properties (such as average density and modu-

lation effects) as the thick target of thickness $T = n \cdot D$.
To construct $\overline{F}(t'|D)$, a shifted Poisson distribution was used in combination with a single weight w_0 at $t' = 0$. This weight accounts for the negative contribution of the normal distribution for small targets of size D. The shifted Poisson distribution is defined only for positive values and has a similar shape compared to a normal distribution making it an optimal candidate. The Poisson distribution was generalized for non-integers by replacing the factorial function by the Gamma function. $\overline{F}(t'|D)$ was determined by optimizing w_0 and the parameters of the shifted Poisson distribution in order to best fulfill equation (3.6).
In figure 3.2 an exemplary distribution $\overline{F}(t'|D)$ is shown for a voxel size D of 2 mm and a modulation power $P_{\mathrm{mod}} = 800$ μm. Generalizing from this optimized function $\overline{F}(t'|D)$ the density-probability function $F(\rho'|D)$ can be derived by substituting the water-equivalent thickness t' with $\rho' = t'/D \cdot \rho_{\mathrm{H_2O}}$.
After optimizing the density-probability function $F(\rho'|D)$, the microscopic voxelized geometries with voxel sizes d between $\sim$130 μm and $\sim$1000 μm were replaced in the MC code TOPAS$/$GEANT4 by voxelized geometries consisting of clinical voxels with an edge length of $D = 2$ mm. This replacement represents the transition from the microscopic heterogeneous structure and hence the lung tissue as it is in the patient to coarser structures and hence the clinical CT-image of the lung. Density probability distributions $F(\rho'|D)$ were derived for $D = 2$ mm and for each modulation power as designed in the first simulations. Subsequently, dose distributions in a water phantom downstream from the clinical voxels were calculated while the density of each of the $2{\times}2{\times}2$ mm^3 voxles was modulated individually following $F(\rho'|D)$. In order to reduce the computing time, the voxels were not modulated for each simulated particle. Instead, 500 different sets of individually modulated voxels were generated and used for the simulation. The depth dose distributions that were created using the clinical voxels and a modulated density (MD) are shown in figure 3.3 (this figure corresponds to figure 6 in **article 1**) for two exemplary modulation powers. Additionally, the depth dose distributions from the microscopic voxelized geometries (BD for binary density since the voxels consist of either air or solid lung material) are shown for comparison. By modulating the density of the clinical CT-voxels the degraded dose distributions from the microscopic voxelized geometries can be reproduced almost perfectly. Subsequently, modulation powers for the geometries consisting of clinical voxels were derived and compared to the modulation powers from the microscopic voxelized geometries. The maximum difference between both modulation powers was 19 μm ($\hat{=}$ 2.7%). Again, the DFW from 80% to 20% of the maximum dose were investigated. For all modulation powers the difference in DFW between the microscopic voxelized geometry and the geometry consisting of clinical voxels was 0.1 mm or even smaller. The difference in z_{p82} between both geometries was 0.2 mm at maximum. Hence, the degraded dose distributions produced with the microscopic voxelized geometries representing human lung tissue can be reproduced on the basis of clinical voxels when the density of these voxels is being modulated

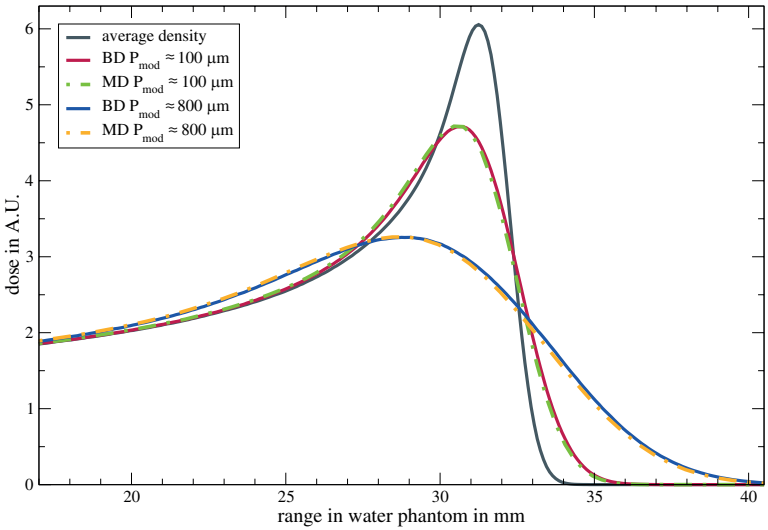

Figure 3.3: Depth dose distributions created using the microscopic voxelized geometries (BD) and the voxels of clinical sizes with a modulated density (MD) for two exemplary modulation powers. Additionally, the dose distribution when the density of the voxels is not modulated but kept constant at the average density. Figure taken from (Baumann et al. 2017).

correspondingly.
Furthermore, the dose distribution in a water phantom was calculated when the density of the clinical voxels was not modulated but kept constant at the average density. This represents the actual clinical case where the microscopic structure of the lung tissue is not resolved in treatment-planning CT-images and hence an average density is assigned to each voxel. In that case, the Bragg peak degradation was not being reproduced and the dose distribution was as narrow as the unperturbed pristine dose distribution resulting in a DFW from 80% to 20% of the maximum dose of 0.9 mm.

3.1.2 Article 2

In the second article (Flatten et al. 2019), this technique of modulating the density in order to reproduce the Bragg peak degradation on the basis of clinical CT-images was used to analyze the effects due to the lung modulation. Therefore, CT-based

phantoms were created representing a human lung while artificial tumors of different volumes were located at different positions within the lung. These phantoms consisted of two slabs of water each 2 cm thick that were separated by 25 cm of lung tissue. Hence, these phantoms represent the lung enclosed by the thorax wall and the mediastinum or other distal tissue. The density of the lung tissue in each voxel was set to 0.26 g/cm^3 which is the density of an inflated lung (Schneider et al. 1996). The CT-voxels were 1.5×1.5×1.5 mm^3 large. The artificial tumors that were placed within the lung were represented by spheres or ellipsoids with a density of 1 g/cm^3. These CT-based phantoms correspond to a clinical treatment-planning CT where the microscopic structure of the lung tissue is not resolved and a homogeneous density is predicted.
In order to extensively evaluate the effects of the Bragg peak degradation, the following parameters were investigated (compare figure 2 in **article 2**):

- **Depth of tumor in lung:** six different depths of the tumors in the lung were investigated: 2 cm, 4 cm, 6 cm, 10 cm, 15 cm, and 20 cm. The depth d_{L} of the tumors corresponds to the distance between the entrance wall and the center of the tumor.

- **Volume of the tumor:** six different spherical tumors with volumes of 1 cm^3, 2 cm^3, 6 cm^3, 14 cm^3, 25 cm^3, and 43 cm^3 were investigated.

- **Shape of the tumor:** the shape of lung tumors can be non-spherically which might have an effect on the Bragg peak degradation. Hence, two different elliptical tumor volumes were investigated with volumes of 9 cm^3 and 19 cm^3.

For each CT-based phantom a treatment plan was optimized using the commercially available treatment-planning system (TPS) Eclipse version 13.7 (Varian). Each plan consisted of one single beam perpendicular to the entrance wall of the CT-based phantom. The lateral spot spacing was 60% of the FWHM of the beam spot. The energy spacing was varied between 1 MeV for small tumor volumes and 3 MeV for larger tumor volumes. No motion was considered. The planning target volume (PTV) was the gross tumor volume (GTV) -in this case all voxels identified as tumor- plus an isotropic margin of 3 mm. The prescribed dose was 30 Gy RBE to be applied in a single fraction.
All treatment plans were subsequently recalculated with TOPAS/GEANT4. Both in Eclipse and in TOPAS/GEANT4 the same beam data were used. The beam data were commissioned to match the beam delivery system at the Marburg Ion-Beam Therapy Center (MIT). The ionization chambers and multi-wire chambers of the beam monitor system were modeled in TOPAS/GEANT4. The source parameters

like initial proton energy, beam divergence and spot size were optimized so that calculated depth dose curves, spot sizes, and dose cubes matched measurements performed at MIT.
The calculation of treatment plans optimized with Eclipse were performed in two scenarios in TOPAS/GEANT4: in a first scenario, the density of each voxel in the lung was not modulated but set to a constant value of 0.26 g/cm^3. This non-modulated case corresponds to the prediction from the TPS that does not consider the heterogeneity of the lung tissue. In a second scenario, the density of each voxel in the lung was modulated according to modulation powers of 250 μm, 450 μm, and 800 μm. The dose distribution from this modulated case corresponds to the dose distribution as it would occur in the patient due to the lung modulation. By comparing the dose distributions from the non-modulated and the modulated case the effects due to the Bragg peak degradation can be investigated. The modulation powers were chosen in order to cover both the average and extreme modulation powers as measured by Witt (Witt 2014). By using a modulation power of 800 μm a conservative estimation of the effects due to the lung modulation is possible.
The general effects due to the Bragg peak degradation were investigated by means of depth dose curves and dose-volume histograms (DVH) as shown in figure 3.4 (this figure corresponds to figure 3 in **article 2**). The Bragg peak degradation leads to a lower dose at both the proximal and especially the distal end of the target region compared to the prediction from the TPS. Additionally, a higher dose is deposited in distal normal tissue. Hence, the TPS overestimates the dose deposited in the PTV and underestimates the dose deposited in distal normal tissue. The underdosage of the GTV can clearly be seen in the DVH. The underdosage of the GTV increases with an increasing modulation power.
In order to investigate the dependency of the Bragg peak degradation on the depth of the tumor in lung and the tumor's volume, the difference in average dose D_{mean} deposited in the PTV between the non-modulated and modulated case was determined for all CT-based phantoms. In figure 3.5 (this figure corresponds to figure 4 from **article 2**) the difference in D_{mean} is shown in dependency on the depth d_{L} of the tumor in lung for the different tumor volumes. The difference in D_{mean} increases with an increasing d_{L}. Additionally, it increases with a decreasing tumor volume. The difference in D_{mean} is almost directly proportional to d_{L} while the slope of the line depends on the tumor volume. For the smallest $d_{\mathrm{L}} = 2$ cm and the largest tumor volume (43 cm^3) the Bragg peak degradation leads to a reduction of D_{mean} by less than 1%. For the largest $d_{\mathrm{L}} = 20$ cm and the smallest tumor volume (1 cm^3) the difference in D_{mean} is $\sim$-8%. For the largest $d_{\mathrm{L}} = 20$ cm and the largest tumor volume (43 cm^3) the difference in D_{mean} is $\sim$-3%.
For the ellipsoid-shaped tumors it was found that the difference in D_{mean} depends on the orientation of the tumor rather than on its volume: for the short axis being parallel to the beam axis the underdosage of the PTV was up to three times larger compared to when the long axis was parallel to the beam axis. An empirical

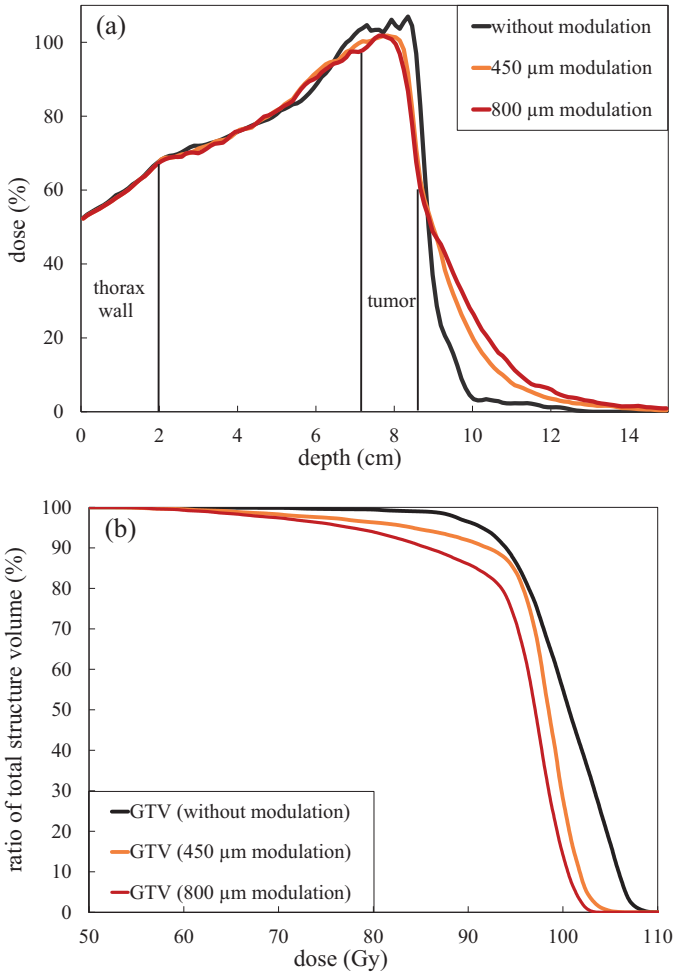

Figure 3.4: Depth-dose curve (a) and the corresponding dose-volume histogram (DVH) (b) with and without simulation of the lung modulation effect for two exemplary modulation powers. The modulating lung tissue starts at a depth of 2 cm. The position of the tumor volume is indicated by black lines. The depth dose curve in panel (a) and the corresponding dose-volume histogram in panel (b) feature a small tumor volume. Figure taken from (Flatten et al. 2019).

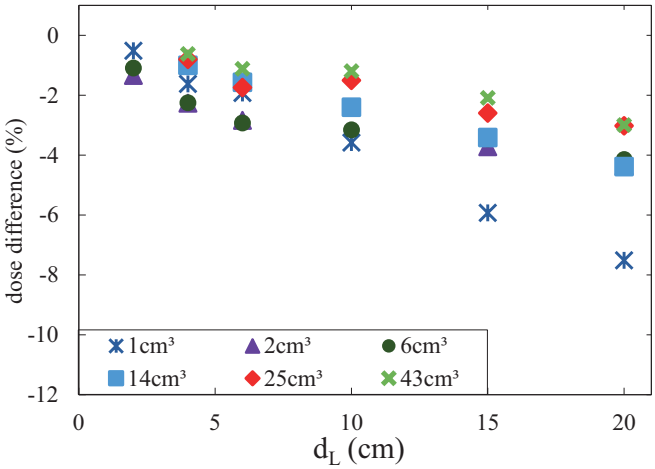

Figure 3.5: Difference in the mean dose due to the Bragg peak degradation for the spherical tumor volumes in dependency on the depth of the tumor in lung d_{L}. In this case the results for a modulation power of 450 μm are shown. Figure taken from (Flatten et al. 2019).

parameter L_{s} was found to describe both the tumor volume and its shape:

$$L_{\mathrm{s}} = 2 \cdot \frac{a^2}{\sqrt{b \cdot c}} \tag{3.7}$$

a denotes the axis of the ellipsoid parallel to the beam while b and c denote the lateral axes perpendicular to the beam. L_{s} can be understood as the scaled length of the tumor in beam direction. Using this scaled tumor length, the effect of the Bragg peak degradation is directly proportional to the term $d_{\mathrm{L}}/L_{\mathrm{s}}$ combining the parameters tumor volume, shape, and depth of the tumor in lung. Figure 3.6 (this figure corresponds to figure 7 in **article 2**) shows the difference in D_{mean} for all CT-based phantoms investigated in the study in dependence on $d_{\mathrm{L}}/L_{\mathrm{s}}$. With an increasing $d_{\mathrm{L}}/L_{\mathrm{s}}$ and hence a larger depth of the tumor in the lung and a smaller scaled tumor length, the difference in D_{mean} increases linearly. The slope is larger for larger modulation powers of the lung tissue. By using a linear fit for each modulation power the effects due to the Bragg peak degradation can be estimated for any clinically possible tumor scenario.
At last, the influence on the longitudinal spot spacing on the effects due to the Bragg peak degradation was analyzed. The effects were smaller for a wider spot spacing of 3 MeV compared to 1 MeV. The background is that plans with a wider

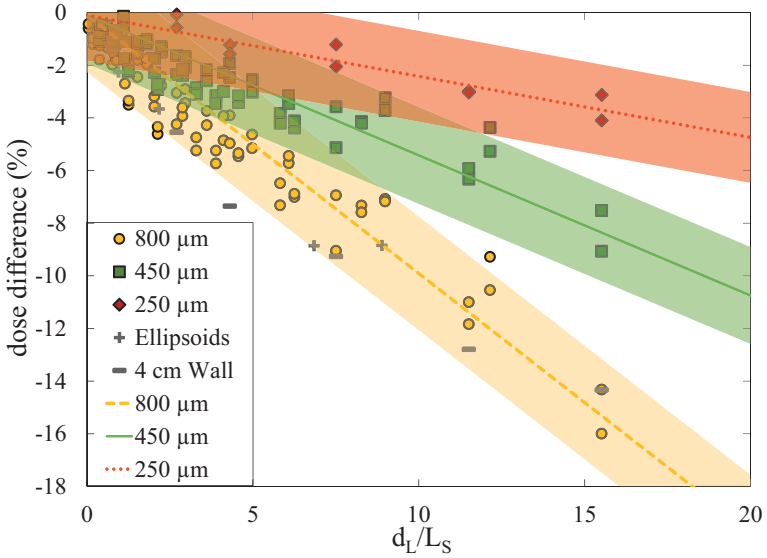

Figure 3.6: Difference in the mean dose in % for all CT-based phantoms investigated in dependency on the depth of the tumor in lung (d_L) divided by the scaled tumor length (L_s). Additionally, a fit through all data points for each of the three modulation powers investigated is shown. The 2σ ranges of the fits are visualized by a red, green or yellow band, respectively. Figure taken from (Flatten et al. 2019). © Institute of Physics and Engineering in Medicine. Reproduced with permission. All rights reserved.

energy spacing often have a worse conformity compared to plans with a narrower spot spacing. In that case, the Bragg peak degradation has a smoothing effect on the dose distribution. Due to this smoothing effect the dose profile is flattened but the reduction in the mean dose D_{mean} is not as large as when compared to plans with a higher conformity where the smoothing effects more likely result in a larger reduction of D_{mean}.
The lateral spot spacing has no significant influence on the effects of the Bragg peak degradation.

3.1.3 Article 3

In the third article (Baumann et al. 2019b), clinical treatment plans of NSCLC patients were investigated to quantify the effects of the Bragg peak degradation for

clinical cases and to give a conservative approximation of the lung modulation effects.
Five exemplary clinical cases with tumor volumes between 2.7 cm^3 and 46.4 cm^3 were investigated. The tumors were located either at the center of the lung or the vicinity of soft tissue as well as organs at risk (OAR), especially the spinal cord. No tumors were located near the chest wall in order to always have lung tissue between the thorax wall and the tumor and hence in the beam path. Although small tumor volumes might not benefit from PT compared to photon-based SBRT as described in chapter 1.3, small tumor volumes were investigated anyway. The background is that such small tumors have been treated at different centers (Hata et al. 2007; Bush et al. 2004; Chen et al. 2019) and hence an investigation of these tumor volumes is reasonable. Additionally, following the results from **article 2** the effects of the Bragg peak degradation increase with a decreasing tumor volume. Hence, by investigating such small tumor volumes an upwards estimation of the lung modulation effects can be made.
For all patients treatment plans were optimized with Eclipse v.13.7 (VARIAN). The total prescribed dose was 30 Gy (RBE) and the only planning objective was to deliver at least 95% of that prescribed dose to at least 98% of the PTV. The PTV was the CTV plus an isotropic margin of 3 mm. The treatment plans were optimized on static CT data ignoring movements of the anatomy due to respiration. For each patient three different treatment plans were optimized as shown in figure 3.7 (this figure corresponds to figure 1 in **article 3**): each plan consisted of one single field coming from either 0°, 270° or 315°. The plans were chosen to be simple in order to highlight the effects due to the Bragg peak degradation. The use of different beam directions enables scenarios with different depths of the tumor in the lung and different relative positions of the PTV and OARs, especially cases where the OAR is located distal to the PTV since the Bragg peak degradation leads to an enhanced dose distal to the PTV. The depths of the tumors in lung were between 1.5 cm and 12.2 cm depending on the patient and beam direction as shown in table 1 in **article 3**. The distal spot spacing was 3 mm and the lateral spot spacing was 0.45 times the FWHM of the beam spot. At last, two exemplary IMPT plans were optimized for the patients with the largest and smallest tumor volume to investigate the lung modulation effects on more complex treatment plans. Multi-field optimization was enabled to optimize three fields for each plan. The same PTV concept and planning objectives were used as for the simple plans.
Analogue to **article 2**, all treatment plans were subsequently calculated in TOPAS/GEANT4 in two different scenarios: in the non-modulated case the density of the voxels associated with the lung was not modulated but the average values as predicted by the CT were taken. In the modulated case the density of the voxels associated with the lung were modulated according to modulation powers P_{mod} of 100 μm, 250 μm, 450 μm, and 800 μm to cover the whole range of modulation powers determined for human lung tissue samples and ex-vivo porcine lungs (Witt

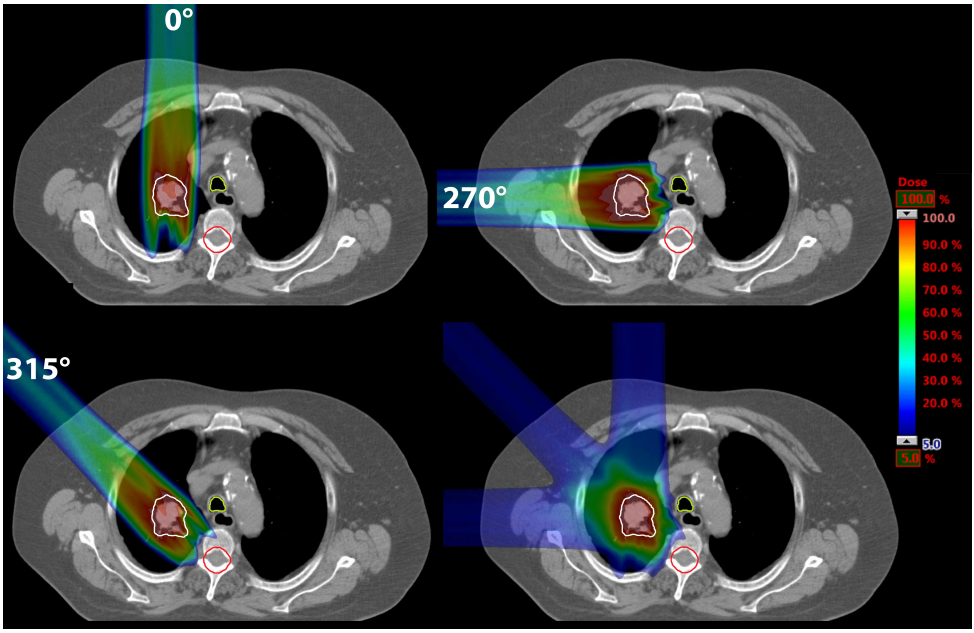

Figure 3.7: CT slices of one exemplary patient: for the beam directions 0°, 270°, and 315° plans were optimized individually consisting of one single field. On the bottom right the sum of these plans is shown. The CTV is marked in white, trachea in light green and spinal cord in red. On the right a color bar is given indicating the relative dose. Figure taken from (Baumann et al. 2019b).

2014) with some additional buffer. By comparing the dose distributions from both scenarios, the effects due to the Bragg peak degradation can be analyzed.
As shown in **article 2**, the lung modulation leads to an underdosage of the PTV and an overdosage of distal normal tissue if not accounted for in the treatment-planning process. This effect is visualized in figure 3.8 (this figure corresponds to figure 6 in **article 3**): exemplary isodose lines (ICRU 1993, 1999) are shown for 95%, 80%, and 20% of the prescribed dose for the non-modulated and modulated case for selected treatment plans. For all cases the region of the 95% and 80% isodose lines is smaller for the modulated case compared to the non-modulated case and hence the prediction from the TPS demonstrating the underdosage of the target volume. Additionally, the range of the 20% isodose lines is greater in the modulated cases. This greater range of the 20% isodose lines demonstrates the potential overdosage of distal normal tissue and OARs - especially for the cases, where the tumor is located near to an OAR. However, the maximum additional range of the 20% isodse lines

is 2 mm in soft tissue and 5 mm in lung tissue. For the 95% and 80% isodose lines the maximum loss in range is 8 mm (for 95% isodose lines) and 10 mm (for 80% isodose lines) in lung tissue. In soft tissue the maximum loss in range is 4 mm (for 95% isodose lines) and 3 mm (for 80% isodose lines).
Additionally, the effects of the Bragg peak degradation were investigated in terms of the mean dose D_{mean} deposited in the CTV as well as the dose values $D_{98\%}$ (dose that is received by 98% of the volume) and $D_{2\%}$. For the CTV the underdosage due to the lung modulation effects was increasing for a) an increasing modulation power P_{mod}, b) an increasing depth of the tumor in lung, and c) a decreasing tumor volume. No systematic differences between D_{mean}, $D_{98\%}$, and $D_{2\%}$ were observed. The maximum underdosage was $\sim$5% for $P_{\text{mod}} = 800$ μm. The average underdosage was in the order of 2%. Note that $P_{\text{mod}} = 800$ μm is an extreme modulation power. For a more common modulation power of 450 μm the maximum underdosage of the CTV was roughly 3% with an average underdosage of $\sim$1%. For smaller modulation powers there were cases where the underdosage of the CTV was smaller than 0.5%. Concerning OARs, effects due to the Bragg peak degradation were only seen for scenarios where an OAR was located distal to the CTV. The overdosage was up to 24% in terms of D_{mean}, however, this large relative overdosage corresponds to low absolute dose values of only 0.3 Gy at maximum.
A gamma index analysis was performed to assess these dose deviations clinically. For each treatment plan the dose distributions from the non-modulated and the modulated scenario were compared. For a gamma index 3%/1 mm (local) the passing rates were 90.4% or larger for a modulation power of 800 μm. The average passing rate for all treatment plans was 96.8%. For a modulation power of 450 μm the minimal passing rate was 93.1% and the average passing rate was 98.5%.
At last, IMPT plans were investigated in order to evaluate whether the results for the simple treatment plans consisting of only one field can be used to estimate the dose uncertainties due to the Bragg peak degradation on more complex plans. The dose reductions in the CTV were -1% and -3% for the two plans investigated and for a modulation power of 450 μm. Hence, the dose uncertainties for complex IMPT plans are in the order of the dose reductions observed for the simple treatment plans.

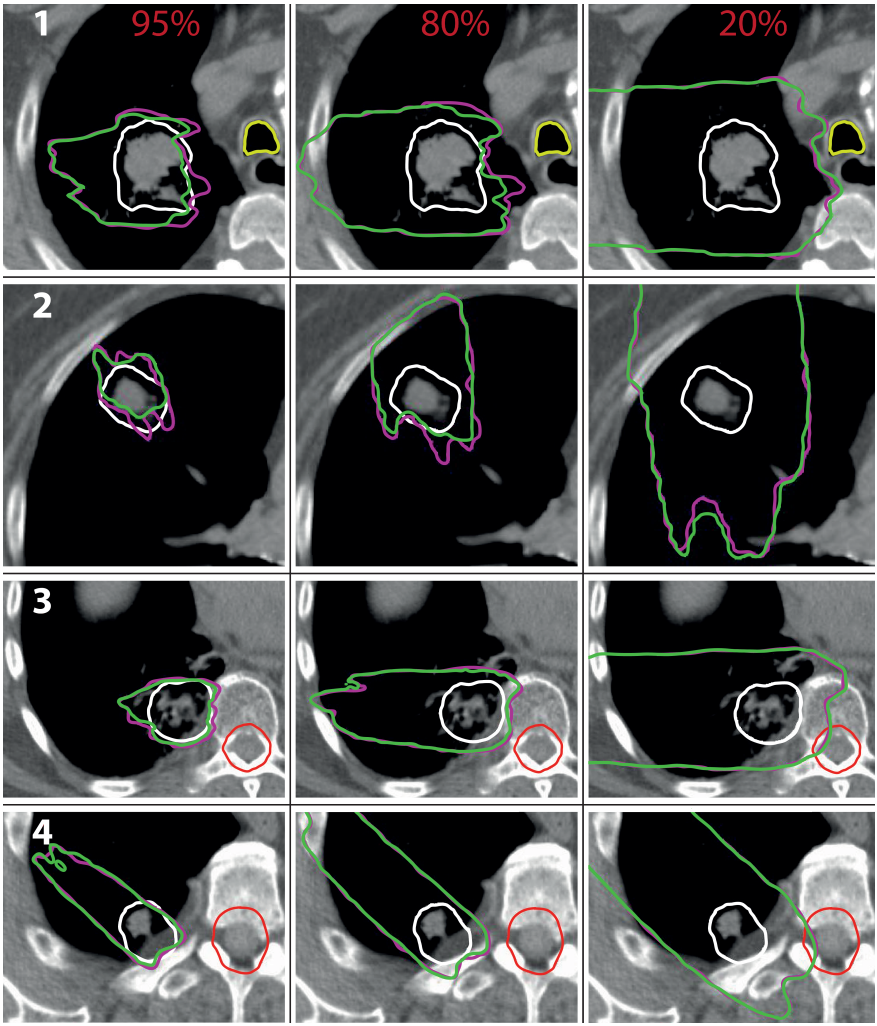

Figure 3.8: Isodose lines for 95%, 80%, and 20% of the prescribed dose. In pink for the non-modulated case, in green for the modulated case based on a modulation power of 800 μm. In the first column the 95%, in the middle column the 80%, and in the right column the 20% isodose lines. Different patient cases are marked in white numbers. The CTV is marked in white, the trachea in light green and the spinal cord in red. Figure taken from (Baumann et al. 2019b).

3.2 Contributions

Article 1:

K.-S. Baumann created the voxelized geometries and applied the density probability functions. K.-S. Baumann performed all MC simulations and analyzed the data. K.-S. Baumann wrote the manuscript and created all figures.
M. Witt contributed to this study with his experimental investigations of modulation powers using ex-vivo porcine lungs. M. Witt helped with the simulation of high-resolution CT images of human lung samples.
U. Weber came up with the idea of modulating the density of lung voxels. U. Weber originally had the idea of the mathematical model describing voxelized geometries. U. Weber created the tool to optimize the density probability functions. U. Weber substantively revised this manuscript.
R. Engenhart-Cabillic substantively revised this manuscript and was supervising the work. R. Engenhart-Cabillic helped with the clinical assessment.
K. Zink substantively revised this manuscript and was supervising the work. K. Zink helped with the physical assessment.

Article 2:

V. Flatten designed the study. V. Flatten optimized all treatment plans and wrote the script to export the treatment plans into TOPAS/GEANT4. V. Flatten analyzed the simulation results. V. Flatten wrote the manuscript and created all figures.
K.-S. Baumann helped with the design of the study and created all CT-based phantoms. K.-S. Baumann created the density modulated CT-based phantoms and executed the MC simulations as well as commissioned the beam monitor system of the Marburg Ion-beam therapy center used in TOPAS/GEANT4. K.-S. Baumann helped with analyzing the simulation results.
U. Weber came up with the idea of modulating the density of lung voxels. U. Weber originally had the idea of the mathematical model. U. Weber created the tool to optimize the density probability functions.
R. Engenhart-Cabillic substantively revised this manuscript and was supervising the work. R. Engenhart-Cabillic helped with the clinical assessment.
K. Zink substantively revised this manuscript and was supervising the work. K. Zink helped with the physical assessment.

Article 3:

K.-S. Baumann used the mathematical model to generate the density modulation functions needed for the density modulation to reproduce the Bragg peak degradation in the MC simulations. K.-S. Baumann created the density modulated DICOM sets and executed the MC simulations as well as designed the beam monitor system of the Marburg Ion-beam therapy center used in TOPAS/GEANT4 for all simulations. K.-S. Baumann analyzed the DVHs produced with Eclipse. K.-S. Baumann wrote the manuscript and created all figures.
V. Flatten optimized the treatment plans and transferred these optimized plans to the MC code TOPAS and subsequently generated the DVHs.
U. Weber came up with the idea of modulating the density of lung voxels. U. Weber originally had the idea of the mathematical model. U. Weber created the tool to optimize the density probability functions.
S. Lautenschläger and F. Eberle contributed to this work by contouring the DICOM sets and helped with clinical information on treatment plans.
K. Zink substantively revised this manuscript and was supervising the work. K. Zink helped with the physical assessment.
R. Engenhart-Cabillic substantively revised this manuscript and was supervising the work. R. Engenhart-Cabillic helped with the clinical assessment.

Hiermit bestätige ich die Richtigkeit der gemachten Angaben bezüglich des Eigenanteiles von Kilian-Simon Baumann an den aufgeführten Publikationen und Beiträgen.
Marburg, Februar 2020

Kilian-Simon Baumann
(Autor)

Prof. Dr. Rita Engenhart-Cabillic
(Betreuerin)

Prof. Dr. Klemens Zink
(Betreuer)

Chapter 4

Discussion

4.1 Mathematical model and modulation power

The microscopic voxelized geometry proved to be a useful tool to generate degraded Bragg peaks. Using a simple mathematical model, the degradation effects of the voxelized geometry can be predicted. It was possible to generate all modulation powers as determined for human lung tissue samples and ex-vivo porcine lungs (Witt 2014). It was shown that the modulation power is directly proportional to the structure size d of the voxels used in the microscopic geometry. This suggests that the modulation power of human lungs is not the same at every position in the lung. In regions with small structure sizes like the peripheral region, the modulation power is predicted to be smaller compared to the central lung where the structures are larger. However, detailed measurements are missing that provide information about region-specific modulation powers.
Furthermore, the mathematical model can be used to determine the modulation power from measured degraded dose distribution. This is done by optimizing the mean value t and standard deviation σ_t of a normal distribution in order to minimize the difference between the degraded dose distribution and the convolution of an unperturbed pristine dose distribution with the normal distribution. The modulation power equals $P_{\mathrm{mod}} = \sigma_t^2/t$. The predicted modulation powers for the voxelized geometries were validated using MC calculations. The actual modulation powers agreed with the predictions within 3.7% or better.
Using the mathematical model, lung substitutes can be designed mimicking different lung tissues that can be used for measurements in proton beams (Baumann et al. 2019a). For a given modulation power P_{mod} and geometrical thickness D of the lung tissue the normal distribution $F(t'|t, \sigma_t)$ can be derived via $t = \rho_{\mathrm{mean}}/\rho_{\mathrm{H_2O}} \cdot D$ and $\sigma_t^2 = P_{\mathrm{mod}} \cdot t$. Both the modulation power and thickness of lung tissue that shall be mimicked can be chosen at will. An exemplary lung substitute is shown in figure 4.1: the substitutes consist of pins each having a lateral extension of $4{\times}4$ mm^2 and each having the same shape. To design the shape of a pin it is divided into $100{\times}100$ columns while the height of each column is sampled following the normal distribution $F(t'|t, \sigma_t)$. The columns within the pin are re-arranged to form a pyramidal shape

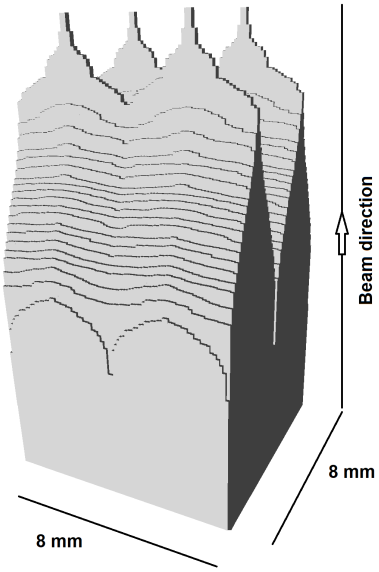

Figure 4.1: An exemplary lung substitute consisting of four pins. The shape of the pins is designed using the mathematical model. Particles traversing the lung substitute at different positions of the pins traverse different heights of material and hence experience different energy losses resulting in a Bragg peak degradation. Figure taken from (Baumann et al. 2019a)

in order to get a higher stability. The substitutes can be produced subsequently using a 3D-printer. Particles traversing the substitute at different positions of the pins traverse different heights of material and hence experience different energy losses resulting in a Bragg peak degradation[1]. The so-designed lung substitutes were validated with MC simulations and proven to reproduce the chosen modulation power (Baumann et al. 2019a).

[1]This technique of modulating the beam is already being exploited in particle therapy with carbon ions where ripple filters are used to improve the depth dose distributions of ^{12}C ions (Weber and Kraft 1999).

4.2 Density modulation of clinical voxels

The microscopic heterogeneous voxelized geometries representing the human lung tissue were replaced by coarser voxels with dimensions typical for treatment-planning CT-images. The current problem is that in these clinical CT-images the heterogeneous structure of the lung tissue is not fully resolved and hence the consideration of lung modulation effects is hardly possible. To solve this problem, density probability functions were derived for these clinical voxels. By modulating the density of each voxel the Bragg peak degradation from the microscopic heterogeneous voxelized geometries could be reproduced. The dose distributions generated with the density-modulated voxels of clinical dimensions matched the dose distributions generated using the microscopic voxelized geometries almost perfectly. The modulation powers agreed within 2.7% or better. Hence, a solution is established to reproduce the Bragg peak degradation due to the heterogeneous lung tissue on the basis of clinical treatment-planning CT-images. The whole range of modulation powers determined for human lung tissue samples and ex-vivo porcine lungs has been covered using this method. Additionally, it is in principle possible to derive the density modulation function for any voxel size and modulation power making this tool usable for any clinical CT-image and patient.
At last, it was shown that the Bragg peak degradation cannot be reproduced when the density is not modulated but an average density is assigned to each voxel. This corresponds to the current clinical state-of-the-art since an average density is applied to each voxel in the CT-image since the heterogeneous structure of the lung tissue is not fully resolved. This demonstrates the potential dose uncertainties due to the current clinical practice. Furthermore, this demonstration motivates the need for the solution presented in this study that enables an estimation of dose uncertainties due to lung modulation effects.

4.3 Dependency of the lung modulation effects on geometrical parameters

The dose uncertainties due to lung modulation effects were estimated using CT-based phantoms. These phantoms were created to simulate typical anatomical scenarios for lung cancer patients. The chest wall as well as the mediastinum or other distal normal tissue were considered. Tumors of different volumes positioned at different depths were inserted in the lung. In all cases, an undersdosage of the tumor volume was found. Hence, the TPS overestimates the dose deposited in the target volume if lung modulation effects are not considered during the treatment-panning process which is currently not possible in state-of-the-art TPS. The underdosage of the target volume increases with a) an increasing modulation power, b) an increasing path the

protons are traversing through lung tissue, and c) a decreasing scaled tumor length in beam direction. The results suggest that the difference in mean dose in the PTV is roughly -2% for clinically realistic scenarios (an average tumor volume that is located at 6 cm depth in lung using a modulation power of 250 μm).

4.4 Effects of the lung modulation on clinical treatment plans

The influence of the Bragg peak degradation due to lung tissue was investigated on treatment plans of lung cancer patients. For all cases the TPS overestimated the dose deposited in the target volume and underestimated the dose deposited in normal tissue or OARs located distal to the target volume. It was shown that this effect increases with an increasing modulation power which is in agreements with the findings from the CT-based phantom study. The maximum overestimation of the mean dose D_{mean} in the CTV was 5% for an extreme modulation power of 800 μm while the average overestimation was 2%. For a more realistic modulation power of 450 μm the maximum overestimation was 3% with an average of 1%.
Concerning the underestimation of dose deposited in OARs, it was shown that the relative position between the target volume and OAR is crucial, since the Bragg peak degradation leads to an overdosage of normal tissue at the distal end. Hence, an overdosage is only expected for scenarios where the OAR is located distal to the target volume. Such beam directions are normally avoided due to the range uncertainties connected to PT as described in chapter 1.4. However, since a patient's anatomy can oblige to use beams where an OAR is positioned distal to the PTV, these cases were investigated anyway. The lung modulation effects resulted in a maximum dose enhancement of $\sim$0.3 Gy in terms of the average dose in the cases investigated. For the $D_{2\%}$ the maximum enhancement was 1.5 Gy. However, the resulting enhanced doses deposited in OARs were far from any dose constraints used in the conventional treatment planning. Thus, the lung modulation effects on OARs distal to the target volume are negligible for the cases investigated. Note that for cases where the OAR is located nearer to or even directly next to the PTV, the effects due to the Bragg peak degradation might become clinically relevant.
Concerning the dependency of the lung modulation effects on geometrical parameters like depth of the tumor in lung and volume of the tumor, the findings from the CT-based phantom study could be reproduced.
The treatment plans used in the study were held simple and consisted of only one field in order to highlight the effects due to the Bragg peak degradation and to create a large variety of clinical scenarios concerning the depth of tumor in lung or if OARs are positioned distal to the PTV. However, two IMPT plans were investigated as well to assess whether the results obtained with the help of simple treatment plans

can be applied to more complex plans. For both IMPT plans the underdosage of the CTV was in the order of the underdosage for the simple treatment plans. Hence, the results from the study can be used to estimate the dose uncertainty due to lung modulation effects for more complex plans.
The passing rate of the gamma index 3%/1 mm (local) was on average 96.8% for an extreme modulation power of 800 μm. For a more realistic modulation power of 450 μm the average passing rate was 98.5%. The high passing rates are reasonable since the investigation of isodose lines showed that the lung modulation effects lead to a shift of these isodose lines. This shift is on average very small and hence, it is covered by the distance-to-agreement in the gamma index. All gamma index passing rates were clinically acceptable for the cases investigated. In combination with the findings that the underdosage of the CTV is on average -1% and at maximum -3% for a realistic modulation power, this supports the statement that the lung modulation effects are clinically tolerable in the current clinical context which will be discussed in more detail in chapter 4.5.
What is more, this shift of the physical dose due to the Bragg peak degradation might partially be balanced out by the biological effectiveness of protons: as described in chapter 1.4 it is well-known that the RBE might be larger than 1.1 at the end of the Bragg peak. Hence, the region of the larger RBE is congruent with the region where the physical dose is reduced due to the lung modulation. However, the larger RBE at the distal end could also potentially increase the effect of the lung modulation that a larger dose is deposited in distal normal tissue.
Since it is not possible to include the Bragg peak degradation during the treatment-planning process in current state-of-the-art TPS, potential PTV concepts might be introduced. The Bragg peak degradation leads to a shift of the dose and hence a reduction of the dose deposited both in the proximal and distal region of the target volume. This shift could be compensated for by adding a corresponding margin at the proximal and distal end of the CTV. In figure 4.2 (this figure corresponds to figure 7 in **article 3**) the results of such a PTV concept are shown. The original isotropic margin of 3 mm as used in the study was enlarged to 5 mm at the proximal end and 7 mm at the distal end resulting in an acceptable dose coverage of the CTV. However, when using such a PTV concept the dose deposited in distal normal tissue is enhanced significantly. An alternative PTV concept might consist of a boost in exactly the region where the dose is decreased due to the lung modulation effects. By prescribing a larger dose in the 3 mm margin at both the proximal and distal end, an acceptable dose coverage in the CTV can be achieved, however, the sparing of distal normal tissue is better compared to the first PTV concept.
In all studies it was shown that the lung modulation effects strongly depend on the modulation power. The larger the modulation power the larger the effects due to the Bragg peak degradation. Hence, the knowledge of the patient-specific modulation power is a crucial issue still to be solved. Until now, the modulation power can only be estimated using measurements as performed by Witt (Witt 2014) or

Titt *et al.* (Titt et al. 2015). To improve the accuracy of PT for lung cancer patients, the knowledge about the space-resolved modulation power for each patient is essential.

4.5 Clinical context of dose uncertainties due to lung modulation effects

As described in chapter 1.4, the lung modulation is not the only challenge connected to PT of lung cancer patients. In a study by Paganetti (Paganetti 2012) an overview of range uncertainties in PT is given. Range uncertainties occur due to measurement uncertainties in water for the commissioning of the particle accelerator ($\pm$0.3 mm), the patient setup ($\pm$0.7 mm) and differences between dose calculations performed with the TPS and MC simulations as a gold standard ($\pm$2 mm). Further range uncertainties arise due to uncertainties in the RBE models (0.8% of the range or $\sim$3 mm (Carabe et al. 2012)) and the approximation of stopping powers from x-ray HU ($\pm$1% of the range). The values as presented by Paganetti (Paganetti 2012) refer to the shift of the 80% distal dose and are average range uncertainties. Furthermore, the values might be larger in lung cancer patients (Paganetti 2012). The maximum shift of the 80% isodose lines due to the lung modulation effects for an extreme modulation power of 800 μm for the patient plans investigated was 10 mm in lung and only 3 mm in soft tissue and hence smaller than the average range uncertainties as described by Paganetti (Paganetti 2012).
Additionally, range and dose uncertainties arise due to possible changes of the patient's anatomy. Szeto *et al.* (Szeto et al. 2016) showed that an undercoverage of the target volume between 2 GyE and 12 GyE can occur when anatomical changes are not accounted for in the treatment-planning process. This corresponds to a relative underdosage of between 3% and 18%. The largest underdosage found for the patient plans investigated was 3% for a realistic modulation power of 450 μm.
Furthermore, motion plays an important role for lung cancer patients. Dowdell *et al.* (Dowdell et al. 2013) investigated interplay effects for 5 lung cancer patients. Due to the interplay effects the average dose in the target volume was only between 88% to 92% of the prescribed dose. Hence, the effects due to motion are significantly larger compared to the lung modulation effects. Note that these interplay effects are highly patient-specific.
In conclusion, the effects due to the lung modulation are currently clinically tolerable to a certain degree in the clinical context considering the various more critical dose and range uncertainties in PT.

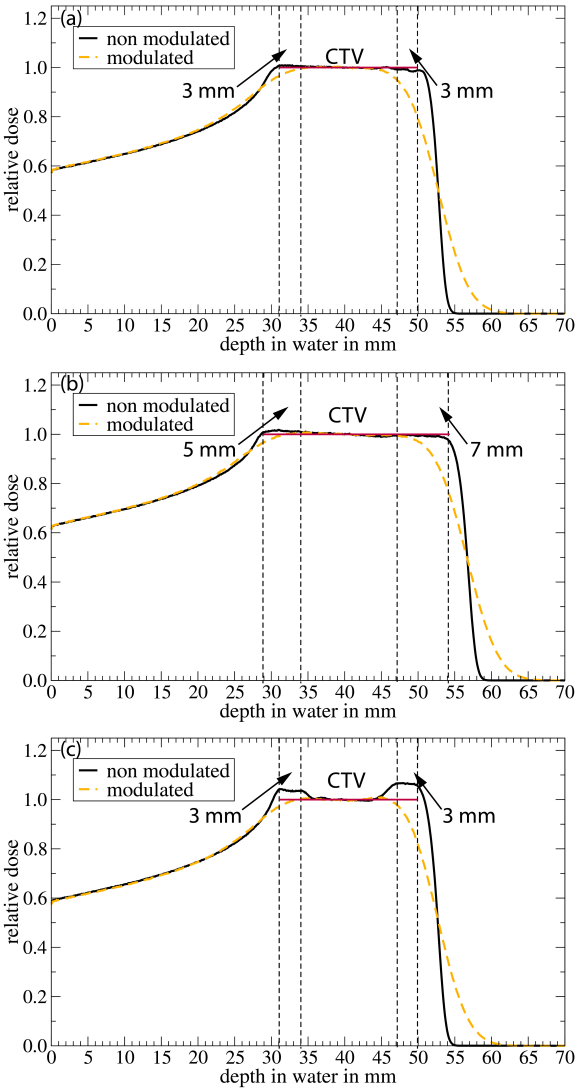

Figure 4.2: The effects of different PTV concepts. In (a) the effects for a 3 mm isotropic margin around the CTV. In (b) for a PTV concept that uses an enlarged margin at the proximal and distal end. The concept in (c) uses a 3 mm isotropic margin and a dose boost at the proximal and distal end. The CTV and the margin as well as the resulting PTV are marked in dashed lines. The red line marks the prescribed dose within the PTV. Figure taken from (Baumann et al. 2019b)

Chapter 5

Conclusion and outlook

The effects of the lung modulation due to the microscopic density heterogeneity of lung tissue were investigated. With the help of microscopic voxelized geometries as representatives of lung tissue degraded Bragg peaks were calculated with the MC code TOPAS/GEANT4. The degradation effects of these voxelized geometries can be described by a normal distribution. This normal distribution gives the probability that a path through the geometry has a specific water-equivalent thickness. Additionally, this normal distribution can be used to estimate the degraded dose distribution by convolving an unperturbed pristine Bragg peak with this normal distribution. Furthermore, the material characteristic modulation power can be derived from the normal distribution.
Intensive MC simulations were carried out to validate this mathematical model. It was shown that the simulated modulation powers for different voxelized geometries agreed with the predictions from the mathematical model within 3.7% or better.
Subsequently, these microscopic voxelized geometries were replaced by clinical voxels with an edge length of 2 mm. Hence, the transition from the microscopic lung tissue as it is present in the patient to coarser clinical structures that cannot resolve the fine lung structure is performed. By modulating the density of these clinical voxels the degraded dose distributions could be reproduced while the modulation powers agreed within 2.7% or better. The density probability function was derived from the normal distribution. Thus, a solution is found to reproduce the Bragg peak degradation due to the heterogeneous structure of lung tissue based on clinical CT-images that do not resolve the microscopic structures of the human lung tissue.
Using this density modulation, the effects of the Bragg peak degradation were investigated on CT-based phantoms. These phantoms were designed to correspond to the anatomical situation for lung cancer patients. Different tumor volumes were placed at different depths in the lung. It was shown that state-of-the-art TPS overestimate the dose deposited in the target volume and underestimate the dose deposited in distal normal tissue when the lung modulation is not accounted for. It was shown that this effect increases with an increasing modulation power, an increasing depth of the tumor in lung, and a decreasing extent of the tumor in beam direction.
At last, the effects due to the lung modulation were investigated for clinical treatment plans. The effects and dependencies found in the CT-based phantom study

were reproduced. The overestimation of the mean dose in the CTV was 5% at maximum for an extreme modulation power of 800 μm. For a more realistic modulation power the overestimation was 3% at maximum. For all cases investigated the effect on OARs distal to the target volume was negligible. The investigation of treatment plans confirms that the lung modulation effects are clinically tolerable to a certain degree in the current clinical context considering the various more critical dose and range uncertainties in PT. Additionally, by using corresponding PTV concepts as suggested, the effects of the Bragg peak degradation might be accounted for.

An essential parameter describing the lung modulation is the modulation power of the lung tissue. So far, there are only scarce experimental data quantifying the modulation power. Hence, an issue still to be solved is a solution to determine the modulation power of lung tissue for each patient individually. Currently under investigation is the possibility to derive the modulation power from CT-images by analyzing the histogram of predicted densities for different resolutions of the CT-scanner. First results suggest that an estimation of the modulation power should be possible on the basis of clinical CT-images.

Furthermore, techniques have to be developed to consider the lung modulation effects during the treatment-planning process. The solution presented in this dissertation can only estimate the dose uncertainties due to the Bragg peak degradation but can currently not be used to consider the lung modulation effects during the treatment-planning process. Such a consideration would enable a robust treatment planning. A solution could be to directly use degraded beam data when optimizing the treatment plans and hence, directly including the lung modulation effects in the optimization and dose calculation process.

Chapter 6

Side project: dosimetric calculations in clinical proton beams

The aim of this project was to adjust the MC code TOPAS/GEANT4 for dosimetry calculations in high-energy photon and proton beams. The main goal was to calculate beam quality correction factors k_{Q,Q_0} for plane-parallel and cylindrical ionization chambers in clinical proton beams.

The background is that most national and international dosimetry protocols for the determination of absorbed dose in photon and proton beams (e.g. IAEA-TRS398 (Andreo et al. 2000), AAPM TG-51 (Almond et al. 1999), DIN 6800-2 (DIN 2006), and DIN 6801-1 (DIN 2019)) are based on standards of absorbed dose to water. The determination of the absorbed dose to water can be performed with air-filled ionization chambers. These chambers are calibrated in a reference beam quality Q_0 in order to get a correlation between the measured charge produced inside the cavity and the absorbed dose to water. However, when an ionization chamber is used in a beam quality Q different from the reference beam quality, the user has to correct the chamber reading for the different response of the chamber in different beam qualities. This beam quality correction factor k_{Q,Q_0} corrects the chamber reading by a few percent and is ideally determined for each chamber used and at exact the beam quality Q at which the chamber will be operated. The experimental determination using calorimetry requires a high experimental effort and hence, is not convenient for most laboratories. The determination with the help of MC simulations is an efficient alternative.

Currently, the IAEA TRS-398 Code of Practice (CoP) is being updated. Beneath other things, fully MC calculated k_{Q,Q_0} factors shall be provided in the upcoming version which is not the case in the current version. Therefore, the RTNORM project (RTNORM 2019) is helping the IAEA working group by providing MC calculated k_{Q,Q_0} factors. However, the data for MC calculated k_{Q,Q_0} factors in proton beams is scarce with only two studies (Gomà et al. 2016; Gomà and Sterpin 2019) that use the MC code PENH to calculate k_{Q,Q_0} factors in proton beams in agreement with experimentally determined values on the 1% level.

In order to provide more MC calculated k_{Q,Q_0} factors in proton beams, especially calculated with a MC code different than PENH, TOPAS (Perl et al. 2012) a toolkit

based on the MC code GEANT4 (Agostinelli et al. 2003) shall be investigated for its suitability to calculate k_{Q,Q_0} factors in proton beams.
In general, k_{Q,Q_0} factors are calculated with the use of MC codes as follows (Andreo et al. 2013):

$$k_{Q,Q_0} = \frac{f_Q}{f_{Q_0}} \frac{W_{\mathrm{air},Q}}{W_{\mathrm{air},Q_0}} = \frac{\left(D_{\mathrm{w}}/\bar{D}_{\mathrm{air}}\right)_Q}{\left(D_{\mathrm{w}}/\bar{D}_{\mathrm{air}}\right)_{Q_0}} \frac{W_{\mathrm{air},Q}}{W_{\mathrm{air},Q_0}} \tag{6.1}$$

Q denotes the user beam quality and Q_0 the reference beam quality (mostly a ^{60}Co spectrum). Note that, when ^{60}Co gamma radiation is the reference beam quality, the subscript Q_0 is typically omitted and k_Q is used instead of k_{Q,Q_0}. The factor f is chamber-specific and depends on the beam quality. It gives the proportionality between the absorbed dose to water at the reference point when the chamber is absent (D_{w}) and the average absorbed dose to air in the cavity of the air-filled ionization chamber ($\bar{D}_{\mathrm{air}}$) (Sempau et al. 2004). $W_{\mathrm{air},Q}$ is the mean energy necessary to create an ion pair in air depending on the beam quality Q.
Thus, for the calculation of k_Q factors in proton beams calculations in both photon and proton beams are necessary. Hence, at first, the MC code TOPAS/GEANT4 has to be adjusted for calculations in proton beams (this was done in **article 4** (Wulff et al. 2018)). Subsequently, the code has to be adjusted for calculations in photon beams (this was done in **article 5** (Baumann et al. 2019c)). At last, TOPAS/GEANT4 can be used to calculate k_Q factors in proton beams for real ionization chambers while the results have to be compared to experimentally determined k_Q factors (this was done in **article 6** (Baumann et al. 2020)).
In **article 4** the main task was to adjust the physics settings for calculations in clinical proton beams. Therefore, a Fano cavity test was performed for different physics lists and values of the parameter *dRoverR*. This parameter controls the length of a CH step in relation to the residual range of the particle. It was shown that the Fano cavity test is violated by less than 0.2% for protons when the physics module *EMStandardOpt4* and a $dRoverR = 0.05$ is used. To adjust the production cut-off range f_Q factors for simple air-filled cavities were calculated in a 150 MeV proton beam for various values of the production cut-off range. It was shown that the f_Q factor depends on the production cut and that the cut has to be smaller than 5 μm which corresponds to $\sim$15 keV electrons in water. After adjusting the physics parameters, f_Q factors were calculated for the IBA NACP-02 and Farmer NE 2571 chamber for various monoenergetic proton beams between 70 MeV and 250 MeV. Two different nuclear interaction models (Binary cascade (BIC) and Bertini cascade (BERT)) were compared. The f_Q factors agreed with f_Q factors calculated by Gomà *et al* (Gomà et al. 2016) within 0.6% or better. The difference in f_Q factors between the nuclear interaction models BIC and BERT was 0.3% at maximum. Hence, the MC code TOPAS/GEANT4 can provide reliable results of ionization chamber response calculations in primary proton beams.
In the next step, TOPAS/GEANT4 was adjusted for the calculation of f_{Q_0} factors of

simple air-filled cavities as representative of plane-parallel and cylindrical ionization chambers in high-energy photon beams in **article 5**. Furthermore, f_Q factors in proton beams were calculated and corresponding f_Q/f_{Q_0} ratios were derived. These f_Q/f_{Q_0} ratios are the basis of MC calculated k_Q factors and the only part that can be calculated using the MC method. Additionally, the same calculations were performed with the MC codes PENH and FLUKA (Salvat 2013; Ferrari et al. 2005; Böhlen et al. 2014). The results were compared between the codes. It was shown that the physics settings used for clinical proton beams cannot be used for high-energy photon beams in TOPAS/GEANT4. Especially the value for *dRoverR* had to be set to a smaller value. The parameters used for the photon simulations were adapted following a study by O'Brien *et al.* (O'Brien et al. 2016) who performed a Fano cavity test for high-energy photon beams. The calculated f_Q/f_{Q_0} ratios agreed within 0.7% or better between the MC codes TOPAS/GEANT4, PENH, and FLUKA. Hence, the results produced with TOPAS/GEANT4 are comparable to those produced with PENH. This suggests that TOPAS/GEANT4 can be used for the calculation of k_Q factors in proton beams since it has been proven that PENH is able to calculate k_Q factors in agreement with experimental values on the 1% level. In order to investigate where the differences between the codes might originate from, spectral fluences of photons and protons as well as secondary electrons were calculated with all codes. The results showed excellent agreement between the MC codes for the spectral fluences of photons and electrons in the high-energy photon field. This implies that the underlying electromagnetic interaction models used in the different MC codes are similar. For the spectral fluences of protons and secondary electrons in the proton field differences were observed for the spectra of secondary protons and electrons produced by prompt gamma photons. The spectra of primary protons and delta electrons showed an almost perfect agreement between the codes. The differences in the spectrum of secondary protons and electrons produced by prompt gamma photons suggests that the underlying more complex nuclear interaction models tend to slight differences between the codes.

After the physics settings were adjusted in the MC code TOPAS/GEANT4, f_{Q_0}, f_Q, and k_Q factors in proton beams were calculated for six plane-parallel and four cylindrical ionization chambers in **article 6**. The f_{Q_0} factors were calculated in ^{60}Co radiation and compared to MC calculated f_{Q_0} factors published in the literature. The f_{Q_0} factors calculated with TOPAS/GEANT4 agreed with those provided in the literature within 0.7% or better. The variance among the values provided in the literature was on the 1% level. Hence, TOPAS/GEANT4 can be used for the calculation of f_{Q_0} factors for both plane-parallel and cylindrical ionization chambers in ^{60}Co beams as long as the physics settings are adapted accordingly. The f_Q factors calculated with TOPAS/GEANT4 in monoenergetic proton beams agreed with MC calculated f_Q factors (calculated with PENH) published in the literature within 1.7% or better. The differences between the MC codes increased for higher energies. The reason might be that possible differences in the nuclear interaction models lead

to larger differences for higher energies. However, the results are not sufficient to clarify the role of nuclear interaction models for the calculation of f_Q factors in proton beams without doubt. The k_Q factors calculated with TOPAS/GEANT4 were compared to k_Q factors calculated with PENH. Again, significant differences appeared for high energies. For smaller energies the agreement was better. Additionally, k_Q factors calculated with TOPAS/GEANT4 were compared to experimentally determined k_Q factors provided in the literature. The agreement was on the 1% level with only two exceptions. Note that these findings are restricted to energies between 100 MeV and 160 MeV since no experimentally determined k_Q factors are available for different energies. Nevertheless, the results prove that TOPAS/GEANT4 can be used to calculate k_Q factors in clinical proton beams.

In conclusion, the physics settings in TOPAS/GEANT4 were adjusted for dosimetry calculations in high-energy photon and proton beams. With the use of a Fano cavity test the physics settings for the proton beams were adjusted. The physics settings for the high-energy photon beams were adjusted following the results from O'Brien *et al.* (O'Brien et al. 2016). Subsequently, f_Q/f_{Q_0} ratios for simple air-filled cavities as representatives of plane-parallel and cylindrical ionization chambers were calculated with different MC codes and compared to each other. The difference in f_Q/f_{Q_0} ratios between the codes was 0.7% at maximum. Based on these finding, TOPAS/GEANT4 was used to calculate k_Q factors in clinical proton beams in agreement with experimental values on the 1% level.

In the next step, perturbation correction factors for ionization chambers in proton beams shall be calculated. From the f_Q factors that are already calculated, total perturbation correction factors p_Q can be derived as $p_Q = f_Q/(s_{\mathrm{w,air}})_Q$ while $(s_{\mathrm{w,air}})_Q$ is the water to air stopping power ratio. The results indicate that p_Q is significantly different than unity for some chambers and proton energies in contrast to the assumption from the TRS-398 CoP. Especially the contributions from the single chamber parts like chamber stem, central electrode, chamber wall, and sleeve shall be investigated.

Additionally, the investigation of nuclear interaction models for the calculation of f_Q factors remains an issue to be solved. This investigation might be performed by building ionization chambers step by step in different MC codes and compare the results for calculated f_Q factors after each step. Hence, one might find the chamber part or material that causes the differences between the MC codes.

Furthermore, the comparison of MC calculated k_Q factors with experimentally determined values is restricted to energies between 100 MeV and 160 MeV at the moment, since no experimentally determined values are published for different energies. Hence, the experimental determination of k_Q factors for higher energies is important. Especially, regarding the differences between the different MC codes for high energies.

Bibliography

Agosteo, S., Birattari, C., Caravaggio, M., Silari, M., and Tosi, G. Secondary neutron and photon dose in proton therapy. *Radiotherapy and Oncology*, 48(3):293 – 305, 1998. 4

Agostinelli, S. et al. Geant4 - a simulation toolkit. *Nucl. Instrum. Methods Phys. Res. A*, 506:250–303, 2003. doi: http://dx.doi.org/10.1016/S0168-9002(03)01368-8. 11, 43

Ahlen, S. P. Theoretical and experimental aspects of the energy loss of relativistic heavily ionizing particles. *Rev. Mod. Phys.*, 52:121–173, 1980. 4

Almond, P. R., Biggs, P. J., Coursey, B. M., Hanson, W. F., Huq, M. S., Nath, R., and Rogers, D. W. O. Aapm's tg-51 protocol for clinical reference dosimetry of high-energy photon and electron beams. *Medical Physics*, 26(9):1847–1870, 1999. 42

Andreo, P., Burns, D. T., Hohlfeld, K., Huq, M. S., Kanai, T., Laitano, F., Smyth, V., and Vynicker, S. Absorbed dose determination in external beam radiotherapy: An international code of practice for dosimetry based on standards of absorbed dose to water. *Technical Report Series TRS-398 (International Atomic Energy Agency, Vienna)*, 2000. 42

Andreo, P., Wulff, J., Burns, D. T., and Palmans, H. Consistency in reference radiotherapy dosimetry: resolution of an apparent conundrum when60co is the reference quality for charged-particle and photon beams. *Physics in Medicine and Biology*, 58(19):6593–6621, sep 2013. 43

Arbor, N., Dauvergne, D., Dedes, G., Létang, J. M., Parodi, K., Quiñones, C. T., Testa, E., and Rit, S. Monte carlo comparison of x-ray and proton CT for range calculations of proton therapy beams. *Physics in Medicine and Biology*, 60(19): 7585–7599, sep 2015. 7

Assmann, W., Kellnberger, S., Reinhardt, S., Lehrack, S., Edlich, A., Thirolf, P. G., Moser, M., Dollinger, G., Omar, M., Ntziachristos, V., and Parodi, K. Ionoacoustic characterization of the proton bragg peak with submillimeter accuracy. *Medical Physics*, 42(2):567–574, 2015. 8

Baumann, K., Weber, U., Fiebich, M., Zink, K., and Mäder, U. 3D-printable lung substitutes for particle therapy on the base of high-resolution CTs for mimicking Bragg peak degradation. In Chen, P.-H. and Bak, P. R., editors, *Medical Imaging 2019: Imaging Informatics for Healthcare, Research, and Applications*, volume 10954, pages 263 – 269. International Society for Optics and Photonics, SPIE, 2019a. 33, 34

Baumann, K.-S., Witt, M., Weber, U., Engenhart-Cabillic, R., and Zink, K. An efficient method to predict and include bragg curve degradation due to lung-equivalent materials in monte carlo codes by applying a density modulation. *Physics in Medicine & Biology*, 62(10):3997–4016, 2017. 14, 16, 18, 20

Baumann, K.-S., Flatten, V., Weber, U., Lautenschläger, S., Eberle, F., Zink, K., and Engenhart-Cabillic, R. Effects of the bragg peak degradation due to lung tissue in proton therapy of lung cancer patients. *Radiation Oncology*, 14(183), 2019b. 25, 27, 29, 39

Baumann, K.-S., Horst, F., Zink, K., and Gomà, C. Comparison of penh, fluka, and geant4/topas for absorbed dose calculations in air cavities representing ionization chambers in high-energy photon and proton beams. *Medical Physics*, 46(10):4639–4653, 2019c. 11, 43

Baumann, K.-S., Kaupa, S., Bach, C., Engenhart-Cabillic, R., and Zink, K. Monte carlo calculation of beam quality correction factors in proton beams using topas/geant4. *Physics in Medicine & Biology*, accepted for publication(2020), 2020. 43

Bert, C. and Durante, M. Motion in radiotherapy: particle therapy. *Physics in Medicine and Biology*, 56(16):R113–R144, jul 2011. 8

Bert, C., Saito, N., Schmidt, A., Chaudhri, N., Schardt, D., and Rietzel, E. Target motion tracking with a scanned particle beam. *Medical Physics*, 34(12):4768–4771, 2007. 8

Bert, C., Grözinger, S. O., and Rietzel, E. Quantification of interplay effects of scanned particle beams and moving targets. *Physics in Medicine and Biology*, 53 (9):2253–2265, apr 2008. 8

Bethe, H. *Zur Theorie des Durchgangs schneller Korpuskelstrahlung durch Materie. Annalen der Physik*, 397(3):320–325, 1930. Online erhältlich unter `http://onlinelibrary.wiley.com/doi/10.1002/andp.19303970303/pdf`; Version vom: 15.12.2014. 3, 17

Bichsel, H., Hiraoka, T., and Omata, K. Aspects of Fast-Ion Dosimetry. *Radiation Research*, 153(2):208 – 219, 2000. doi: 10.1667/0033-7587(2000)153[0208:AOFID]2.0.CO;2. 4, 15

Bielajew, A. The Monte Carlo Simulation of Radiation Transport. *The University of Michigan, Department of Nuclear Engineering and Radiological Sciences*, 2001. 11

Bloch, F. *Zur Bremsung rasch bewegter Teilchen beim Durchgang durch Materie. Annalen der Physik*, 408(3):285–320, 1933. Online erhältlich unter `http://onlinelibrary.wiley.com/doi/10.1002/andp.19334080303/pdf`; Version vom: 15.12.2014. 3, 17

Böhlen, T. T., Cerutti, F., Chin, M. P. W., Fassò, A., Ferrari, A., Ortega, P. G., Mairani, A., Sala, P. R., Smirnov, D., and Vlachoudis, V. The FLUKA Code: Developments and Challenges for High Energy and Medical Applications. *Nuclear Data Sheets*, 120:221–214, 2014. 44

Bohr, N. Lx. on the decrease of velocity of swiftly moving electrified particles in passing through matter. *The London, Edinburgh, and Dublin Philosophical Magazine and Journal of Science*, 30(178):581–612, 1915. doi: 10.1080/14786441008635432. 4

Bragg, W. H. and Kleeman, R. Xxxix. on the alpha particles of radium, and their loss of range in passing through various atoms and molecules. *The London, Edinburgh, and Dublin Philosophical Magazine and Journal of Science*, 10(57):318–340, 1905. doi: 10.1080/14786440509463378. 2

Bush, D. A., Slater, J. D., Shin, B. B., Cheek, G., Miller, D. W., and Slater, J. M. Hypofractionated proton beam radiotherapy for stage i lung cancer. *Chest*, 126 (4):1198 – 1203, 2004. 26

Carabe, A., Moteabbed, M., Depauw, N., Schuemann, J., and Paganetti, H. Range uncertainty in proton therapy due to variable biological effectiveness. *Physics in Medicine and Biology*, 57(5):1159–1172, feb 2012. 8, 38

Chang, J., Zhang, X., Wang, X., Kang, Y., Riley, B., Bilton, S., Mohan, R., Komaki, R., and Cox, J. Significant reduction of normal tissue dose by proton radiotherapy compared with three-dimensional conformal or intensity-modulated radiation therapy in stage i or stage iii non-small-cell lung cancer. *International Journal of Radiation Oncology Biology Physics*, 65(4):1087–1096, 2006. 6

Chang, J. Y., Komaki, R., Lu, C., Wen, H. Y., Allen, P. K., Tsao, A., Gillin, M., Mohan, R., and Cox, J. D. Phase 2 study of high-dose proton therapy with concurrent chemotherapy for unresectable stage iii nonsmall cell lung cancer. *Cancer*, 117(20):4707–4713, 2011. 6, 7

Chang, J. Y., Senan, S., Paul, M. A., Mehran, R. J., Louie, A. V., Balter, P., Groen, H. J. M., McRae, S. E., Widder, J., Feng, L., van den Borne, B. E. E. M., Munsell, M. F., Hurkmans, C., Berry, D. A., van Werkhoven, E., Kresl, J. J., Dingemans,

A.-M., Dawood, O., Haasbeek, C. J. A., Carpenter, L. S., Jaeger, K. D., Komaki, R., Slotman, B. J., Smit, E. F., and Roth, J. A. Stereotactic ablative radiotherapy versus lobectomy for operable stage i non-small-cell lung cancer: a pooled analysis of two randomised trials. *The Lancet Oncology*, 16(6):630–637, 2015. 5, 6

Chang, J. Y., Jabbour, S. K., Ruysscher, D. D., Schild, S. E., Simone, C. B., Rengan, R., Feigenberg, S., Khan, A. J., Choi, N. C., Bradley, J. D., Zhu, X. R., Lomax, A. J., and Hoppe, B. S. Consensus statement on proton therapy in early-stage and locally advanced non-small cell lung cancer. *International Journal of Radiation Oncology*Biology*Physics*, 95(1):505 – 516, 2016. 5, 6, 7

Chen, J., Lu, J., Ma, N., Zhao, J., Chen, C., Fan, M., Jiang, G., and Mao, J. Early stage non-small cell lung cancer treated with pencil beam scanning particle therapy: retrospective analysis of early results on safety and efficacy. *Radiation Oncology*, 14(16), 2019. 26

Chvetsov, A. V. and Paige, S. L. The influence of CT image noise on proton range calculation in radiotherapy planning. *Physics in Medicine and Biology*, 55(6): N141–N149, feb 2010. 7

Dekking, M. *A Modern Introduction to Probability and Statistics*, pages 181–190. Springer, 2005. ISBN 9781852338961. 11

DIN. Dosismessverfahren nach der Sondenmethode für Photonen- und Elektronenstrahlung - Teil 2: Dosimetrie hochenergetischer Photonen- und Elektronenstrahlung mit Ionisationskammern (DIN 6800-2). Technical report, Deutsches Institut für Normung (DIN), 2006. 42

DIN. Dosismessverfahren nach der Sondenmethode für Protonen- und Ionenstrahlung - Teil 1: Ionisationskammern (DIN 6801-1). Technical report, Deutsches Institut für Normung (DIN), 2019. 42

Dowdell, S., Grassberger, C., Sharp, G. C., and Paganetti, H. Interplay effects in proton scanning for lung: a 4d monte carlo study assessing the impact of tumor and beam delivery parameters. *Physics in Medicine and Biology*, 58(12):4137–4156, may 2013. 8, 38

Enghardt, W., Crespo, P., Fiedler, F., Hinz, R., Parodi, K., Pawelke, J., and Pönisch, F. Charged hadron tumour therapy monitoring by means of pet. *Nuclear Instruments and Methods in Physics Research Section A: Accelerators, Spectrometers, Detectors and Associated Equipment*, 525(1):284 – 288, 2004. ISSN 0168-9002. Proceedings of the International Conference on Imaging Techniques in Subatomic Physics, Astrophysics, Medicine, Biology and Industry. 8

Engwall, E., Glimelius, L., and Hynning, E. Effectiveness of different rescanning techniques for scanned proton radiotherapy in lung cancer patients. *Physics in Medicine & Biology*, 63(9):095006, may 2018. 8

España, S. and Paganetti, H. Uncertainties in planned dose due to the limited voxel size of the planning CT when treating lung tumors with proton therapy. *Physics in Medicine and Biology*, 56(13):3843–3856, may 2011. 9

Ferrari, A., Sala, P. R., Fasso, A., and Ranft, J. FLUKA: a multi-particle transport code. Technical report, CERN-2005-10 (2005), INFN/TC_05/11, SLAC-R-773, 2005. 44

Flatten, V., Baumann, K.-S., Weber, U., Engenhart-Cabillic, R., and Zink, K. Quantification of the dependencies of the bragg peak degradation due to lung tissue in proton therapy on a CT-based lung tumor phantom. *Physics in Medicine & Biology*, 64(15):155005, aug 2019. 20, 23, 24, 25

Gomà, C. and Sterpin, E. Monte carlo calculation of beam quality correction factors in proton beams using PENH. *Physics in Medicine & Biology*, 64(18):185009, sep 2019. 42

Gomà, C., Andreo, P., and Sempau, J. Monte carlo calculation of beam quality correction factors in proton beams using detailed simulation of ionization chambers. *Physics in Medicine and Biology*, 61(6):2389–2406, mar 2016. 42, 43

Goudsmit, S. and Saunderson, J. L. Multiple scattering of electrons. *Phys. Rev.*, 57 (24), 1940a. 11

Goudsmit, S. and Saunderson, J. L. Multiple scattering of electrons ii. *Phys. Rev.*, 58(36), 1940b. 11

Grassberger, C., Dowdell, S., Lomax, A., Sharp, G., Shackleford, J., Choi, N., Willers, H., and Paganetti, H. Motion interplay as a function of patient parameters and spot size in spot scanning proton therapy for lung cancer. *International Journal of Radiation Oncology*Biology*Physics*, 86(2):380 – 386, 2013. 8

Grutters, J. P., Kessels, A. G., Pijls-Johannesma, M., Ruysscher, D. D., Joore, M. A., and Lambin, P. Comparison of the effectiveness of radiotherapy with photons, protons and carbon-ions for non-small cell lung cancer: A meta-analysis. *Radiotherapy and Oncology*, 95(1):32 – 40, 2010. 6

Harada, H. and Murayama, S. Proton beam therapy in non-small cell lung cancer: state of the art. *Lung Cancer: Targets and Therapy*, 8:141–145, 2017. 6, 7

Hata, M., Tokuuye, K., Kagei, K., Sugahara, S., Nakayama, H., Fukumitsu, N., Hashimoto, T., Mizumoto, M., Ohara, K., and Akine, Y. Hypofractionated high-dose proton beam therapy for stage i non-small-cell lung cancer: Preliminary results of a phase i/ii clinical study. *International Journal of Radiation Oncology*Biology*Physics*, 68(3):786 – 793, 2007. 6, 26

Hoffmann, L., Alber, M., Jensen, M. F., Holt, M. I., and Møller, D. S. Adaptation is mandatory for intensity modulated proton therapy of advanced lung cancer to ensure target coverage. *Radiotherapy and Oncology*, 122(3):400 – 405, 2017. 7

Hoppe, B. S., Huh, S., Flampouri, S., Nichols, R. C., Oliver, K. R., Morris, C. G., Mendenhall, N. P., and Li, Z. Double-scattered proton-based stereotactic body radiotherapy for stage i lung cancer: A dosimetric comparison with photon-based stereotactic body radiotherapy. *Radiotherapy and Oncology*, 97(3):425–430, 2010. 6

Hoppe, B. S., Henderson, R., Pham, D., Cury, J. D., Bajwa, A., Morris, C. G., D'Agostino, H., Flampouri, S., Huh, S., Li, Z., McCook, B., and Nichols, R. C. A phase 2 trial of concurrent chemotherapy and proton therapy for stage iii non-small cell lung cancer: Results and reflections following early closure of a single-institution study. *International Journal of Radiation Oncology*Biology*Physics*, 95(1):517 – 522, 2016. 6

Hui, Z., Zhang, X., Starkschall, G., Li, Y., Mohan, R., Komaki, R., Cox, J. D., and Chang, J. Y. Effects of interfractional motion and anatomic changes on proton therapy dose distribution in lung cancer. *International Journal of Radiation Oncology*Biology*Physics*, 72(5):1385 – 1395, 2008. 7

IARC. World cancer report. *2014 (2014), Edited by Stewart and Wild, International Agency for Research on Cancer under World Health Organization (WHO)*, 2014. 1

ICRU. report volume 50: prescribing, recording, and reporting photon beam therapy. Technical report, Bethesda, Maryland, USA: International Comission on Radiation Units and Measurements (ICRU), 1993. 27

ICRU. report volume 62: prescribing, recording and reporting photon beam therapy (supplement to ICRU report 50). Technical report, Bethesda, Maryland, USA: International Comission on Radiation Units and Measurements (ICRU), 1999. 27

Ivanchenko, V. N., Kadri, O., Maire, M., and Urban, L. Geant4 models for simulation of multiple scattering. *Journal of Physics: Conference Series*, 219(3):032045, 2010. URL `http://stacks.iop.org/1742-6596/219/i=3/a=032045`. 11

Kanehira, T., Matsuura, T., Takao, S., Matsuzaki, Y., Fujii, Y., Fujii, T., Ito, Y. M., Miyamoto, N., Inoue, T., Katoh, N., Shimizu, S., Umegaki, K., and Shirato, H. Impact of real-time image gating on spot scanning proton therapy for lung tumors: A simulation study. *International Journal of Radiation Oncology*Biology*Physics*, 97(1):173 – 181, 2017. 8

Kase, Y., Yamashita, H., Fuji, H., Yamamoto, Y., Pu, Y., Tsukishima, C., and Murayama, S. A Treatment Planning Comparison of Passive-Scattering and Intensity-Modulated Proton Therapy for Typical Tumor Sites. *Journal of Radiation Research*, 53(2):272–280, 12 2011. 4

Knopf, A., Parodi, K., Paganetti, H., Cascio, E., Bonab, A., and Bortfeld, T. Quantitative assessment of the physical potential of proton beam range verification with PET/CT. *Physics in Medicine and Biology*, 53(15):4137–4151, jul 2008. 8

Kraft, G. Tumor therapy with heavy charged particles. *Progress in Particle and Nuclear Physics*, 45:S473 – S544, 2000. 2, 3

Lehrack, S., Assmann, W., Bertrand, D., Henrotin, S., Herault, J., Heymans, V., Stappen, F. V., Thirolf, P. G., Vidal, M., de Walle, J. V., and Parodi, K. Submillimeter ionoacoustic range determination for protons in water at a clinical synchrocyclotron. *Physics in Medicine & Biology*, 62(17):L20–L30, aug 2017. 8

Litzlbauer, H. D., Neuhaeuser, C., Moell, A., Greschus, S., Breithecker, A., Franke, F. E., Kummer, W., and Rau, W. S. Three-dimensional imaging and morphometric analysis of alveolar tissue from microfocal x-ray-computed tomography. *American Journal of Physiology-Lung Cellular and Molecular Physiology*, 291(3): L535–L545, 2006. 10

Loeffler, J. and Durante, M. Charged particle therapy-optimization, challenges and future directions. *Nat Rev Clin Oncol*, 10:411 – 424, 2013. 6

Lomax, A. J., Bortfeld, T., Goitein, G., Debus, J., Dykstra, C., Tercier, P.-A., Coucke, P. A., and Mirimanoff, R. O. A treatment planning inter-comparison of proton and intensity modulated photon radiotherapy. *Radiotherapy and Oncology*, 51(3):257 – 271, 1999. ISSN 0167-8140. 6

Lomax, A. J., Böhringer, T., Bolsi, A., Coray, D., Emert, F., Goitein, G., Jermann, M., Lin, S., Pedroni, E., Rutz, H., Stadelmann, O., Timmermann, B., Verwey, J., and Weber, D. C. Treatment planning and verification of proton therapy using spot scanning: Initial experiences. *Medical Physics*, 31(11):3150–3157, 2004. 5

Lomax, M., Folkes, L., and O'Neill, P. Biological consequences of radiation-induced dna damage: Relevance to radiotherapy. *Clinical Oncology*, 25(10):578 – 585, 2013. ISSN 0936-6555. doi: https://doi.org/10.1016/j.clon.2013.06.007. Advances in Clinical Radiobiology. 1

Lu, H.-M., Brett, R., Sharp, G., Safai, S., Jiang, S., Flanz, J., and Kooy, H. A respiratory-gated treatment system for proton therapy. *Medical Physics*, 34(8): 3273–3278, 2007. 8

Macdonald, O. K., Kruse, J. J., Miller, J. M., Garces, Y. I., Brown, P. D., Miller, R. C., and Foote, R. L. Proton beam radiotherapy versus three-dimensional conformal stereotactic body radiotherapy in primary peripheral, early-stage non-small-cell lung carcinoma: A comparative dosimetric analysis. *International Journal of Radiation Oncology*Biology*Physics*, 75(3):950–958, 2009. 6

Matsufuji, N., Tomura, H., Futami, Y., Yamashita, H., Higashi, A., Minohara, S., Endo, M., and Kanai, T. Relationship between CT number and electron density, scatter angle and nuclear reaction for hadron-therapy treatment planning. *Physics in Medicine and Biology*, 43(11):3261–3275, nov 1998. 7

Metropolis, N. and Ulam, S. The monte carlo method. *Journal of the American Statistical Association*, 44(247):335–341, 1949. 11

Nakayama, H., Sugahara, S., Tokita, M., Satoh, H., Tsuboi, K., Ishikawa, S., and Tokuuye, K. Proton beam therapy for patients with medically inoperable stage i non-small-cell lung cancer at the university of tsukuba. *International Journal of Radiation Oncology*Biology*Physics*, 78(2):467 – 471, 2010. 6

Nguyen, Q.-N., Ly, N. B., Komaki, R., Levy, L. B., Gomez, D. R., Chang, J. Y., Allen, P. K., Mehran, R. J., Lu, C., Gillin, M., Liao, Z., and Cox, J. D. Long-term outcomes after proton therapy, with concurrent chemotherapy, for stage ii-iii inoperable non-small cell lung cancer. *Radiotherapy and Oncology*, 115(3):367 – 372, 2015. 6

Nichols, R. C., Huh, S. N., Henderson, R. H., Mendenhall, N. P., Flampouri, S., Li, Z., D'Agostino, H. J., Cury, J. D., Pham, D. C., and Hoppe, B. S. Proton radiation therapy offers reduced normal lung and bone marrow exposure for patients receiving dose-escalated radiation therapy for unresectable stage iii non-small-cell lung cancer: A dosimetric study. *Clinical Lung Cancer*, 12(4):252 – 257, 2011. 6

Nihei, K., Ogino, T., Ishikura, S., and Nishimura, H. High-dose proton beam therapy for stage i non-small-cell lung cancer. *International Journal of Radiation Oncology*Biology*Physics*, 65(1):107 – 111, 2006. 6

Nill, S., Bortfeld, T., and Oelfke, U. Inverse planning of intensity modulated proton therapy. *Zeitschrift für Medizinische Physik*, 14(1):35 – 40, 2004. ISSN 0939-3889. 6

O'Brien, D. J., Roberts, D. A., Ibbot, G. S., , and Sawakuchi, G. O. Reference dosimetry in magnetic fileds: formalism and ionization chamber correction factors. *Medical Physics*, 43:4915–4927, 2016. doi: 10.1118/1.4959785. 12, 44, 45

Ohno, T., Oshiro, Y., Mizumoto, M., Numajiri, H., Ishikawa, H., Okumura, T., Terunuma, T., Sakae, T., and Sakurai, H. Comparison of dose-volume histograms between proton beam and X-ray conformal radiotherapy for locally advanced non-small-cell lung cancer. *Journal of Radiation Research*, 56(1):128–133, 11 2015. 6

Oshiro, Y., Okumura, T., Kurishima, K., Homma, S., Mizumoto, M., Ishikawa, H., Onizuka, M., Sakai, M., Goto, Y., Hizawa, N., Sato, Y., and Sakurai, H. High-dose concurrent chemo-proton therapy for Stage III NSCLC: preliminary results of a Phase II study. *Journal of Radiation Research*, 55(5):959–965, 05 2014. 6, 7

Paganetti, H. Range uncertainties in proton therapy and the role of monte carlo simulations. *Physics in Medicine and Biology*, 57(11):R99–R117, may 2012. 7, 8, 38

Parodi, K. and Enghardt, W. Potential application of PET in quality assurance of proton therapy. *Physics in Medicine and Biology*, 45(11):N151–N156, oct 2000. 8

Parodi, K., Paganetti, H., Shih, H. A., Michaud, S., Loeffler, J. S., DeLaney, T. F., Liebsch, N. J., Munzenrider, J. E., Fischman, A. J., Knopf, A., and Bortfeld, T. Patient study of in vivo verification of beam delivery and range, using positron emission tomography and computed tomography imaging after proton therapy. *International Journal of Radiation Oncology*Biology*Physics*, 68(3):920 – 934, 2007. 8

Pedroni, E., Meer, D., Bula, C., Safai, S., and Zenklusen, S. Pencil beam characteristics of the next-generation proton scanning gantry of psi: design issues and initial commissioning results. *The European Physical Journal Plus*, 126(66), 2011. 5

Perl, J., Shin, J., Schuemann, J., Faddegon, B., and Paganetti, H. Topas: an innovative proton monte carlo platform for research and clinical applications. *Medical Physics*, 39(11):6818–6837, 2012. doi: http://dx.doi.org/10.1118/1.4758060. 11, 12, 42

Perles, L. A., Mirkovic, D., Sawakuchi, G. O., and Titt, U. Monte carlo investigation of rebinning material density distributions of lung parenchyma phantoms in proton therapy. *Nuclear Technology*, 175(1):22–26, 2011. 9

Podgorsak. Review of radiation oncology physics: A handbook for teachers and students. *(2003), Editor: Ervin B. Podgorsak, Department of Medical Physics, McGill University Health Centre Montreal, Quebec, Canada*, 2003. 2

PTCOG. `https://www.ptcog.ch/index.php/patient-statistics`, 2019a. last accessed: December 2019. 2

PTCOG. `https://www.ptcog.ch/index.php/facilities-in-operation`, 2019b. last accessed: December 2019. 2

PTCOG. `https://www.ptcog.ch/index.php/facilities-under-construction`, 2019c. last accessed: December 2019. 2

Register, S. P., Zhang, X., Mohan, R., and Chang, J. Y. Proton stereotactic body radiation therapy for clinically challenging cases of centrally and superiorly located stage i non-small-cell lung cancer. *International Journal of Radiation Oncology*Biology*Physics*, 80(4):1015–1022, 2011. 6

Richter, C., Pausch, G., Barczyk, S., Priegnitz, M., Keitz, I., Thiele, J., Smeets, J., Stappen, F. V., Bombelli, L., Fiorini, C., Hotoiu, L., Perali, I., Prieels, D., Enghardt, W., and Baumann, M. First clinical application of a prompt gamma based in vivo proton range verification system. *Radiotherapy and Oncology*, 118 (2):232 – 237, 2016. 8

Ringbæk, T. P., Simeonov, Y., Witt, M., Engenhart-Cabillic, R., Kraft, G., Zink, K., and Weber, U. Modulation power of porous materials and usage as ripple filter in particle therapy. *Physics in Medicine and Biology*, 62(7):2892–2909, mar 2017. 10, 15

Rogers, D. W. O. Fifty years of monte carlo simulations for medical physics. *Physics in Medicine and Biology*, 51(13):R287–R301, jun 2006. 12

RTNORM. `http://www.rtnorm.eu/`, 2019. last accessed: December 2019. 42

Salvat, F. A generic algorithm for monte carlo simulation of proton transport. *Nuclear Instruments and Methods in Physics Research Section B: Beam Interactions with Materials and Atoms*, 316:144 – 159, 2013. 44

Sawakuchi, G. O., Titt, U., Mirkovic, D., and Mohan, R. Density heterogeneities and the influence of multiple coulomb and nuclear scatterings on the bragg peak distal edge of proton therapy beams. *Physics in Medicine and Biology*, 53(17): 4605–4619, aug 2008. 9

Schaffner, B. and Pedroni, E. The precision of proton range calculations in proton radiotherapy treatment planning: experimental verification of the relation between CT-HU and proton stopping power. *Physics in Medicine and Biology*, 43(6):1579–1592, jun 1998. 7

Schardt, D., Elsässer, T., and Schulz-Ertner, D. Heavy-ion tumor therapy: Physical and radiobiological benefits. *Rev. Mod. Phys.*, 82:383–425, Feb 2010. doi: 10.1103/RevModPhys.82.383. 1, 2

Schippers, J. M. and Lomax, A. J. Emerging technologies in proton therapy. *Acta Oncologica*, 50(6):838–850, 2011. 4

Schneider, U., Pedroni, E., and Lomax, A. The calibration of CT hounsfield units for radiotherapy treatment planning. *Physics in Medicine and Biology*, 41(1): 111–124, jan 1996. 7, 12, 14, 21

Seco, J., Gu, G., Marcelos, T., Kooy, H., and Willers, H. Proton arc reduces range uncertainty effects and improves conformality compared with photon volumetric modulated arc therapy in stereotactic body radiation therapy for non-small cell lung cancer. *International Journal of Radiation Oncology*Biology*Physics*, 87(1): 188 – 194, 2013. 6

Sell, M., Titt, U., Perles, L., Mirkovic, D., Mohan, R., Bangert, M., and Oelfke, U. We-e-brb-02: Evaluation of analytical proton dose predictions with a lung-like plastic phantom. *Medical Physics*, 39(6Part27):3956–3956, 2012. 9

Sempau, J., Andreo, P., Aldana, J., Mazurier, J., and Salvat, F. Electron beam quality correction factors for plane-parallel ionization chambers: Monte Carlo calculations using the PENELOPE system. *Phys. Med. Biol.*, 49:4427–4444, 2004. 43

Shioyama, Y., Tokuuye, K., Okumura, T., Kagei, K., Sugahara, S., Ohara, K., Akine, Y., Ishikawa, S., Satoh, H., and Sekizawa, K. Clinical evaluation of proton radiotherapy for non-small-cell lung cancer. *International Journal of Radiation Oncology*Biology*Physics*, 56(1):7 – 13, 2003. 6

Shirvani, S. M., Jiang, J., Chang, J. Y., Welsh, J., Likhacheva, A., Buchholz, T. A., Swisher, S. G., and Smith, B. D. Lobectomy, Sublobar Resection, and Stereotactic Ablative Radiotherapy for Early-Stage Non-Small Cell Lung Cancers in the Elderly. *JAMA Surgery*, 149(12):1244–1253, 12 2014. 5, 6

Smeets, J., Roellinghoff, F., Prieels, D., Stichelbaut, F., Benilov, A., Busca, P., Fiorini, C., Peloso, R., Basilavecchia, M., Frizzi, T., Dehaes, J. C., and Dubus, A. Prompt gamma imaging with a slit camera for real-time range control in proton therapy. *Physics in Medicine and Biology*, 57(11):3371–3405, may 2012. 8

Sonke, J.-J., Rossi, M., Wolthaus, J., van Herk, M., Damen, E., and Belderbos, J. Frameless stereotactic body radiotherapy for lung cancer using four-dimensional cone beam ct guidance. *International Journal of Radiation Oncology*Biology*Physics*, 74(2):567 – 574, 2009. 6

Sterpin, E., Sorriaux, J., Souris, K., Vynckier, S., and Bouchard, H. A fano cavity test for monte carlo proton transport algorithms. *Medical Physics*, 41(1):011706, 2014. 12

Stuschke, M., Kaiser, A., Pöttgen, C., Lübcke, W., and Farr, J. Potentials of robust intensity modulated scanning proton plans for locally advanced lung cancer in comparison to intensity modulated photon plans. *Radiotherapy and Oncology*, 104(1):45 – 51, 2012. 8

Szeto, Y. Z., Witte, M. G., van Kranen, S. R., Sonke, J.-J., Belderbos, J., and van Herk, M. Effects of anatomical changes on pencil beam scanning proton plans

in locally advanced nsclc patients. *Radiotherapy and Oncology*, 120(2):286 – 292, 2016. 7, 38

Testa, M., Schuemann, J., Lu, H.-M., Shin, J., Faddegon, B., Perl, J., and Paganetti, H. Experimental validation of the topas monte carlo system for passive scattering proton therapy. *Medical Physics*, 40(12):1–16, 2013. doi: http://dx.doi.org/10.1118/1.4828781. 11

Timmerman, R., Paulus, R., Galvin, J., Michalski, J., Straube, W., Bradley, J., Fakiris, A., Bezjak, A., Videtic, G., Johnstone, D., Fowler, J., Gore, E., and Choy, H. Stereotactic Body Radiation Therapy for Inoperable Early Stage Lung Cancer. *JAMA*, 303(11):1070–1076, 03 2010. 5, 6

Titt, U., Sell, M., Unkelbach, J., Bangert, M., Mirkovic, D., Oelfke, U., and Mohan, R. Degradation of proton depth dose distributions attributable to microstructures in lung-equivalent material. *Medical Physics*, 42(11):6425–6432, 2015. 9, 15, 38

Unkelbach, J., Chan, T. C. Y., and Bortfeld, T. Accounting for range uncertainties in the optimization of intensity modulated proton therapy. *Physics in Medicine and Biology*, 52(10):2755–2773, apr 2007. 7

Urban, L. Multiple scattering model in geant4. *Res. Inst. Part. Nucl. Phys.*, 07 2002. 11

Urie, M., Goitein, M., Holley, W. R., and Chen, G. T. Y. Degradation of the bragg peak due to inhomogeneities. *Physics in Medicine and Biology*, 31(1):1–15, jan 1986. 9

Vavilov, P. V. Ionization losses of high-energy heavy particles. *Sov. Phys. JETP*, 5: 749–751, 1957. 4

Weber, U. and Kraft, G. Design and construction of a ripple filter for a smoothed depth dose distribution in conformal particle therapy. *Physics in Medicine and Biology*, 44(11):2765–2775, oct 1999. 34

Webpage. `https://www.webmd.com/lung/picture-of-the-lungs#1`, 2019. last accessed: December 2019. 8

Welsh, J., Amini, A., Ciura, K., Nguyen, N., Palmer, M., Soh, H., Allen, P. K., Paolini, M., Liao, Z., Bluett, J., Mohan, R., Gomez, D., Cox, J. D., Komaki, R., and Chang, J. Y. Evaluating proton stereotactic body radiotherapy to reduce chest wall dose in the treatment of lung cancer. *Medical Dosimetry*, 38(4):442 – 447, 2013. 6

Wilson, R. R. Radiological use of fast protons. *Radiology*, 47(5):487–491, 1946. 2

Witt, M. Modulationseffekte von Kohlenstoffionen bei der Bestrahlung von Lungen. *master thesis, Technische Hochschule Mittelhessen - University of applied sciences, Giessen, Germany*, 2014. URL `https://www.thm.de/lse/images/user/KZink-105/Abschlussarbeiten/Masterarbeit_Matthias_Witt_2014.pdf`. [last accessed: December 2019]. 10, 15, 16, 22, 26, 33, 37

Witt, M., Weber, U., Simeonov, Y., and Zink, K. Su-e-t-671: Range-modulation effects of carbon ion beams in lung tissue. *Medical Physics*, 42(6Part23):3491–3491, 2015. 10, 15

Wulff, J., Baumann, K.-S., Verbeek, N., Bäumer, C., Timmermann, B., and Zink, K. TOPAS/geant4 configuration for ionization chamber calculations in proton beams. *Physics in Medicine & Biology*, 63(11):115013, jun 2018. 12, 43

Yan, X., Titt, U., Koehler, A., and Newhauser, W. Measurement of neutron dose equivalent to proton therapy patients outside of the proton radiation field. *Nuclear Instruments and Methods in Physics Research Section A: Accelerators, Spectrometers, Detectors and Associated Equipment*, 476(1):429 – 434, 2002. 4

Yang, M., Zhu, X. R., Park, P. C., Titt, U., Mohan, R., Virshup, G., Clayton, J. E., and Dong, L. Comprehensive analysis of proton range uncertainties related to patient stopping-power-ratio estimation using the stoichiometric calibration. *Physics in Medicine and Biology*, 57(13):4095–4115, jun 2012. 7

Zhang, X., Li, Y., Pan, X., Xiaoqiang, L., Mohan, R., Komaki, R., Cox, J. D., and Chang, J. Y. Intensity-modulated proton therapy reduces the dose to normal tissue compared with intensity-modulated radiation therapy or passive scattering proton therapy and enables individualized radical radiotherapy for extensive stage iiib non-small-cell lung cancer: A virtual clinical study. *International Journal of Radiation Oncology*Biology*Physics*, 77(2):357 – 366, 2010. 5, 6

Ziegler, J. F. Stopping of energetic light ions in elemental matter. *Journal of Applied Physics*, 85(3):1249–1272, 1999. 3

Published articles

Article 1, **article 2** and **article 4** are printed with permission from the Institute of Physics and Engineering in Medicine. Reproduced with permission. All rights reserved.

Article 3, **article 5** and **article 6** have been published with an open access and are freely available.

IOP Publishing | Institute of Physics and Engineering in Medicine Physics in Medicine & Biology

Phys. Med. Biol. **62** (2017) 3997–4016 https://doi.org/10.1088/1361-6560/aa641f

An efficient method to predict and include Bragg curve degradation due to lung-equivalent materials in Monte Carlo codes by applying a density modulation

Kilian-Simon Baumann[1,2], Matthias Witt[3], Uli Weber[4], Rita Engenhart-Cabillic[1] and Klemens Zink[1,2,5]

[1] Department of Radiotherapy and Radiooncology, University Medical Center Giessen-Marburg, Marburg, Germany
[2] University of Applied Sciences, Institute of Medical Physics and Radiation Protection, Giessen, Germany
[3] Marburg Ion-Beam Therapy Center (MIT), Marburg, Germany
[4] GSI Helmholtzzentrum für Schwerionenforschung, Biophysics Division, Darmstadt, Germany
[5] Frankfurt Institute for Advanced Studies (FIAS), Frankfurt, Germany

E-mail: kilian-simon.baumann@staff.uni-marburg.de

Received 2 December 2016, revised 10 February 2017
Accepted for publication 2 March 2017
Published 13 April 2017

Abstract

Sub-millimetre-sized heterogeneities such as lung parenchyma cause Bragg peak degradation which can lead to an underdose of the tumor and an overdose of healthy tissue when not accounted for in treatment planning. Since commonly used treatment-planning CTs do not resolve the fine structure of lungs, this degradation can hardly be considered.

We present a mathematical model capable of predicting and describing Bragg peak degradation due to a lung-equivalent geometry consisting of sub-millimetre voxels filled with either lung tissue or air. The material characteristic 'modulation power' is introduced to quantify the Bragg peak degradation. A strategy was developed to transfer the modulating effects of such fine structures to rougher structures such as 2 mm thick CT voxels, which is the resolution of typically used CTs. This is done by using the modulation power to derive a density distribution applicable to these voxels. By replacing the previously used sub-millimetre voxels by 2 mm thick voxels filled with lung tissue and modulating the lung tissue's density in each voxel individually, we were able to reproduce the Bragg peak degradation. Hence a solution is found to include Bragg curve degradation due to lung-equivalent materials in Monte Carlo-based treatment-planning systems.

Keywords: Monte Carlo, lung tissue, Bragg curve degradation, density modulation, proton therapy

(Some figures may appear in colour only in the online journal)

1. Introduction

Since proposed for radiation therapy, ion beams are of increasing interest in radiation oncology (Wilson 1946, Smith 2006). The characteristic dose profile of ions in homogeneous media consists of a low dose plateau at small depths followed by the so-called Bragg peak with a well-defined distal fall-off and—in the case of protons—no dose behind. This finite range and sharp distal fall-off of the energy deposition are the major advantages of protons in radiation therapy, creating the possibility of conformal dose distribution in the target while sparing surrounding healthy tissue (Chang *et al* 2006).

It was shown that this distal fall-off is blurred and the Bragg peak is broadened when the particles pass through heterogeneous media (Urie *et al* 1986, Sawakuchi *et al* 2008). On the one hand this effect is deployed for the benefit of particle therapy, for example in the case of ripple filters that are used to broaden the Bragg peak of mono-energetic particles (Weber and Kraft 1999, Ringbaek *et al* 2014). On the other hand, if it is not considered correctly, the broadening due to the heterogeneity of human lungs can lead to an underdose of the target volume and an overdose of the healthy tissue distal to the target (Goitein 1977, Sawakuchi *et al* 2008), which could significantly influence the dose distribution in lung cancer patients (Espana and Paganetti 2011). Furthermore, the fine structure of the lung is not fully resolved in typical CT images due to the restricted resolution, predicting a more homogeneous tissue distribution (Espana and Paganetti 2011, Titt *et al* 2015), making it even more challenging to consider the Bragg peak degradation due to missing information in the CT image. The effect that the CT averages the density over the volume of a voxel can—in the case of lung parenchyma—lead to variations in the Bragg peak dose of up to 11% and the distal fall-off width of up to 1.1 mm compared to the dose distribution obtained when the heterogeneous structure is exactly considered (Perles *et al* 2011).

To visualise the broadening effect of lung parenchyma, Sell *et al* and Titt *et al* used a 3d-printed geometry built up of voxels each consisting of either air or plastics and both measured and simulated the effect on a 150 and 200 MeV proton dose distribution in a water phantom downstream from the voxelised geometry (Sell *et al* 2012, Titt *et al* 2015). Furthermore Titt *et al* quantified the Bragg peak degradation when irradiating a plastinated human lung. The distal fall-off width from 80% to 20% of the maximum dose increased by up to 60% compared to an unperturbed reference curve, thus indicating that distal edge degradation must be expected in proton treatment of lung tumors.

In other works by Ringbaek *et al* and Witt *et al* a voxelised geometry similar to the one used by Titt *et al* was taken to develop a mathematical model capable of predicting and describing Bragg peak degradation due to lung-like materials (Witt *et al* 2015, Ringbaek *et al* 2017). This mathematical model was verified by Monte Carlo simulations.

In this study we present a simple solution to include and consider this Bragg peak degradation in Monte Carlo codes and therefore Monte Carlo-based treatment-planning systems.

We implemented a voxelised geometry consisting of sub-millimetre voxels filled with either lung tissue or air in the Monte Carlo code Geant4 using the toolkit TOPAS. This geometry is used to demonstrate and understand the modulating effects due to heterogeneous materials such as lung parenchyma.

The broadened dose distribution downstream from the voxelised geometry can be described by convolving an unperturbed reference curve with a normal distribution. From

the parameters of this normal distribution a material characteristic we refer to as 'modulation power' is derived, which quantifies the strength of the modulating effect.

Since the resolution of CT images typically used for treatment planning is too low to resolve such fine sub-millimetre voxels, a strategy is developed to transfer the modulating effects of such fine structures to rougher structures such as 2 mm thick voxels: the previously used voxelised geometry consisting of sub-millimetre voxels was replaced by 2 mm thick voxels filled with lung tissue. In subsequent simulations the density of the lung tissue in each voxel was artificially modulated individually following a density distribution we derived using the modulation power. When modulating the density we were able to reproduce the broadened dose distribution.

We thereby developed a simple tool to implement Bragg curve degradation due to heterogeneous materials such as lung parenchyma in Monte Carlo codes and MC-based treatment-planning systems on the base of clinical CT data.

In an additional simulation the density of the lung tissue in each voxel was not modulated but kept constant to demonstrate the situation when using CT data where the fine structure of the sub-millimetre voxels is not resolved.

As a proof of principle of this strategy we also simulated the broadened Bragg curve downstream from a high-resolution CT of a human lung sample and derived the corresponding modulation power and density distribution for 2 mm thick voxels.

2. Materials and methods

2.1. Mathematical model

To describe the broadening effect on the Bragg peak when traversing heterogeneous materials such as lung parenchyma, a binary cube is taken similar to considerations from Ringbaek *et al*, Titt *et al* and Witt *et al* that consists of $n_x \times n_y \times n_z$ voxels as shown in figure 1. n_z is the number of voxels in beam direction z. n_x, n_y are the numbers of voxels in the lateral directions x and y. The voxel-size in z direction d is called 'structure size'. Each voxel consists of either the material lung tissue with a density $\rho_l = 1.05\,\mathrm{g\,cm^{-3}}$ or air with a density $\rho_a = 0.0012\,\mathrm{g\,cm^{-3}}$ (McConn *et al* 2011). Hence the voxelised geometry provides a binarised density distribution. In this study we distinguish between the terms 'lung parenchyma' and 'lung tissue': by lung tissue we mean the solid structures of the respiratory organ. Lung parenchyma is a collective term for the lung tissue and air in a human lung. The density of the lung parenchyma is hence dependent on the filling status. For an inflated lung the density is $0.26\,\mathrm{g\,cm^{-3}}$ (Schneider *et al* 1996).

The probability that the material lung tissue is assigned to a voxel is p_l. A particle traversing this voxelised geometry will cross n_z voxels. The probability $F(k)$ that k voxels consist of lung tissue is given by the Bernoulli distribution:

$$F(k) = \binom{n_z}{k} \cdot p_l^k \cdot (1 - p_l)^{n_z - k} \tag{1}$$

Following the Moivre–Laplace central limit theorem this distribution can for large n_z be approximated to a sufficient degree of accuracy by a normal distribution:

$$F(k) = \frac{1}{\sqrt{2\pi\sigma_{n_l}^2}} \cdot \exp\left(-\frac{(k - \mu_{n_l})^2}{2\sigma_{n_l}^2}\right) \tag{2}$$

where the expectation value μ_{n_l} and the width σ_{n_l} are given by:

$$\mu_{n_l} = n_z \cdot p_l \quad \text{and} \quad \sigma_{n_l} = \sqrt{n_z \cdot p_l \cdot (1 - p_l)} \tag{3}$$

Hence, a particle traversing the voxelised geometry at one of $n_x \times n_y$ possible paths will cross on average μ_{n_l} voxels of lung tissue with a standard deviation of σ_{n_l} voxels.

From this distribution the function $F(t'|t, \sigma_t)$ can be derived giving the probability that the path a particle takes through the voxelised geometry has the water-equivalent thickness t':

$$F(t'|t, \sigma_t) = \frac{1}{\sqrt{2\pi\sigma_t^2}} \cdot \exp\left(-\frac{(t'-t)^2}{2\sigma_t^2}\right) \tag{4}$$

with t being the mean water-equivalent thickness:

$$t = \frac{\rho_{\text{mean}}}{\rho_{\text{H}_2\text{O}}} \cdot D \text{ with } \rho_{\text{mean}} = p_l \cdot \rho_l + (1 - p_l) \cdot \rho_a \approx \rho_l \cdot p_l \tag{5}$$

where $D = n_z \cdot d$ is the geometrical thickness of the voxelised geometry, $\rho_{\text{H}_2\text{O}} := 1$ g cm^{-3}, and ρ_{mean} is the average water-equivalent density of the geometry. The approximation takes into account that $\rho_a \ll \rho_l$.

The width σ_t of the distribution can be calculated with σ_{n_l} from equation (3) where $n_z = D/d$ and using that the difference in the water-equivalent thickness between a voxel filled with lung tissue and a voxel filled with air is $d \cdot \frac{\rho_l - \rho_a}{\rho_{\text{H}_2\text{O}}}$:

$$\sigma_t^2 = \frac{D}{d} \cdot p_l \cdot (1 - p_l) \cdot d^2 \cdot \left(\frac{\rho_l - \rho_a}{\rho_{\text{H}_2\text{O}}}\right)^2 \approx t \cdot d \cdot (1 - p_l) \cdot \frac{\rho_l}{\rho_{\text{H}_2\text{O}}} \tag{6}$$

The values for t', t and σ_t are given in units of length in water. Hence the density ρ_{mean} from equation (5) is also given in water-equivalent units. However, the difference between water-equivalent density and physical density caused by the stopping power ratio (ICRU 1994) is very small for lung tissue since it consists of over 85% water. We therefore approximate that the water-equivalent density is equal to the physical density in the case of lung tissue.

Using a normal distribution with the width σ_t to describe the broadening of the Bragg peak is in correspondence with other works (Titt *et al* 2015, Witt *et al* 2015, Ringbaek *et al* 2017). Mathematically the broadened dose distribution $b_*(z)$ in depth z in water can be derived by a convolution of the unperturbed reference curve $b_0(z)$ with $F(t'|t, \sigma_t)$:

$$b_*(z) = (F * b_0)(z) = \int_{-\infty}^{\infty} F(t'|t, \sigma_t)\, b_0\,(z + t')\, \mathrm{d}t' \tag{7}$$

The displacement of the broadened dose distribution $b_*(z)$ compared to the unperturbed reference curve $b_0(z)$ is always smaller than or equal to zero such shifting to smaller depths z, since the water-equivalent thickness t' is $\geqslant 0$. Hence we use $(z + t')$ instead of the common convolution $(z - t')$. By the terms reference curve and broadened dose distribution we mean the 'integrated depth dose distribution' (IDD).

In figure 1 the broadening of the dose distribution due to the binary voxelised geometry and the use of the mathematical model are visualised: in the water phantom downstream from the voxelised geometry an unperturbed reference curve $b_0(z)$ and a broadened dose distribution $b_*(z)$ are shown. The displacement t and the broadening σ_t of $b_*(z)$ can be described by the convolution of the reference curve with the distribution $F(t'|t, \sigma_t)$. The average displacement is given by t. It does not refer to the depth of the maximum of the Bragg peak but rather to the depth at the distal fall-off where the dose is ~82% of the maximum dose. This depth will be called z_{p82} in this study. The background that the shift refers better to this depth z_{p82} is that each dose distribution is the superposition of each single particle's dose depositions, in which

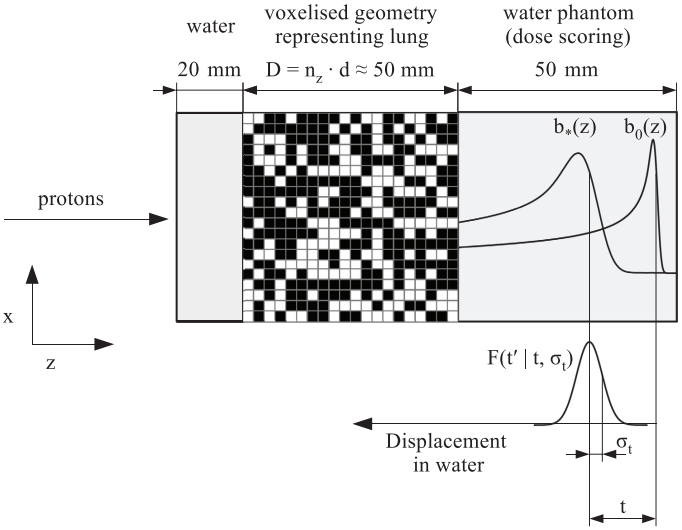

Figure 1. Schematic description of the MC set-up. The proton beam direction is in positive z, traversing a 20 mm thick slice of water and the binary voxelised geometry with a length in z of $D = n_z \cdot d \approx 50$ mm. Black voxels represent air, white ones lung tissue. The water phantom in which the dose distributions are scored is placed downstream from the voxelised geometry. To visualise the mathematical model an exemplary unperturbed reference curve $b_0(z)$ and a broadened dose distribution $b_*(z)$ are shown. The broadening and displacement of $b_*(z)$ can be described by the convolution of the reference curve with a normal distribution $F(t'|t, \sigma_t)$ giving the probability that the path a particle is taking through the voxelised geometry has a water-equivalent thickness t'. The displacement of $b_*(z)$ is given by the mean value t and does not exactly refer to the maximum of the Bragg peak but rather to the depth z_{p82} where the dose of the distal fall-off is ∼82% of the maximum dose. The broadening is given by the value of σ_t.

connection each particle has a certain range following a normally distributed range distribution. The maximum of this range distribution lies in the depth of the ∼82% maximum dose for all dose distributions (Bichsel *et al* 2000). The shift of this range distribution is quantified by t and its broadening is quantified by the parameter σ_t.

From the values of t and σ_t (see equations (5) and (6)) a material characteristic for inhomogeneous materials such as lung parenchyma can be introduced, which we call 'modulation power' P_{mod} (in analogy with 'stopping power' or 'scatter power'):

$$P_{\mathrm{mod}} \equiv \frac{\sigma_t^2}{t} = d \cdot \frac{p_l(1-p_l)(\rho_l-\rho_a)}{p_l(\rho_l-\rho_a)+\rho_a} \cdot \frac{(\rho_l-\rho_a)}{\rho_{H_2O}} \approx d \cdot (1-p_l) \cdot \frac{\rho_l}{\rho_{H_2O}} \tag{8}$$

P_{mod} has the unit of length in water and does not depend on the geometrical thickness D of the geometry, but rather on the size of the voxels in the beam direction, the so-called structure

size d. Furthermore P_{mod} can be easily determined by measuring dose distributions in a water phantom downstream from the lung parenchyma as done by Titt *et al* (2015) and Witt (2014). In the study by Witt (2014) the modulation power of porcine lungs for a 80 MeV u^{-1} carbon beam was measured to be in the range of 150–750 μm water-equivalent length.

Using P_{mod} the distribution $F(t'|t,\sigma_t)$ from equation (4) can be derived for any geometrical thickness D using that $t = \frac{\rho_{\mathrm{mean}}}{\rho_{\mathrm{H_2O}}} \cdot D$ and $\sigma_t^2 = P_{\mathrm{mod}} \cdot t$.

2.2. $F(t'|t,\sigma_t)$ for small geometries—especially CT voxels

However, for a given modulation power P_{mod} and average density ρ_{mean} the value of t decreases for decreasing D, which can lead to non-negligible contributions for negative water-equivalent thicknesses in $F(t'|t,\sigma_t)$ from equation (4). This can especially be the case when D has the size of a CT voxel. This normally distributed $F(t'|t,\sigma_t)$ can therefore not be used for thin targets. To just cut off $F(t'|t,\sigma_t)$ at $t' = 0$ g cm^{-3} is not a suitable solution since this would result in a higher average water-equivalent thickness t.

Hence a different distribution $\overline{F}(t'|D)$ must be developed without negative contributions describing the distribution of water-equivalent thicknesses t' of a thin target with geometrical thickness D.

To do so, in a first step the normally distributed $F_T(t'|t,\sigma_t)$ from equation (4) with $t = \rho_{\mathrm{mean}}/\rho_{\mathrm{H_2O}} \cdot T$ and $\sigma_t^2 = P_{\mathrm{mod}} \cdot t$ is derived for a sufficiently thick target with thickness $T = n \cdot D$ with $n \in \mathbb{N}$ assuring, that $F_T(t'|t,\sigma_t) \approx 0$ for $t' < 0$.

The requirements to $\overline{F}(t'|D)$ then are:

- $\overline{F}(t'|D)$ consists of single weights w_i based on fine steps of e.g. $\Delta = 50$ μm: $w_i = \overline{F}(t' = i \cdot \Delta|D)$ with $\sum w_i = 1$
- $\overline{F}(t'|D) = 0$ for $t' < 0$
- $\overline{F}(t'|D)$ convolved n times with itself equals the normal distribution $F_T(t'|t,\sigma_t)$:

$$\underbrace{\overline{F}(t'|D) * \overline{F}(t'|D) \ldots * \overline{F}(t'|D)}_{n \text{ times}} \approx F_T(t'|t,\sigma_t) \tag{9}$$

The last and most important requirement assures that n thin targets of thickness D have the same physical characteristics as the thick target of thickness $T = n \cdot D$, such as the same average water-equivalent thickness and the same modulation power P_{mod}.

There are various options to construct $\overline{F}(t'|D)$ as discussed in section 4. We used a combination of a shifted Poisson distribution and a single high weight w_0 at $t' = 0$. The shifted Poisson distribution is defined only for positive values and has a shape similar to the normal distribution. The Poisson distribution was generalised for non-integers by replacing the factorial function by the Gamma function. The weight w_0 at $t' = 0$ is necessary to compensate for negative water-equivalent thicknesses t' that the normally distributed $F_D(t'|t,\sigma_t)$ for the thin target of thickness D would have.

$\overline{F}(t'|D)$ is determined by optimising the parameters of the Poisson distribution and the single weight w_0 to best fulfill equation (9).

An example for such a discrete distribution $\overline{F}(t'|D)$ for a modulation power $P_{\mathrm{mod}} = 800$ μm and a geometrical thickness $D = 2$ mm is shown in figure 2 and compared to the normal distribution $F_D(t'|t,\sigma_t)$ for the thin target of thickness D: the solid line represents the normal distribution $F_T(t'|t,\sigma_t)$ for a target of thickness $T = n \cdot D$ where normally $F_T(t'|t,\sigma_t) \approx 0$ for $t' < 0$. In this example $n = 20$ and $T = 40$ mm. The dashed line gives the normal distribution $F_D(t'|t,\sigma_t)$ for a target of thickness D with non-negligible contributions for negative t'. In

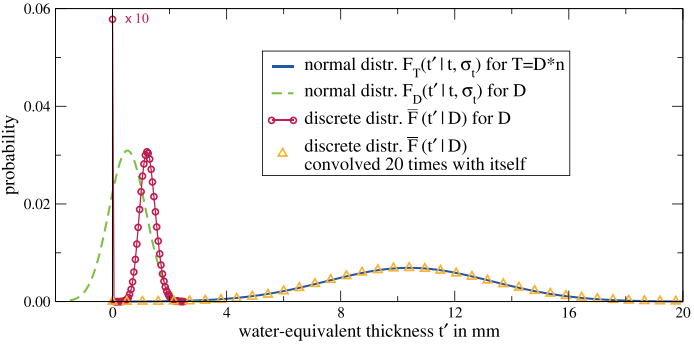

Figure 2. Deriving $\overline{F}(t'|D)$ for small targets. In solid line the normal distribution $F_T(t'|t,\sigma_t)$ for the thickness $T = n \cdot D = 20 \cdot 2\,\text{mm} = 40\,\text{mm}$ using a modulation power $P_{\text{mod}} = 800\,\mu\text{m}$. In dashed line the normal distribution $F_D(t'|t,\sigma_t)$ for $D = 2\,\text{mm}$ with non-negligible contributions for negative t'. In circles the optimised discrete distribution $\overline{F}(t'|D)$ with no negative ratios consisting of a single high weight w_0 at $t' = 0$ and a shifted Poisson distribution generalised for non-integers by replacing the factorial function by the Gamma function. The weight w_0 at $t' = 0$ was scaled with a factor of 0.1 for better clarity. The result when convolving this distribution $\overline{F}(t'|D)$ 20 times with itself is shown in triangles. For better clarity only every tenth step is shown. It matches the normal distribution $F_T(t'|t,\sigma_t)$.

circles the optimised discrete distribution $\overline{F}(t'|D)$ is shown. The weight w_0 at $t' = 0$ is scaled with a factor of 0.1 for better clarity. The result when convolving this distribution $\overline{F}(t'|D)$ $n = 20$ times with itself is showed in triangles. It matches the normal distribution $F_T(t'|t,\sigma_t)$. In this application folding 20 times proved to be sufficient. It should be noted, that the normal distribution $F_T(t'|t,\sigma_t)$ is only a temporary construct to derive $\overline{F}(t'|D)$ and is not further used.

Generalising from this optimised function $\overline{F}(t'|D)$ a density probability-function $\overline{F}(\rho'|D)$ can be derived by substituting t' with $\rho' = t'/D \cdot \rho_{H_2O}$. $\overline{F}(\rho'|D)$ then gives the probability that a voxel of size D has a certain water-equivalent density ρ'. For lung tissue the physical density is approximately equal to the water-equivalent density as discussed in section 2.1.

2.3. Monte Carlo simulations

All simulations were performed with the TOPAS code ('TOol for PArticle Simulation') (Perl *et al* 2012) version 3.0.p1, based on Geant4 ('GEometry ANd Tracking') (Agostinelli *et al* 2003) version 10.02.p01. Previous studies have extensively validated the code against experimental data (Perl *et al* 2012, Testa *et al* 2013). The default TOPAS physics list was used. The production cut for all particles was set to 0.05 mm, corresponding to an energy of ~55 keV for electrons in water. The mean ionization potential for water was set to $I = 78\,\text{eV}$.

2.3.1. MC simulations for small voxels with a binary density distribution. A set-up as shown in figure 1 was used in TOPAS: a mono-energetic parallel proton beam with Gaussian profile (FWHM of 1 cm) traversed a 20 mm thick slice of water, the voxelised geometry representing lung parenchyma and was stopped in a water phantom downstream from the voxelised

geometry. No nozzle geometry was used. The set-up was surrounded by vacuum. The proton's energy was chosen to be 90 MeV u^{-1}, so that the protons have enough energy to penetrate the voxelised geometry. To minimise energy-straggling effects which superimpose with the degradation from the voxelised geometry, the energy was set as small as possible. The voxelised geometry consisted of 100×100 voxels in lateral directions x and y with length of 0.5 mm. The thickness in z direction of the voxels d was varied between 129 μm and 1020 μm. The voxels consisted of either the material lung tissue with density $\rho_l = 1.05$ g cm^{-3} or air with density $\rho_a = 0.0012$ g cm^{-3}, hence providing a binary density distribution as used in the mathematical model described in section 2.1. The probability p_l that a voxel consisted of lung tissue was set to 0.25 resulting in the average density $\rho_{\text{mean}} = 0.26$ g cm^{-3} (as described in section 2.1 and equation (5)), which is the density of an inflated lung (Schneider *et al* 1996). Using equation (8) these values of d and p_l result in theoretical modulation powers P_{mod} between 100 and 800 μm, hence covering the range of modulation powers of lung parenchyma measured by Witt (2014). The exact values of P_{mod} in dependence on d are listed in table 1. The compositions and densities of lung tissue and air were taken from McConn *et al* (2011). The thickness of the whole voxelised geometry $D = n_z \cdot d$ was held constant at roughly 50 mm.

The depth-dose distributions in the water phantom were scored with a resolution of 0.1 mm. Further on the lateral dose profile in x direction at depth z_{p82} was scored for each dose distribution. In a first simulation the depth-dose distribution was scored without the voxelised geometry in the beam path to obtain an unperturbed reference curve $b_0(z)$. In following simulations the voxelised geometry was implemented and the broadened dose distributions $b_*(z)$ were scored for each d.

To calculate the modulation powers P_{mod} analogue to equation (7) the values of t and σ_t of the normal distribution $F(t'|t, \sigma_t)$ from equation (4) were optimised, so that the broadened dose distribution $b_*(z)$ gained from the MC simulations fitted the unperturbed reference curve $b_0(z)$ convolved with $F(t'|t, \sigma_t)$.

2.3.2. MC simulations for CT voxels of clinically relevant sizes. In the next step we present our solution to reproduce the Bragg peak degradation in Monte Carlo codes for the case that CT data are used where the small voxels of size d as used in the previous simulations are not resolved.

The modulation powers $P_{\text{mod}} = \sigma_t^2/t$ were calculated for each value of d using the values of t and σ_t obtained form the optimisation of $F(t'|t, \sigma_t)$. From these P_{mod} the discrete density distributions $\overline{F}(\rho'|D)$ for 2 mm thick voxels were derived using the method described in section 2.2.

In the next step the binary voxelised geometry consisting of small voxels filled either with lung tissue or air as used in the previous simulations was replaced by a geometry consisting of $25 \times 25 \times 25$ voxels each $2 \times 2 \times 2$ mm^3 in size, which is the voxel size of CTs typically used in lung cancer treatment. Each voxel was filled with lung tissue. For each P_{mod} a simulation was run where the density of the lung tissue in each voxel was modulated individually according to the determined density distribution $\overline{F}(\rho'|D)$. This was done by creating 500 different dicom sets each consisting of 25 slices. Each slice consisted of 25×25 voxels filled with lung tissue. For each voxel the density of the lung tissue was randomly set to a value ρ' with the corresponding probability $\overline{F}(\rho'|D)$. The dicom slices thus consisted of voxels each filled with lung tissue, albeit with different, randomised densities. In TOPAS N primaries were simulated in 500 subsequent runs. In the first run, the first dicom set of 25 slices was read in and N/500 particles were simulated. In the second run the second dicom set consisting of 25 slices was read in and N/500 particles were simulated. This was done for each of the 500 runs. At the end the dose distributions from each run were summed up.

In principle it is possible to create an individual dicom set for each simulated particle. However, this leads to longer computing times in both the creation process of the dicom sets and the MC simulations. It was assumed that 500 dicom sets are a sufficiently good approximation.

In an additional simulation only one dicom set consisting of 25 slices was used for all N particles. Each voxel consisted of the material lung tissue. The density of the lung tissue was fixed at the value $\rho_{\text{mean}} = 0.26\,\text{g cm}^{-3}$ corresponding to the average density of an inflated lung. This density correlates to the density a CT image would provide, not capable of resolving the heterogeneous structure of the voxelised geometry or lung parenchyma in particular, hence only providing an average density. In all simulations the depth-dose distribution and lateral dose profile in x direction at the depth z_{p82} were scored.

2.3.3. The influence of the Bragg peak degradation on the dose distribution in a PTV. To visualise the broadening effect of a heterogeneous material on a treatment plan when planning on the base of CT images not capable of resolving the fine structure of lung parenchyma, the irradiation of a $10 \times 10 \times 30\,\text{mm}^3$ planning target volume (PTV) was optimised for homogeneous dose. The same set-up as shown in figure 1 was used and the PTV was placed in the water phantom downstream from the voxelised geometry.

To optimise the treatment plan of the PTV, the voxelised geometry from figure 1 was replaced by a cube of $25 \times 25 \times 25$ voxels each $2 \times 2 \times 2\,\text{mm}^3$ in size homogeneously filled with lung tissue. The lung tissue's density was set to $\rho = 0.26\,\text{g cm}^{-3}$. After scoring proton dose distributions for energies between 70 and 100 MeV u^{-1}, the weight for each energy was optimised to obtain a homogeneous dose distribution within the PTV. This optimisation process would correspond to the optimisation of a treatment plan based on CT images typically used in clinics, where the fine structure of the lung parenchyma is not resolved, so only an average density is provided. The target dose was set to 60 Gy.

The dose distribution for the optimised treatment plan was then simulated in two scenarios: in a first simulation the density of the lung tissue in each voxel was set to a constant $\rho = 0.26\,\text{g cm}^{-3}$ as was the case in the optimisation process. In a second simulation the density of the lung tissue in each voxel was modulated using a density distribution derived for 2 mm thick voxels based on a modulation power $P_{\text{mod}} = 800\,\mu\text{m}$. The randomisation of the density in each voxel was done as described in section 2.3.2. Using a modulation power of 800 μm an upwards estimation can be made, since the modulation power of lung parenchyma lies in the range from 150 μm to 750 μm.

2.3.4. MC simulation of a high-resolution CT of a human lung sample. To prove that the described mathematical model is applicable to real lung parenchyma and to determine the modulation power of human lung parenchyma, in an additional simulation the Bragg curve of 50 MeV u^{-1} protons after traversing a high-resolution CT of a human lung sample was calculated. The sample was prepared as described in Rau *et al* (1980) and Litzlbauer *et al* (2006). The sample consisted of $1000 \times 1000 \times 1000$ voxels with an edge length of 0.004 mm resulting in a cube of $4 \times 4 \times 4\,\text{mm}^3$. Since the CT data were not calibrated in the same way as common treatment-planning CTs, the data were binarised to voxels consisting of lung tissue and voxels consisting of air using a threshold technique. An example is shown in figure 3. Black voxels represent air, white ones lung tissue.

As in the simulations before the dose distribution downstream from the CT data was scored, the modulation power P_{mod} was calculated from the Monte Carlo simulation results and a discrete density distribution $\overline{F}(\rho'|D)$ was derived for 2 mm thick voxels. In a second simulation the CT data were replaced by a geometry consisting of $2 \times 2 \times 2$ voxels each $2 \times 2 \times 2\,\text{mm}^3$

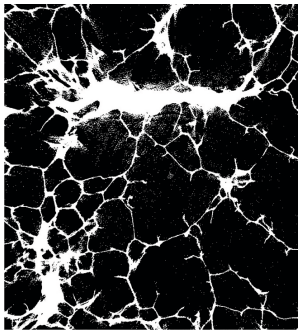

Figure 3. An exemplary section of 650×720 voxels of a binarised high-resolution CT of the human lung sample: black voxels represent air, white ones lung tissue. A threshold technique was used to binarise the CT data.

in size filled with lung tissue and the density of the lung tissue was modulated following the found density distribution as described in section 2.3.2.

3. Results

3.1. MC simulations for small voxels with a binary density distribution

The Bragg peak degradation due to the voxelised geometry from figure 1 consisting of small voxels filled with either lung tissue or air and hence providing a binary density distribution is shown in figure 4. In the upper graph the unperturbed reference curve and the dose distributions after traversing the geometry consisting of small voxels with a binary density distribution (BD) for $d = 129$ μm and $d = 1020$ μm are shown in dotted, straight and dashed lines. The corresponding theoretical modulation powers P_{mod} calculated using equation (8) with the values for d and $p_l = 0.25$ are $P_{\mathrm{mod}} \approx 100$ μm and $P_{\mathrm{mod}} \approx 800$ μm. The distal fall-off widths from 80% to 20% maximum dose (DFW) are 0.9 mm for the reference curve and 1.9 mm and 4.2 mm for the broadened curves corresponding to $P_{\mathrm{mod}} \approx 100$ μm and $P_{\mathrm{mod}} \approx 800$ μm, respectively. In correspondence to the degradation of the Bragg peak the maximum dose is decreased compared to the reference distribution. However, this is only the case for monoenergetic particles. As shown later in this study, in spread out Bragg Peaks the maximal dose in the plateau is not reduced due to energy conservation. Hence the dose reduction of monoenergetic beams can been seen; this effect is not, however, a suitable parameter to describe Bragg peak degradation.

In figure 4 in the upper graph the convolution of the reference curve with the optimised normal distributions $F(t'|t, \sigma_t)$ from equation (4) presented in the lower graph are shown in symbols. For better clarity only every fifth data point is shown. They match the dose distributions from the geometry consisting of small voxels with a binary density distribution resulting in the same values for the DFW. The mean values t are 13.2 mm for both modulation powers and the widths σ_t are 1.1 mm and 3.2 mm. From these values the actual modulation powers of the voxelised geometry $P_{\mathrm{mod}} = \sigma_t^2/t$ were calculated to be 100 μm and 793 μm, which is in good accordance with the theoretical values.

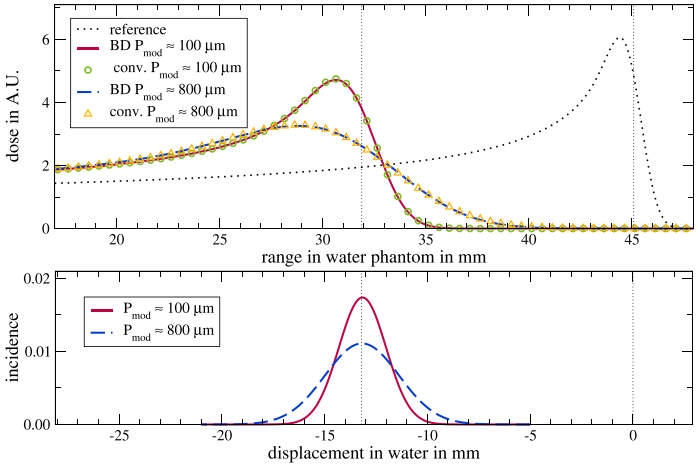

Figure 4. Bragg peak degradation due to heterogeneous geometries. In straight, dashed and dotted lines in the upper graph the unperturbed reference curve and the dose distributions downstream the geometry consisting of small voxels with a binary density distribution (BD) for $d = 129$ μm and $d = 1020$ μm resulting in theoretical modulation powers $P_{\mathrm{mod}} \approx 100$ μm and $P_{\mathrm{mod}} \approx 800$ μm. In symbols (conv.) the results are shown when the reference curve is convolved with the optimised normal distributions $F(t'|t, \sigma_t)$ from equation (4) shown in the lower graph. For better clarity only the region around the Bragg peak is shown. The statistical uncertainties from the MC simulations lie in the region of the line widths. In addition, vertical dotted lines are shown in depths of 45.1 mm and 31.9 mm, referring to the depths z_{p82} in the upper graph, and at displacements of 0 mm and -13.2 mm in the lower graph to visualise, that the displacement refers to the depth z_{p82} and not to the maximum of the Bragg peak itself.

Further on in the upper graph the depths z_{p82} for the reference curve and the broadened dose distributions are shown in vertical dotted lines. In correspondence in the lower graph at the displacements 0 mm and -13.2 mm vertical, dotted lines are shown. This visualises that the shift t refers to the depth z_{p82} as described in section 2.1 and not to the maximum of the Bragg peaks. This depth z_{p82} is 31.9 mm for both broadened dose distributions and 45.1 mm for the reference curve, resulting in a shift of 13.2 mm, equal to the value of t.

The results for the other values of d and P_{mod} are shown in table 1. The deviations between the theoretical values for P_{mod} (calculated with equation (8) and using the voxel size d and the probability $p_l = 0.25$) and the values for P_{mod} gained from the simulations and the optimisation of the convolution ($P_{\mathrm{mod}} = \sigma_t^2/t$) are on average 1.8% with a maximum deviation of 4.2%. The DFWs increase with increasing modulation power.

3.2. MC simulations for CT voxels of clinically relevant sizes

To reproduce the Bragg peak degradation, density distributions $\overline{F}(\rho'|D)$ for 2 mm thick voxels were derived using the values of P_{mod} gained from the previous simulations. These density distributions are shown in figure 5 for the modulation powers 100 μm and 800 μm.

Table 1. The values for the structure sizes d of the voxels and the corresponding theoretical values for the modulation powers $P_{\mathrm{mod}}^{\mathrm{theo}}$ calculated with d and $p_l = 0.25$ using equation (8). Additionally the modulation powers $P_{\mathrm{mod}} = \sigma_t^2/t$ gained from the simulation results after optimising $F(t'|t, \sigma_t)$ for the geometry consisting of small voxels with a binary density distribution and the geometry consisting of 2 mm thick voxels filled with lung tissue, where the density of the lung tissue was modulated for each voxel individually. Also listed are the resulting distal fall-off widths DFW from 80% to 20% maximum dose and the FWHMs of the lateral dose distributions at depth z_{p82}.

	Small voxels with binary density				2 mm voxels with modulated density		
d (μm)	$P_{\mathrm{mod}}^{\mathrm{theo}}$ (μm)	P_{mod} (μm)	DFW (mm)	FWHM (mm)	P_{mod} (μm)	DFW (mm)	FWHM (mm)
129	101	100	1.9	11.0	98	1.8	11.3
256	200	209	2.3	11.3	208	2.3	11.3
384	301	301	2.8	10.8	304	2.7	11.3
510	399	403	3.1	10.9	396	3.1	11.3
641	502	486	3.4	11.9	483	3.4	11.3
769	602	606	3.8	11.5	598	3.7	11.2
892	698	724	4.1	11.5	705	4.1	11.2
1020	799	793	4.2	11.2	779	4.3	11.2

The density distributions consist of a weight w_0 at $\rho' = 0$ g cm^{-3} and a shifted Poisson distribution generalised for non-integers by using the Gamma function instead of the factorial function. For an increasing modulation power P_{mod} the distribution becomes broader, is shifted to the right and has a greater weight w_0 at $\rho' = 0$ g cm^{-3}. For each density distribution the centre is at $\rho = 0.26$ g cm^{-3} correlating to the average density ρ_{mean} of the voxelised geometry.

Using these density distributions the geometry consisting of small voxels with a binary density distribution was replaced by a geometry consisting of 2 mm thick voxels filled with lung tissue and the density of the lung tissue was modulated for each voxel individually following $\overline{F}(\rho'|D)$. The resulting dose distributions are shown in figure 6 in symbols (MD: modulated density) for the modulation powers $P_{\mathrm{mod}} \approx 100$ μm and $P_{\mathrm{mod}} \approx 800$ μm. For better clarity only every fifth data point and only the region around the Bragg peak is shown. The dose distributions for the same modulation powers after traversing the original geometry consisting of small voxels with a binary density distribution (BD) are shown in straight and dashed lines. The dose distributions when modulating the density almost perfectly match the broadened dose distributions downstream from the original voxelised geometry. The DFWs are 1.8 mm and 4.3 mm, compared to 1.9 mm and 4.2 mm for the distributions downstream from the original voxelised geometry. The modulation powers for the dose distributions when modulating the density are 98 μm and 779 μm, hence reproducing the modulation power from the original voxelised geometry with an accuracy of 2%. The depths z_{p82} are 31.8 mm and 31.7 mm, resulting in a deviation of 0.1–0.2 mm compared to the original voxelised geometry.

The results for all P_{mod}-values are listed in table 1. For all modulation powers the deviation in the DFWs compared to the original voxelised geometry are on average 1.7% with a maximal deviation of 5.3%. The modulation powers could be reproduced with an accuracy of on average 1.4%.

When the density was not modulated but instead held constant at the average density $\rho_{\mathrm{mean}} = 0.26$ g cm^{-3} as shown by the dotted line in figure 6, the dose distribution is as narrow as the reference curve with a DFW of 0.9 mm. The depth z_{p82} is 31.9 mm.

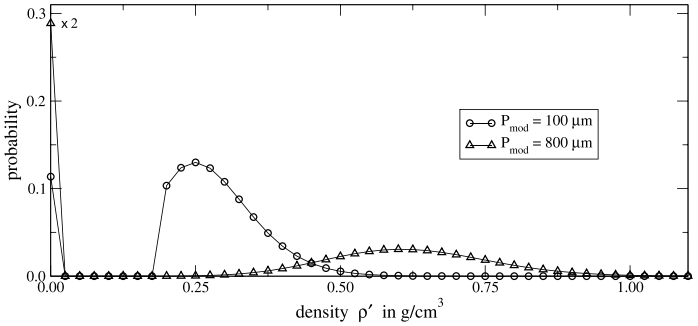

Figure 5. The optimised discrete density distributions $\overline{F}(\rho'|D)$ for $D = 2$ mm and the modulation powers $P_{\mathrm{mod}} = 100\ \mu$m and $P_{\mathrm{mod}} = 800\ \mu$m in circles and triangles. The data points are connected for better clarity. For the modulation power 800 μm the weight w_0 at $\rho' = 0$ g cm^{-3} is scaled with a factor of 0.5 for better clarity.

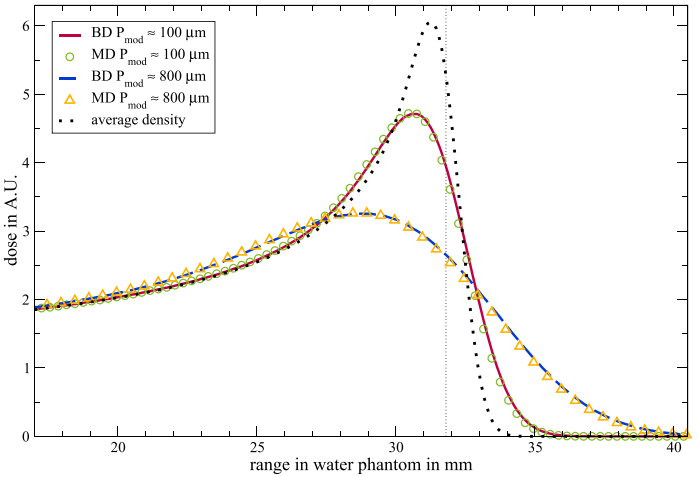

Figure 6. Reproducing the Bragg peak degradation when modulating the density of 2 mm thick voxels. The dose distributions after traversing the original geometry consisting of small voxels with a binary density distribution (BD) for the modulation powers $P_{\mathrm{mod}} \approx 100\ \mu$m and $P_{\mathrm{mod}} \approx 800\ \mu$m in solid and dashed lines. For the same values of P_{mod} the dose distributions when applying the density modulation to 2 mm thick voxels (MD) in symbols and when using the average density ρ_{mean} in dotted line. For better clarity only the region around the Bragg peak is shown. The statistical uncertainties from the MC simulations lie in the region of the line widths. The depth z_{p82} is marked as a vertical dotted line.

Table 1 also shows the FWHMs of the lateral dose distributions scored at depth z_{p82}. The FWHM for the geometry consisting of small voxels with a binary density distribution vary between 10.8 mm and 11.9 mm whereas the FWHMs for the geometry consisting of 2 mm thick voxels filled with lung tissue where the lung tissue's density was modulated are between 11.2 mm and 11.3 mm.

3.3. The influence of the Bragg peak degradation on the dose distribution in a PTV

In figure 7 the results for the irradiation of a hypothetical PTV are shown. The PTV was placed in a water phantom downstream from a 50 mm thick slice of lung tissue. The irradiation was optimised using an average density of $\rho_{\text{mean}} = 0.26$ g cm^{-3} in each voxel of the lung tissue. The irradiation of the PTV was then simulated using this average density and additionally in a second scenario, where the density of the lung tissue in each voxel was modulated according to a modulation power P_{mod} of 800 μm. The upper panel shows the 2d dose distribution in the *x*-*z* plane in the water phantom when irradiating through the geometry filled with lung tissue with a fixed density of 0.26 g cm^{-3}. The black box represents the PTV. The dose in the PTV is almost perfectly homogeneously distributed with a sharp distal fall-off. Further on the isodoses 80%, 90% and 95% are indicated in colored lines. The PTV is completely enclosed by the 95% isodose. The lower panel shows the same 2d dose distribution, when irradiating through the lung tissue where the lung tissue's density is modulated for each voxel individually using a density distribution based on a modulation power $P_{\text{mod}} = 800$ μm. The dose at the proximal and distal ends of the PTV is lower compared to the first case. Further on the isodoses now lie within the PTV at the distal end. The dose at the centre of the PTV is almost perfectly homogeneously distributed. The distal fall-off is broader compared to the first case, resulting in greater doses downstream from the PTV.

In figure 8 on the left side the 1d dose distribution along the beam axis is shown. The distal fall-off widths are 1.3 mm and 5.6 mm. The dose at the proximal end of the SOBP is lower for the degraded Bragg peak. As already described before the maximum dose in the plateau is the same for both distributions.

In figure 8 on the right side a dose-volume histogram is shown for the PTV and the healthy tissue, which in this case includes the whole volume around the PTV. The black line marks the volume receiving 95% of the prescribed dose. The histogram for the PTV and the unmodulated, average density shows a sharp fall-off at ∼60 Gy. The relative volume receiving 95% prescribed dose is 100%. For the modulated density representing real lung parenchyma the fall-off is broader and the relative volume irradiated with 95% prescribes dose is only 88%. The dose values $D_{98\%}$ for 98% irradiated volume are 59.0 Gy and 47.0 Gy, respectively. In contrast to the clear underdose of the PTV the dose deposited in the healthy tissue is greater for the modulated density.

3.4. MC simulation of a high-resolution CT of a human lung sample

In figure 9 the unperturbed reference curve and the broadened dose distribution downstream from the high-resolution CT of a human lung sample and the dose distribution when replacing these CT data with a geometry consisting of $2 \times 2 \times 2$ mm^3 voxels filled with lung tissue and modulating the lung tissue's density. For better clarity only every fifth data point is shown for the distribution gained from the density modulation. The values of t and σ_t from the distribution $F(t'|t, \sigma_t)$ from equation (4) were optimised so that $F(t'|t, \sigma_t)$ convolved with the reference curve fits the broadened dose distribution downstream from the high-resolution CT. From t

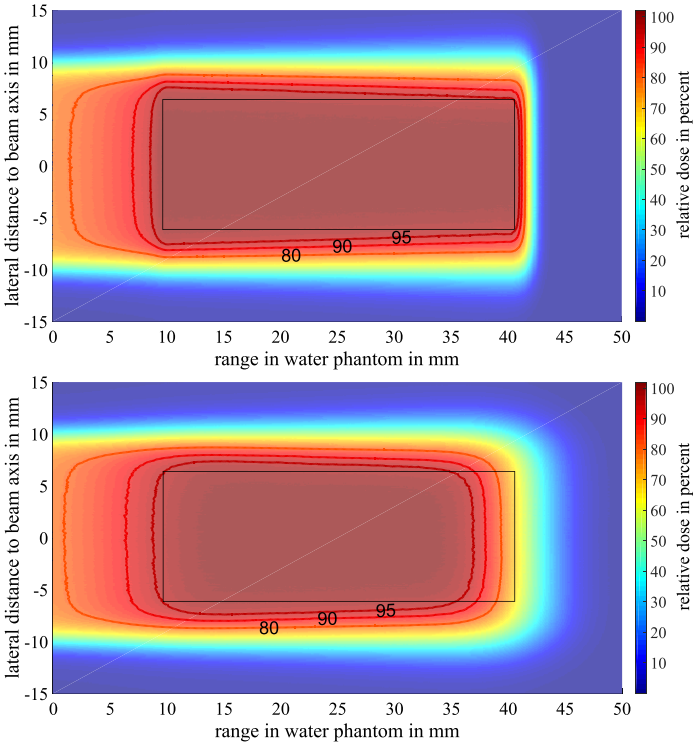

Figure 7. 2d dose distribution with and without Bragg peak degradation. In the upper panel the 2d dose distribution in the x-z plane in the water phantom when irradiating through the voxelised geometry with a fixed density $\rho = 0.26$ g cm^{-3}. The black box represents the PTV. The lower panel shows the same dose distribution when irradiating through the voxelised geometry where the lung tissue's density is modulated in each voxel individually. The isodoses 80%, 90% and 95% are indicated in colored lines.

and σ_t the modulation power P_{mod} was calculated and used to derive a density distribution $\overline{F}(\rho'|D)$ for 2 mm thick voxels.

The modulation power P_{mod} is 66 μm resulting in a DFW of 0.4 mm. When modulating the density of 2 mm thick voxels the modulation power is 65 μm resulting in the same DFW of 0.4 mm. The DFW for the reference curve is 0.3 mm. The depth z_{p82} for the reference curve is 22.6 mm and for the other two dose distributions it is 21.9 mm.

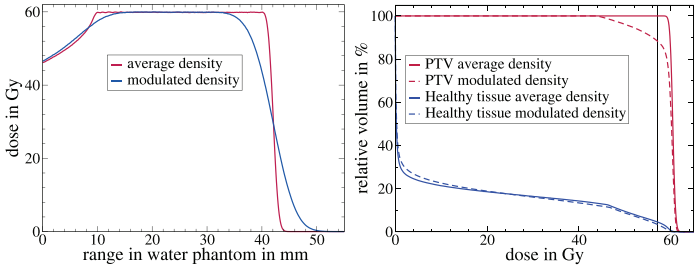

Figure 8. 1d dose distribution and dose-volume histogram with and without Bragg peak degradation. On the left side the 1d dose distribution along the beam axis for both irradiation modalities of the hypothetical PTV (average and modulated density). On the right side the dose-volume histogram is shown: in straight and dashed lines the histograms for both modalities. The healthy tissue includes the whole volume around the PTV.

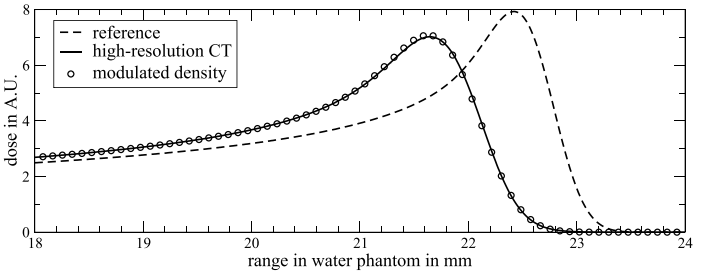

Figure 9. Bragg peak degradation due to lung parenchyma. The broadened dose distribution after traversing the high-resolution CT of a human lung sample as a straight line. As circles the dose distribution when replacing these CT data with a cube of $2 \times 2 \times 2$ mm^3 voxels filled with lung tissue and modulating the lung tissue's density. The unperturbed reference curve is shown as a dashed line. For better clarity only the region around the Bragg peak is shown. The statistical uncertainties from the MC simulations lie in the region of the line widths.

4. Discussion

The degradation of a Bragg peak due to a heterogeneous voxelised geometry in the beam line was shown. This degradation could be described successfully by a new model-based quantity called modulation power P_{mod} which depends on the structure size d of the heterogeneous geometry but is independent of the geometrical thickness D. The modulation power was derived from the function $F(t'|t, \sigma_t)$ describing the probability that a path through the heterogeneous geometry has a water-equivalent thickness t'. The value t equals the average water-equivalent thickness and describes the displacement of the depth z_{p82}. The parameter σ_t^2 describes the broadening compared to an unperturbed reference curve. For all structure sizes

$F(t'|t, \sigma_t)$ could be optimised after t and σ_t so that the unperturbed reference curve convolved with $F(t'|t, \sigma_t)$ was equal to the broadened depth-dose. $P_{\text{mod}} = \sigma_t^2/t$ could be derived from the results of the Monte Carlo simulations and was equal to the predictions from the mathematical model. This proves the correctness of the mathematical model.

From each modulation power it was possible to derive the water-equivalent density distribution for 2 mm thick voxels, hence going from the binary density distribution in the original voxelised geometry to a discrete distribution based on several fine steps. The transition to clinically relevant CT data was achieved by replacing the original geometry consisting of small voxels by voxels measuring $2 \times 2 \times 2\,\text{mm}^3$. The voxels were then homogeneously filled with lung tissue. By modulating the density of the lung tissue in each voxel individually according to the found density distribution, it was possible to reproduce the broadened dose distribution downstream from the original voxelised geometry almost perfectly. The deviations in the DFWs were maximally 0.1 mm (5.3%). The approximation was made, that the physical density of lung tissue equals the water-equivalent density, which proved to be alright. That only 500 density modulations were executed, as described in section 2.3, is also a sufficient approximation.

When the density of the lung tissue was not modulated but instead the average density $\rho_{\text{mean}} = 0.26\ \text{g cm}^{-3}$ was used, the dose distribution was as narrow as the reference curve. This average density correlates to the density a CT image would provide that is not capable of resolving the heterogeneous structures in the voxelised geometry. Considering the Bragg peak degradation due to the heterogeneous lung parenchyma is therefore not possible in treatment-planning on the base of such CT data. However, if the modulation power of lung parenchyma is known—for example by measurements as performed by Titt *et al* (2015) and Witt (2014) or simulations of high-resolution CTs as done in this study—the density distribution for each voxel of a CT image can be derived. By modulating the density of each voxel inside the lung the broadening effect can be reproduced on the base of clinical CT data. Hence a solution is found to take into account the modulating effect of lung parenchyma in Monte Carlo-based treatment-planning systems. This could for example be done by indicating the voxels belonging to the lung in the treatment-planning system. While optimising the plan the density in each voxel associated with the lung should then be modulated for each simulated particle individually using a density distribution as described in this study. The choice of the modulation power used to derive the density distribution is a topic we are currently working on. We expect that the modulation power is dependent on the position in the lung itself and is perhaps different for each patient.

Another critical point is lung motion which leads to a different average density of the lung and—as we assume—a different structure sizes d of the lung parenchyma due to varying filling conditions of the lung. This would influence the modulation power since it is dependent on the structure size, as shown in equation (8). Further on the density distribution would differ since it depends on the average density of the lung.

Therefore in a next step we will perform a sensitivity analysis by evaluating the effects of Bragg peak degradation due to lung parenchyma on the treatment plans of real patient CT data for different modulation powers.

In this study the functionality of the mathematical model and the usage of the density distribution was proven to work especially for 2 mm thick CT voxels and modulation powers between 100 μm and 800 μm, hence covering the range of modulation powers for porcine

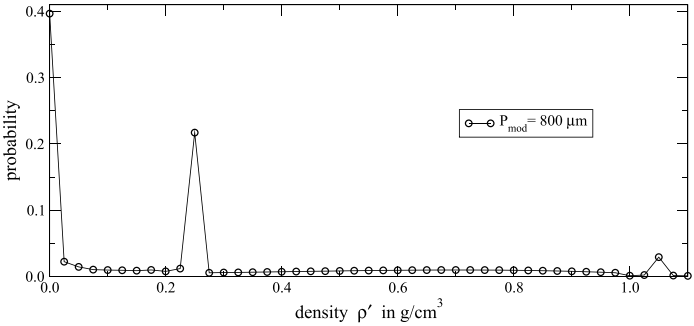

Figure 10. Another possibility for the density distribution $\overline{F}(\rho'|D)$ for $D = 2$ mm and a modulation power $P_{\text{mod}} = 800$ μm. In contrast to the density distributions shown in figure 5 this one is based on three densities at 0.00, 0.26 and 1.05 g cm^{-3} corresponding to the densities of air, lung tissue and the average density of the voxelised geometry and hence an inflated lung.

lungs measured by Witt (2014). We expect that the values of modulation powers for human lungs are similar. However, measuring the modulation power in an actual patient is not possible. Next to measurements as performed by Titt *et al* (2015) and Witt (2014) and simulating high-resolution CTs, measurements with lung phantoms are a possible way to determine the modulation power of human lung tissue. In another study it was shown that porous materials have similar characteristics as lung tissue and can potentially be used to craft lung-like phantoms (Ringbaek *et al* 2017). For the case that the modulation power of human lung parenchyma is different from that of porcine lungs it should be pointed out that the mathematical model and usage of the density distribution can in principle be used for any modulation power.

We also proved the functionality of the mathematical model for higher energies up to 220 MeV u^{-1}. For higher energies the range straggling effect increases and interferes with the modulating effect of the heterogeneous materials used in this study making it harder to see these modulating effects. Hence only the results for the low energy of 90 MeV u^{-1} are shown.

The density distribution $\overline{F}(\rho'|D)$ for targets of small thicknesses D used in this study was derived from the discrete distribution $\overline{F}(t'|D)$ describing the probability that a target of thickness D has the water-equivalent thickness t'. $\overline{F}(t'|D)$ consisted of a weight w_0 at $t' = 0$ and a Poisson distribution generalised for non-integers by using the Gamma function instead of the factorial function. $\overline{F}(t'|D)$ was optimised to fulfill the requirements that $\overline{F}(t'|D)$ is discrete, has no negative ratios and that $\overline{F}(t'|D)$ convolved n times with itself equals the normal distribution $F_T(t'|t, \sigma_t)$ for a target of thickness $T = n \cdot D$.

However, there are infinite possibilities to optimise a distribution fulfilling these requirements. An example is shown in figure 10: this distribution is based on three weights at $\rho' = 0.00$, 0.26 and 1.05 g cm^{-3}. These densities correspond to the density of air, lung tissue and the average density of the voxelised geometry and hence an inflated lung.

Modulating the density of 2 mm thick voxels in a geometry consisting of $n = 20$ voxels in beam direction using this distribution would result in the same dose distribution as when using the original density distribution from figure 5, since both distributions are optimised for $n = 20$ convolutions. However, when modulating less than $n = 20$ voxels, the results would

differ. For the extreme case that the density of only $n = 1$ voxel is modulated, the density distribution based on three weights would result in a dose distribution with three Bragg peaks. The dose distribution from the original density distribution as shown in figure 5 would result in a broadened Bragg peak resulting from the Poisson distribution and an additional Bragg peak resulting from the weight w_0.

Concerning the lateral scattering it was shown that only minor changes occur (<5%) when the geometry consisting of small voxels filled with either lung tissue or air is replaced by 2 mm thick voxels filled with lung tissue. This is reasonable since the mass of air in the original voxelised geometry is negligible and the mass fractions of the different elements in both geometries are therefore roughly the same, resulting in a similar effective atomic number Z_{eff}.

The influence of Bragg peak degradation on a clinical target volume was demonstrated for a hypothetical PTV downstream from a heterogeneous geometry. When not considering Bragg peak degradation due to heterogeneous materials when optimising a treatment plan, an underdose of the PTV and an overdose of the healthy tissue downstream from the PTV are the consequences.

For the high-resolution CT of a human lung sample the modulation power was 66 μm resulting in a DFW of 0.4 mm for 4 mm lung parenchyma. The modulation power is low compared to the results by Witt (2014). The reason is that the CT data used in this study were prepared using a 'critical point drying' method (Litzlbauer *et al* 2006), resulting in a loss of water of up to 37%. As a consequence the structures of the lung tissue are reduced in size. Since the modulation power is proportional to this structure size d (see equation 8), P_{mod} is smaller than it would be in a non-dried lung.

Nevertheless, a discrete density distribution $\overline{F}(\rho'|D)$ could be derived for 2 mm thick voxels. By modulating the density of 2 mm thick voxels we were able to reproduce the broadened dose distribution downstream from the high-resolution CT, hence proving that our strategy works for real lung parenchyma.

5. Conclusion

In this study we developed an efficient method to describe Bragg curve degradation using a mathematical model: the values t and σ_t of a normal distribution $F(t'|t, \sigma_t)$ have to be adjusted so that an unperturbed reference curve convolved with $F(t'|t, \sigma_t)$ equals the broadened dose distribution. The material characteristics 'modulation power' was introduced. It can be determined from the values of t and σ_t using that $P_{\text{mod}} = \sigma_t^2/t$. The modulation power is independent on the actual thickness of a material and can easily be measured. From the modulation power a density distribution can be derived for any thickness of the material—especially for 2 mm thick voxels, which is the typical size of voxels in a CT image used for planning the treatment of lung cancers. By modulating the density of each 2 mm thick voxel individually following this density distribution, we were able to reproduce broadened Bragg curves. Hence a simple tool is developed to include Bragg curve degradation in Monte Carlo-based treatment-planning systems on the base of clinical CT data.

Acknowledgments

The authors acknowledge Dr Marian Kampschulte for providing the high-resolution CT data. The authors acknowledge the TOPAS forum for fruitful discussions.

References

Agostinelli S *et al* 2003 Geant4—a simulation toolkit *Nucl. Instrum. Methods Phys. Res.* A **506** 250–303

Bichsel H, Hiraoka T and Omata K 2000 Aspects of fast-ion dosimetry *Radiat. Res.* **153** 208–19

Chang J, Zhang X, Wang X, Kang Y, Riley B, Bilton S, Mohan R, Komaki R and Cox J 2006 Significant reduction of normal tissue dose by proton radiotherapy compared with three-dimensional conformal or intensity-modulated radiation therapy in stage I or stage III nonsmall-cell lung cancer *Int. J. Radiat. Oncol. Biol. Phys.* **65** 1087–96

Espana S and Paganetti H 2011 Uncertainties in planned dose due to the limited voxel size of the planning CT when treating lung tumors with proton therapy *Phys. Med. Biol.* **56** 3843

Goitein M 1977 The measurement of tissue heterodensity to guide charged particle radiotherapy *Int. J. Radiat. Oncol. Biol. Phys.* **3** 27–33

ICRU 1994 ICRU: report 49 stopping powers and ranges for protons and alpha particles *Technical Report* International Comission on Radiation Units and Measurements, Bethesda, MD, USA

Litzlbauer H, Neuhaeuser C, Moell A, Greschus S, Breithecker A, Franke F, Kummer W and Rau W 2006 Three-dimensional imaging and morphometric analysis of alveolar tissue from microfocal x-ray-computed tomography *Am. J. Physiol.—Lung Cell. Mol. Physiol.* **291** L535–45

McConn R J, Gesh C, Pagh R, Rucker R and Williams R III 2011 Radiation Portal Monitor Project. Compendium of Material Composition Data for Radiation Transport Modeling PIET-43741-TM-963 PNNL-15870 Revision 1 Prepared for the U.S. Department of Homeland Security, U.S. Customs and Border Protection and Domestic Nuclear Detection Office under U.S. Department of Energy Contract DE-AC0576RL01830 (www.pnnl.gov/main/publications/external/technical_reports/PNNL-15870Rev1.pdf)

Perl J, Shin J, Schuemann J, Faddegon B and Paganetti H 2012 TOPAS: an innovative proton Monte Carlo platform for research and clinical applications *Med. Phys.* **39** 6818–37

Perles L A, Dragan M, Sawakuchi G and Titt U 2011 Monte Carlo investigation of rebinning material density distributions of lung parenchyma phantoms in proton therapy *Nucl. Technol.* **175** 22–6

Rau W, Hauenstein K, Mittermayer C and Volk P 1980 A simple and rapid method for postmortem radiographic investigation of lung fine structure *Pathol. Res. Pract.* **170** 426–32

Ringbaek T P, Simeonov Y, Witt M, Engenhart-Cabillic R, Kraft G, Zin K and Weber U 2017 Modulation power of porous materials and usage as ripple filter in particle therapy *Phys. Med. Biol.* **82** 2892–2909

Ringbaek T P, Weber U, Peterson J B, Thomsen B and Bassler N 2014 Monte Carlo simulations of new 2D ripple filters for particle therapy facilities *Acta Oncol.* **53** 40–9

Sawakuchi G, Titt U, Mirkovic D and Mohan R 2008 Density heterogeneities and the influence of multiple Coulomb and nuclear scatterings on the Bragg peak distal edge of proton therapy beams *Phys. Med. Biol.* **53** 4605–19

Schneider U, Pedroni E and Lomax A 1996 The calibration of CT Hounsfield units for radiotherapy treatment planning *Phys. Med. Biol.* **41** 111

Sell M, Titt U, Perles L, Mirkovic D, Mohan R, Babert M and Oelfke U 2012 WE-E-BRB-02: evaluation of analytical proton dose predictions with a lunglike plastic phantom *Med. Phys.* **39** 3956

Smith A 2006 Proton therapy *Phys. Med. Biol.* **51** R491

Testa M, Schuemann J, Lu H M, Shin J, Faddegon B, Perl J and Paganetti H 2013 Experimental validation of the TOPAS Monte Carlo system for passive scattering proton therapy *Med. Phys.* **40** 1–16

Titt U, Sell M, Unkelbach J, Bangert M, Mirkovic D, Oelfke U and Mohan R 2015 Degradation of proton depth dose distribution attributable to microstructures in lung-equivalent material *Med. Phys.* **42** 6425

Urie M, Goitein M, Holley W and Chen G 1986 Degradation of the Bragg peak due to inhomogeneities *Phys. Med. Biol.* **31** 1–15 (PMID: 3952143)

Weber U and Kraft G 1999 Design and construction of a ripple filter for a smoothed depth dose distribution in conformal particle therapy *Phys. Med. Biol.* **44** 2765

Wilson R 1946 Radiological use of fast protons *Radiology* **47** 487–491

Witt M 2014 Modulationseffekte von Kohlenstoffionen bei der Bestrahlung von Lungen *Master's Thesis* Technische Hochschule Mittelhessen—University of Applied Sciences, Giessen, Germany

Witt M, Weber U, Simeonov Y and Zink K 2015 SU-E-T-671: range-modulation effects of carbon ion beams in lung tissue *Med. Phys.* **42** 3491

IOP Publishing Phys. Med. Biol. 64 (2019) 155005 (11pp) https://doi.org/10.1088/1361-6560/ab2611

Physics in Medicine & Biology

IPEM Institute of Physics and Engineering in Medicine

PAPER

RECEIVED
1 February 2019

REVISED
6 May 2019

ACCEPTED FOR PUBLICATION
31 May 2019

PUBLISHED
1 August 2019

Quantification of the dependencies of the Bragg peak degradation due to lung tissue in proton therapy on a CT-based lung tumor phantom

Veronika Flatten[1,2,4], **Kilian-Simon Baumann**[1,2], **Uli Weber**[3], **Rita Engenhart-Cabillic**[1] **and Klemens Zink**[1,2]

[1] Department of Radiotherapy and Radiooncology, University Medical Center Giessen–Marburg, Marburg, Germany
[2] Institute of Medical Physics and Radiation Protection, University of Applied Sciences, Giessen, Germany
[3] Biophysics Department, GSI Helmholtzzentrum für Schwerionenforschung, Darmstadt, Germany
[4] Author to whom any correspondence should be addressed.

E-mail: flatten@staff.uni-marburg.de

Keywords: Monte Carlo, Bragg peak degradation, proton therapy, lung modulation, lung tissue

Abstract

The fine, sub-millimeter sized structure of lung tissue causes a degradation of the Bragg peak curve in particle therapy. The Bragg peak is degraded because particles of the same energy traverse lung tissue of different compositions of high and low density materials. Hence, they experience different energy losses resulting in variable ranges and a broadened Bragg peak.

Since this fine structure of lung tissue is not resolved in standard treatment-planning CTs, current state-of-the-art dose calculation procedures used in the clinical routine are unable to account for this degradation. Neglecting this Bragg peak degradation in treatment planning can lead to an underdose in the target volume and an overdose distal to the target.

Aim of this work is to systematically investigate the potential effects of the Bragg peak degradation on the dose distribution in dependence of different parameters like the tumor volume and its depth in lung.

Proton plans were optimized on CT based phantoms without considering the Bragg peak degradation and afterwards recalculated with the Monte Carlo toolkit TOPAS: first, without consideration of the degradation and second, with the Bragg peak degradation accounted for. The direct comparison of these two dose distributions enables a quantification of the degradation effect. To carve out the dependencies of various parameters that could influence the Bragg peak degradation and thus the target dose, the simulations were performed for a variety of tumor sizes and shapes, as well as different positions within the lung.

The results show that due to the Bragg peak degradation the mean dose in the target volume can be reduced by a few percent up to 14% (for extreme cases) depending on the geometry. It was shown that this effect increases with a decreasing tumor volume and increasing depth of the tumor.

For the first time, a tumor specific estimation of the effect on the dose distribution due to the Bragg peak degradation in lung tissue is presented.

1. Introduction

Since first proposed by Wilson (1946), proton irradiation to treat cancer has evolved from an experimental treatment in research facilities to a routine treatment option in specialized cancer centers. In scanned proton beam facilities, each tumor is irradiated with an optimized combination of proton beams of different energies and positions, concentrating the Bragg peaks in a plateau which encloses the tumor. The low dose in the entrance channel and the high energy deposition at a finite range qualify for a good tumor control with a low toxicity in the surrounding tissue and organs (Schulz-Ertner and Tsujii 2007, Zhang *et al* 2010). As in all common radiation therapy treatments, treatment plans nowadays are optimized for the specific anatomy of the patient by calculating the specific dose distributions on the acquired CT images. Eventhough CT resolution allows a macroscopic

visualization and delineation of the organs in combination with additional dose calculation information, no information about microscopic tissue characteristics can be obtained with a conventional CT scanner. The CT resolution results in an averaged representation of the lung as homogenous medium in CTs while on a microscopic scale it consists of pulmonary alveoli with a density close to water filled with air having a much smaller density. For ion therapy this is challenging as heterogeneous materials on a microscopic scale cause the Bragg peak to smear out (Urie *et al* 1986, Sawakuchi *et al* 2008). The smearing-out arises because some particles might pass through more lung tissue with a high density and others through more air cavities with a low density. Hence, these particles are slowed down unevenly resulting in different ranges and the degradation of the Bragg peak. Even though the Bragg peak degradation when traversing heterogeneous media has been known for some time and it was shown that this could have a significant impact on the target dose (Goitein 1977, Espana and Paganetti 2011), state-of-the-art treatment planning systems and routines do not account for this Bragg peak degradation, ignoring the potential of an underdose in the target volume and an overdose distal to the target (Goitein 1977, Sawakuchi *et al* 2008).

Nevertheless, first steps to include the Bragg peak degradation in treatment planning have been performed. To quantify the effect of the Bragg peak degradation on a depth dose curve, measurements in waterphantoms positioned downstream from 3D-printed and other porous lung substitutes (Sell *et al* 2012, Titt *et al* 2015, Ringbaek *et al* 2017) have been performed. With the help of Monte Carlo simulations, the concept of the 'modulation power' based on a mathematical model was introduced to describe and quantify the effects of the Bragg peak degredation on a mono-energetic Bragg peak (Witt *et al* 2015, Ringbaek *et al* 2017). Baumann *et al* (2017) introduced and extensively tested a mathematical model to reproduce this artificial Bragg peak degradation on rougher structures like CT voxels with dimensions in the millimeter range: by sequentially modulating the density of the CT voxels within the lung, the Bragg peak degradation can be reproduced. Hence, it is possible to reproduce the Bragg peak degradation due to lung tissue on the basis of clinically acquired CT images, although they do not resolve the fine structure of the lung tissue.

In this study, the effects of the Bragg peak degradation on various target volumes in dependence on their depth in lung were analyzed. As the individual anatomy of each patient and thus the tumor shape and its position in the lung differs, the comparison and analysis of the degradation effect is more evident and systematic when performing the calculation of this effect on geometrical, CT-based phantoms. For each of these dicom-based CT slab phantoms a treatment plan was optimized without considering the degradation. These plans were subsequently recalculated with TOPAS in two scenarios: with and without the density modulation reproducing the Bragg peak degradation. Therefore, we were able to perform Monte Carlo simulations for different tumor sizes and distances in lung on the regular CT, as well as on the modulated CTs as proposed by Baumann *et al* (2017). This allows the analysis of the effects of the Bragg peak degradation dependent on tumor size and the depth in lung and thus enabling an uncertainty estimation for proton therapy treatments for lung carcinomas in clinical cases. The effects of other parameters like the tumor shape, the energy and the planning setup on the Bragg peak degradation were also evaluated.

2. Materials and methods

2.1. CT modulation

As shown by Baumann *et al* (2017), on a macroscopic level the Bragg peak degradation can be reproduced by alternating the density of the voxel that the particle passes through between either the density of air or tissue. To reproduce the effect of the Bragg peak degradation a sequence of 100 CTs with differently randomized lung density voxels was implemented in the Monte Carlo simulations, as displayed in figure 1. The expectation value of the density of each voxel is 0.26 g cm^{-3} corresponding to the average density of an inflated lung (Schneider *et al* 1996). The superposition of the dose distributions from each of the 100 randomized CTs modulates the density and hence the Bragg peak degradation is reproduced. A more detailed description of the mathematical model and the modulation process is described by Baumann *et al* (2017).

Measurements indicated that the modulation power for lung tissue ranges between 100 μm and 800 μm (Witt 2014). To be able to conduct an approximation for the effect of the Bragg peak degradation, a modulation of 450 μm was chosen for most setups in this study. Some simulations were repeated with a more probable modulation power of 250 μm and a extreme modulation power of 800 μm, to allow an estimation of the influence of the modulation power.

2.2. Phantoms

To fulfill the objective of the pure assessment of the differences in the dose distribution especially in the target due to the Bragg peak degradation in lung tissue, a phantom study was conducted in a static setup so that organ motion was ignored. Reducing the phantom to the most simplistic case as shown in figure 2, each CT consisted of two water slabs of 2 cm thickness seperated by 25 cm of lung tissue, representing the lung enclosed by the thorax wall and the mediastinum or other distal tissue. The density of the water slabs was 1.00 g cm^{-3}. The lung was set to have a density of 0.26 g cm^{-3} corresponding to the density of an inflated lung (Schneider *et al* 1996). The

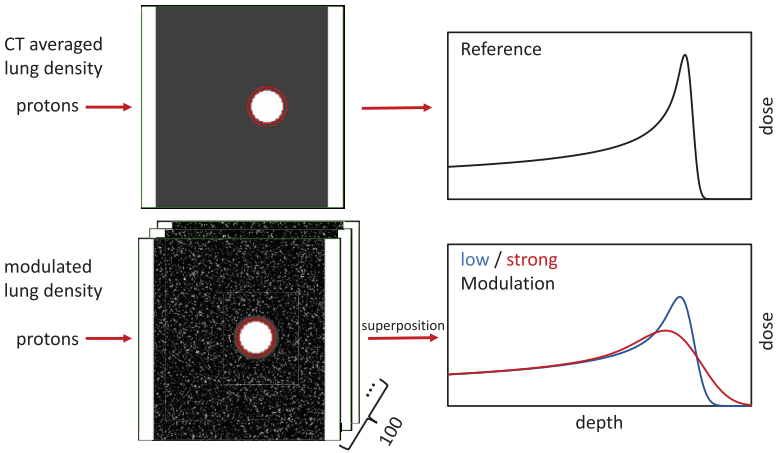

Figure 1. Schematic overview of the setup and the occurring effects on the depth dose curve, when ignoring (top) and accounting for (bottom) the Bragg peak degradation. On the left side, the phantom is shown for the CT clinical (averaged) case (lung window) in the upper part and modulated in the lower part for one exemplary tumor size and position. On the right side the resulting depth dose curves are shown for the CT averaged in black (top), a high modulation effect (modulation power 800 μm) in red and a low modulation effect (modulation power 250 μm) in blue (bottom).

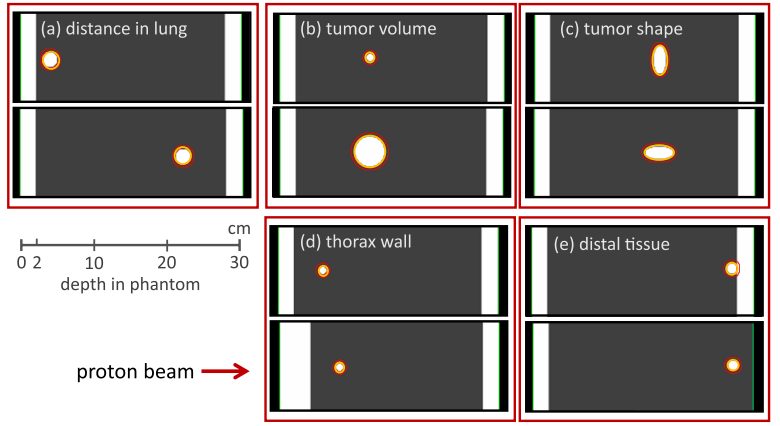

Figure 2. The major variations of the used CT phantoms are displayed. Featuring two exemplary options for the five major differences in the phantom setups. From left to right, different depths of the tumor in the lung, different tumor volumes and shapes are visible. As well as a change in the thickness of the proximal and distal water slab. The yellow lines enclosing the tumor display the solid GTV and the larger red line surrounds the PTV, respectively.

CT voxels had a size of $1.5 \times 1.5 \times 1.5$ mm^3. The artificial tumors were represented by spheres or ellipsoids of different sizes with a density of 1.00 g cm^{-3} that were positioned at various depths within the lung.

Various phantoms and thus treatment plans were produced to allow an extensive evaluation of the dependencies of the Bragg Peak degradation. In the following, a brief description of the varied parameters is given (compare figure 2):

2.2.1. (a) Distance traveled in lung tissue

Six different depths in lung were investigated ranging from 2 cm to 20 cm (2 cm, 4 cm, 6 cm, 10 cm, 15 cm, 20 cm) for the distance (d_L) between the beginning of the lung and the tumor center. The smallest and largest distance are displayed in figure 2.

2.2.2. (b) Size of tumor volume

Six different spherical volumes (1 cm^3, 2 cm^3, 6 cm^3, 14 cm^3, 25 cm^3, 43 cm^3) were chosen to be evaluated, the smallest, with a volume of 1 cm^3, and largest, which has a volume of 43 cm^3, are shown in figure 2.

2.2.3. (c) Shape of tumor volume

As tumor volumes in patients are not always shaped spherically, two different ellipsoids were investigated. The parameters *a*,*b* and *c* denote semi-axes of the ellipsoid. Length *a* always describes the axis parallel to the beam direction and *b* and *c* the axis perpendicular to the beam. Two axis had always the same length for both ellipsoids. The smaller ellipsoid (9 cm^3) features the short axis ($a = b = 2$ cm) twice and the long axis ($c = 4$ cm) once while the larger one (19 cm^3) features the short axis only once and thus the long axis twice ($a = 2$ cm, $b = c = 4$ cm). Both ellipsoids were irradiated with the short axis (as just described) and the long axis (by switching $a \leftrightarrow c$) in beam direction.

2.2.4. (d) Thickness of thorax wall

The simulations for the smallest tumor volume (1 cm^3) were also performed with a thicker wall as displayed in figure 2.

2.2.5. (e) Tissue distal to the tumor volume

The simulations for the longest distance in lung were performed with and without the wall distal to the tumor. This represents tumors close to the mediastinum in comparison to tumors only surrounded by lung.

2.3. Planning setup and Monte Carlo simulations

Treatment plans for spot scanning protons were optimized using the commercially available treatment planning system Eclipse version 13.7 (Varian). One single field from the left side was optimized with a lateral spot spacing of 60% of the FWHM in air and an energy spacing of 3 MeV or 1 MeV for larger or smaller volumes, respectively. The volume optimized for was the PTV, which encloses the voxels identified as tumor (GTV) with a margin of 3 mm lung tissue. 30 Gy RBE were planned to be applied in a single fraction.

All simulations were conducted with the Monte Carlo code TOPAS (TOol for PArticle Simulations) version 3.1.p1 (Perl *et al* 2012) which is a Geant4 (GEometry ANd Tracking) (Agostinelli *et al* 2003) based toolkit focused on proton therapy applications. Each optimized RTplan was recalculated with TOPAS in two scenarios: with and without the Bragg Peak modulation model.

The dose distributions of both scenarios were scored as dose-to-water and compared by evaluating the mean dose (D_{mean}), the dose in at least 20% of the volume (D_{20}) and 95% of the volume (D_{95}), respectively. These three dose values were determined for both, the GTV and the PTV. To evaluate also small dependencies, the modulation effects for the setups shown in figures 2(c)–(e) are presented with the strong modulation power of 800 μm. All other results are presented with a modulation power of 450 μm to give a more reasonable estimation of the effect.

3. Results

3.1. General effect of the Bragg peak degradation

Figures 3(a) and (c) show two exemplary depth-dose curves along the beam axis. For the first 2 cm the particles travel through the water slab and thus no modulation is observed. From depth 2 cm on, small discrepancies in dose can be observed as the particles traverse the lung. Reaching the Bragg peak plateau, the differences between the non-modulated scenario giving the dose distribution as predicted by the TPS and the modulated scenario giving the dose distribution, as it would be in the patient, increase and show the systematic effect of the degradation: on the one hand less dose at the beginning and the end of the spread out Bragg peak and on the other hand an higher dose distal to the Bragg peaks induced due to a broader fall off.

The dose curve for the modulated cases is smoother in the high-dose region showing that the Bragg peak degradation leads to a smoothing effect on the dose in beam direction similar to a ripple filter (Ringbaek *et al* 2017).

The dose-volume histogram (DVH) presented in figures 3(b) and (d) show the influence of the Bragg peak degradation on the GTV. It can be observed, that the mean dose in the GTV is reduced in the modulated case in comparison to the predicted dose. In general, the dose coverage in significantly deteriorated.

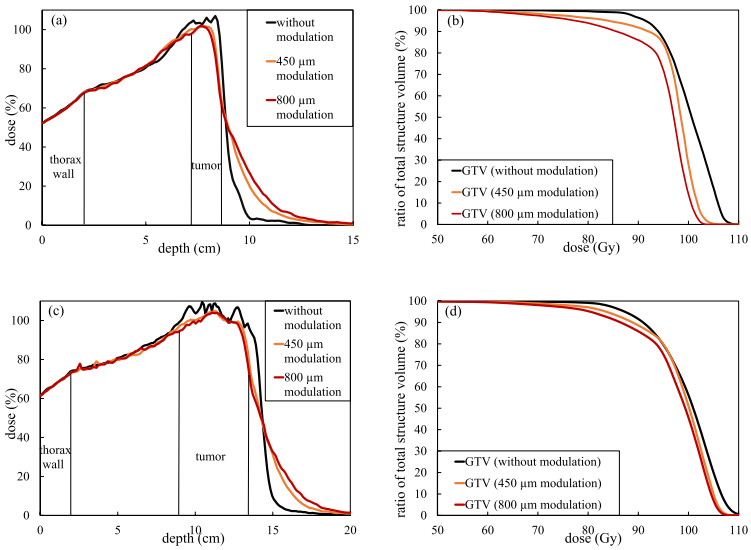

Figure 3. Depth-dose curves ((a) and (c)) through the central beam line and the corresponding DVHs ((b) and (d)) with and without simulation of the lung modulation effect. The modulating lung tissue, with a modulation power of 800 μm (red line) or 450 μm (orange line), starts at 2 cm. The depth dose curve in panel (a) and the corresponding dose-volume histogram in panel (b) feature a small tumor while panel (c) and (d) present a larger tumor extension.

3.2. Dependency on depth in lung tissue and the tumor volume

Figure 4 shows the evaluated dose parameters (D_{mean}, D_{95} and D_{20}) for the modulated and non-modulated cases in dependency on the depth of the tumor in lung and different tumor volumes. All results are presented as a relative difference of the modulated and TPS calculated dose, which is used as reference dose. To make an estimate of the statistical error done with the Monte Carlo simulation, several plans were recalculated with different random number seeds. The reference mean dose without the modulation effect was found to have an uncertainty of about 0.05% for the presented values, nevertheless as the modulation is produced by the sum of 100 dose plans with each one-hundredth of the total number of particles, the uncertainty is increased to roughly 0.5%. Thus all presented values have to be reviewed with an uncertainty of 0.5%, which corresponds in most cases to the marker size. For single voxel values such as the maximum and minimum dose the uncertainty is slightly, as only a minor part of the simulated particles contribute to the dose value of this voxel.

In the upper part of figure 4, the mean dose is evaluated for the PTV (a) and the GTV (b), respectively. A clear correlation between the tumor depth and the dose reduction can be observed: the greater the distance traveled in lung, the higher the dose difference. Additionally, a clear dependence on the tumor volume is visible: the smaller the tumor size, the larger the dose difference. Figures 4(a) and (b) show a almost linear relationship between tumor depth and the dose difference.

The highest deviation from the expected value of D_{mean} is found to be -8% for the largest distance of 20 cm in combination with the smallest volume of 1 cm^3. With decreasing distance in the lung it decreases below -1%. The smallest differences occur for the largest sphere with a volume of 43 cm^3. D_{mean} rises from -1% at a 4 cm distance between the beginning of the lung and the sphere center to -3% at 20 cm distance.

Even though both upper plots look quite similar, differences can be noted. On the one hand, the effect for the smallest tumor is higher when only the GTV is evaluated, while on the other hand the effect for the larger sized tumors is reduced for the GTV in larger distances, broadening the range covered in figure 4(b). For the GTV, the smallest tumor shows differences from a 0% difference at 2 cm lung distance up to -9% at 20 cm, while differences for the largest tumor are between -1% and -2% for 4 cm and 20 cm, respectively.

In the bottom panel of figure 4 the relative differences of the dose values enclosing 95% (D_{95}) and 20% (D_{20}) of the volume, respectively, are shown. The D_{20} show more scatter but the trend of more passed lung resulting in a higher dose reduction is still valid. For the largest distance, a D_{20} dose difference between -2% and -11% is observed.

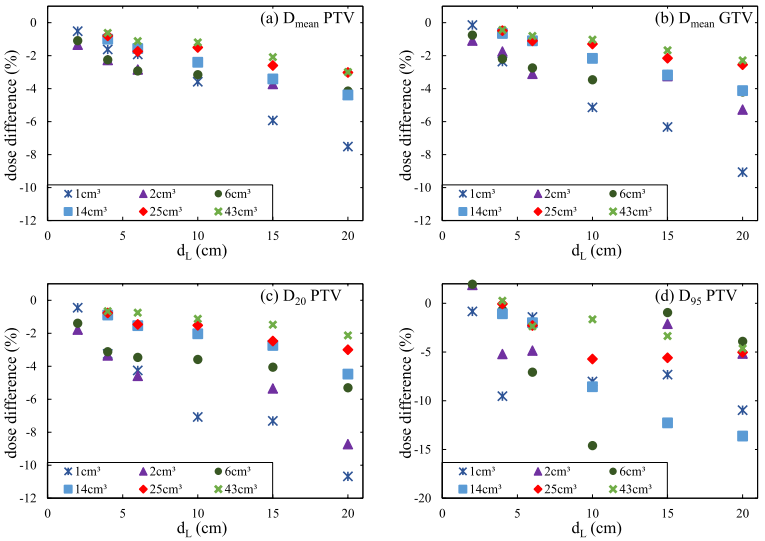

Figure 4. Relative effect of the Bragg peak degradation on the dose distribution in dependency of the tumor depth in lung tissue with a modulation power of 450 μm for (a) the mean dose (D_{mean}) of the PTV and (b) the GTV and (c) for the D_{20} and (d) D_{95} dose, respectively. Different markers indicate the tumor volume. Note the different scaling in (d).

For the D_{95}, the data points scatter more randomly. Some points show even a positive discrepancy between the modulated and original calculation. Thus no clear correlation can be found.

The lung modulation influences the dose at the distal end of the tumor the most. Thus, plans optimized in a way that all the high dose area coincidences with the distal region of the PTV show more effect on the D_{20}. On the other hands plans barely surrounding the distal region with the proposed 95% of the planned dose, will show a significant reduction of the D_{95}. For example, two identical volumes positioned in the dose distribution presented in figure 3(c) at depths 10–11.5 cm and 11–12.5 cm show a similar behavior in their decrease of the mean dose (around 1%). The D_{20} is decreased by 2% for the proximal volume and by only 1% for the distal volume. The big difference is observed for the D_{95}: while the coverage for the proximal volume is even increased by 2% due to the smoothing effect of the Bragg peak degradation, the D_{95} for the distal volume is decreased by -5% because of the strong impact of the degradation effect at the distal end. Thus, small variation in the optimized plan, which are not observable from the DVH but only from the actual dose distribution have a great influence on parameters like the D_{95}.

In the further analysis only the mean dose is evaluated as (accounting to figure 4) it is a good indicator for the effects of the modulation.

3.3. Dependency on the shape of the radiated volume

It was found that the underdosage of the ellipsoid-shaped PTV depends on its orientation rather than on its volume: if the short axis was orientated in beam direction, the underdosage was about -9% for both volumes. For the long axis in beam direction the underdose was around -3%.

To be able to approximate the decrease of the mean dose not only for different positions in lung but also for different tumor sizes and shapes, an empirically found parameter is presented, which well describes the geometrical dependencies:

$$L_S = 2 \cdot \frac{a^2}{\sqrt{b \cdot c}} \tag{1}$$

a denotes the axis in beam direction (as described in section 2.2(d)). L_S, which can be described as the scaled tumor length in beam direction, offers the possibility to normalize the different orientations of the tested ellipsoids with the spherical setups. This means if the x-axis in figure 4(a) is transformed from d_L to d_L/L_S, the different slopes for the different tumor sizes are leveled into one and thus a simple approximation for all cases can be made.

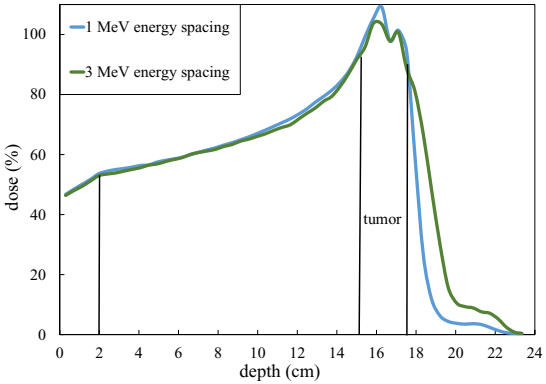

Figure 5. Depth dose curve for reference plan of the same tumor set-up with a different longitudinal energy spacing.

3.4. Dependency on the lateral and longitudinal spot spacing

As the Bragg peak degradation changes the width of each Bragg peak in beam direction, differences in the energy spacing may have an influence on the outcome of the Bragg peak degradation effects.

For the simulations redone with a different energy (longitudinal) spacing, a higher dose difference was observed in the cases where a more narrow spot spacing was optimized. For the 1 MeV energy spacing, the underdosage showed an about 40% higher dose difference in comparison to the 3 MeV energy spacing. Plans with a wider energy spacing have often a lower conformity and the smoothing effect of the Bragg peak degradation flattens the profile but does not reduce the mean dose significantly. For a high conformity plan, the smoothing leads to a more decreased mean dose. A higher conformity also allows the optimizer to spare dose in the surrounding normal tissue, which leads to a steeper dose fall-off which is also closer to the PTV. Figure 5 shows two different reference plans, which show the steeper gradient for the closer energy spacing. Of course, this can be accounted for during the planning procedure.

Regarding the lateral spot spacing, no difference within the uncertainties of the simulation with a lower lateral spot spacing was observed.

3.5. Energy dependency

To analyze the dependency of the Bragg peak degradation on the energy, the plans for the 1 cm^3 spherical tumor were also calculated with a thicker entrance wall (4 cm instead of 2 cm) leading to higher proton energies to enclose the tumor volume. Because this effect is expected to be smaller, the highest modulation power was chosen. The results are displayed in table 1. While for the GTV, only the small distances in lung show some discrepancies when the energy is increased, all dose differences for the mean PTV dose increase when applying a thicker wall. Higher proton energies have a smaller peak to plateau ratio as well as smaller lateral FWHM. Thus, lower energy plans might show less conformity than higher energy plans. As presented in section 3.4, a plan with higher conformity is more affected by the Bragg peak degradation. In general, applying higher proton energies increases the dose differences about additional -2% for the PTV .

3.6. Effect of distal tissue

If the tumor is placed in the vicinity to the mediastinum, tissue follows distal to the tumor. Simulations for the 2 cm^3 tumor were performed to analyze the effects of the Bragg peak degradation with and without distal tissue. Again, the highest modulation power of 800 μm was used, to give a very conservative approximation. The results are presented in table 2. The mean dose was reduced by 19%, if the plan was optimized with no tissue distal to the tumor. However, with the optimization performed with distal tissue, the mean dose was only decreased by 10%, independent on the presence of distal tissue during the dose calculation. This outlines that the effect caused in the presence of distal tissue is solely caused by the optimized spot setting, as plans optimized with distal tissue feature more energy layers behind the tumor volume and thus leading to a smoother distal fall-off.

For a smaller distance of 6 cm and a larger distance between the PTV and the distal tissue, the effect is significantly reduced as the case in brackets in table 2 shows. The closer the tumor lays to distal tissue and the more the

Table 1. Dose differences for the mean dose of the GTV and the PTV, for a wall of 2 cm and a wall of 4 cm thickness (see figure 2). The tumor volume was 1 cm^3 and the modulation power 800 μm.

	GTV_{mean} dose difference (%)			
Depth	4 cm	6 cm	10 cm	15 cm
2 cm wall	−4	−5	−9	−12
4 cm wall	−3	−7	−9	−12
	PTV_{mean} dose difference (%)			
Depth	4 cm	6 cm	10 cm	15 cm
2 cm wall	−3	−4	−7	−11
4 cm wall	−5	−7	−9	−13

Table 2. Dose differences for the PTV mean dose when calculated and optimized on a CT with or without tissue distal to the tumor. The distance in lung was 25 cm (6 cm) for all settings and the modulation power 800 μm.

	PTV_{mean} dose difference (%)	
	Calculated on CT with distal tissue	Calculated on CT without distal tissue
Optimized on CT with distal tissue	−10 [−4]	−10 [−4]
Optimized on CT without distal tissue	−19 [−5]	−19 [−5]

of PTV overlaps with the mediastinal wall, the smaller is the effect of the lung modulation. The occurrence of this effect depends on the settings of the machine in the treatment planning system.

3.7. Modulation power

As described in section 2.1 and by Baumann *et al* (2017), the modulation power is a parameter in the mathematical model used to reproduce the Bragg peak degradation, indicating the strength of the modulation effect. Measurements indicate a modulation power between 100 μm and 800 μm (Witt 2014). The modulation power in the simulations presented was chosen to be mostly 450 μm but also 800 μm to make a conservative approximation for clinical cases. As the modulation power has a great influence on the modulation effect, some of the simulations were redone with a modulation power of 250 μm as presented in figure 6 to also give a less conservative approximation of the Bragg peak degradation. As expected, a lower modulation power decreases the dose differences occurring due to the Bragg peak degradation. For a linear approximation a lower slope would be assigned. Still, the increase of the dose difference for both, the GTV and the PTV in dependency of the distance in lung is clearly visible. A lower modulation power of 250 μm reduces the effect further to 0% for a depth of 4 cm and to −3% for the 20 cm depth.

3.8. Combined approximation of the degradation

As the aim was to allow an estimation of the change in the dose distribution for clinical cases, all data were combined in figure 7. To connect all different setups and results, the dose difference was plotted against the ratio of the penetration depth in lung and the scaled tumor length in beam direction as proposed in equation (1). This condenses all data allowing a linear approximation and thus enabling a prediction of the reduction of the mean dose in the tumor.

The GTV volumes and the depths in lung were chosen to represent a realistic variety over all possible lung tumor scenarios.

For a less conservative approach, figure 7 also gives the approximation for a modulation power of 250 μm, which seems to be clinically more likely. The slope was gained by a fit through all data calculated with 250 μm whereas the width of the uncertainty band was taken from the 800 μm fit.

4. Discussion

The presence of the Bragg peak degradation due to microscopic inhomogeneities is well known, however its effects are not accounted for in any TPS, hence the impact of the patient dose is not know.

In this phantom based study, the impact of the Bragg peak degradation on the dose of lung tumors was estimated in dependence on different clinical treatment parameters such as the tumor depth in lung, the tumor volume and its shape, the proton energy and the energy spacing. All in all, the results show that the longer the

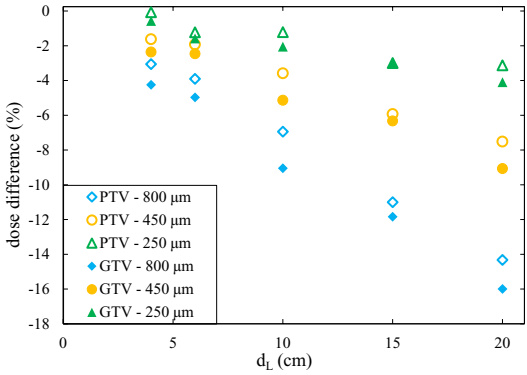

Figure 6. The dose difference of the mean dose of the PTV and GTV for a modulation power of 250 μm, 450 μm and 800 μm, respectively is plotted against the distance in lung. As size, the smallest volume of 1 cm^3 was chosen.

distance the particles travel through lung and the smaller the tumor volume, the higher is the difference between planned mean dose and actual mean dose of the target volume. In all cases an underdosage of the tumor volume was found. The most extreme case investigated in this work showed an underestimation of the mean dose of −14% (800 μm,). But more clinical relevant setups (distance of 6 cm, modulation power of 250 μm, see figure 6) result in an underestimation of about 2%.

In general, it was found that the Bragg peak modulation smooths the dose distribution: hot spots are reduced leading to a steeper gradient in the DVH around a reduced mean value in comparison to the DVH predicted by the TPS.

Another dependency that was investigated was the energy selection by the TPS, which was found to have an influence on the dose distribution. All plans calculated with a thicker thorax wall and thus higher energy selection showed an increased dose difference. This correlates with the results obtained for the spot spacing as parameter under investigation: energy spacing has a relevant impact on the dose when the Bragg peak degradation is accounted for. An increased number of energy layers throughout the tumor (and not distal to the tumor) leads to a decrease of the weight of each spot. With the Bragg peak degradation the peak dose is decreased and as the missing dose is only distributed in the distal region, more spots result in a decreased peak dose thus a decreased mean dose.

At last, the effect of tissue distal to the tumor was investigated as it is the case when the tumor is attached to the meadiastinum. It was found that this has no direct influence on the dose calculated with and without the Bragg peak degradation accounted for. However, for the given TPS settings, the plan optimization process was highly influenced by distal tissue. When a plan is optimized with tissue distal to the tumor with the same margin around the tumor more energy layers have spots within this margin because a spot spacing of e.g. 1 MeV results in about 1 mm distance in water but a far higher distance in air. Therefore, plans optimized with distal tissue feature a higher dose behind the tumor, resulting in a decreased dose reduction when accounting for the Bragg peak degradation. For small tumor volumes, the dose difference could be decreased by a half.

It was possible to include most results in the dose difference band in figure 7. This band allows an estimation of the uncertainty when not including the Bragg peak degradation in lung tissue for many clinical cases. If an approximation of the effect on the dose distribution for clinical case is of interest, the average distance in lung needs to be estimated and the tumor length in beam direction needs to be measured and evaluated. With these information and the results presented in figure 7 the reduction of the mean dose can be estimated in a conservative approach or a more probable approach.

In comparison to the intra- and interfractional motion in proton treatment of lung cancer (Widesott *et al* 2008, De Ruysscher *et al* 2015), the underestimation of 2% in the best case seems negligible, but differences around 10% that were also observed should rather not be neglected. Nevertheless, as tumor movement is more and more accounted for by robust planning, gating, tracking and plan-of-the-day concepts thus reducing the effect on the dose distribution to a minimum, future treatment concepts should aim for an incorporation of the Bragg peak degradation.

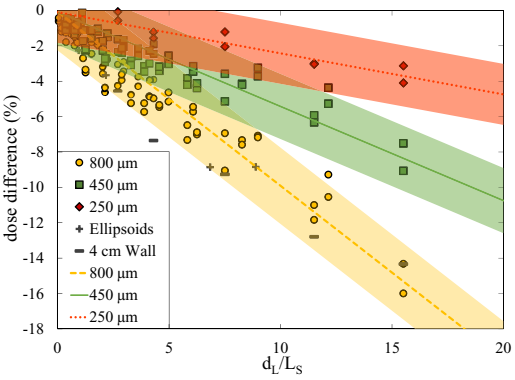

Figure 7. All dose differences for the mean dose are presented in a combined format as they are plotted against the depth in lung (d_L) divided by the scaled tumor length in beam direction (L_S) as proposed in equation (1). All PTV and GTV mean dose differences are displayed. The yellow band marks the fit through all data points as presented for a modulation power of 800 μm, visualizing the 2σ-range of the dose differences in dependence of the parameters. The green band fits through all data points calculated with the 450 μm modulation power. The red band has the same dimension as the yellow band but the slope is optimized to fit to all results present for a modulation power of 250 μm.

As the measurements of the modulation power covers a broad range and the change in the modulation power shows the most severe changes in the dose effects, more data for the modulation power in human lungs are needed.

5. Conclusion

A detailed 3D systematic analysis of the effect of the Bragg peak degradation was performed. The results were presented in dependency of the distance through lung tissue, the size and shape of the treatment volume, as well as plan specific parameters as particle energy and spot distance. The effects were estimated for different modulation powers, giving a worst-case scenario and more likely scenarios. The results allow for the first time an approximation of the uncertainty on the mean dose for a clinical scanned proton treatment plan. Even though tumor movement affects the treatment outcome more than the Bragg peak degradation, an inclusion of the dose changes due to the Bragg peak degradation is bringing proton therapy for lung carcinomas closer to a high precision therapy.

References

Agostinelli S *et al* 2003 Geant4—a simulation toolkit *Nucl. Instrum. Methods Phys. Res.* A **506** 250–303
Baumann K-S, Witt M, Weber U, Engenhart-Cabillic R and Zink K 2017 An efficient method to predict and include Bragg curve degradation due to lung-equivalent materials in Monte Carlo codes by applying a density modulation *Phys. Med. Biol.* **62** 3997
De Ruysscher D, Sterpin E, Haustermans K and Depuydt T 2015 Tumour movement in proton therapy: solutions and remaining questions: a review *Cancers* **7** 1143–53
Espana S and Paganetti H 2011 Uncertainties in planned dose due to the limited voxel size of the planning CT when treating lung tumors with proton therapy *Phys. Med. Biol.* **56** 3843
Goitein M 1977 The measurement of tissue heterodensity to guide charged particle radiotherapy *Int. J. Radiat. Oncol. Biol. Phys.* **3** 27–33
Perl J, Shin J, Schuemann J, Faddegon B and Paganetti H 2012 TOPAS: an innovative proton Monte Carlo platform for research and clinical applications *Med. Phys.* **39** 6818–37
Ringbaek T P, Simeonov Y, Witt M, Engenhart-Cabillic R, Kraft G, Zink K and Weber U 2017 Modulation power of porous materials and usage as ripple filter in particle therapy *Phys. Med. Biol.* **62** 2892
Sawakuchi G, Titt U, Mirkovic D and Mohan R 2008 Density heterogeneities and the influence of multiple Coulomb and nuclear scatterings on the Bragg peak distal edge of proton therapy beams *Phys. Med. Biol.* **53** 4605–19
Schneider U, Pedroni E and Lomax A 1996 The calibration of CT Hounsfield units for radiotherapy treatment planning *Phys. Med. Biol.* **41** 111
Schulz-Ertner D and Tsujii H 2007 Particle radiation therapy using proton and heavier ion beams *J. Clin. Oncol.* **25** 953–64
Sell M, Titt U, Perles L, Mirkovic D, Mohan R, Babert M and Oelfke U 2012 WE-E-BRB-02: evaluation of analytical proton dose predictions with a lunglike plastic phantom *Med. Phys.* **39** 3956
Titt U, Sell M, Unkelbach J, Bangert M, Mirkovic D, Oelfke U and Mohan R 2015 Degradation of proton depth dose distribution attributable to microstructures in lung-equivalent material *Med. Phys.* **42** 6425
Urie M, Goitein M, Holley W and Chen G 1986 Degradation of the Bragg peak due to inhomogeneities *Phys. Med. Biol.* **31** 1

Widesott L, Amichetti M and Schwarz M 2008 Proton therapy in lung cancer: clinical outcomes and technical issues a systematic review *Radiother. Oncol.* **86** 154–64

Wilson R 1946 Radiological use of fast protons *Radiology* **47** 487–91

Witt M 2014 Modulationseffekte von Kohlenstoffionen bei der Bestrahlung von Lungen *Master's Thesis* Technische Hochschule Mittelhessen—University of Applied Sciences, Giessen, Germany

Witt M, Weber U, Simeonov Y and Zink K 2015 SU-E-T-671: range-modulation effects of carbon ion beams in lung tissue *Med. Phys.* **42** 3491

Zhang X, Li Y, Pan X, Xiaoqiang L, Mohan R, Komaki R, Cox J D and Chang J Y 2010 Intensity-modulated proton therapy reduces the dose to normal tissue compared with intensity-modulated radiation therapy or passive scattering proton therapy and enables individualized radical radiotherapy for extensive stage iiib non-small-cell lung cancer: a virtual clinical study *Int. J. Radiat. Oncol. Biol. Phys.* **77** 357–66

Baumann et al. Radiation Oncology (2019) 14:183
https://doi.org/10.1186/s13014-019-1375-0

Radiation Oncology

RESEARCH Open Access

Effects of the Bragg peak degradation due to lung tissue in proton therapy of lung cancer patients

Kilian-Simon Baumann[1,2*], Veronika Flatten[1,2], Uli Weber[3], Stefan Lautenschläger[1,4], Fabian Eberle[1,4], Klemens Zink[1,2,5] and Rita Engenhart-Cabillic[1,4]

Abstract

Purpose: To quantify the effects of the Bragg peak degradation due to lung tissue on treatment plans of lung cancer patients with spot scanning proton therapy and to give a conservative approximation of these effects.

Methods and materials: Treatment plans of five lung cancer patients (tumors of sizes 2.7–46.4 cm^3 at different depths in the lung) were optimized without consideration of the Bragg peak degradation. These treatment plans were recalculated with the Monte Carlo code TOPAS in two scenarios: in a first scenario, the treatment plans were calculated without including the Bragg peak degradation to reproduce the dose distribution predicted by the treatment-planning system (TPS). In a second scenario, the treatment plans were calculated while including the Bragg peak degradation. Subsequently, the plans were compared by means of D_{mean}, $D_{98\%}$ and $D_{2\%}$ in the clinical target volume (CTV) and organs at risk (OAR). Furthermore, isodose lines were investigated and a gamma index analysis was performed.

Results: The Bragg peak degradation leads to a lower dose in the CTV and higher doses in OARs distal to the CTV compared to the prediction from the TPS. The reduction of the mean dose in the CTV was − 5% at maximum and − 2% on average. The deeper a tumor was located in the lung and the smaller its volume the bigger was the effect on the CTV. The enhancement of the mean dose in OARs distal to the CTV was negligible for the cases investigated.

Conclusions: Effects of the Bragg peak degradation due to lung tissue were investigated for lung cancer treatment plans in proton therapy. This study confirms that these effects are clinically tolerable to a certain degree in the current clinical context considering the various more critical dose uncertainties due to motion and range uncertainties in proton therapy.

Keywords: Proton therapy, Lung modulation, Bragg peak degradation, Treatment planning

Background

Since proposed for radiation therapy, ion beams are of increasing interest in radiation oncology [1, 2]. In homogeneous materials the dose profile of heavy charged particles such as protons consists of a low dose plateau at small depths followed by the so-called Bragg peak where most of the dose is deposited. The Bragg peak is followed by a sharp distal fall-off. This finite range and sharp distal fall-off of the dose deposition as well as the comparable low entrance dose lead to a reduction in the integral dose. These advantages of protons in radiation therapy lead to the possibility of a conformal dose distribution in the target while sparing surrounding healthy tissue [3]. Mainly two approaches for the use of proton therapy have evolved [4]: 1) to escalate the dose in the tumor while allowing the same dose to organs at risk (OAR) compared to conventional photon therapy and 2) keeping the target dose constant compared to conventional photon therapy and reducing the dose deposited

* Correspondence: kilian-simon.baumann@staff.uni-marburg.de
[1]University Medical Center Giessen-Marburg, Department of Radiotherapy and Radiooncology, Marburg, Germany
[2]University of Applied Sciences, Institute of Medical Physics and Radiation Protection, Giessen, Germany
Full list of author information is available at the end of the article

to OARs as much as possible. Both approaches can be considered for the treatment of lung cancer patients with protons. On the one hand, it has been shown in some studies that a dose escalation in the tumor improves local control and survival in non-small cell lung cancer (NSCLC) patients [4]. On the other hand, the sparing of healthy tissue is of interest for tumors in difficult anatomies where the tumor is located near to sensitive structures or even enclosed by OARs. This is often the case for lung cancer patients due to the possible proximity of OARs like the heart, esophagus, trachea, large blood vessels and the spinal cord [4].

For early-stage NSCLC patients the outcomes achieved with proton therapy are similar to those achieved with stereotactic body radiotherapy (SBRT) [4] despite excellent dose distributions and sparing of OARs. This holds especially for small peripheral lesions, since these are mostly located far from critical structures (except for ribs and chest wall) and hence a sparing of OARs is well achievable with SBRT. However, for larger tumors, especially those located near to OARS, proton therapy might be superior to SBRT.

For locally advanced (stage III) lung cancer patients, virtual clinical studies showed that in proton plans it is possible to reduce the dose deposition in normal tissue, especially in the heart, compared to photon plans [3–5]. Additionally, a phase II study with 44 patients showed an enhanced median survival in a combined radiochemotherapy when irradiating with protons compared to photons. The patients treated with protons showed minimal grade 3 toxicities [4, 6].

In addition to the debatable benefits of proton therapy compared to SBRT in lung cancers, some difficulties in treating lung cancers with protons arise due to the underlying physics as well as the technical application of the proton beam. One of the main issues is the range of protons that depends on the material in the beam path: in case that the patient's anatomy changes and hence is different during the treatment compared to the treatment-planning process, the range and hence the dose deposition can be different to that predicted by the TPS. Hence, the outcome of the treatment is vulnerable to changes in the anatomy of the patient as the patient moves, is not optimally positioned or the anatomy of the patient changes between fractions, e.g. due to a shrinkage of the tumor or weight loss [7–10]. Especially the change in the anatomy between fractions causes a need in plan adaption strategies for proton therapy [11].

Another issue is that the range of protons is predicted based on X-ray CT images while the conversion of stopping powers from X-ray CT images is inaccurate [12, 13]. Furthermore, uncertainties in the dose deposited arise from uncertainties in biological effectiveness models [7, 14].

A crucial topic in the proton therapy of lung cancer patients is motion management since interplay effects due to respiratory motion or motion of the heart combined with the precise application of actively scanned proton beams can lead to a severe underdosage of the target volume [15–20].

Another uncertainty in proton therapy of lung cancer patients arises from the characteristics of the lung tissue itself: The heterogeneous structure of the lung tissue leads to a degradation of the Bragg peak and to a wider distal fall-off [21, 22]. If this degradation is not considered correctly during the treatment planning of lung cancer patients, it might lead to an underdosage of the target volume and an overdosage of normal tissue distal to the target volume [22, 23]. Although this degradation has been described in numerous works [24–29], it cannot be considered in the clinical treatment-planning process and dose calculation on treatment-planning CT images. The reason is that due to the restricted resolution of treatment-planning CTs, the microscopic structure of lung tissue is not resolved sufficiently and a more homogeneous tissue distribution is predicted [26, 30].

Baumann et al. [29] introduced and extensively tested an efficient method to consider the Bragg peak degradation on the base of typically used treatment-planning CT data in Monte Carlo codes by applying a density modulation to voxels associated with the lung. Flatten et al. [31] used this model to estimate the effects of the Bragg peak degradation based on a phantom study where spherical tumors of different sizes were placed at different depths in the lung and the underdosage of the target volume was quantified. The result showed that the underdosage of the target volume increases with an increasing depth of the tumor in lung and a decreasing tumor volume. The maximum underdosage in terms of the mean dose was − 15% compared to the dose distribution predicted by the treatment-planning system that did not consider the Bragg peak degradation.

In this study the effects of the Bragg peak degradation were investigated on clinical cases for various anatomical locations of the tumor in the lung and different treatment plans. We chose simple field configurations so that the results can be used by a large variety of proton centers. The goal is to give upwards estimations for the dose uncertainty in the target volume and OARs. For that, we included also extreme cases (e.g small tumor volumes and large depths in lung) to quantify the maximum degradation effect in realistic patient anatomies.

Methods and materials

Selection of patients

We investigated five exemplary clinical cases with tumor volumes between 2.7 cm^3 and 46.4 cm^3. The tumors were located in the right lung in the upper lobe (two

cases) or the central lobe (three cases). We chose the clinical cases to have tumors located in the center of the lung as well as tumors that are located near to soft tissue or OARs. In doing so we are able to investigate different depth of the tumor in the lung as well as the effects of the Bragg peak degradation on surrounding normal tissue and OARs. For two cases the tumor was located near to the spinal cord. No tumor was located directly at the thorax wall in order to always have lung tissue between the thorax wall and the tumor and hence in the beam path. The patients were originally treated with photons and retrospectively re-planned with protons for this study. We used different beam directions in the proton plans to generate different path lengths in the lung (see Fig. 1 and Table 1).

As described in the introduction, small tumor volumes as investigated in this study might not benefit from proton therapy compared to SBRT and hence tend to be less relevant for proton therapy. Yet, small tumor volumes have been treated with protons at different centers [32–34], with volumes going down to only 1 cm^3. Furthermore, Flatten et al. [31] showed that the effects of the Bragg peak degradation increase with a decreasing tumor volume. Thus, we investigated these small tumors as well, in particular to derive an upwards estimation for larger and thus clinically more relevant tumor volumes.

Treatment planning

All treatment plans were optimized with Eclipse v.13.7 (VARIAN) using the non-linear universal proton optimizer, v.13.7.15. The total prescribed dose was 30 Gy (RBE) and the only planning objective was to deliver at least 95% of the prescription dose to at least 98% of the planning target volume (PTV). For small tumor volumes we accepted hot spots (up to 115% of the prescribed dose) in the PTV. The PTV was the clinical target volume (CTV) plus an isotropic margin of 3 mm, although most PTV concepts proposed in the literature [7, 34–36] are field specific and account for uncertainties of the proton's range or the positioning of the patient. However, in the majority of clinical situations, an isotropic margin around the CTV is used for treatment planning as done in this study. Additionally, we planned on static CT data, ignoring movements of the anatomy due to respiration in both the planning and dose calculation. By excluding any effects due to motion, positioning of the patient or range uncertainties, we are able to extract the pure effects of the Bragg peak degradation. We analyzed these effects on the CTV and not the PTV, since the CTV

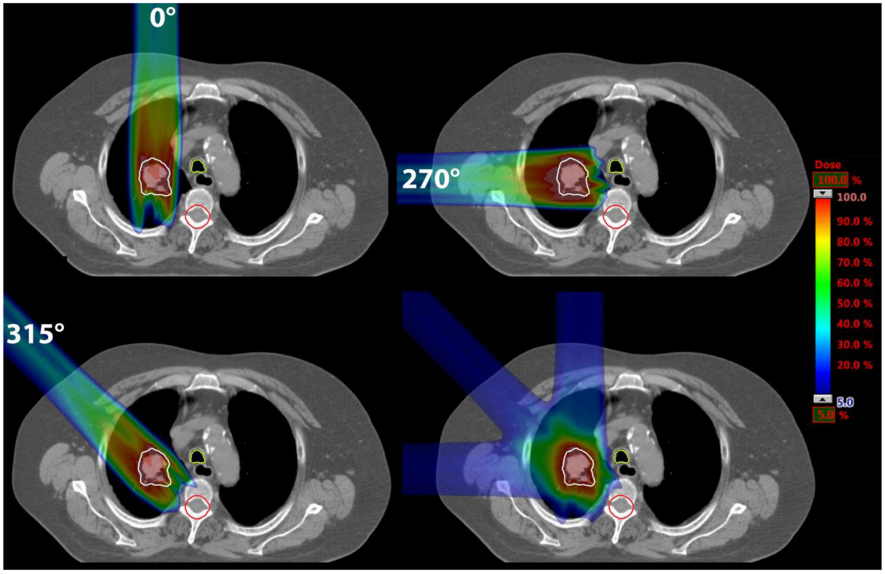

Fig. 1 CT slices of one exemplary patient (patient 1): for the beam directions 0°, 270° and 315° plans were optimized individually consisting of one single field. On the bottom right the sum of these plans is shown. The CTV is marked in white, trachea in light green and spinal cord in red. On the right a color bar is given indicating the relative dose

Table 1 Volumes of the CTVs and lungs for the five patients and minimum and maximum diameter of the CTVs as well as depths in lung of the CTVs for each beam direction. The depth of the CTV corresponds to the path length through lung tissue for the spot at the isocenter

Patient	Lung volume in cm^3	Volume of CTV in cm^3	min./max. diameter of CTV in cm	Depth of CTV in cm for different beam directions		
				0°	270°	315°
1	2294	46.4	2.9/4.2	6.2	3.3	3.6
2	1882	4.2	1.8/2.3	1.8	2.1	1.5
3	1705	32.1	3.5/5.2	12.2	9.2	9.2
4	1780	6.2	2.2/2.4	6.9	2.7	5.3
5	1600	2.7	1.6/2.0	4.5	3.8	3.6

is the clinically relevant structure. Since for each optimized plan the dose deposited in the OARs was below any critical value we did not include any constraints for OARs in the treatment-plan optimization.

We decided to investigate simple treatment plans consisting of only one single field coming from either 0°, 270° or 315°. We used different beam directions to generate different depths of the CTV in the lung. The distal spot spacing was 3 mm, the lateral spot spacing was 0.45 times the full-width-half-maximum (FWHM) in air. The FWHM for 70 MeV protons was 32.5 mm and for 221 MeV protons it was 8.1 mm.

The different beam directions are shown in Fig. 1 for one exemplary patient. As described later in the text, we also made a sum plan of the three single field plans for each patient as shown in Fig. 1 bottom right. In Fig. 2 the remaining four patients are shown with one exemplary treatment plan each.

Although some of these beams may not be the best choice from a clinical point of view (e.g. OARs distal to the PTV, large depth of the tumor in the lung), we decided to investigate these cases anyway to give an upwards estimation for the effects of the Bragg peak degradation also for worst-case scenarios.

The motivation for using simple treatment plans is to highlight the effects of the Bragg peak degradation. Furthermore, there is no gold standard in plan design for lung cancer patients, especially concerning the choice of number of fields and beam directions, although several proton centers have already treated lung cancer patients with protons [6, 32–34]. Thus, in keeping the treatment plans simple, we can assure that the results from this study are usable for as many different proton centers as possible since the dependencies of the Bragg peak degradation (e.g. on the depth of tumor in lung) can be assessed more easily using simple treatment plans compared to complex IMPT plans.

In order to assess whether the results from this study can be used to estimate the effects of the Bragg peak degradation for more complex plans, we investigated two IMPT plans, one each for patient 1 and 5 as shown in Fig. 3. The choice fell on these two patients since they have the largest and smallest tumor volume (compare Table 1). Multi-field optimization was enabled to optimize three fields for each plan. The same PTV concept and planning objectives were used as for the simple plans. For patient 1 the beam directions were 180°, 270° and 330°. For patient 5 the beam directions 10°, 180° and 270° were used.

Simulations

Simulations were performed using the Monte Carlo code TOPAS (Tool for Particle Simulations) version 3.1.p1 [37], a toolkit based on Geant4 (Geometry And Tracking) version geant4–10-03-patch-01 [38]. We used the same beam data in both TOPAS and Eclipse and commissioned these data to match the beam delivery system at the Ion-Beam Therapy Center Marburg. Dose calculation results in water between TOPAS and Eclipse agreed well. The passing rate of the gamma index 1%/1 mm for voxels with dose values greater than 20% of the maximum dose was larger than 98% for single spots. It is known that differences between dose calculation algorithms as used in Eclipse and Monte Carlo codes such as TOPAS exist especially for dose calculations in the lung [39]. Hence, all dose calculations were performed with TOPAS so that differences in the dose calculation between TOPAS and Eclipse do not falsify the results.

Each treatment plan optimized with Eclipse was recalculated in TOPAS in two scenarios: In the first scenario, each optimized treatment plan was calculated on the original CT data. Hence, this calculation corresponds to the prediction from the treatment-planning system. In a second scenario, the plans were recalculated while considering the Bragg Peak degradation. To do so, we used the mathematical model presented by Baumann et al. [29]. The strength of the Bragg peak degradation is quantified by the material characteristic "modulation power" P_{mod}: The greater the modulation power of a heterogeneous material like lung tissue the broader the

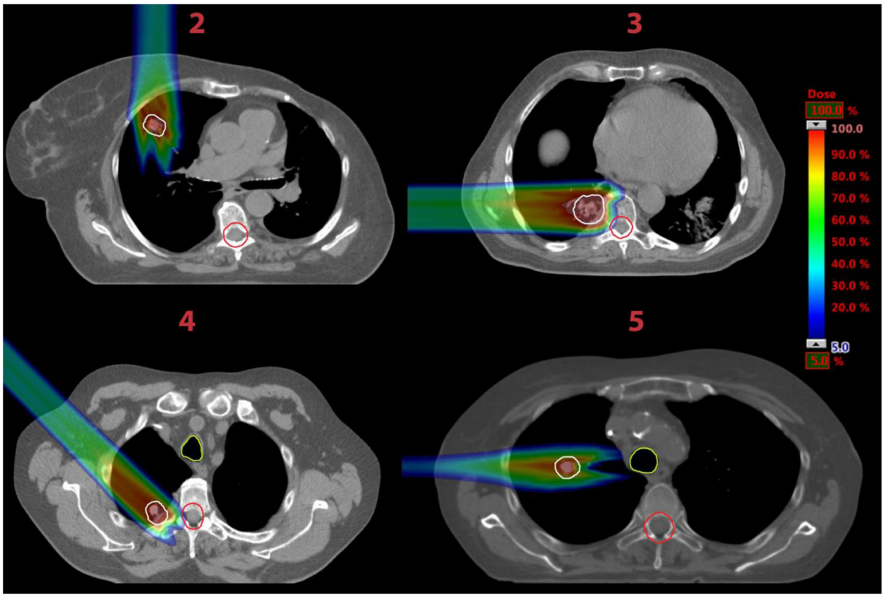

Fig. 2 CT slices of the remaining patients. The patient's numbers are marked in red. For each patient one exemplary plan is shown. The CTV is marked in white, trachea in light green and spinal cord in red. On the right a color bar is given indicating the relative dose

Bragg peak and the less steep the distal fall-off as shown in Fig. 4. Based on the modulation power a density distribution can be derived. When modulating the density of each voxel associated with the lung within the patient following this density distribution, the Bragg peak degradation due to the lung tissue is being reproduced [29]. The dose distributions for each plan obtained from using the original CT data (non-modulated case) and when applying the density modulation (modulated case) were compared in means of cumulative dose volume histograms (DVH), mean doses D_{mean}, $D_{98\%}$ and $D_{2\%}$ in the CTV and OARs. Additionally, we investigated the differences in the dose distribution when combining the dose distributions from the single plans (beam directions 0°,

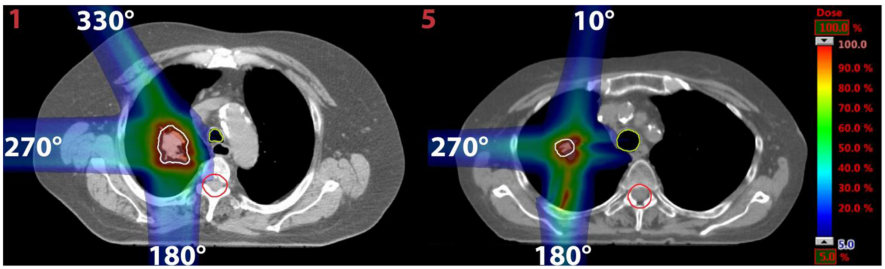

Fig. 3 CT slices of the patients 1 and 5 (marked in red numbers) with the dose distributions for the optimized IMPT plans. The CTV is marked in white, trachea in light green and spinal cord in red. On the right a color bar is given indicating the relative dose

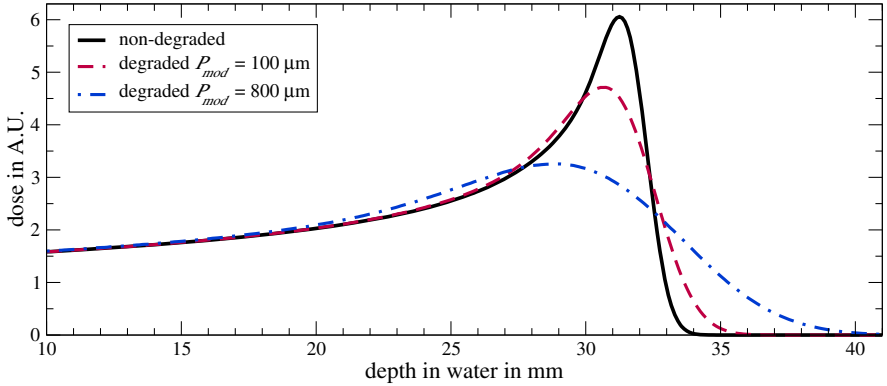

Fig. 4 Depth dose curves of protons in water. In black the Bragg curve as predicted by the treatment-planning system that does not consider the Bragg peak degradation due to the lung tissue. In red and blue the degraded Bragg curves based on modulation powers P_{mod} of 100 µm and 800 µm. The greater the modulation power the broader the Bragg peak and the less steep the distal fall-off

270° and 315°) for each patient to an added-up dose distribution to investigate the influence of the number of irradiated fields on the degradation effects.

In a study by Witt [40] the modulation powers of porcine lungs were measured in proton beams to be in the range from 300 µm to 750 µm. Since the measurements were performed with complete lungs, the measured modulation powers correspond to integrated modulation powers of all the structures of the lung being arranged in the beam that cannot be identified in CT images. The modulation power increases with increasing structure sizes [29]. Thus, the modulation power varies with the position in the lung. In the peripheral region of the lung the modulation power tends to be smaller compared to the central lung where the size of the structures is greater. For almost each measurement the modulation power was in the range from 300 µm to 500 µm with an average of 450 µm. For one measurement the modulation power was 750 µm. However, for this measurement the lung was positioned in a way that a large bronchial structure was in the beam line.

To clarify whether these results obtained with porcine lungs are applicable for human lung tissue, high-resolution CT images with a resolution of 4 µm of human lung tissue samples were investigated by Witt [40] and Baumann et al. [29]. The so-gained modulation powers were in the range from 50 µm to 250 µm. The authors discussed that the preparation of the tissue samples resulted in a noticeable loss of water of up to 37% and hence in a reduction of the sizes of the lung structures. Therefore, the modulation powers gained in this investigation are lower compared to the measurements with porcine lungs.

Both the measurements with porcine lungs and the investigation of human lung tissue samples indicate that the modulation power of lung tissue is in the order of some hundred micrometers. However, until now there is no possibility to determine a patient-specific modulation power for each region of the lung. Therefore, in this study we investigated the effects of the Bragg peak degradation based on modulation powers of 100 µm, 250 µm, 450 µm and 800 µm, covering the whole range of modulation powers found in the measurements of porcine lungs and the investigation of human lung tissue samples with some additional buffer to determine the minimum and maximum degradation effects in exemplary clinical cases. For the IMPT plans we only used a modulation power of 450 µm.

Results

In Fig. 5 on the left side the DVH for patient 1 and the beam direction 270° is shown for the CTV and the OAR trachea. The Monte Carlo calculated DVH for each volume is shown for the non-modulated case representing the dose distribution predicted by the treatment-planning system and the modulated cases where the Bragg peak degradation based on modulation powers between 100 µm and 800 µm is considered. The dose coverage of the CTV decreases with an increasing modulation power. The dose deposited in the trachea increases with an increasing modulation power. On the right side the depth dose curves along the center of the beam for the non-modulated scenario and the modulated one based on the maximum modulation power of 800 µm are shown. The positions of the body, the lung and the CTV are marked by dashed black lines. We

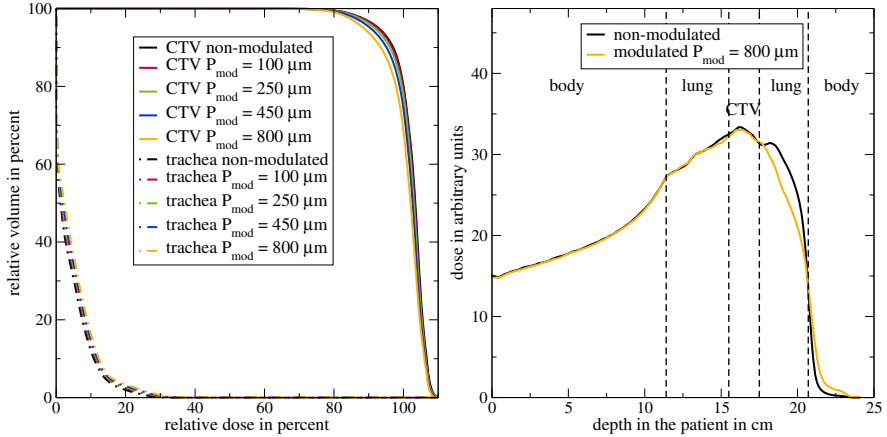

Fig. 5 Left side: Cumulative dose-volume histogram for the CTV and trachea for patient 1 and the beam direction 270° for both the non-modulated case and the modulated cases based on modulation powers between 100 µm and 800 µm. Right side: depth dose curve along the center of the beam. The positions of the body, the lung and the CTV are marked by dashed black lines

decided to show the results for the extreme modulation power of 800 µm since for a smaller modulation power the effects are not visible as clearly: when entering the body both dose distributions are the same. In the lung the effects of the degradation can be seen resulting in a broader dose curve and a less steep fall-off for the modulated case. Within the CTV there is a slightly higher dose for the non-modulated case. In the lung distal to the CTV there is a significantly higher dose for the non-modulated case. The background is that in this case a spot is used by the TPS where the Bragg peak is located distal to the CTV in order to achieve a sufficient dose coverage within the CTV. This peak is smoothed in the modulated case as described by Flatten et al. [31]. In the body distal to the lung the dose for the modulated case is higher due to the broader fall-off resulting in a larger range and hence a higher dose deposition.

In Fig. 6 exemplary isodose lines [41, 42] for 95, 80 and 20% of the prescribed dose are shown for the non-modulated case (pink) and the modulated case based on a modulation power of 800 µm (green). Additionally, the CTV is marked in white, the trachea in light green and the spinal cord in red. Again, we decided to show the results for the extreme modulation power of 800 µm. The 95% isodose lines are shown in the left column, the 80% in the middle column and the 20% in the right column. In the first line the isodose lines for patient 1 (marked with a white number) are shown for the beam direction 270°. The regions enclosed by the 95 and 80% isodose lines are larger for the non-modulated cases indicating the underdosage of the CTV due to the Bragg peak degradation (compare DVH and depth dose in Fig. 5). The 20% isodose line for the modulated case reaches farther compared to the non-modulated case. The same effects can be seen for all patients.

The greater range of the 20% isodose lines shows the potential risk of an overdosage in OARs distal to the target volume. Especially for patient 3 and 4 in Fig. 6 the isodose lines for 20% of the prescribed dose reach into the spinal cord. However, the additional range of the 20% isodose lines is 2 mm at maximum for these two patients. The maximum shift of each isodose line for the modulated case compared to the non-modulated case for the patients as shown in Fig. 6 are listed in Table 2. A negative sign marks a shorter range compared to the non-modulated case. The range uncertainties of the isodose lines in lung (patient 1 and patient 2 except for the 20% isodose line) are larger compared to those in tissue (patient 3 and 4 all isodose lines and 20% isodose line of patient 1).

To quantify the effects shown in Figs. 5 and 6 in terms of dose, the absolute dose values for the non-modulated case and the differences in percent of the mean dose D_{mean}, $D_{98\%}$ (the dose that is received by 98% percent of the volume) and $D_{2\%}$ between the modulated cases and the non-modulated case for patient 1 are reported in Table 3 for the CTV, the trachea and the spinal cord. The $D_{98\%}$ is taken to quantify the minimum dose received by a volume while the $D_{2\%}$ is taken to quantify the maximum dose received by a volume. For the OARs

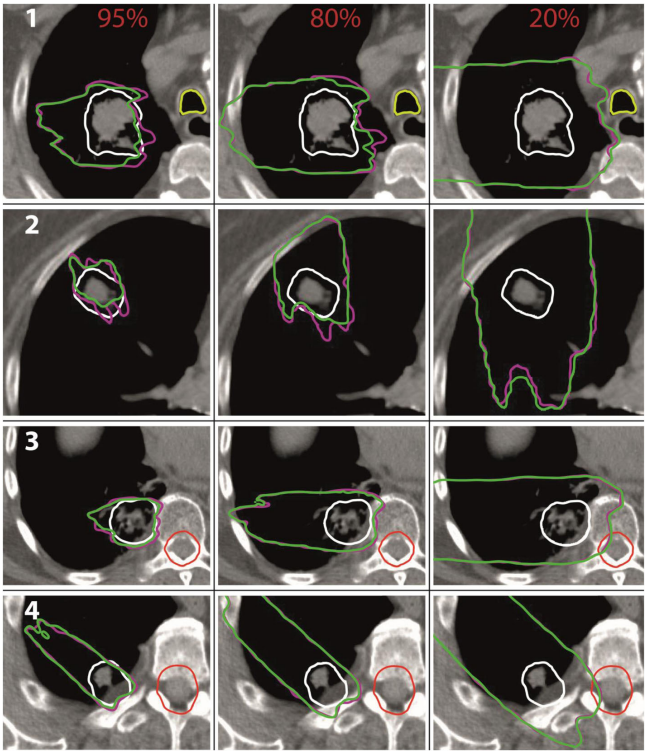

Fig. 6 Isodose lines for 95, 80 and 20% of the prescribed dose. In pink for the non-modulated case, in green for the modulated case based on a modulation power of 800 μm. In the first column the 95%, in the middle column the 80% and in the right column the 20% isodose lines. Different patient cases are marked in white numbers. The CTV is marked in white, the trachea in light green and the spinal cord in red

the mean dose D_{mean} and the $D_{2\%}$ as a quantification of the maximum dose are shown.

The mean dose D_{mean}, $D_{98\%}$ and $D_{2\%}$ in the CTV are smaller for the modulated cases compared to the non-modulated case and hence the prediction from the treatment-planning system. The differences increase with an increasing modulation power. The largest differences can be seen for the beam direction 0° (corresponding to the largest depth in lung) and the maximum modulation power of 800 μm. Concerning the OARs trachea and spinal cord, the doses deposited in the modulated cases are greater compared to the non-modulated case for the beam directions 270° and 315°. The differences increase with an increasing modulation power. The maximum difference in the mean dose D_{mean} is + 24% for the trachea as well as the spinal cord. However, these relative deviations correspond to low absolute deviations of 0.3 Gy and < 0.1 Gy, respectively. The largest difference for the $D_{2\%}$ value for the trachea is + 24% and + 21% for the spinal cord. These deviations correspond to 1.5 Gy and 0.2 Gy, respectively. It can be seen, that the effects of the Bragg peak degradation on the OARs are almost non-existent for a beam direction 0° since in this case no OAR is positioned distal to the PTV. The effects on the trachea are largest for the beam direction 270°. For the spinal cord the effects are largest for the beam direction 315°.

In Table 4 the absolute dose values and the differences in percent of the mean dose D_{mean}, $D_{98\%}$ and $D_{2\%}$ for the CTV between the modulated cases and the non-modulated case are shown for the patients 2 to 5. The results are given for a modulation power of 800 μm to

Table 2 Maximum shift in mm of the isodose lines for the modulated case based on a modulation power of 800 μm compared to the non-modulated case for the patients and beam directions as shown in Fig. 6. A negative sign stands for a shorter range

Patient/beam direction	Maximum range uncertainty in mm for isodose lines		
	95%	80%	20%
1 / 270°	−8	−5	3
2 / 0°	−8	−10	5
3 / 270°	−4	−3	2
4 / 315°	−2	−2	2

give an estimation of the maximum effects. Additionally, the results for a more realistic modulation power of 450 μm are given. The deviations between the modulated cases and the non-modulated case for the OARs are as small and negligible as for patient 1 and hence not shown for the other patients. As it is the case with patient 1, the dose coverage of the CTV in the modulated cases is lower compared to the non-modulated case.

For a modulation power of 800 μm the maximum differences in the mean dose D_{mean} as well as the $D_{98\%}$ are roughly − 5%. For the $D_{2\%}$ it is about − 4%. The average difference in the mean dose D_{mean} is in the order of − 2%, for $D_{98\%}$ it is − 3% and for $D_{2\%}$ it is about − 2%.

For a more realistic modulation power of 450 μm the maximum differences in the mean dose D_{mean}, the $D_{98\%}$ as well as the $D_{2\%}$ are roughly − 3%. The average difference in the mean dose D_{mean} is in the order of − 1%, for $D_{98\%}$ it is roughly − 2% and for $D_{2\%}$ it is − 1%.

Additionally, we looked at the differences in the mean dose D_{mean}, $D_{98\%}$ and $D_{2\%}$ for the CTV between the modulated cases and the non-modulated case when all three plans from the beam directions 0°, 270° and 315° are combined. As for the irradiation with one single field, in the combined scenario with three fields, the differences between the modulated cases and the non-modulated case are at maximum about − 5% for a modulation power of 800 μm. For a modulation power of 450 μm the maximum difference is about − 3%.

In Table 5 the passing rates for the gamma index 3%/1 mm (local) are shown for each patient and the dose distributions based on modulation powers of 450 μm and 800 μm. All voxels with at least 20% of the maximum dose were included in the analysis. We chose to set a small

Table 3 Absolute dose values for the non-modulated case and differences in percent of the mean dose D_{mean}, $D_{98\%}$ (only for the CTV) and $D_{2\%}$ for the CTV and OARs between the modulated and the non-modulated cases for patient 1

Modulation	CTV			Trachea		Spinal cord	
	D_{mean}	$D_{98\%}$	$D_{2\%}$	D_{mean}	$D_{2\%}$	D_{mean}	$D_{2\%}$
beam direction: 0° (depth in lung: 6.2 cm)							
$D_{non\text{-}mod}$ in Gy (RBE)	29.9	25.7	32.2	0.1	0.5	< 0.1	0.1
100 μm	−0.3%	−0.4%	−0.4%	−1%	+ 1%	0%	− 1%
200 μm	−0.7%	− 1.2%	− 0.8%	0%	+ 1%	0%	− 1%
450 μm	− 1.3%	− 3.0%	− 1.2%	0%	+ 2%	0%	− 1%
800 μm	−2.1%	−4.9%	− 1.8%	0%	+ 2%	+ 1%	− 1%
beam direction: 270° (depth in lung: 3.3 cm)							
$D_{non\text{-}mod}$ in Gy (RBE)	30.1	27.3	30.4	1.1	5.6	0.1	0.7
100 μm	−0.2%	−0.1%	−0.2%	+ 7%	+ 9%	+ 2%	+ 6%
200 μm	−0.5%	−1.0%	− 0.3%	+ 12%	+ 13%	+ 2%	+ 9%
450 μm	− 0.5%	−2.2%	− 0.5%	+ 16%	+ 17%	+ 7%	+ 14%
800 μm	− 0.9%	−4.1%	−0.6%	+ 24%	+ 24%	+ 9%	+ 21%
beam direction: 315° (depth in lung: 3.6 cm)							
$D_{non\text{-}mod}$ in Gy (RBE)	29.8	26.6	41.6	0.2	1.0	0.1	0.7
100 μm	0.0%	0.0%	+ 0.1%	+ 3%	+ 2%	+ 6%	+ 7%
200 μm	−0.4%	−1.5%	−0.2%	+ 2%	+ 1%	+ 11%	+ 11%
450 μm	−0.8%	−1.5%	− 0.4%	+ 2%	+ 2%	+ 15%	+ 14%
800 μm	− 1.5%	−3.0%	− 0.6%	+ 5%	+ 5%	+ 24%	+ 21%

Table 4 Absolute dose values for the non-modulated case and differences in percent of the mean dose D_{mean}, $D_{98\%}$ and $D_{2\%}$ between the modulated and the non-modulated cases for the CTV and the patients 2 to 5. The modulation powers used in these cases are 450 μm and 800 μm

Patient	Modulation	Beam direction: 0°			Beam direction: 270°			Beam direction: 315°		
		D_{mean}	$D_{98\%}$	$D_{2\%}$	D_{mean}	$D_{98\%}$	$D_{2\%}$	D_{mean}	$D_{98\%}$	$D_{2\%}$
2	$D_{non\text{-}mod}$ in Gy (RBE)	29.9	23.4	32.0	30.1	25.2	31.1	30.0	22.1	32.3
	450 μm	−1.8%	−0.7%	−0.2%	− 1.1%	− 0.8%	− 0.7%	−1.1%	− 1.5%	− 0.7%
	800 μm	− 3.1%	− 2.9%	− 3.8%	− 1.9%	−1.4%	− 1.1%	− 2.0%	− 2.5%	−1.2%
3	$D_{non\text{-}mod}$ in Gy (RBE)	30.0	25.8	32.2	30.1	28.3	31.5	30.0	27.0	31.9
	450 μm	−1.1%	−1.4%	−0.9%	−0.6%	−2.9%	− 0.5%	− 0.8%	− 2.2%	− 0.8%
	800 μm	− 1.8%	−2.8%	−1.5%	− 1.1%	−5.1%	−0.8%	−1.4%	− 4.2%	− 1.1%
4	$D_{non\text{-}mod}$ in Gy (RBE)	30.0	25.7	31.0	30.0	24.2	32.2	30.0	26.8	30.8
	450 μm	−1.3%	−2.5%	−0.8%	−0.6%	−1.2%	− 0.3%	− 0.6%	−1.1%	− 0.4%
	800 μm	− 2.2%	−4.2%	− 1.2%	−1.0%	−2.0%	− 0.5%	−1.0%	−2.0%	− 0.7%
5	$D_{non\text{-}mod}$ in Gy (RBE)	30.1	27.2	32.8	30.0	23.7	31.6	30.1	27.9	33.8
	450 μm	−2.6%	−0.5%	−1.1%	−2.0%	−3.0%	− 2.1%	−3.0%	− 1.5%	−3.2%
	800 μm	−4.7%	− 2.8%	−2.1%	− 3.1%	− 4.6%	− 3.2%	− 4.9%	−2.5%	−4.3%

distance-to-agreement since the effect of the Bragg peak degradation leads to a broadening of the Bragg peak and hence a small shift in the dose (compare Figs. 5 and 6). The allowed dose difference was set to 3% since this is roughly the average effect on the mean dose in the CTV for a modulation power of 800 μm. For a modulation power of 800 μm, the minimal passing rate is 90.4% for patient 5 and the beam direction 315° corresponding to the maximum difference in the mean dose (compare Table 3). The average passing rate is 96.8%. For a modulation power of 450 μm the minimum passing rate is 93.1% and the average passing rate is 98.5%. We also investigated the gamma index when including only those voxels with at least 80% of the maximum dose. For this gamma index the minimum passing rate is 84.0% with an average passing rate of 94.6% for a modulation power of 800 μm.

Table 5 Passing rates in percent of the gamma index 3%/1 mm including all voxels with at least 20% of the maximum dose for all patients depending on the modulation power and beam direction

Patient	Modulation power	Beam direction		
		0°	270°	315°
1	450 μm	98.5	97.2	99.0
	800 μm	96.4	95.4	97.3
2	450 μm	97.3	99.3	99.9
	800 μm	94.7	95.5	99.2
3	450 μm	99.5	99.8	99.6
	800 μm	98.8	99.0	99.0
4	450 μm	99.9	100	99.9
	800 μm	99.6	100	99.9
5	450 μm	96.0	98.2	93.1
	800 μm	91.7	95.6	90.4

In order to assess whether the results from this study being derived using simple treatment plans can be used to estimate the dose uncertainty due to the Bragg peak degradation on more complex plans like IMPT plans, we investigated two IMPT plans - one each for patient 1 and 5. The reduction of the mean dose D_{mean} of the CTV was − 1% for patient 1 and a modulation power of 450 μm. For patient 5 it was about − 3%. For patient 1, the reduction of the mean dose of the CTV approximately corresponds to the average dose reduction for the simple treatments plans with beam directions 0°, 270° and 315° (compare Table 3). For patient 5 the dose reduction for the IMPT plan is in the order of the maximum effect for the simple treatment plans.

Discussion

The influence of the Bragg peak degradation due to lung tissue on treatment plans of lung cancer patients was investigated. For all cases the treatment-planning system overestimated the dose delivered to the CTV and in some cases underestimated the dose delivered to distal OARs. This effect increases with an increasing modulation power. The maximum underestimation of the mean dose D_{mean} is − 5% for the CTV and an extreme modulation power of 800 μm. The average underestimation is in the order − 2%. This extreme modulation power of

800 μm can occur in cases where a larger bronchial structure in the lung is positioned in the proton beam. However, for a more realistic modulation power of 450 μm, the underestimation of the mean dose D_{mean} is only about − 3% at maximum. The average underestimation is roughly − 1%.

Concerning the effects on OARs, it was shown that the effects are dependent on the beam direction which defines the relative position between the target volume and OAR for a given anatomy: As shown in Fig. 5 on the right side, the Bragg peak degradation results in a higher dose distal to the Bragg peak. Hence, only OARs distal to the PTV can receive a higher dose than predicted by the treatment-planning system. Due to range uncertainties in proton therapy it would typically be avoided to arrange fields in a way that an OAR is located directly distal to the PTV. Nevertheless, in some cases this is inevitable for example when the patient has been previously irradiated in this region or due to technical limitations of the beam delivery system. Additionally, anatomical characteristics could enforce an irradiation where an OAR is positioned distal to the PTV as it is the case with patient 3 as shown in Fig. 2: for the beam directions 315° and 270° the spinal cord is positioned distal to the PTV. However, for the beam direction 0° the beam crosses the heart and the distance in lung is quite large. Since a patient's anatomy can oblige to use beams where an OAR is positioned distal to the PTV, we also investigated these cases. The underestimation of the mean dose D_{mean} in the OARs trachea and spinal cord was 0.3 Gy at maximum. For the $D_{2\%}$ quantifying the maximum dose deposited in these OARs it was 1.5 Gy at maximum. The resulting enhanced dose deposited to OARs is far from any dose constraints used in the conventional treatment planning. Thus, the effects of the Bragg Peak degradation on OARs distal to the PTV are negligible for the cases investigated. However, in cases where the OAR is located directly distal to the PTV the effects might be larger and significant.

We were able to reproduce the findings from Flatten et al. [31] that the effects of the Bragg peak degradation increase with an increasing depth of the tumor in the lung and a decreasing tumor volume: for example, for patient 1 the underdosage of the CTV increases from − 0.5% to − 1% (for a modulation power of 450 μm) between the beam direction 270° where the tumor depth is 3.3 cm and the beam direction 0° where the depth is 4.6 cm.

When comparing the results from patient 1 for the beam direction 315° with the results from patient 5 for the beam direction 315° one can see that in both cases the tumor is at a depth of 3.6 cm (see Table 1). However, the CTV of patient 1 is with 46.4 cm^3 much larger compared to patient 5 with a volume of 2.7 cm^3. The effect of the Bragg peak degradation on the mean dose in the CTV for patient 1 is with − 1% much smaller compared to patient 5 with − 3% (for a modulation power of 450 μm).

Regarding the number of fields used to irradiate the CTV, it was shown that as expected, the effect of the Bragg peak degradation is independent on the number of fields as long as these fields are optimized individually.

Concerning the complexity of the irradiation plans, we decided to investigate simple plans with only one single field as described in the Methods & materials section. By investigating different beam directions, a large variety of scenarios (depth of tumor in lung, OAR distal to the PTV) has been covered and even for the worst cases the underdosage of the CTV was − 5% at maximum for an extreme modulation power of 800 μm and only about − 3% for a more realistic modulation power of 450 μm. To assess whether these results can be applied to more complex treatment plans, we investigated two IMPT plans for a realistic modulation power of 450 μm. For both patients the reduction of the mean dose of the CTV was in the same order compared to the simple treatment plans. This supports the statement that the results found in this study – although being derived using simple treatment plans – can be used to estimate the dose uncertainties due to the Bragg peak degradation for more complex plans.

The passing rate of the gamma index was on average 96.8% for a modulation power of 800 μm and 98.5% for a modulation power of 450 μm. The minimum passing rate for a realistic modulation power of 450 μm was 93.1%. The high passing rate of the gamma index is reasonable because as shown in Figs. 5 and 6 the Bragg peak degradation leads to a shift of the isodose lines. This shift is on average very small and hence covered by the distance-to-agreement in the gamma index. For all cases investigated in this study the passing rate was clinically acceptable. In addition to the finding that the reduction of the mean dose is on average only in the order of − 1% and at maximum − 3% for a realistic modulation power of 450 μm, this supports that the effects of the Bragg peak degradation are clinically tolerable.

What is more, it is well-known in the literature that the relative biological effectiveness (RBE) of protons is larger than 1.1 at the distal part of the Bragg peak [43]. At the moment, this change in RBE is not considered in commonly used treatment-planning systems, hence, this larger biological effect might partially balance out the physical underdosage of the target volume due to the Bragg peak degradation which mainly occurs at the distal end of the Bragg peak and hence the target volume (compare Fig. 5). However, this change in RBE could also

potentially increase the effects of the larger dose deposited in normal tissue distal to the Bragg peak.

The Bragg peak degradation due to lung tissue is only one of various issues in proton therapy in general and in proton therapy of lung cancer patients in particular as mentioned in the introduction. Thus, the dose and range uncertainties due to this degradation shall be compared to these other uncertainties in order to quantify its importance in the current clinical context. In a study by Paganetti [7] an overview of range uncertainties is given. Range uncertainties in proton therapy arise – among other things – from measurement uncertainties in water for commissioning (±0.3 mm), patient setup (±0.7 mm) or differences in the dose calculation between the treatment-planning system and Monte Carlo codes as a gold standard for dose calculation (±2 mm). Other reasons for range uncertainties are due to the conversion of x-ray HU to stopping powers (±1% of the range) or biological effects (~ 0.8% of the range or ~ 3 mm [14]). These range uncertainties refer to the range of the 80% distal dose and correspond to average values. Furthermore, these uncertainties might be bigger in lung treatments [7]. The maximum range uncertainties for the 80% isodose lines due to the Bragg peak degradation based on an extreme modulation power of 800 μm found in this study (see Table 2) are 10 mm in lung and 4 mm in tissue and hence are in the order of the mentioned average range uncertainties. Note that the values given by Paganetti [7] are average values while the range uncertainties investigated in this study are maximum values.

Additionally, range and dose uncertainties arise when changes of the anatomy due to weight loss or a shrinkage of the tumor are not accounted for. Szeto et al. [10] analyzed robust intensity modulated treatment plans of 16 patients with locally advanced NSCLC. The treatment dose was recalculated based on daily anatomy variations. Eight patients had an undercoverage of the target volume larger than 2 GyE with a maximum of 12 GyE in terms of the D_{99} (dose that is received by 99% of the target volume). With a prescribed dose of 66 GyE this corresponds to relative deviations in the $D_{99\%}$ of 3% to 18%. The maximum difference in the $D_{98\%}$ found in this study was 3% for a realistic modulation power of 450 μm.

Another crucial issue in proton therapy of lung cancer patients is motion. Dowdell et al. [20] investigated treatment plans for 5 lung cancer patients. Due to the interplay effects caused by the patient's motion, the mean dose in the target volume was only 88% to 92% of the prescribed dose. These interplay effects are however highly patient specific.

At last, we want to introduce and discuss two possible PTV concepts to account for and to avoid an underdosage of the target volume due to the Bragg peak degradation: following the range shifts as shown in Fig. 6, one possible PTV concept could be to increase the margin around the CTV at both the distal and proximal end. The effects of such a PTV concept are depicted in Fig. 7: the dose distributions in a water phantom downstream from 80 mm of lung tissue with a modulation power of 450 μm are shown for the non-modulated (black) and the modulated case (yellow). The CTV marked with dashed lines is at depths between 34 mm and 47 mm. In (a) the dose distributions can be seen for a PTV concept as used in this study with an isotropic margin of 3 mm around the CTV. The red line marks the prescribed dose within the CTV and PTV. In (b) the dose distributions are shown for the case where the PTV is the CTV plus a margin of 5 mm at the proximal end and a margin of 7 mm at the distal end. The dose coverage within the CTV and PTV is better compared to (a). The disadvantage of such a PTV concept is that the dose distribution reaches farther and hence leads to a higher integral dose in the normal tissue and maybe OARs distal to the PTV.

To avoid this larger range and additional dose deposited in normal tissue, another PTV concept might be used as depicted in Fig. 7c: in this case the same PTV concept as in (a) is used (isotropic margin of 3 mm around the CTV), however, during the treatment-planning process a larger dose is prescribed within the margin at both the proximal as well as the distal end. In this case we used a 3% larger dose in the proximal and a 6% larger dose in the distal margin. By doing so a comparable dose distribution in the CTV as in Fig. 7b can be achieved, however, the dose deposited in normal tissue is smaller due to the shorter range. Note that such a PTV concept is connected to challenges since it is hard to guarantee a dose homogeneity in such a small volume. Furthermore, a difference of only 3% in dose in such a small volume is in the order of the uncertainties in proton therapy as discussed above, hence, it would hardly be possible to measure this difference in dose (e.g. as part of quality assurance).

For both PTV concepts an exact knowledge of the anatomy (depth of tumor in lung, tumor volume, location of tumor relative to soft tissue) is important to choose the appropriate values for the additional margin (case b) or the additional dose (case c). Furthermore, the knowledge of the modulation power within the lung tissue is important, since this defines the range and dose uncertainties connected to the Bragg peak degradation. Unfortunately, there is currently no solution to determine the modulation power in patients in-vivo. This is a critical issue still to be solved.

Altogether, the effects of the Bragg peak degradation are at maximum about 5% concerning the

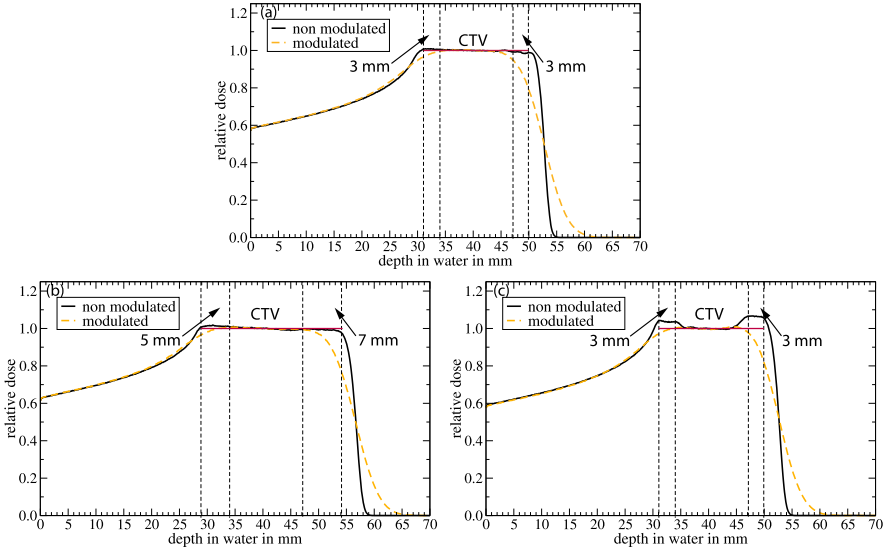

Fig. 7 The effects of different PTV concepts. In **a** the effects for a PTV as used in this study consisting of an isotropic margin of 3 mm around the CTV are shown. In **b** for a PTV concept that has a 5 mm margin at the proximal end and a 7 mm margin at the distal end of the CTV. In **c** for the same PTV concept as used in **a**, however, in this case the prescribed dose within this margin is larger than the prescribed dose in the CTV. In black the dose distribution for the non-modulated case and in yellow the dose distribution for the modulated case based on a modulation power of 450 μm. The CTV and the margin as well as the resulting PTV are marked in dashed lines. The red line marks the prescribed dose within the PTV

underestimation of the mean dose D_{mean} in the CTV when optimizing the treatment plan without considering the degradation due to the lung tissue. Compared to the range and dose uncertainties in proton therapy of lung cancer patients due to the addressed reasons, the effects of the Bragg peak degradation are clinically tolerable to a certain degree in the current clinical context. However, these mentioned dose uncertainties are constantly being reduced which might change this clinical context. Hence, a consideration of the Bragg peak degradation could become more relevant in the future and would bring proton therapy for lung cancer patients closer to a high-precision therapy. The effects of the degradation might be accounted for in the treatment-planning process by applying a corresponding PTV concept as suggested in this study. What is more, this PTV concept and hence the dose deposition in the patient could be optimized when having a detailed knowledge of the lung tissue's modulation power. In our opinion, the exact determination of this modulation power is one crucial issue still to be solved.

Conclusion

The effects of the Bragg peak degradation due to lung tissue on lung cancer patients were investigated. The maximum effect on the mean dose D_{mean} in the CTV according to this study was about 5% at maximum for an extreme modulation power of 800 μm, a long distance travelled through lung and a small tumor volume. For a more realistic modulation power of 450 μm the maximum effect was only about 3% in terms of D_{mean}. For OARs the effect was negligible for the cases investigated. This study confirms that the effects of the Bragg peak degradation are clinically tolerable to a certain degree in the current clinical context considering the various more critical dose uncertainties due to motion and range uncertainties in proton therapy. Furthermore, these effects might be accounted for by using corresponding PTV concepts as suggested in this study.

Abbreviations

CTV: Clinical target volume; $D_{2\%}$: Dose that is received by 2% of a structure's volume; $D_{98\%}$: Dose that is received by 98% of a structure's volume; D_{mean}: Average dose within a structure; IMPT: Intensity modulated proton

therapy; OAR: Organ at risk; PTV: Planning target volume; RBE: Relative biological effectiveness; SBRT: Stereotactic body radiation therapy

Acknowledgements
We would like to thank the reviewers which helped to improve this manuscript.

Authors' contributions
K-SB used the mathematical model to generate the density modulation functions needed for the density modulation to reproduce the Bragg peak degradation in the Monte Carlo simulations. K-SB created the density-modulated DICOM sets and executed the Monte Carlo simulations as well as analyzed the DVHs produced with Eclipse. K-SB wrote the manuscript. VF optimized the treatment plans and transferred these optimized plans to the Monte Carlo code TOPAS and subsequently generated the DVHs. UW contributed to the mathematical model to consider the Bragg peak degradation in Monte Carlo codes underlying to this study. SL and FE contributed to this work by contouring the DICOM sets and helped with clinical information on treatment plans. KZ substantively revised this work and was supervising the work. RE-C substantively revised this work and was supervising the work.

Funding
We did not receive any funding for this work.

Availability of data and materials
The datasets generated during and/or analyzed during the current study are available from the corresponding author on reasonable request.

Ethics approval and consent to participate
Not applicable.

Consent for publication
Not applicable.

Competing interests
The authors declare that they have no competing interests.

Author details
[1]University Medical Center Giessen-Marburg, Department of Radiotherapy and Radiooncology, Marburg, Germany. [2]University of Applied Sciences, Institute of Medical Physics and Radiation Protection, Giessen, Germany. [3]GSI Helmholtzzentrum für Schwerionenforschung, Biophysics Division, Darmstadt, Germany. [4]Marburg Ion-Beam Therapy Center (MIT), Marburg, Germany. [5]Frankfurt Institute of Advanced Studies – FIAS, Frankfurt, Germany.

Received: 19 February 2019 Accepted: 6 September 2019
Published online: 25 October 2019

References

1. Wilson RR. Radiological use of fast protons. Radiology. 1946;47:487–91.
2. Smith AR. Proton therapy. Phys Med Biol. 2006;51(13):R491.
3. Chang JY, Zhang X, Wang X, et al. Significant reduction of normal tissue dose by proton radiotherapy compared with three-dimensional conformal or intensity-modulated radiation therapy in stage I or stage III non–small-cell lung cancer. Int J Radiat Oncol Biol Phys. 2006;65(4):1087–96.
4. Chang JY, Jabbour SK, de RD, et al. Consensus statement on proton therapy in early-stage and locally advanced non-small cell lung cancer. Int J Radiat Oncol Biol Phys. 2016;95(1):505–16.
5. Nichols RC, Huh SN, Henderson RH, et al. Proton radiation therapy offers reduced normal lung and bone marrow exposure for patients receiving dose-escalated radiation therapy for unresectable stage iii non-small-cell lung cancer: a dosimetric study. Clin Lung Cancer. 2011;12(4):252–7.
6. Chang JY, Komaki R, Lu C, et al. Phase 2 study of high-dose proton therapy with concurrent chemotherapy for unresectable stage III nonsmall cell lung cancer. Cancer. 2011;117(20):4707–13.
7. Paganetti H. Range uncertainties in proton therapy and the role of Monte Carlo simulations. Phys Med Biol. 2012;57(11):R99–117.
8. Unkelbach J, Chan TCY, Bortfeld T. Accounting for range uncertainties in the optimization of intensity modulated proton therapy. Phys Med Biol. 2007; 52(10):2755–73.
9. Hui Z, Zhang X, Starkschall G, et al. Effects of interfractional motion and anatomic changes on proton therapy dose distribution in lung cancer. Int J Radiat Oncol Biol Phys. 2008;72(5):1385–95.
10. Szeto YZ, Witte MG, van Kranen SR, et al. Effects of anatomical changes on pencil beam scanning proton plans in locally advanced NSCLC patients. Radiother Oncol J Eur Soc Ther Radiol Oncol. 2016;120(2):286–92.
11. Hoffmann L, Alber M, Jensen MF, et al. Adaptation is mandatory for intensity modulated proton therapy of advanced lung cancer to ensure target coverage. Radiother Oncol J Eur Soc Ther Radiol Oncol. 2017;122(3):400–5.
12. España S, Paganetti H. The impact of uncertainties in the CT conversion algorithm when predicting proton beam ranges in patients from dose and PET-activity distributions. Phys Med Biol. 2010;55(24):7557–71.
13. Arbor N, Dauvergne D, Dedes G, et al. Monte Carlo comparison of x-ray and proton CT for range calculations of proton therapy beams. Phys Med Biol. 2015;60(19):7585–99.
14. Carabe A, Moteabbed M, Depauw N, et al. Range uncertainty in proton therapy due to variable biological effectiveness. Phys Med Biol. 2012;57(5): 1159–72.
15. Bert C, Grözinger SV, Rietzel E. Quantification of interplay effects of scanned particle beams and moving targets. Phys Med Biol. 2008;53:2253–65.
16. Bert C, Durante M. Motion in radiotherapy: particle therapy. Phys Med Biol. 2011;56:R113.
17. Grassberger C, Dowdell S, Lomax A, et al. Motion interplay as a function of patient parameters and spot size in spot scanning proton therapy for lung cancer. Int J Radiat Oncol Biol Phys. 2013;86(2):380–6.
18. Moyers MF, Miller DW, Bush DA, et al. Methodologies and tools for proton beam design for lung tumors. Int J Radiat Oncol Biol Phys. 2001;49(5):1429–38.
19. Bert C, Saito N, Schmidt A, et al. Target motion tracking with a scanned particle beam. Med Phys. 2007;34(12):4768–71.
20. Dowdell S, Grassberger C, Sharp GC, et al. Interplay effects in proton scanning for lung: a 4D Monte Carlo study assessing the impact of tumor and beam delivery parameters. Phys Med Biol. 2013;58(12):4137–56.
21. Urie M, Goitein M, Holley WR, et al. Degradation of the Bragg peak due to inhomogeneities. Phys Med Biol. 1986;31:1.
22. Sawakuchi GO, Titt U, Mirkovic D, et al. Density heterogeneities and the influence of multiple coulomb and nuclear scatterings on the Bragg peak distal edge of proton therapy beams. Phys Med Biol. 2008;53(17):4605–19.
23. Goitein M. The measurement of tissue heterodensity to guide charged particle radiotherapy. Int J Radiat Oncol Biol Phys. 1977;3:27–33.
24. Perles LA, Mirkovic D, Sawakuchi GO, et al. Monte Carlo investigation of rebinning material density distributions of lung parenchyma phantoms in proton therapy. Nucl Technol. 2011;175(1):22–6.
25. Sell M, Titt U, Perles L, et al. WE-E-BRB-02: evaluation of analytical proton dose predictions with a lung–like plastic phantom. Med Phys. 2012;39(6):3956.
26. Titt U, Sell M, Unkelbach J, et al. Degradation of proton depth dose distribution attributable to microstructures in lung-equivalent material. Med Phys. 2015;42(11):6425.
27. Ringbaek TP, Simeonov Y, Witt M, et al. Modulation power of porous materials and usage as ripple filter in particle therapy. Phys Med Biol. 2017; 62:2892.
28. Witt M, Weber U, Simeonov Y, et al. SU-E-T-671: range-modulation effects of carbon ion beams in lung tissue. Med Phys. 2015;42(6):3491.
29. Baumann K-S, Witt W, Weber U, et al. An efficient method to predict and include Bragg curve degradation due to lung-equivalent materials in Monte Carlo codes by applying a density modulation. Phys Med Biol. 2017, 62: 3997–4016.
30. Espana S, Paganetti H. Uncertainties in planned dose due to the limited voxel size of the planning CT when treating lung tumors with proton therapy. Phys Med Biol. 2011;56(13):3843.
31. Flatten V, Baumann K-S, Weber U, et al. Quantification of the dependencies of the Bragg peak degradation due to lung tissue in proton therapy on a CT-based lung tumor phantom. Phys Med Biol. 2019;64:155005.
32. Hata M, Tokuuye K, Kagei K, et al. Hypofractionated high-dose proton beam therapy for stage I non-small-cell lung cancer: preliminary results of a phase I/II clinical study. Int J Radiat Oncol Biol Phys. 2007;68(3):786–93.
33. Bush DA, Slater JD, Shin BB, et al. Hypofractionated proton beam radiotherapy for stage I lung cancer. Chest. 2004;126(4):1198–203.
34. Chen J, Lu JJ, Ma N, et al. Early stage non-small cell lung cancer treated with pencil beam scanning particle therapy: retrospective analysis of early results on safety and efficacy. Radiat Oncol (London, England). 2019;14(1):16.

35. Góra J, Stock M, Lütgendorf-Caucig C, et al. Is there an advantage in designing adapted, patient-specific PTV margins in intensity modulated proton beam therapy for prostate cancer? Int J Radiat Oncol Biol Phys. 2013;85(3):881–8.
36. Park PC, Zhu XR, Lee AK, et al. A beam-specific planning target volume (PTV) design for proton therapy to account for setup and range uncertainties. Int J Radiat Oncol Biol Phys. 2012;82(2):e329–36.
37. Perl J, Shin J, Schuemann J, et al. TOPAS: an innovative proton Monte Carlo platform for research and clinical applications. Med Phys. 2012;39(11):6818–37.
38. Agostinelli S, et al. Geant4 - a simulation toolkit. Nucl Instrum Methods Phys Res A. 2003;506:250–303.
39. Taylor PA, Kry SF, Followill DS. Pencil beam algorithms are unsuitable for proton dose calculations in lung. Int J Radiat Oncol Biol Phys. 2017;99(3):750–6.
40. Witt M. Modulationseffekte von Kohlenstoffionen bei der Bestrahlung von Lungen, master thesis, University of Applied Sciences, Giessen, Germany. URL: https://www.thm.de/lse/images/user/KZink-105/Abschlussarbeiten/Masterarbeit_Matthias_Witt_2014.pdf (last called: 11/09/2019).
41. International Commission on Radiation Units and Measurements (ICRU). ICRU report volume 50: prescribing, recording, and reporting photon beam therapy. 1993.
42. International Commission on Radiation Units and Measurements (ICRU). ICRU report volume 62: prescribing, recording and reporting photon beam therapy (supplement to ICRU report 50). 1999.
43. Paganetti H, Blakely E, Carabe-Fernandez A, et al. Report of the AAPM TG-256 on the relative biological effectiveness of proton beams in radiation therapy. Med Phys. 2019;46(3):e53–78.

Publisher's Note

IOP Publishing Phys. Med. Biol. 63 (2018) 115013 (10pp) https://doi.org/10.1088/1361-6560/aac30e

Physics in Medicine & Biology

IPEM Institute of Physics and Engineering in Medicine

RECEIVED
9 February 2018

REVISED
19 April 2018

ACCEPTED FOR PUBLICATION
8 May 2018

PUBLISHED
7 June 2018

PAPER

TOPAS/Geant4 configuration for ionization chamber calculations in proton beams

Jörg Wulff[1], Kilian-Simon Baumann[2,3], Nico Verbeek[1], Christian Bäumer[1], Beate Timmermann[1,5,6] and Klemens Zink[2,3,4]

[1] Westdeutsches Protonentherapiezentrum Essen, Essen, Germany
[2] Institut für Medizinische Physik und Strahlenschutz, Technische Hochschule Mittelhessen, Gießen, Germany
[3] Klinik für Strahlentherapie und Radioonkologie, Universitätsklinikum Gießen, Marburg, Germany
[4] Frankfurt Institute for Advanced Studies (FIAS), Frankfurt, Germany
[5] Clinic for Particle Therapy, University Hospital Essen, West German Cancer Center (WTZ), Essen, Germany
[6] German Cancer Consortium (DKTK), Heidelberg, Germany

E-mail: joerg.wulff@uk-essen.de

Keywords: Monte Carlo simulations, proton dosimetry, ionization chambers

Abstract

Monte Carlo (MC) calculations are a fundamental tool for the investigation of ionization chambers (ICs) in radiation fields, and for calculations in the scope of IC reference dosimetry. Geant4, as used for the toolkit TOPAS, is a major general purpose code, generally suitable for investigating ICs in primary proton beams. To provide reliable results, the impact of parameter settings and the limitations of the underlying condensed history (CH) algorithm need to be known.

A Fano cavity test was implemented in Geant4 (10.03.p1) for protons, based on the existing version for electrons distributed with the Geant4 release. This self-consistent test allows the calculation to be compared with the expected result for the typical IC-like geometry of an air-filled cavity surrounded by a higher density material. Various user-selectable parameters of the CH implementation in the *EMStandardOpt4* physics-list were tested for incident proton energies between 30 and 250 MeV. Using TOPAS (3.1.p1) the influence of production cuts was investigated for bare air-cavities in water, irradiated by primary protons. Detailed IC geometries for an NACP-02 plane-parallel chamber and an NE2571 Farmer-chamber were created. The overall factor f_Q as a ratio between the dose-to-water and dose to the sensitive air-volume was calculated for incident proton energies between 70 and 250 MeV.

The Fano test demonstrated the *EMStandardOpt4* physics-list with the WentzelIV multiple scattering model as appropriate for IC calculations. If protons start perpendicular to the air cavity, no further step-size limitations are required to pass the test within 0.1%. For an isotropic source, limitations of the maximum step length within the air cavity and its surrounding as well as a limitation of the maximum fractional energy loss per step were required to pass within 0.2%. A production cut of $\leqslant 5$ μm or $\sim$15 keV for all particles yielded a constant result for f_Q of bare air-filled cavities. The overall factor f_Q for the detailed NACP-02 and NE2571 chamber models calculated with TOPAS agreed with the values of Gomà *et al* (2016 *Phys. Med. Biol.* **61** 2389) within statistical uncertainties (1σ) of $<$0.3% for almost all energies with a maximum deviation of 0.6% at 250 MeV for the NE2571. The selection of hadronic scattering models (*QGSP_BIC* versus *QGSP_BERT*) in TOPAS impacted the results at the highest energies by 0.3% $\pm$ 0.1%.

Based on the Fano cavity test, the Geant4/TOPAS Monte Carlo code, in its investigated version, can provide reliable results for IC calculations. Agreement with the detailed IC models and the published values of Gomà *et al* can be achieved when production cuts are reduced from the TOPAS default values. The calculations confirm the reported agreement of Gomà *et al* for k_{Q,Q_0} with IAEA-TRS398 values within the given uncertainties. An additional uncertainty for the MC-calculated k_{Q,Q_0} of $\sim$0.3% by hadronic interaction models should be considered.

1. Introduction

At the time of writing, 64 proton therapy facilities are in clinical operation and a further 40 are under construction[5]. In order to guarantee successful treatment and to make the clinical outcomes of these centers comparable, the absorbed dose in the target needs to be known precisely. Although some centers employ Faraday-cup-based dosimetry as a method for reference dosimetry (Palmans and Vatnitsky 2015), and a portable calorimeter is even being envisioned for use in the UK (Green *et al* 2017), the most common procedure to relate the output of the proton treatment machine to the absorbed dose is the use of air-filled ionization chambers in water. As ionization chambers are typically calibrated in ^{60}Co beams, the proton beam-quality at the user end needs to be corrected for. This step takes into account the different stopping-power ratios between water and air $s_{w,\mathrm{air}}$ and the differing mean energy to create an ion pair in air, W/e. Further, specific ionization chamber perturbation factors p_Q for different proton beam qualities Q need to be included in this overall correction. Currently, only the IAEA TRS398 code of practice (Andreo *et al* 2001) and ICRU78 (International Commission on Radiation Units and Measurements 2007) contain tabulated data for the beam-quality correction factor k_{Q,Q_0} for commonly used ionization chambers, while the latter standard directly uses the values of TRS398. The k_{Q,Q_0} values in TRS398 assume a $p_Q = 1$ for protons. There is good evidence that p_Q stays nearly constant for the range of proton treatment energies and can be considered as unity within 1% (Palmans and Vatnitsky 2015). Nevertheless, it can be expected that Monte Carlo (MC)-based k_{Q,Q_0} factors with detailed ionization chamber calculations will update and extend the tabulations, most likely with lower uncertainties. This is one of the goals of the RTNORM-Project[6] organized by EURAMET, aiming to update the IAEA TRS398 k_{Q,Q_0} values.

Recently, Gomà *et al* (2016) used the PENELOPE-based code PENH (Salvat 2013) in combination with the GAMOS toolkit (Arce *et al* 2014) to calculate k_{Q,Q_0} factors for a variety of ionization chambers. They showed an agreement with the TRS398 values within respective uncertainties of 2.3% or better. Sorriaux *et al* (2017) performed Geant4 calculations to investigate how the broad-beam conditions requested by TRS398 impact the k_{Q,Q_0} values in scanned beams or double-scattering beams.

The MC calculation of the ionization chamber response is known to be demanding for the condensed history (CH) implementations of charged particles, as the high-density gradient between the surrounding material and air in the cavity can cause significant artifacts. The so-called Fano cavity test can be used to test the accuracy of the MC code's CH implementation for various code-specific settings in a self-consistent way. Different varieties of this test exist, and they all aim to create a situation in which the Fano-theorem holds (Andreo *et al* 2017) and the calculation result is known *a priori*, normalized to the used cross-sections. The deemed pass-rate is typically set to ∼0.1%, to consider a code 'artifact-free'.

The EGSnrc (Kawrakow 2000, Kawrakow *et al* 2017) and PENELOPE (Sempau and Andreo 2006, Salvat *et al* 2014) codes have been demonstrated to calculate the ionization chamber for photon/electron response at the ∼0.1% level. The electron transport of Geant4 (Agnostelli *et al* 2003) was benchmarked by a Fano cavity test in Elles *et al* (2008), showing an agreement of ∼1%. Subsequently, a Fano cavity test was part of the validation for each new release of Geant4, but the published results were strongly step-size dependent and up to a few percent (Ivanchenko *et al* 2011). More recently, O'Brien and Sawakuchi (2017) demonstrated that the electron Geant4 CH implementation, relying on the Goudsmit–Saunderson multiple Coulomb scattering (MCS) theory, leads to an agreement within 0.1%.

General purpose codes capable of simulating transport for charged particles other than electrons have not yet been benchmarked as thoroughly. Given the limited scattering of protons compared to electrons, the possible artifacts in the CH-transport can generally be expected to be smaller. Nevertheless, they need to be known for the meaningful reporting of results in this type of calculation. Sterpin *et al* (2014) presented a version of the Fano cavity test for protons, and demonstrated that the Urban model for multiple scattering (Geant4Collaboration 2016) in the CH approach is dependent on various step-size limitations. They did not, however, come to a conclusion on the optimum settings for Geant4. Lourenco *et al* (2017) implemented a Fano cavity test for FLUKA with protons and showed that the test is passed at the 0.1% level if the maximum step-size in the FLUKA CH algorithm is restricted.

The TOPAS MC code (Perl *et al* 2012) is becoming a valuable tool for various problems in proton therapy due to its flexible and versatile parameter system. TOPAS is built upon Geant4 and hence uses the same physics models, processes and interaction cross-sections. In the present study, we used the TOPAS system version 3.1.p1 based on Geant4 10.03.p1 to calculate the factor f_Q following (Sempau and Andreo 2006) as

$$f_Q = D_w/D_{\mathrm{gas}} \tag{1}$$

[5] https://ptcog.ch
[6] http://rtnorm.eu

with D_w being the dose-to-water in a small reference volume at the reference depth and D_{gas} as the dose to the sensitive air-volume of an ionization chamber model. We used models of the cylindrical NE2571 and the plane-parallel NACP-02 ionization chamber in proton beams at different initial energies. Note, the quantity f_Q is the proton specific part of a MC-calculated beam-quality correction factor (Andreo *et al* 2013)

$$k_{Q,Q0} = \frac{f_Q}{f_{Q_0}} \frac{W_{\text{air},Q}}{W_{\text{air},Q_0}} \tag{2}$$

with W_{air} being the mean energy needed to create an ion pair in air for the beam-qualities Q and Q_0. Following this approach, the quantity f_Q can also be understood as

$$f_Q = p_Q \cdot S_{w,\text{air}} \tag{3}$$

in proton beams.

Beforehand, by applying a Fano cavity test, the current CH implementation in TOPAS/Geant4 was investigated, and settings leading to reliable calculation results were defined.

It is supposed that f_{Q_0}, i.e. equation (1) in a ^{60}Co field, has been explored sufficiently in the past in the context of the $k_{Q,Q0}$-factors for primary photon and electron beams (Sempau *et al* 2004, Zink and Wulff 2008, Wulff *et al* 2008a, Muir and Rogers 2010, Muir *et al* 2012, Zink and Wulff 2012, Erazo and Lallena 2013), and is thus not covered in this work.

2. Methods

For all calculations Geant4 (Agnostelli *et al* 2003) version 10.03.p1 and TOPAS (Perl *et al* 2012) version 3.1.p1 have been used. Details of the geometries, sources and transport parameters are given in the subsequent sections.

2.1. Proton transport in Geant4

The Geant4 code groups electromagnetic (EM) interactions of the charged particles in the condensed history approach. The latter is implemented following a *mixed* algorithm, which simulates the discrete collisions with energy loss above a user-defined threshold one by one and groups the angular deflection of all soft collisions at the end of a given step employing the appropriate MCS theory (Geant4Collaboration 2016). As a real trajectory is not a straight line, step length corrections and lateral displacements are considered at the end of the step, where a mean scattering angle is applied.

The multiple scattering in the artificial CH step is calculated according to the appropriate MCS theory. Geant4 offers different models, and depending on the version and different default physics-lists, defines the employed models and their parameters. The default physics-list for electromagnetic interactions used in TOPAS version 3.0.p1 is *EMStandardOpt4*, which makes use of the WentzelVI model (Ivanchenko *et al* 2010). Makarova *et al* (2017) compared the MCS models for protons in Geant4 with the Molière/Fano/Hanson theory and showed better agreement in the proton-therapy energy range for the WentzelVI model than the Urban model, which is used in various other physics-lists of Geant4. More recently, Fuchs *et al* (2017) compared the Geant4 models for the proton MCS against measurements of Gottschalk *et al* (1993). They concluded on the satisfactory agreement of the characteristic MCS angle with experiments when using the WentzelVI model. This model is based on the Wentzel MCS scattering function for small scattering angles below 0.2 radian, while larger angles are calculated using the single Coulomb scattering model (Ivanchenko *et al* 2010, Allison *et al* 2016).

The length of a CH-step is limited by tracking limits, such as geometric boundaries and physics-related parameters, which control the maximum fractional energy loss in a single step (*dRoverR*), for example. Further competing step limitations are combined in the *G4MscStepLimitType*, which provides a conservative reduction based on particle ranges and geometrical considerations (Ivanchenko *et al* 2010, Geant4Collaboration 2016). As part of this, the *RangeFactor* is a multiplier to the particle range with a value of less than unity.

As particles lose energy, their CH step length gradually decreases until it becomes smaller than the *finalRange*, below which the particle is ranged out in a single straight step. In the vicinity of geometrical boundaries, the MCS is disabled and particles are transported via single scattering in a region controlled by the *skin* parameter as a multiplier for the mean free path length of elastic scattering (Geant4Collaboration 2016).

The simulation of elastic and non-elastic nuclear interactions is sampled discretely and leads to interceptions of the continuous CH transport. Another indirect step limitation is the simulation of hard or discrete interactions in the ionization process. When the energy transfer between subsequent CH steps exceeds a user-defined limit, the CH process is discontinued and a discrete scattering event occurs resulting in a secondary particle. Generally, the more limitations are applied to the CH, the less the results are susceptible to artifacts, but the longer the simulation times become. This logic applies to all the charged particles in Geant4.

The parameter controlling the production of secondaries is given in a unit of range in Geant4. The rationale for using a range instead of energy for the production thresholds is the theoretically more precise location for the

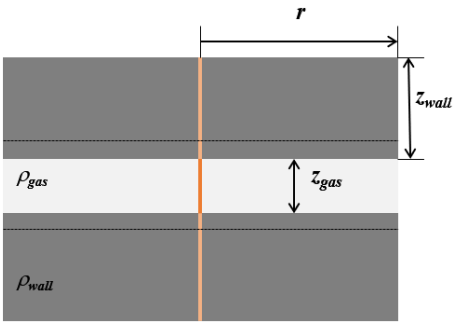

Figure 1. Slab-geometry for the Fano test with a line-source of primary protons (central line). The broken horizontal lines indicate an extra region in the wall for reducing the step size. For details see text.

energy release (Geant4Collaboration 2016). The default values for range cuts in TOPAS version 3.0.p1 are set to 0.05 mm. For secondary delta electrons, which carry a non-negligible amount of energy, this relates to an energy of approximately 54 keV if released in water and 2 keV in air. In the case of an ionization chamber-like geometry with a large density change between the wall and cavity, this situation possibly leads to a fluence artifact. Reducing the production cut generally increases the simulation time, hence a balance between accuracy and efficiency needs to be found.

2.2. Investigation of production cuts

The impact of range-cuts was investigated by calculating the factor f_Q within TOPAS using its default settings.

A set of single simulations with a bare air-filled cylindrical (radius = 3 mm/length = 20 mm) and plane parallel (radius = 5 mm/height = 2.5 mm) cavity placed at 2 cm depth in water was performed, testing different range cuts between 0.065 and 43.2 μm, which correspond to 1 and 50 keV for electrons in water. The cut was applied to photons, electrons/positrons and protons within the cavity and a 5 mm wide region surrounding it. Additionally, the dose to water was calculated in a small reference volume (radius = 5 mm/height = 0.25 mm) using the same approach. The geometry was irradiated by a square field of 10 × 10 cm^2 with 150 MeV monoenergetic protons. The dose to water D_w and dose to the sensitive air-volume D_{gas} were scored with the *DoseToMedium*-scorer, and the factor f_Q was calculated afterwards.

2.3. A Fano cavity test for protons in Geant4

The release of Geant4 (10.03p1) contains an implementation of the efficient Fano cavity test as introduced by Sempau and Andreo (2006). The basic idea is to calculate the dose deposited in an ionization chamber-like, plane-parallel geometry irradiated with a perpendicular 1D, mono-energetic line source of energy E_0. By choosing a radius r of the chamber that is larger than the maximum range of charged particles, the reciprocity theorem holds, i.e. the geometry is identical to a plane-parallel chamber being irradiated by a laterally extended source. The geometry effectively consists of three slabs, mimicking a cavity of thickness z_{gas} surrounded by walls with thickness z_{wall} that are larger than the maximum range of the initial protons (see figure 1). The source density is sampled according to the local mass-density in the wall with ρ_{wall} and the gas-filled cavity ρ_{gas}, and, as long as the density effect is the same throughout the geometry, the result is irradiation under the conditions of charged particle equilibrium. If no interactions then occur that lead to uncharged, long-range secondary particles, the quantity Q can be defined as (Sempau and Andreo 2006):

$$Q = \frac{\Delta E}{N \cdot E_0} \left(1 + \frac{2\rho_{\text{wall}} z_{\text{wall}}}{\rho_{\text{gas}} z_{\text{gas}}}\right) \tag{4}$$

for ΔE as energy deposited with N simulated particles. Any deviation of Q from unity violates the Fano theorem and indicates an artifact in the condensed history implementation.

The existing implementation of the `fanoCavity2` code was used and a few modifications were applied. The density effect correction was disabled by a modified version of the *G4hBetheBlochModel* class. Besides the line source in the original version, which keeps the direction of initial particles perpendicular to the slab, an option for sampling protons along the line with uniform distribution of directions over 4π was added.

The implementation of the Fano cavity test only considers EM interactions by setting the cut-offs for secondary particle production to infinity. This effectively disables the generation of any secondary particle. At the same

time, this can be considered as a conservative approximation, leading to rather large steps as range cuts of a few mm are applied in a normal calculation.

Various user-accessible transport parameters (see section 2.1) were altered to study the sensitivity of the results to different step-limitations. *dRoverR* was reduced from its default of 0.1 down to 0.005. The *MscMuHadRangeFactor* was varied from the default of 0.2 in steps down to 0.01, the *skin* parameter was increased from the default of 1 to 3. Most calculations were performed with the *fUseDistanceToBoundary* step-limit type for hadrons, but we also compared them to the default *fUseMinimal*. Additionally, the maximum deflection angle in the WentzelVI model above which a single scattering is performed was changed from the default value 0.2–0.05 radian. Furthermore, an optional fixed step limitation in the cavity and the wall was applied in some of the calculations, by defining an extra region with a 1 mm thickness around the cavity.

The remaining transport parameters for the Fano cavity test were based on the *EMStandardOpt4* physics-list of version Geant4 10.03.p1. The factor Q in equation (4) was calculated for initial energies between 30 and 250 MeV for either water or carbon as a material. In both cases, the mass-density of the cavity was reduced by a factor 1000 compared to the surrounding.

2.4. Ionization chamber calculations in TOPAS

Ionization chamber models for the NE2571 thimble type and NACP-02 plane-parallel type ionization chambers were created in TOPAS. Both have been used in many MC-based studies in the past and a large set of direct k_Q measurements in photons and electrons exist for them. The geometry details were taken from Andreo *et al* (2013) for the NE2571 and from the work of Zink and Wulff (2012) for the NACP-02. The latter model was adjusted slightly to match exactly the mass-densities and thicknesses as used in Gomà *et al* (2016).

The mean excitation energies of carbon, water and air were used exactly as in the work of Gomà *et al*, with $I_{\text{air}} = 85.7$ eV, $I_{\text{w}} = 78$ eV and $I_{\text{Carbon}} = 81.1$ eV to allow for a direct comparison. This matches the recommendations of ICRU (International Commission on Radiation Units and Measurements 2014), with a slight discrepancy of 0.1 eV for carbon.

The ionization chamber models were placed at 2 cm depth in a water-phantom with a 5 cm thickness and irradiated by mono-energetic, parallel proton beams at 70, 100, 150, 200 and 250 MeV with a field size of 10×10 cm^2. The dose to water D_w was calculated in a disc of 250 μm height and a radius of 1 cm, placed with its geometric center at a depth of 2 cm.

The production cuts for photons, electrons/positrons and protons were changed from the default of 50 μm to 1 μm (see section 3.1 below) in the chamber geometry and water volume, respectively, plus an additional small region around it.

Following the findings of O'Brien and Sawakuchi (2017), we selected the Goudsmit–Saunderson model for electrons in all simulations as an addition to the used *EMStandardOpt4* physics-list. Note, this is also the change in the *EMStandardOpt4* list of the recently published version 10.4 of Geant4. Based on the findings of the Fano cavity test, one calculation for the NACP-02 chamber was also tested with a limitation of $dRoverR = 0.05$ and a maximum step-size of 1 mm within the ionization chamber geometry and a 1 mm surrounding layer of water. Further, the effect of changing the step-limit type to *fUseDistanceToBoundary* was tested.

Two different hadronic interaction models were compared. Besides the TOPAS default binary cascade (*QGSP_BIC*) of Geant4, the Bertini cascade (*QGSP_BERT*) was tested. All other physics options were left at the TOPAS 3.1.p1 defaults, i.e. setting *EMRangeMin* = 100 eV, *EMRangeMax* = 500 MeV and including the *G4DecayPhysics*, *G4IonBinaryCascadePhysics*, *G4HadronElasticPhysicsHP* and *G4StoppingPhysics* classes.

3. Results and discussion

3.1. Impact of secondary particle production thresholds

In figure 2 the impact of the different production cuts on the calculated f_Q values is shown. The cut was applied to photons, electrons/positrons and protons. Secondary electrons have a range that is roughly one order of magnitude longer compared to protons. Hence, the lower production cut mainly affects the fluence and thus dose contribution by electrons. There is a clear variation, and a convergence is reached for the production cuts $\leqslant 5$ μm. This corresponds to a threshold for secondary electrons below $\sim$15 keV. The change in calculation time between the 50 μm and 1 μm was a factor of $\sim$1.3.

One can discuss the required threshold from a cavity theory point of view. In the energy regime of proton therapy, the ionization chamber is expected to behave under Bragg–Gray or Spencer–Attix conditions (International Commission on Radiation Units and Measurements 2007). This requires a constant fluence of secondary δ-electrons, and when using a cut-off in terms of range, a fluence-artifact can result between the interface of two regions with different media. One would need to create region-based cut-off values to avoid such a fluence artifact; however, this was considered much more complicated than selecting a sufficiently small value for the complete geometry. Additionally, one could select different production cuts for different secondary particles—

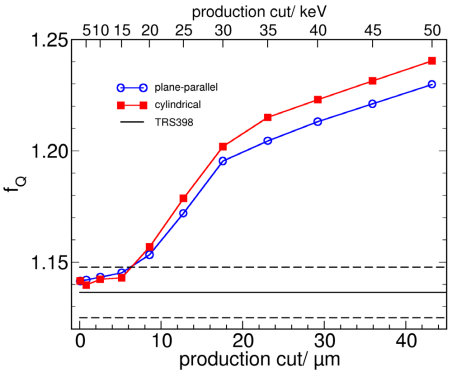

Figure 2. The calculated f_Q at 150 MeV for bare air-cavities in water as a function of the production threshold for secondary electrons in TOPAS. The 1σ statistical uncertainty is smaller than the symbol size. The lines are a guide to the eyes. The abscissa is given in units of keV and μm. The horizontal line corresponds to the TRS398 value for $S_{w,air}$ at 150 MeV with a respective uncertainty of 1% (broken lines).

but as discussed above, the main impact of reduced cuts can be expected for δ-electrons. Different values for the different particle types were not investigated, but given the fact that at the price of a longer calculation time there is no disadvantage, we applied the cut to all protons and electrons/positrons without investigating different cuts by particle type. Furthermore, a technical limitation of the investigated TOPAS release prohibited the choice based on particle type.

The optimal results for production cuts of $\leqslant$20 keV, at least for electrons, is somehow expected. The dependence of $S_{w,air}$ values was demonstrated by Medin and Andreo (1997) for protons and later by Sànchez-Parcerisa *et al* (2013) for carbon ions, and the cut-off energy Δ in the evaluation of the Spencer–Attix stopping power ratios is typically set to 10 keV. This energy corresponds to the mean chord length of electrons passing a typical ionization chamber cavity (Wulff *et al* 2008b, Andreo *et al* 2017). If no fluence perturbation existed, f_Q calculated here should simply correspond to the water-to-air stopping power ratios in the proton beams. An agreement with the TRS398 $S_{w,air}$ values, which are based on the fluence calculations with the PETRA MC code (Medin and Andreo 1997), is reached for secondary electron production cuts at about 15 keV, as shown in figure 2.

In their study on ionization chamber correction factors in proton beams, Sorriaux *et al* (2017) used a production threshold of 5 μm for protons, electrons/positrons and 1 mm for all other particles. According to the results shown here (figure 2), this is an appropriate choice, although the authors did not give a rationale for the setting.

Generally, the default of TOPAS with 50 μm seems too large for application in ionization-chamber-related calculations. In the subsequent calculations, the production cuts were set to 1 μm for all particles.

3.2. Fano cavity test

When using a line source with protons starting perpendicular to the cavity, all calculations for water and carbon agreed with the expected result at 0.1% level within a 1σ statistical uncertainty of $\leqslant$0.05%. This means the implementation of CH within the WentzelIV model, as part of the *EMStandardOpt4* physics-list, is sufficiently accurate for this situation. This result is different from the findings of Sterpin *et al* (2014), who also used a parallel/perpendicular proton beam incident to a plane-parallel chamber. In their test, restrictions of maximum step-sizes to 10^{-2} mm for Geant4 (version 9.5.p02) with the Urban MCS model were necessary to pass the Fano test, although in a different implementation.

In contrast to the results when particles start perpendicular to the cavity, the source which samples directions isotropically along the line led to larger deviations, as shown in figure 3. From all tested transport parameters (see section 2.3), only the reduction of fractional energy loss per step *dRoverR* to a value of 0.005 yielded an agreement within 0.1%. This, however, led to an increase of a factor twelve in the calculation time and was deemed rather impractical. Note, the calculation times at 250 MeV using default transport parameters was $\sim$30 min on a single Intel Xeon 2.3 GHz CPU.

The reduction of step-size to $\leqslant$1 mm in the cavity and in a region 1 mm around it allowed for an agreement within 0.5% at 250 MeV. Note, the result stayed constant even for step-size limitations of 10^{-3} mm, even though one could expect an improvement in the result with shorter steps. However, in our implementation, the step-size was only limited in the cavity and its direct surrounding within 1 mm. A combination of step-size reduction to

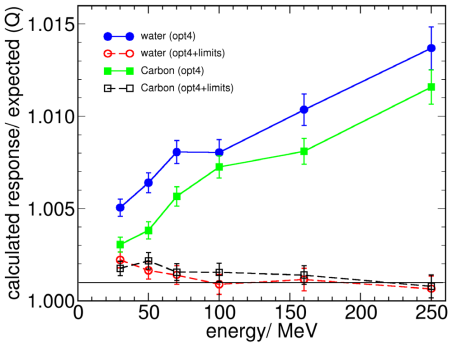

Figure 3. Results for the Fano cavity test with an *isotropic* source of protons in Geant4 10.03.p1 for water (circles) and carbon (squares). The full symbols show results using the *EMStandardOpt4*(opt4) physics-list. The open symbols represent results for *dRoverR* = 0.05 and a step-size limit of 1 mm in the cavity and surrounding. The lines are a guide to the eyes. The horizontal line indicates a deviation of 0.1% from the expected result Q (see equation (4)).

1 mm and *dRoverR* = 0.05 was identified as a reasonable compromise, allowing for an agreement at the 0.2% level (see figure 3). As expected, this gain in accuracy came at the expense of an increased calculation time with a factor 1.3–4 between 30 and 250 MeV.

One needs to view the results within the conditions of the test implementation here. With the cut-offs for secondary particle production set to infinity, the primary protons have larger steps, as in a typical calculation. As outlined in the previous section for ionization chamber calculations, we identified the need to limit the production cuts to rather small values, which effectively limits the step sizes. Furthermore, in a realistic ionization chamber simulation, more complex geometries with layers of different materials exist, which impose geometric limitations. The calculation of the expected response for an isotropic source is considered an extreme case, as some protons start directly at the cavity boundary with directions parallel to it, which typically does not occur in normal situations.

3.3. Ionization chamber calculations TOPAS

Figures 4 and 5 show the calculated f_Q values for the NACP-02 and NE2571 ionization chamber models. The values are given as a function of incident energy and residual range R_{res}, respectively, together with the values from Gomà *et al* (2016) and corresponding values from the TRS398 protocol. The latter was deduced from the tabulated k_{Q,Q_0} values, $S_{w,air}$ for ^{60}Co, the fit function for $S_{w,air}$ in protons and W_{air}/e for protons and electrons, as found in TRS398 together with the respective uncertainty estimates for each value. The overall calculation time for a single data point was the equivalent of up to 330 days on a single 2.4 GHz-CPU, and was distributed over 800 CPUs of a cluster.

Except for the highest energy of 250 MeV, the f_Q values for the NACP-02 model agree with the published values of Gomà *et al* within the statistical uncertainties (figure 4). A slightly better agreement with the values is achieved for the calculations using the *QGSP_BERT* model. This is surprising as Gomà *et al* used the *QGSP_BIC* model for the simulation outside the ionization chamber model. The TOPAS calculations for the NE2571 show, however, a slightly better agreement with the Gomà *et al* values when the *QGSP_BIC* nuclear interaction models are used (figure 5). The remaining maximum deviations are 0.5% and 0.6% for the NACP-02 and NE2571 respectively at the highest energies, which is just slightly out of the combined two standard statistical uncertainties (<0.3%) for the NE2571. This is a noteworthy level of agreement considering the completely independent geometry and physics implementations between the PENH/PENELOPE and Geant4 MC codes.

In general, despite the good agreement of the f_Q values with Gomà *et al*, the discrepancy in our results for the two non-elastic scattering models can be interpreted as a systematic uncertainty in this type of calculation. It is not clear *per se* which of the two hadronic models yields more realistic results, even though the impact is small with the maximum 0.3% ± 0.1%. Jarlskog and Paganetti (2008) demonstrated the best agreement between multilayer Faraday cup measurements and Geant4 calculations when selecting the binary cascade. On the other hand, Patel *et al* (2017) investigated the physics-list options for accurate LET calculations in an experimental setup. They came to a conclusion on the best results for the FTFP_BERT physics-list. As long as no conclusion can be drawn on which model is the more accurate, one can at least add a ∼0.3% contribution of type B uncertainties to the k_{Q,Q_0} results of Gomà *et al*.

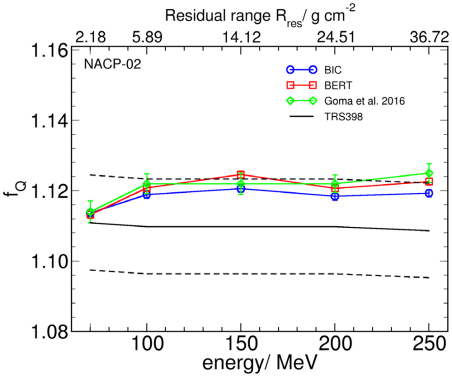

Figure 4. The calculated f_Q as a function of energy and residual range for the NACP-02 plane-parallel ionization chamber, i.e. the ratio between the dose to a thin disc of water and the sensitive air volume of the ionization chamber model at 2 cm depth. Results are shown for calculations in TOPAS3.1.p1/Geant4 10.03.p1 using the binary cascade nuclear interaction model (BIC) and Bertini cascade (BERT). Values from Gomà *et al* are directly taken from their publication. The full line represents the values taken from TRS398 with the uncertainty given therein (broken line).

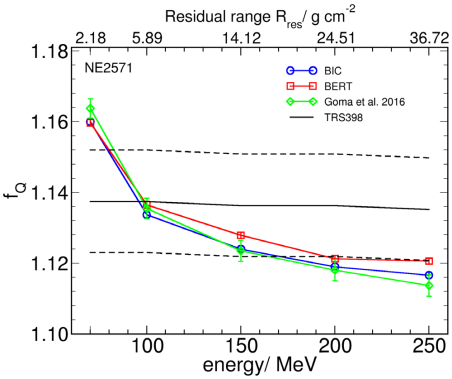

Figure 5. TOPAS calculated f_Q for the NE2571 cylindrical ionization chamber at 2 cm depth in water. The results are shown for calculations using the binary cascade nuclear interaction model (BIC) and Bertini cascade (BERT) of TOPAS3.1.p1/Geant4 10.03.p1. Values from Gomà *et al* are taken from the publication. The full line represents the values taken from TRS398 with the uncertainty given therein (broken line).

The impact of reducing *dRoverR* and the introduction of an additional step limitation (see section 3.2) resulted in no significant change of the results outside the statistical uncertainty. As discussed, the already existing step-limitations, and the fact that the protons are entering the cavity predominantly perpendicularly, obviously does not lead to observable artifacts in this type of calculation.

The agreement with the TRS398 protocol for the NACP-02 is just within the uncertainties given therein and shows only a small variation with energy, in accordance with an assumed unity p_Q in TRS398. The agreement for NE2571 is, however, less good, and f_Q varies by almost 3.5% over the considered energy range. The shape of the data-point distribution in figure 5 is presumably caused by the fact that the cylindrical ion chamber was placed with its center at 2 cm. At this depth, the lower energy beams already exhibit a gradient in the proximal rise of the proton depth-dose distribution that is large enough to show a gradient effect (Palmans 2006) and clearly leads to a deviation of $p_Q = 1$. This could, in principle, be compensated by placing the ionization chamber with its reference point at a larger depth. Interestingly, this is considered in the reference conditions of TR398 for heavy ion beams, while it is not the case for primary proton beams. At any rate, these results demonstrate the usefulness of MC calculations, if smaller uncertainties in the k_{Q,Q_0} values are aimed for.

4. Conclusion

Based on the Fano cavity test, the Geant4/TOPAS Monte Carlo code, in its investigated version, can provide reliable results of ion chamber response calculations in primary proton beams. When selecting appropriate production cuts, the f_Q values of Gomà *et al* (2016) for the NACP-02 and NE2571 chamber can be reproduced and thus confirmed with TOPAS calculations. Apart from a small additional systematic uncertainty in the work of Gomà *et al*, the present work supports their published k_{Q,Q_0} values. The shown agreement of our calculations with the TRS398 values needs to be emphasized. The values and corresponding estimated uncertainties can still be considered usable today, despite the fact that TRS398 was published 18 years ago, with the limited computational tools and measurements available at that time. Nevertheless, the RTNORM-Project will update these values with smaller uncertainties in the future.

The findings of the present work could help other researchers determine appropriate simulation parameters, such as the physics-list and production cut-off selection, when using TOPAS for ionization-chamber-related simulations in proton beams. The appropriate settings in Geant4/TOPAS when calculating k_{Q,Q_0} values in primary megavoltage photon and electron beams need to be determined in future studies.

Acknowledgments

We thank Carles Gomà (KU Leuven) for helpful discussions on his calculations. Lorenzo Brualla (Essen) is acknowledged for giving access to the CONTESSA cluster, which was used for some of the Fano cavity test calculations.

ORCID iDs

Jörg Wulff https://orcid.org/0000-0001-8260-3523
Nico Verbeek https://orcid.org/0000-0001-9166-6972

References

Agnostelli S *et al* 2003 Geant4—a simulation toolkit *Nucl. Instrum. Methods Phys. Res.* A **506** 250–303
Allison J *et al* 2016 Recent developments in Geant4 *Nucl. Instrum. Methods Phys. Res.* A **835** 186–225
Andreo P, Burns D, Nahum A, Seuntjens J and Attix F 2017 *Fundamentals of Ionizing Radiation Dosimetry* (New York: Wiley)
Andreo P, Burns D T, Hohlfeld K, Huq M, Kanai T, Laitano F, Smyth V and Vynckier S 2001 *TRS-398: Absorbed Dose Determination in External Beam Radiotherapy: An International Code of Practice for Dosimetry based on Standards of Absorbed Dose to Water* (International Atomic Energy Agency)
Andreo P, Wulff J, Burns D and Palmans H 2013 Consistency in reference radiotherapy dosimetry: resolution of an apparent conundrum when (60)Co is the reference quality for charged-particle and photon beams *Phys. Med. Biol.* **58** 6593–5621
Arce P *et al* 2014 GAMOS: a framework to do Geant4 simulations in different physics fields with an user-friendly interface *Nucl. Instrum. Methods Phys. Res.* A **735** 304–13
Elles S, Ivanchenko V, Maire M and Urban L 2008 Geant4 and Fano cavity test: where are we? *J. Phys.: Conf. Ser.* **102** 012009
Erazo F and Lallena A 2013 Calculation of beam quality correction factors for various thimble ionization chambers using the Monte Carlo code PENELOPE *Phys. Med.* **29** 163–70
Fuchs H, Vatnitsky S, Stock M, Georg D and Grevillot L 2017 Evaluation of GATE/Geant4 multiple Coulomb scattering algorithms for a 160 MeV proton beam *Nucl. Instrum. Methods Phys. Res.* B **410** 122–6
Geant4Collaboration 2016 GEANT4: Physics Reference Manual—Geant4 10.3 (9 December 2016) http://cern.ch/geant4/support/userdocuments.shtml
Gomà C, Andreo P and Sempau J 2016 Monte Carlo calculation of beam quality correction factors in proton beams using detailed simulation of ionization chambers *Phys. Med. Biol.* **61** 2389
Gottschalk B, Koehler A, Schneider R, Sisterson J and Wagner M 1993 Multiple Coulomb scattering of 160 MeV protons *Nucl. Instrum. Methods Phys. Res.* B **74** 467–90
Green S, Amos R, Van den Heuvel F, Kacperek A, MacKay R, Palmans H, D'Souza D and Thomas R 2017 EP-1467: IPEM Code of Practice for proton and ion beam dosimetry: update on work in progress *Radiother. Oncol.* **123** S783–4
International Commission on Radiation Units Measurements (ed) 2007 *Prescribing, Recording, and Reporting Proton-Beam Therapy* (*ICRU Report 78* vol 7) (Bethesda, MD: ICRU)
International Commission on Radiation Units Measurements (ed) 2014 *Key Data For Ionizing-Radiation Dosimetry* (*ICRU Report 90* vol 14) (Bethesda, MD: ICRU)
Ivanchenko V *et al* 2011 Recent improvements in Geant4 electromagnetic physics models and interfaces *Prog. Nucl. Sci. Technol.* **2** 898–903
Ivanchenko V N, Kadri O, Maire M and Urban L 2010 Geant4 models for simulation of multiple scattering *J. Phys.: Conf. Ser.* **219** 032045
Jarlskog C Z and Paganetti H 2008 Physics settings for using the Geant4 toolkit in proton therapy *IEEE Trans. Nucl. Sci.* **55** 1018–25
Kawrakow I 2000 Accurate condensed history Monte Carlo simulation of electron transport. II. Application to ion chamber response simulations *Med. Phys.* **27** 499–513
Kawrakow I, Mainegra-Hing E, Rogers D W O, Tessier F and Walters B R B 2017 *The EGSnrc Code System: Monte Carlo Simulation of Electron and Photon Transport* (*NRCC Report PIRS-701*) (National Research Council of Canada)
Lourenco A, Bouchard H, Galer S, Royle G and Palmans H 2017 OC-0064: a Fano test for proton beams and the influence of nuclear interactions on ionization chamber factors *Radiother. Oncol.* **123** S31–2

Makarova A, Gottschalk B and Sauerwein W 2017 Comparison of Geant4 multiple Coulomb scattering models with theory for radiotherapy protons *Phys. Med. Biol.* **62** 5959

Medin J and Andreo P 1997 Monte Carlo calculated stopping-power ratios, water/air, for clinical proton dosimetry (50–250 MeV) *Phys. Med. Biol.* **42** 89

Muir B R and Rogers D W O 2010 Monte Carlo calculations of kQ, the beam quality conversion factor *Med. Phys.* **37** 5939–50

Muir B R, McEwen M R and Rogers D W O 2012 Beam quality conversion factors for parallel-plate ionization chambers in MV photon beams *Med. Phys.* **39** 1618–31

O'Brien D and Sawakuchi G 2017 TU-D-205-4: evaluation of the electron condensed history algorithms in Geant4 for radiotherapy simulations *Med. Phys.* **44** 8

Palmans H 2006 Perturbation factors for cylindrical ionization chambers in proton beams. Part I: corrections for gradients *Phys. Med. Biol.* **51** 3483

Palmans H and Vatnitsky V 2015 Chapter: dosimetry and beam calibration *Principles, Practice of Proton Beam Therapy* (*Medical Physics Monograph* vol 37) (Madison, WI: Medical Physics) pp 317–51

Patel D *et al* 2017 Optimization of Monte Carlo particle transport parameters and validation of a novel high throughput experimental setup to measure the biological effects of particle beams *Med. Phys.* **44** 6061–73

Perl J, Shin J, Schümann J, Faddegon B and Paganetti H 2012 Topas: an innovative proton Monte Carlo platform for research and clinical applications *Med. Phys.* **39** 6818–37

Salvat F 2013 A generic algorithm for Monte Carlo simulation of proton transport *Nucl. Instrum. Methods Phys. Res.* B **316** 144–59

Salvat F, Fernandez-Varea J M and Sempau J 2014 *PENELOPE-2014: A Code Systen for Monte Carlo Simulation of Electron and Photon Transport* (Issy-les-Moulineaux: OECD Nuclear Energy Agency)

Sànchez-Parcerisa D, Gemmel A, Jäkel O, Rietzel E and Parodi K 2013 Influence of the delta ray production threshold on water-to-air stopping power ratio calculations for carbon ion beam radiotherapy *Phys. Med. Biol.* **58** 145

Sempau J and Andreo P 2006 Configuration of the electron transport algorithm of PENELOPE to simulate ion chambers *Phys. Med. Biol.* **51** 3533–48

Sempau J, Andreo P, Aldana J, Mazurier J and Salvat F 2004 Electron beam quality correction factors for plane-parallel ionization chambers: Monte Carlo calculations using the PENELOPE system *Phys. Med. Biol.* **49** 4427–44

Sorriaux J, Testa M, Paganetti H, Bertrand D, Lee J, Palmans H, Vynckier S and Sterpin E 2017 Consistency in quality correction factors for ionization chamber dosimetry in scanned proton beam therapy *Med. Phys.* **44** 4919–27

Sterpin E, Sorriaux J, Souris K, Vynckier S and Bouchard H 2014 A Fano cavity test for Monte Carlo proton transport algorithms *Med. Phys.* **41** 011706

Wulff J, Heverhagen J and Zink K 2008a Monte-Carlo-based perturbation and beam quality correction factors for thimble ionization chambers in high-energy photon beams *Phys. Med. Biol.* **53** 2823–36

Wulff J, Jany D and Zink K 2008b Quantitative determination of cutoff perturbation factor pdelta in the DIN 6800-2 (2008) by means of Monte Carlo simulations *Z. Med. Phys.* **18** 203–10

Zink K and Wulff J 2008 Monte Carlo calculations of beam quality correction factors kQ for electron dosimetry with a parallel-plate Roos chamber *Phys. Med. Biol.* **53** 1595–607

Zink K and Wulff J 2012 Beam quality corrections for parallel-plate ion chambers in electron reference dosimetry *Phys. Med. Biol.* **57** 1831

Comparison of PENH, FLUKA, and GEANT4/TOPAS for absorbed dose calculations in air cavities representing ionization chambers in high-energy photon and proton beams

Kilian-Simon Baumann[a)]
Department of Radiotherapy and Radiooncology, University Medical Center Giessen-Marburg, Marburg, Germany
Institute of Medical Physics and Radiation Protection, University of Applied Sciences, Giessen, Germany

Felix Horst
Institute of Medical Physics and Radiation Protection, University of Applied Sciences, Giessen, Germany
GSI Helmholtzzentrum für Schwerionenforschung, Darmstadt, Germany

Klemens Zink
Department of Radiotherapy and Radiooncology, University Medical Center Giessen-Marburg, Marburg, Germany
Institute of Medical Physics and Radiation Protection, University of Applied Sciences, Giessen, Germany
Frankfurt Institute for Advanced Studies (FIAS), Frankfurt, Germany

Carles Gomà
Department of Oncology, Laboratory of Experimental Radiotherapy, KU Leuven, Leuven, Belgium

(Received 3 December 2018; revised 1 July 2019; accepted for publication 16 July 2019; published 19 August 2019)

Purpose: The purpose of this work is to analyze whether the Monte Carlo codes PENH, FLUKA, and GEANT4/TOPAS are suitable to calculate absorbed doses and f_Q/f_{Q_0} ratios in therapeutic high-energy photon and proton beams.
Methods: We used PENH, FLUKA, GEANT4/TOPAS, and EGSNRC to calculate the absorbed dose to water in a reference water cavity and the absorbed dose to air in two air cavities representative of a plane-parallel and a cylindrical ionization chamber in a 1.25 MeV photon beam and a 150 MeV proton beam — EGSNRC was only used for the photon beam calculations. The physics and transport settings in each code were adjusted to simulate the particle transport as detailed as reasonably possible. From these absorbed doses, f_{Q_0} factors, f_Q factors, and f_Q/f_{Q_0} ratios (which are the basis of Monte Carlo calculated beam quality correction factors k_{Q,Q_0}) were calculated and compared between the codes. Additionally, we calculated the spectra of primary particles and secondary electrons in the reference water cavity, as well as the integrated depth–dose curve of 150 MeV protons in water.
Results: The absorbed doses agreed within 1.4% or better between the individual codes for both the photon and proton simulations. The f_{Q_0} and f_Q factors agreed within 0.5% or better for the individual codes for both beam qualities. The resulting f_Q/f_{Q_0} ratios for 150 MeV protons agreed within 0.7% or better. For the 1.25 MeV photon beam, the spectra of photons and secondary electrons agreed almost perfectly. For the 150 MeV proton simulation, we observed differences in the spectra of secondary protons whereas the spectra of primary protons and low-energy delta electrons also agreed almost perfectly. The first 2 mm of the entrance channel of the 150 MeV proton Bragg curve agreed almost perfectly while for greater depths, the differences in the integrated dose were up to 1.5%.
Conclusion: PENH, FLUKA, and GEANT4/TOPAS are capable of calculating beam quality correction factors in proton beams. The differences in the f_{Q_0} and f_Q factors between the codes are 0.5% at maximum. The differences in the f_Q/f_{Q_0} ratios are 0.7% at maximum. © *2019 The Authors. Medical Physics published by Wiley Periodicals, Inc. on behalf of American Association of Physicists in Medicine.* [https://doi.org/10.1002/mp.13737]

Key words: beam quality correction factors dosimetry high-energy photon and proton radiation Monte Carlo simulation radiation therapy

1. INTRODUCTION

Current national and international dosimetry protocols for the determination of absorbed dose in photon beams (e.g., AAPM TG-51[1] or IAEA TRS-398[2] or the DIN 6800-2[3]) as well as proton beams (e.g., IAEA TRS-398[2]) are based on standards of absorbed dose to water. The absorbed dose to water can be determined with air-filled ionization chambers. When using these chambers, the user needs to correct the chamber reading with the beam quality correction factor k_{Q,Q_0}. This correction factor accounts for the different response of the chamber in the calibration beam quality Q_0 and the clinical or user beam quality Q (e.g., MV photons or high-energy protons) and typically corrects the ionization chamber reading by a few percent. Ideally, these k_{Q,Q_0} factors should be determined directly using calorimetry for each

chamber model used and at exactly the radiation quality Q at which the chamber will be operated. Although performed in several studies,[4–8] the experimental determination of these k_{Q,Q_0} factors requires a high experimental effort and is not convenient for most laboratories. Furthermore, standard laboratories do not have access to all beam qualities Q — this holds especially for proton and carbon ion beams. Hence, the calculation of beam quality correction factors by means of Monte Carlo simulations is an efficient alternative.

At the time, the IAEA TRS-398 Code of Practice (CoP) is currently being updated. Within this framework, the RTNORM project[9] is supporting the IAEA working group with experimental as well as Monte Carlo calculated k_{Q,Q_0} factors for different ionization chambers and beam qualities such as photons and protons. Whereas the use of Monte Carlo codes for the determination of k_{Q,Q_0} factors in high-energy photon and electron beams has been extensively tested and is well established in the literature for the Monte Carlo codes EGSnrc and PENELOPE,[10–14] data for protons are scarce with only one study by Gomà et al.[15] where PENH was used to calculate k_{Q,Q_0} factors in clinical proton beams in agreement with experimental data within 1% or better. Furthermore, data for ions heavier than protons are nonexistent. Although PENH has been shown appropriate for the calculation of k_{Q,Q_0} factors in proton beams,[15] this code cannot transport ions heavier than protons. Hence, to provide more data for protons and especially heavier ions, the use of general purpose codes such as FLUKA and Geant4, primarily designed for high-energy physics applications, needs to be investigated for the use in ionization chamber calculations. A first study proved that TOPAS, a toolkit based on Geant4, may be used to calculate f_Q factors in proton beams.[16] On this basis, its usage for the determination of beam quality correction factors in clinical photon and especially proton beams shall be investigated in this work.

Hence, the aim of this work is to assess whether FLUKA and GEANT4/TOPAS are suitable to calculate k_{Q,Q_0} factors in clinical photon and proton beams. To do so, the f_{Q_0} and f_Q factors as well as the f_Q/f_{Q_0} ratios were calculated for simplified beam settings and simplified geometries representing ionization chambers at typical water depths. The f_Q/f_{Q_0} ratio is the basis of k_{Q,Q_0} factors and the only part that can be calculated with the Monte Carlo method. The residual part consists of the $W_{\mathrm{air},Q}/W_{\mathrm{air},Q_0}$ ratio that has to be determined experimentally (or can be taken from the literature[17]). Hence, if a Monte Carlo code is able to calculate f_Q/f_{Q_0} ratios, it can be used to determine k_{Q,Q_0} factors. We compared the results with the already established Monte Carlo codes EGSnrc and PENH. The comparison of the f_{Q_0} factors with the results from EGSnrc is necessary to verify if FLUKA and GEANT4/TOPAS can be used for photon calculations since EGSnrc is well established for high-energy photon calculations and benchmarked against experimental data.[18,19] The comparison of the f_Q factors and f_Q/f_{Q_0} ratios with the results from PENH is necessary to verify if FLUKA and GEANT4/TOPAS can be used for the calculation of f_Q/f_{Q_0} ratios and hence k_{Q,Q_0} factors in proton beams since PENH has been shown appropriate for the calculation of k_{Q,Q_0} factors in proton beams.[15] By choosing simplified beam settings and simplified geometries, we could ensure the use of the same geometry descriptions in each of the Monte Carlo codes used so that only the differences in the particle transport and the physics settings will have an impact on the absorbed dose predictions. The particle transport parameters and the lists of physics models used in each of these Monte Carlo codes were adjusted to simulate the transport of primary photons and protons as well as their secondary electrons at clinically relevant energies as detailed as reasonably possible.

2. MATERIALS AND METHODS

Simulations were performed with the Monte Carlo codes PENH, FLUKA, GEANT4/TOPAS, and EGSnrc. In the next subsection, the geometry and beam parameters are explained. In the following subsection, the calculated quantities are described. In the subsections thereafter, the particle transport for each of the Monte Carlo codes used is described. To report the Monte Carlo simulations, we followed the recommendations of the AAPM Research Committee Task Group 268.[20]

2.A. Geometries, materials, and source parameters

For each Monte Carlo code, the geometries as shown in Fig. 1 were used: A water cavity used as reference consisting of a disk with a diameter of 10 mm and a thickness in beam direction of 0.25 mm. The first air cavity was a disk with a diameter of 10 mm and a thickness in beam direction of 2.5 mm representing a plane-parallel chamber. The investigated volume was $\sim$0.2 cm^3, comparable to the Scanditronix NACP02 chamber with an active volume of 0.16 cm^3 or the PTW-34001 Roos chamber with an active volume of 0.35 cm^3.[21]

The second air cavity was a cylinder with a height of 20 mm and a diameter of 6 mm representing a cylindrical ionization chamber. The investigated volume was $\sim$0.6 cm^3, comparable to the Farmer chamber Exradin A12 with an active volume of 0.65 cm^3[22] or the NE2571 chamber with an active volume of 0.69 cm^3.[21]

These volumes were positioned in a water phantom of $20 \times 20 \times 15$ cm^3 for the irradiation with photons and $20 \times 20 \times 10$ cm^3 for protons. The center of each volume marked with an "**x**" in Fig. 1 was positioned in the center of the beam at a depth of 5 cm in the water phantom for the irradiation with photons and at a depth of 2 cm for protons.

Table I shows the elemental compositions of water and air used in the Monte Carlo simulations. For all elements, only the main isotopes were considered (e.g., no ^{17}O but only ^{16}O in water as well as air). Water had a density of 1.0 g/cm^3 and a mean ionization potential of $I_w = 78$ eV.[17,23] For air, the density was 1.20479 mg/cm^3 and the mean ionization potential was set to $I_{air} = 85.7$ eV.[17]

As a ^{60}Co source, we used a monoenergetic 1.25 MeV photon beam[14] applied in an homogeneous field of 10×10 cm^2. The beam had no divergence and the space

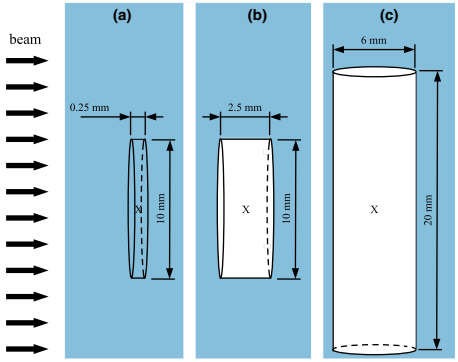

FIG. 1. Geometries used for the simulations: (a) reference volume: a water-filled plane-parallel volume with a diameter of 10 mm and a height of 0.25 mm, (b) air-filled plane-parallel volume with a diameter of 10 mm and a height of 2.5 mm and (c) air-filled cylindrical volume with a height of 20 mm and a diameter of 6 mm. The direction of the broad beam is marked with black arrows on the left. [Color figure can be viewed at wileyonlinelibrary.com]

between the source and the water phantom was filled with vacuum.

For the irradiation with protons, the same settings were used. The energy of the protons was 150 MeV (also monoenergetic). The simulations for protons were not performed with the EGSNRC code since it can only transport photons, electrons, and positrons.

Concerning the beam quality and depths of the volumes, the setup corresponds to the recommendations of the TRS-398 Code of Practice for the 1.25 MeV photons.[2] For monoenergetic protons, TRS-398 suggests the plateau region at a depth of 3 g cm^{-2}. However, several works[24,25] established a depth of 2 g cm^{-2} for protons, which is the depth also used in this work.

2.B. Calculated quantities

The absorbed dose to water (D_w) in the water-filled volume from Fig. 1 and the absorbed dose to air (D_{air}) in the air-filled volumes were calculated with each Monte Carlo code for photons and each code excluding EGSNRC for protons.

TABLE I. Elemental compositions of water and air used in the simulations. All fractions are given in mass fractions.

Element	Water	Air
^{1}H	0.111894	0.0
^{12}C	0.0	0.000124
^{14}N	0.0	0.755268
^{16}O	0.888106	0.231781
^{40}Ar	0.0	0.012827

From these results, the factor f_Q was calculated as[12]:

$$f_Q = \left(\frac{D_w}{D_{air}}\right)_Q \quad (1)$$

where Q denotes the beam quality.

Using this factor f_Q, the beam quality correction factor k_{Q,Q_0} can be derived[26]:

$$k_{Q,Q_0} = \frac{f_Q}{f_{Q_0}} \frac{W_{air,Q}}{W_{air,Q_0}} \quad (2)$$

where W_{air} is the mean energy required to create an ion pair in air for the beam qualities Q_0 and Q. In this work, the beam quality Q_0 corresponds to 1.25 MeV monoenergetic photons applied in a homogeneous, parallel beam of 10 × 10 cm^2 representing a ^{60}Co beam and the beam quality Q corresponds to 150 MeV monoenergetic protons applied in a homogeneous, parallel beam of 10 × 10 cm^2.

In this study, only the ratios f_Q/f_{Q_0} from Eq. 2 and not the beam quality correction factors k_{Q,Q_0} were investigated since the f_Q/f_{Q_0} ratios are the only part of the beam quality correction factors that can be calculated with Monte Carlo codes. The ratio of the W_{air} values has to be determined experimentally or can be taken from the literature (e.g., the ICRU report 90[17]). Additionally, the aim of this study is to investigate whether the Monte Carlo codes used are feasible for ionization chamber calculations in general and not to calculate any real beam quality correction factors.

In addition to the determination of the f_Q/f_{Q_0} ratios, the spectra of the primary particles (photons or protons) as well as the spectra of secondary electrons were scored in the water-filled reference volume in order to try to explain differences in the particle transport and physics models for the different Monte Carlo codes.

As shown in a recent study by Pfuhl et al.,[27] the dose buildup effects which are present in the entrance channel of a proton Bragg curve provide an excellent test of both the electromagnetic interaction models (delta electron buildup in the first few millimeters) as well as the nuclear interaction models (secondary proton buildup in the first few cm) implemented in a radiation transport code. Therefore, the integrated depth–dose curve of 150 MeV protons was calculated with all three studied proton transport codes (PENH, FLUKA, GEANT4/TOPAS). The Bragg curve was scored in a 10 × 10 × 20 cm^3 water phantom when irradiating with a pencil beam of 150 MeV protons. The same physics settings as in the cavity simulations were used. The binning of the scored dose distribution was 10 × 10 cm^2 laterally and 0.1 mm in the direction of beam.

In the following subsections, the Monte Carlo codes used are described shortly.

2.C. Monte Carlo code 1: PENH

PENH[28] is an extension of the Monte Carlo code PENELOPE[29] that includes the transport of protons based on their electromagnetic interactions in matter. Proton nuclear interactions

and prompt-gamma emission are included for a limited number of isotopes: ^{1}H, ^{12}C, ^{14}N, ^{16}O, ^{31}P, ^{40}Ca.[30] Both PENELOPE and PENH have been reported to pass the Fano test within 0.1%[31,33] for the energy range of interest to this work. Furthermore, PENH has been shown to yield k_Q factors in proton beams in good agreement with experimental data.[15] Photon, electron, and positron cross sections, as well as transport simulation parameters are described in detail in Ref. [29] Cross sections for proton electromagnetic interactions are described in Ref. [28] Cross sections for proton nuclear interactions and prompt-gamma emission are described in Ref. [30], as it is also described the approximate transport of secondary charged particles heavier than protons. Neutrons are not transported.

To improve efficiency without compromising on accuracy, the geometry of all PENH simulations was constructed as follows[15]: (a) a scoring volume (see Fig. 1), (b) a 540 μm-thick "skin" (around the scoring volume) — with a thickness equal to the *continuous slowing down approximation* range (R_{CSDA}) in water of a 200 keV electron, multiplied by a safety factor of 1.2 to account for the possibility that an electron may travel a distance beyond its R_{CSDA} due to energy-loss straggling[31] (c) a 5 mm envelope around the skin and (d) the water phantom. In the scoring volume and 540 μm-thick skin, we performed detailed simulation (i.e., every single interaction was simulated as a catastrophic event[32]); whereas in the 5 mm-thick envelope and the water phantom, we used a mixed (class II[32]) simulation scheme. The absorption energies (E_{abs}) and transport simulation parameters (C_1, C_2, W_{cc}, W_{cr} and DSMAX) used in these regions are detailed in Table II. No variance reduction techniques were used.

As the main program, we used PENEASY.[34] We scored the energy deposited in the scoring volume with the `tallyEnergyDeposition` and the fluence differential in energy with the `tallyFluenceTrackLength`. The output of the `tallyEnergyDeposition` (in units of eV/history) was converted to absorbed dose (in units of gray) by converting eV to joules (J) and dividing the energy by the density and volume of the scoring volume. The output of the `tallyFluenceTrackLength` (in units of cm/eV per history) was converted to $MeV^{-1} \cdot cm^{-2}$ by converting eV to MeV and dividing by the volume of the water cavity. Statistical uncertainties were estimated using the history-by-history method.[29]

2.D. Monte Carlo code 2: FLUKA

The second code chosen for the comparison is the Monte Carlo code FLUKA[35,36] (FLUKA2011 Version 2c.6). Originally developed for high-energy physics applications, nowadays it is also widely used for simulations in proton and heavy ion therapy.[37–40] The code is capable of transporting various kinds of particles including photons, electrons, positrons, neutrons, protons, and heavy ions. Charged particles can be transported down to 1 keV and their energy loss is treated in a condensed history approach. Single Coulomb scattering events are condensed in a multiple scattering algorithm. Hadron–nucleus interactions are treated via the PEANUT model. The models implemented in FLUKA are under ongoing development[38] and are frequently updated.

Also for FLUKA, a Fano cavity test was performed by Lourenco et al.[41] (for proton transport only) with the result that FLUKA passes the test within 0.15% if the step size in the multiple Coulomb scattering algorithm is set small enough compared to the dimensions of the cavity of interest (step size of 0.01 cm in the case of Lourenco et al. where the radii of the plane-parallel cavities were between 0.78 cm and 4.08 cm and the cavities were positioned at a depth where the charged particle equilibrium is reached[41]).

In FLUKA, the user can in most cases not choose between different physics models (unlike, e.g., in Geant4), but only enhance their precision level in certain steps. On the one hand, this reduces the flexibility of the code but, on the other hand, its predictions are well reproducible and very robust.

For all FLUKA simulations performed in this work, the physics models were set to the highest precision level (e.g., full Rayleigh and Coulomb scatter corrections, heavy fragment evaporation, and coalescence) and both the transport and production thresholds for charged particles and photons were set to 1 keV in the region of interest (the region around and within the scoring cavities; see also Section 2.C). In order to further enhance the transport precision for the simulations of the energy deposition in the small cavities, the multiple Coulomb scattering was suppressed in these regions by adding the MULSOPT card to the input file. Using this card, single scattering was activated and the minimum step length for multiple Coulomb scattering was increased by a factor of 10 000 to force the code to simulate the Coulomb scattering as detailed as possible.

Since the standard material definitions in FLUKA consider the natural isotopic composition of a given element (e.g., carbon consists of 98.9% ^{12}C and 1.1% ^{13}C), but in our material definitions (see Table I), only the main isotopes are present (e.g., carbon consists of 100% ^{12}C), the FLUKA material definitions were adapted.

The statistical uncertainties were estimated by calculating the standard deviation of the results from independent runs performed with different random seeds.[36]

2.E. Monte Carlo code 3: GEANT4/TOPAS

Simulations were performed with the TOPAS code ("TOol for PArticle Simulation")[42] version 3.1.p1, a toolkit based on Geant4 ("GEometry ANd Tracking")[43] version geant4-10-03-patch-01. Since TOPAS is based on GEANT4, it uses the same physics models, processes, and interaction cross sections. Previous studies have extensively validated the code against experimental data.[44,42] The code is capable of transporting various kinds of particles including photons, electrons, positrons, neutrons, protons, and heavy ions.

In Geant4, electromagnetic (EM) interactions of the charged particles are grouped in the condensed history (CH) approach. While discrete collisions with an energy loss above

TABLE II. Absorption energies and transport simulation parameters used in PENH simulations.

Region	$E_{abs}(e^-)$	$E_{abs}(\gamma)$	$E_{abs}(e^+)$	$E_{abs}(p)$	C_1	C_2	W_{cc}	W_{cr}	DSMAX
Scoring volume	1 keV	1 keV	1 keV	1 MeV	0	0	0	0	n/a
540 μm skin	1 keV	1 keV	1 keV	1 MeV	0	0	0	0	n/a
5 mm envelope	200 keV	1 keV	200 keV	1 MeV	0.05	0.05	10 keV	1 keV	200 μm
Water phantom	200 keV	1 keV	200 keV	1 MeV	0.1	0.1	10 keV	1 keV	2 mm

a user-defined threshold are simulated one by one, angular deflections of all soft collisions are grouped at the end of a given step using a given multiple scattering (MSC) theory.[45] Since a real trajectory is not a straight line, the lateral displacement is considered at the end of the step.

For the simulations with TOPAS, we investigated both the physics lists ***g4em-standard_opt3*** and ***g4em-standard_opt4***. The physics list ***g4em-standard_opt3*** makes use of the *G4UrbanMscModel*[46] for the multiple scattering of all charged particles. O'Brien et al.[47] showed that when using the Urban scattering model, the Fano test is passed in clinical photon radiation fields within 0.1%. The physics list ***g4em-standard_opt4*** makes use of the *WentzelVI* model[48] as well as the Goudsmit–Saunderson model[49,50] for the multiple scattering: For electrons and positrons with energies below 100 MeV, the Goudsmit–Saunderson model is used. For electrons and positrons with an energy above 100 Mev and for protons with energies below 500 MeV, the WentzelVI model is used. It was shown that the WentzelVI model shows better agreement in the proton therapy range compared to the Urban model.[51] Furthermore, Wulff et al.[16] showed that the Fano test is passed in clinical proton beams within 0.1%–0.2% (depending on the beam geometry) when using the physics list ***g4em-standard_opt4***.

The results obtained when using the physics list ***g4em-standard_opt4*** for the photon simulations were unreasonable in terms of the f_Q factor as described in Appendix A. For the proton simulations, the differences for the results between the physics lists ***g4em-standard_opt3*** and ***g4em-standard_opt4*** were small (<0.4% in terms of the f_Q factor). Hence, we decided to only show the results obtained with the physics list ***g4em-standard_opt3*** in the main text and show the results from the physics list ***g4em-standard_opt4*** in Appendix A.

The length of a step in the CH is limited by tracking limits, such as geometric boundaries and physics-related parameters. A parameter to control the step length is the parameter *dRoverR* which defines the maximum length of one single step in relation to the range of the particle. For the photon simulations, this parameter *dRoverR* was set to 0.003 following O'Brien et al.[47] The fixed step size limiter *MaximumStepSize* was disabled (by setting it to 1000 m) also following O'Brien et al.[47] For the proton simulations, the parameter *dRoverR* was set to 0.05 following a study by Wulff et al.[16] and the *MaximumStepSize* was set to 1000 m, too. Further step limitations are combined in the *G4MscStepLimitType* which was set to *fUseDistanceToBoundary* for electrons and positrons in the used physics list.

While losing energy, the CH step length for each particle decreases until it is smaller than the *finalRange*, below which the particle is ranged out in a single straight step. The *finalRange* was set to 1 nm in the photon simulations and to 100 nm in the proton simulations.

For Compton scattering simulations, the *G4KleinNishinaModel*[53] was used. For ion ionization, the *G4IonParametrisedLossModel* based on the ICRU73[54] ion stopping data was applied.

The simulation of nonelastic nuclear interactions was managed by the physics list ***g4h-phy_QGSP_BIC_HP***. For inelastic nucleon–nucleus processes, the Binary Cascade model[55] was used. To get inelastic cross sections, the *G4BGGNucleonInelasticXS* was taken for protons and neutrons.

For elastic scattering processes, the *G4ChipsElasticModel* was used for protons and neutrons from 0 to 100 TeV. *ChipsProtonElasticXS* provided the proton cross sections while *G4NeutronElasticXS* provided the neutron cross sections.

The default physics list ***g4ion-binarycascade*** was implemented so that the Binary Cascade model was also used for inelastic nuclear interactions of ions. The physics list ***g4decay*** was implemented in order to calculate the decay of particles like muons. Furthermore, the physics lists ***g4h-elastic_HP*** and ***g4stopping*** were used for high-precission calculation of elastic processes of hadrons and to activate and provide the nuclear capture of negatively charged particles at rest.

The parameter controlling the production of secondaries is given in units of length in Geant4. The reason for this is that using a range instead of energy for the production thresholds is theoretically the more precise determination of the location for the energy release.[45] The production cut for all particles was set to 0.5 mm in the whole geometry (which corresponds to ~200 keV electrons in water), except in a region enveloping and including the scoring volume where the cut was set to 0.065 μm (which corresponds to ~1 keV electrons in water). For the simulations of the air-filled cavities, the cut in air was set to 47.2 μm, which corresponds to 990 eV electrons in air. The enveloping region was — equally to the setup in PENH in Section 2.C set to be equal to the R_{CSDA} in water of 200 keV electrons, multiplied by a safety factor of 1.2.

The parameters explained in the text are also listed in Tables III and IV. No variance reduction techniques were used. The statistical uncertainties were estimated by combining the uncertainties from independent runs performed with different random seeds as described in Ref. [56].

To score the spectral fluence of primary photons and protons as well as the spectra of secondary electrons, we did not use the default scorer *fluence* provided by TOPAS. Instead, we took a self-programmed scorer as described in the Appendix B.

2.F. Monte Carlo code 4: EGSNRC

The EGSNRC code is capable of transporting photons, electrons, and positrons and is widely used for dosimetric applications in medical physics. It was included in this study as a benchmark for the 1.25 MeV photon case; details of the transport models and physics behind the code can be found in Ref. [57]. It has been shown that the code is able to calculate the response of ionization chambers with an accuracy of 0.1% normalized to its own cross sections.[58,59] All simulations in this study were performed with the EGSNRC version 2017, applying the user codes *egs_chamber*[60] for dose calculations and *cavity*[61] as well as *FLURZnrc*[62] for fluence calculations. Photons, electrons, and positrons were transported down to a kinetic energy of 1 keV (total energy of 512 keV for electrons/positrons). The energy thresholds for the production of secondary particles from electron interactions (δ-electrons/bremsstrahlungs-photons) was set to AE = 512 keV (δ-electrons) and AP = 1 keV (bremsstrahlungs-photons). Further transport parameters and applied cross sections are summarized in Table V. Statistical uncertainties were estimated using the history-by-history method.[63]

3. RESULTS

3.A. Absorbed dose in the water and air cavities

The results for the absorbed dose in the different geometries given in Fig. 1 for the Monte Carlo codes investigated are shown in Fig. 2; in panel (a) for the irradiation with 1.25 MeV photons and in panel (b) for the irradiation with 150 MeV protons. In the bottom graphs, the deviations relative to the PENH results are shown to visualize the relative differences between the codes. Since no experimental data are available, we chose to investigate the deviations relative to one of the Monte Carlo codes used. Our choice fell on PENH because, among the codes capable of transporting both electrons and protons, it was the one that reached the smallest statistical uncertainty within a reasonable calculation time. However, this normalization is still arbitrary and does not claim that PENH gave the most accurate results.

For the irradiation with photons, the absorbed doses in the water-filled reference volume are for all Monte Carlo codes $\sim$12% larger than the absorbed doses in the air-filled volumes.

The absorbed doses for the Monte Carlo codes PENH and EGSNRC agree within one standard deviation for the air-filled volumes and within two standard deviations for the water-filled volume. The largest deviation between these two codes is 0.1%. The absorbed doses calculated with FLUKA are up to 1.4% larger compared to PENH, those calculated with GEANT4/TOPAS are up to 0.5% larger.

For the irradiation with protons, the absorbed doses in the water-filled reference volume are for all Monte Carlo codes $\sim$13% larger than the absorbed doses in the air-filled volumes.

The absorbed doses calculated with FLUKA are up to 0.5% smaller compared to PENH, those obtained with GEANT4/TOPAS are up to 1.0% smaller.

3.B. f_{Q_0} factors, f_Q factors, and f_Q/f_{Q_0} ratios

In Fig. 3, the f_{Q_0} and f_Q factors calculated with Eq. 1 as well as the f_Q/f_{Q_0} ratios are summarized.

The f_{Q_0} factors for the irradiation with 1.25 MeV photons shown in panel (a) are in the range of $\sim$1.120–1.125. The results for all codes agree within two standard deviations or better. The largest deviation is between FLUKA and GEANT4/TOPAS for the plane-parallel cavity with 0.4% .

The f_Q factors for the irradiation with 150 MeV protons are shown in panel (b). For both volumes, the f_Q factors are in the range of 1.130–1.138. Except for the plane-parallel volume and the codes PENH and GEANT4/TOPAS, the results for all codes coincide within two standard deviations. The largest deviation is that between PENH and GEANT4/TOPAS for the plane-parallel volume with 0.5%.

In panel (c), the f_Q/f_{Q_0} ratios are shown for 150 MeV protons and both air-filled volumes. The f_Q/f_{Q_0} ratios are

TABLE IV. Multiple scattering models used in GEANT4/TOPAS for the photon and proton simulations.

Radiation field	Multiple scattering model for e^+/e^-	Multiple scattering model for primaries
1.25 MeV photons	Urban model	/
150 MeV protons	Goudsmit–Saunderson (E $\leq$ 100 MeV) Wentzel VI (E > 100 MeV)	Wentzel VI (E $\leq$ 500 MeV)

TABLE III. Production cuts and transport simulation parameters used in GEANT4/TOPAS for the photon and proton simulations.

			dRoverR		*finalRange* in nm	
Region	Production cut in µm	Maximum stepsize in m	Photon-sim.	Proton-sim.	Photon-sim.	Proton-sim.
Scoring volume and envelope	0.065 for water and 47.2 for air	1000	0.003	0.05	1	100
Water phantom	500	1000	0.003	0.05	1	100

in the range of 1.005–1.015. For both volumes, the results for all codes coincide within two standard deviations or better. The largest difference can be seen for the plane-parallel volume and the codes PENH and FLUKA with a deviation of 0.7%.

The ratios f_Q/f_{Q_0} from Fig. 3 were calculated for each of the codes PENH, FLUKA and GEANT4/TOPAS using the f_{Q_0} and f_Q factors both calculated with the same code. While f_Q has to be calculated with a code capable of transporting protons if Q is a proton radiation field, the f_{Q_0} factor could theoretically be calculated using another code such as EGSNRC being a commonly used code for the calculations of photons. In Table VI, the f_Q/f_{Q_0} ratios for the codes PENH, FLUKA, and GEANT4/TOPAS are listed for both air-filled volumes once determined using the f_{Q_0} and f_Q factors both calculated with the same code vs the results when using f_{Q_0} calculated with EGSNRC. The differences are smaller than or equal to their statistical uncertainties; hence, we cannot conclude any differences.

TABLE V. Transport simulation parameters used in the EGSNRC simulations.

Photon cross section	NIST
Brems cross section	KM
Brems angular sampling	KM
Electron Impact Ionization	ik
Rayleigh scattering	ON
Spin effects	ON
Bound Compton Scattering	ON
Radiative Compton corrections	ON
Atomic relaxations	ON
Pair angular sampling	KM
Triplet production	ON
PE angular sampling	ON
Photonuclear attenuation	ON
Photonuclear cross section	default
Boundary crossing algorithm	Exact
Skin depth for BCA	3
Electron-step algorithm	EGSNRC

3.C. Spectral fluences in water

Figure 4 shows the spectral fluences in water of the photons (a) and the secondary electrons (b) within the water-filled reference volume for the irradiation with 1.25 MeV photons. The peak of the primary photons at an energy of 1.25 MeV can clearly be seen. The spectrum of the Compton-scattered photons with the peak of the backscattered photons at an energy of $\sim$0.2 MeV is also clearly visible. Accordingly, the Compton edge can be seen in the spectral fluence of the secondary electrons at an energy of $\sim$1.05 MeV. The broad Compton spectrum is clearly visible, too. The spectra for both the photons and electrons agree almost perfectly between all Monte Carlo codes.

The spectral fluence in water of protons in the 150 MeV proton beam at the cavity position is shown in fig. 5(a). The peak of the primary protons lies at an energy of $\sim$139 MeV (corresponding to 150 MeV minus

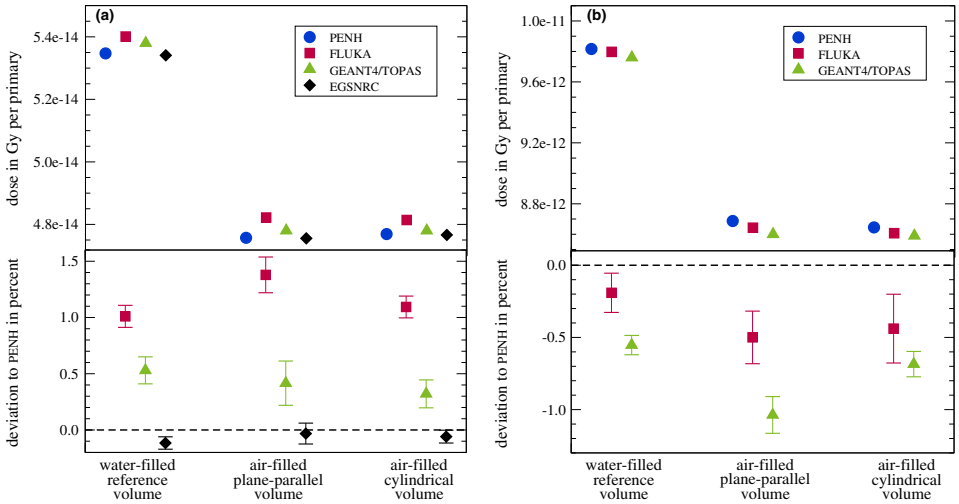

FIG. 2. Absorbed dose in Gy per primary scored in each volume from Fig. 1 for all Monte Carlo codes. (a) 1.25 MeV photons, (b) 150 MeV protons. In the bottom graph, the deviations relative to PENH are shown (see text for explanation). The statistical uncertainties of the absolute absorbed doses are smaller than the symbol size. The statistical uncertainties represented by bars in the bottom graphs correspond to one standard deviation. [Color figure can be viewed at wileyonlinelibrary.com]

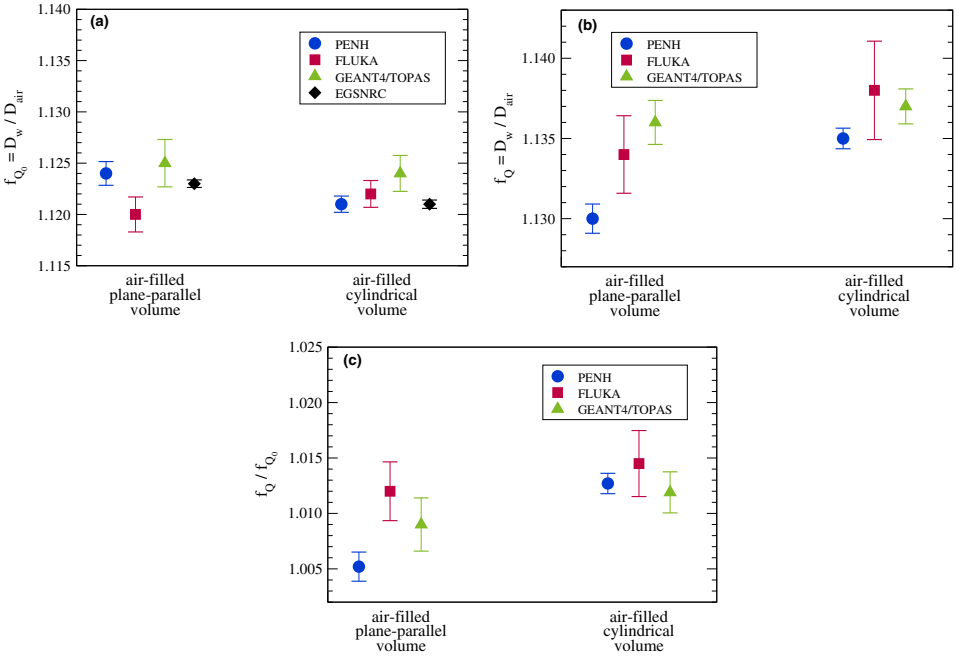

FIG. 3. Results for f_{Q_0} and f_Q factors: (a) 1.25 MeV photons and (b) 150 MeV protons. (c) The f_Q/f_{Q_0} ratios for 150 MeV protons. The statistical uncertainties represented by bars correspond to one standard deviation. [Color figure can be viewed at wileyonlinelibrary.com]

TABLE VI. f_Q/f_{Q_0} ratios for the Monte Carlo codes PENH, FLUKA, and GEANT4/TOPAS using the f_{Q_0} factors calculated with the same Monte Carlo code and using f_{Q_0} determined with EGSNRC. The given statistical uncertainties are one standard deviation.

		ratio f_Q/f_{Q_0}		
Monte Carlo code	Volume	f_{Q_0} from same code	f_{Q_0} from EGSNRC	Difference in %
PENH	Plane-parallel	1.005 ± 0.001	1.006 ± 0.001	−0.09 ± 0.16
	Cylindrical	1.013 ± 0.001	1.013 ± 0.001	−0.06 ± 0.11
FLUKA	Plane-parallel	1.012 ± 0.003	1.009 ± 0.002	0.3 ± 0.3
	Cylindrical	1.015 ± 0.003	1.016 ± 0.003	−0.1 ± 0.4
GEANT4TOPAS	Plane-parallel	1.009 ± 0.002	1.011 ± 0.001	−0.2 ± 0.3
	Cylindrical	1.012 ± 0.002	1.015 ± 0.001	−0.3 ± 0.2

the energy loss in the first 2 cm of water). The spectrum of the secondary protons ranges over the whole spectrum up to the primary protons. Differences between the individual codes can be observed for very low energies up to ~20 MeV and higher energies between 125 and 135 MeV. The spectral fluence of the secondary protons scored with PENH develops a small peak at an energy of ~80 MeV. This might be due to the fact that in PENH fragments heavier than protons (like deuterons) are simulated as secondary protons and the energy of these "protons" is adjusted to match the range of the real fragments.[30] In this case, these fragments are deuterons that are simulated as 80 MeV protons which would have a range in water of about 5 cm.

The spectral fluence in water of the delta electrons in the 150 MeV proton beam can be seen in Fig. 5(b). As expected, the fluence is dominated by low-energy electrons. The maximum energy transferred to electrons in ionization processes by 139 MeV protons [compare energy of primary protons in Fig. 5(a)] is ~0.3 MeV.[64] Electrons with higher energies are not produced by protons but by prompt gamma photons from nuclear reactions. The spectral fluence of these high-energy

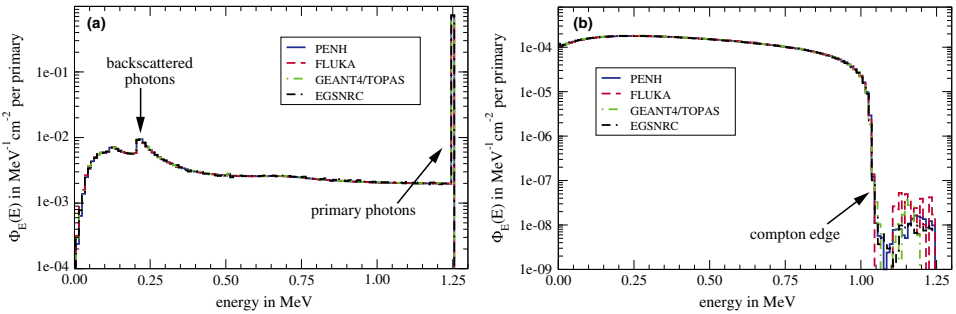

FIG. 4. Spectral fluence $\Phi_E(E)$ in water of photons (a) and electrons (b) in the 1.25 MeV photon beam at a depth of 5 cm. [Color figure can be viewed at wile yonlinelibrary.com]

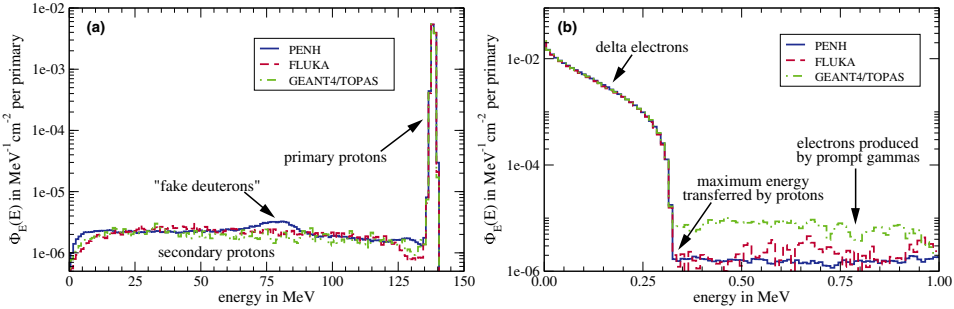

FIG. 5. Spectral fluence $\Phi_E(E)$ in water of protons (a) and electrons (b) in the 150 MeV proton beam at a depth of 2 cm. [Color figure can be viewed at wileyon linelibrary.com]

electrons is considerably larger for GEANT4/TOPAS than for PENH and FLUKA.

For all codes, there are no relevant differences between the individual spectra except for the secondary protons and electrons produced by prompt gamma photons as pointed out.

3.D. Electronic and nuclear buildup, ranges, and stopping powers

Figure 6(a) shows the integrated depth–dose curve of 150 MeV protons in water. Among all codes, the dose curves are in a good agreement. In panel (b), a zoom to the Bragg peak is shown. As can be seen, the dose at the peak calculated with FLUKA is about ∼1.5% smaller compared to the doses calculated with PENH and GEANT4/TOPAS. Furthermore, the ranges of all codes agree within ∼0.1 mm which is the resolution of the scored dose curves. In panel (c), a zoom to the first 95 mm is shown. In this region, the secondary proton buildup takes place. Small discrepancies between the codes can be seen at small depths of ∼5 mm (1.3% difference in dose) and at greater depth of ∼70 mm and ∼90 mm (1.5% difference in dose). These differences are statistically significant. The best agreement between the codes is at depths of 20–40 mm supporting the IAEA reference depth for monoenergetic protons of 3 g cm.$^{-2}$ Note that these dose curves were produced with a pencil beam and the dose was laterally integrated. Hence, the absolute doses differ from the ones presented in Fig. 2(b).

In Fig. 6(d), the first 2 mm of the Bragg curve is shown while the dose values are normalized to the dose value at a depth of 1 mm. As already mentioned, this region provides an excellent test of the electromagnetic interaction models implemented in the different Monte Carlo codes. Within the first millimeters of the depth–dose curve, the buildup is dominated by the creation of delta electrons with energies up to 0.33 MeV.[64] The range of these electrons is about 1 mm. Accordingly, an equilibrium is reached and the electron buildup is completed at this depth [see Fig. 6(d)]. The electron buildup is reproduced by all three Monte Carlo codes identically, indicating that the underlying electromagnetic interaction models are similar in these codes [also compare Fig. 5(b)]. The completion of the electronic buildup at a

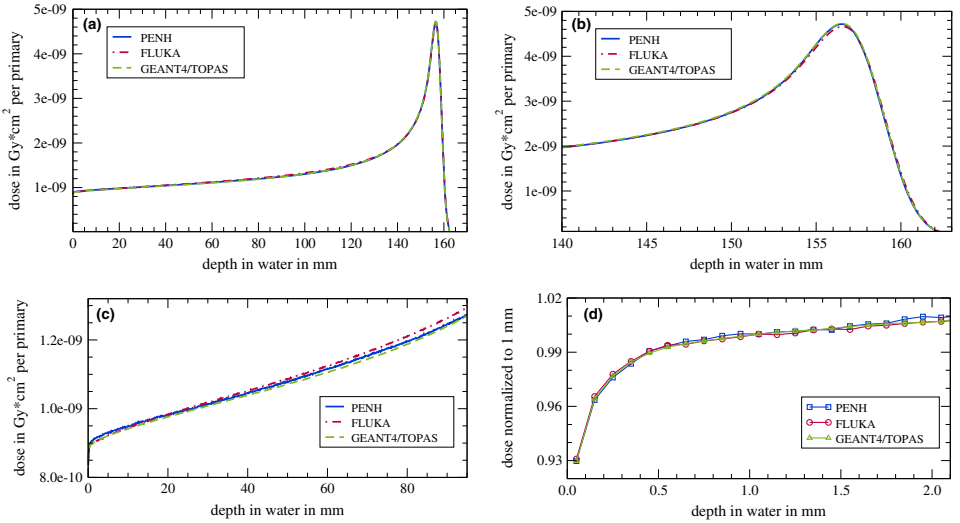

FIG. 6. (a) Integrated depth–dose curve of 150 MeV protons in water (dose integrated over an area of 100 cm^2). (b) Zoom to the Bragg peak. (c) Zoom to the first 90 mm. (d) Zoom to the first 2 mm while the dose values are normalized to the dose at a depth of 1 mm. The single data points in (d) are connected with lines to guide the eye. No statistical uncertainties are indicated since one standard deviation is smaller than the line width [panels (a)–(c)] or the symbol size [panel (d)]. [Color figure can be viewed at wileyonlinelibrary.com]

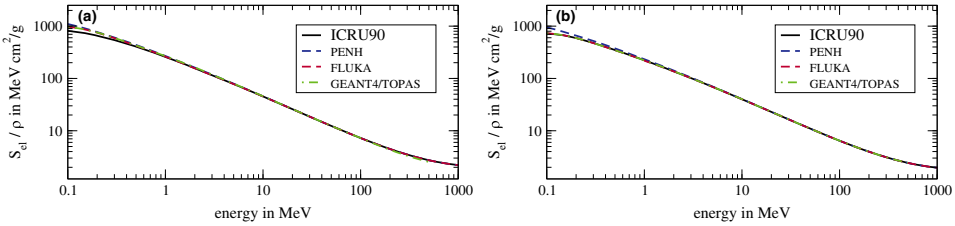

FIG. 7. Electronic mass-stopping powers of (a) water and (b) air for protons. The data labeled with *ICRU90* are taken from Ref. [17]. [Color figure can be viewed at wileyonlinelibrary.com]

depth of 1 mm is the reason why the depth–dose curves are normalized to the dose at this depth.

To ensure that the stopping powers are the same for the different Monte Carlo codes for the given mean ionization potentials of water I_w = 78 eV and air I_{air} = 85.7 eV, we compared the stopping powers of water and air for protons and electrons. In Fig. 7, the electronic mass-stopping powers of (a) water and (b) air for protons for the Monte Carlo codes PENH, FLUKA, and GEANT4/TOPAS are shown. As reference, the ICRU90 data[17] are shown. For energies between 0.3 MeV and 1000 MeV, there are no significant differences between the codes and the ICRU90 data. Only for energies below 0.3 MeV, differences can be seen. The stopping powers of water and air for electrons agreed almost perfectly among the Monte Carlo codes and with the reference data from the ICRU90 in the energy range from 10 keV to 900 MeV (not shown).

4. DISCUSSION

Simulations of the absorbed dose in simple water- and air-filled geometries and the calculation of f_Q factors as well as f_Q/f_{Q_0} ratios were carried out with different Monte Carlo codes for different beam qualities and particle types. Although the absorbed dose to medium per primary particle does not always agree for all Monte Carlo codes, these differences tend to cancel out in the f_Q factors and the f_Q/f_{Q_0} ratios. The f_Q/f_{Q_0} ratios agree within 0.7% for protons for the Monte Carlo codes PENH, FLUKA, and GEANT4/TOPAS. Since these ratios are the only part of k_{Q,Q_0} factors that can be

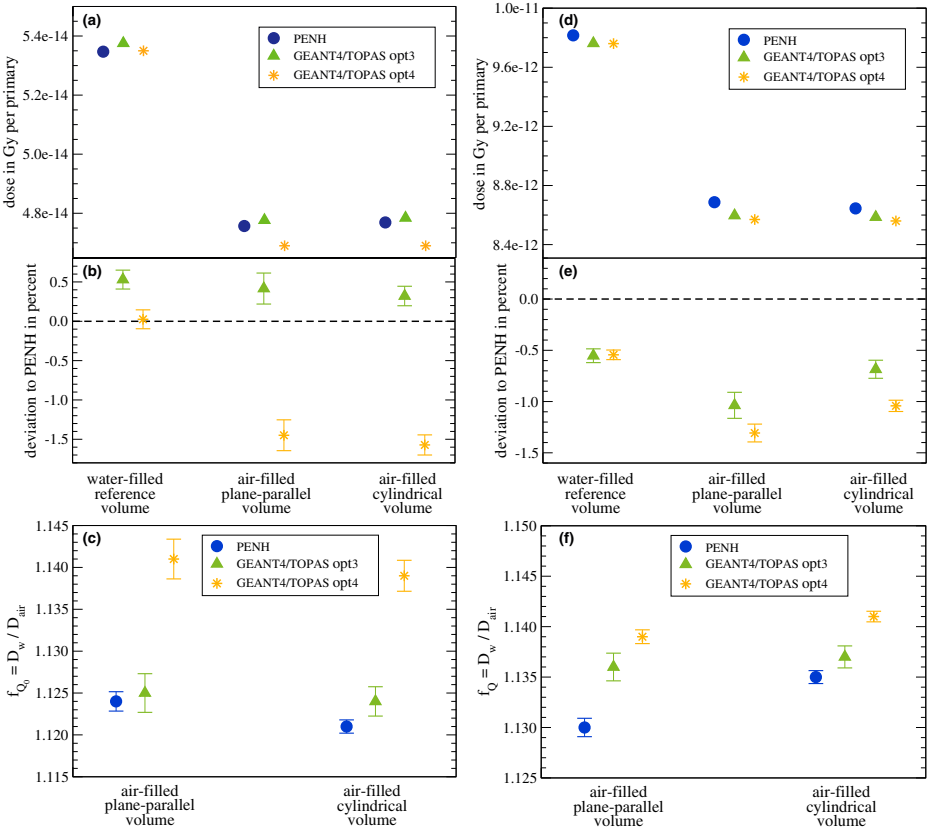

FIG. 8. Absorbed dose in Gy per primary scored in each volume from Fig. 1 for the 1.25 MeV photons (a) and 150 MeV protons (d) calculated with PENH and GEANT4/TOPAS using the physics lists *g4em-standard_opt3* and *g4em-standard_opt4*. In (b) and (e), the deviations relative to PENH are shown. The statistical uncertainties of the absolute absorbed doses are smaller than the symbol size. The statistical uncertainties represented by bars in panel (b) and (e) correspond to one standard deviation. (c) The results for f_{Q_0} factors for 1.25 MeV photons; (f) the results for f_Q factors for 150 MeV protons. The statistical uncertainties represented by bars correspond to one standard deviation. [Color figure can be viewed at wileyonlinelibrary.com]

determined with the Monte Carlo method and since it was shown, that PENH can be used to calculate k_{Q,Q_0} factors in clinical proton beams,[15] we conclude that FLUKA and GEANT4/TOPAS can also be used to calculate k_{Q,Q_0} factors in clinical proton beams.

When mixing the codes in a way that the f_Q factor is taken from a code capable of transporting protons and f_{Q_0} is derived using EGSNRC, the differences in the f_Q/f_{Q_0} ratios are not significant compared to the case when both f_Q and f_{Q_0} are calculated within the same code. Although no significant differences were seen, it is commonly advised to always use the same code to calculate the f_Q as well as the f_{Q_0} factor to avoid a mixing of physical models and to enhance the chance that code-internal systematic uncertainties are canceled out in the D_w/D_{air} ratios, that is, in the f_Q factors, as well as the f_Q/f_{Q_0} ratios.

The f_{Q_0} factors for 1.25 MeV photons for the air-filled volumes are in the range of 1.120–1.125 and the f_Q factors for 150 MeV protons for the air-filled volumes are in the range of 1.130–1.138. These factors correspond approximately to the Spencer–Attix water to air mass stopping power ratio $s_{w,air}$. For a ^{60}Co beam, this mass stopping power ratio is $\sim$1.127[65,66], and for a 150 MeV proton beam, it is 1.130.[67] The f_{Q_0} and f_Q factors calculated in this study agree with these values within a few permille. Differences are due to the fact that the stopping power

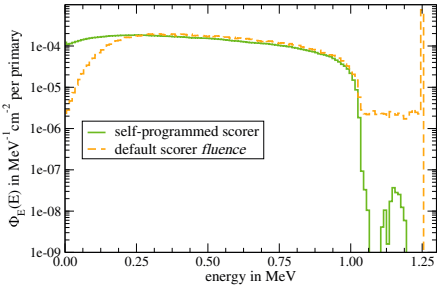

FIG. 9. Energy-dependent fluence $\Phi_E(E)$ in water of secondary electrons binned by energy in a 1.25 MeV photon beam scored in TOPAS with the self-programmed scorer (fluence binned by energy the particle had when generating the scoring hit; corresponding to the spectral fluence) and the default scorer *fluence* implemented in TOPAS (fluence binned by the energy the particle had when entering the scoring volume). [Color figure can be viewed at wileyonlinelibrary.com]

ratio is defined on the fluence in water, whereas in this work, we scored the fluence in air.

In order to try to explain differences in the particle transport and the physics models used in the Monte Carlo codes, we presented spectral fluences in water of the primary particles and secondary electrons. In spite of possible differences due to the use of different approaches and models, we found remarkable agreements between the codes: For the photons and secondary electrons in the 1.25 MeV photon field, the spectra agree almost perfectly. For the spectral fluence of protons and electrons in the 150 MeV proton field, the spectra also agree reasonably well, except for the secondary protons and high-energy electrons produced by prompt gamma photons. For the secondary protons, we observed differences between the spectra generated with the different Monte Carlo codes for energies between 125 and 135 MeV. The production of a secondary proton from an ^{16}O nucleus requires an energy of $\sim$12 MeV,[68]; therefore, the gap between the primary and secondary protons visible in the spectra generated with TOPAS and FLUKA is reasonable. However, this gap cannot be observed in the spectrum generated with PENH. Anyway, this difference in the spectral fluence of secondary protons has only a very small effect on the absorbed dose D_w at a water depth of 2 cm (where the spectral fluence and the absorbed dose were calculated), since the fluence of secondary protons is >3 orders of magnitudes smaller than the fluence of primary protons.

The spectral fluence of high-energy electrons produced by prompt gamma photons is considerably larger for GEANT4/TOPAS than for PENH and FLUKA. It was shown by Robert et al. that in Geant4, many more prompt gamma photons are produced compared to FLUKA,[40] which might be the explanation for the differences observed in this work. However, for dosimetry purposes, these differences in the prompt gamma photon production are negligible since the fluence of electrons generated by prompt gamma photons is >2 orders of magnitudes smaller than the fluence of the delta electrons.

On the one hand, the agreement in the spectra of secondary electrons shows that the different electromagnetic interaction models yield similar results. On the other hand, the differences in the spectra of secondary protons show that the more complex nuclear interaction models tend to slight differences. Accordingly, discrepancies in the proton depth–dose curves as shown in Fig. 6 due to the different predictions of the secondary proton production were observed. However, the impact of these differences at small depths is so low that the f_Q/f_{Q_0} ratios at a water depth of 2 cm calculated with the different codes agree within 0.7%. Pfuhl et al.[27] have compared dose profiles similar to those shown in Fig. 6(d) with measured dose profiles. FLUKA could reproduce both the electronic and the nuclear buildup quite well, with a maximum underestimation of $\sim$1% at large depths. In another study by Yang et al.[69], depth–dose curves were calculated with both FLUKA and Geant4 and compared to measurements. Yang et al. concluded that FLUKA and Geant4 are "capable of performing dose calculations for therapeutic scanning proton beams with proper physics settings."[69] Furthermore, Monte Carlo codes like, for example, FLUKA are already used to generate basic data for treatment-planning systems and are hence intensively validated against experimental dose measurements.[70,71]

We also showed that the ranges of protons in water agree within $\sim$0.1 mm between the codes [see Fig 6(b)]. Since the range is connected with the stopping power of water, we investigated the stopping powers of water for protons and electrons and found good agreements between the codes and the ICRU90 stopping powers. The only differences for protons were found for energies below 0.3 MeV. Since the range in water of protons with an energy of 0.3 MeV is only $\sim$5 μm, these differences in the stopping powers have no visible effect on the range that we calculated with a resolution of 0.1 mm.

Finally, a last consideration regarding uncertainties in Monte Carlo calculations: while type A uncertainties are easy to calculate and can be reduced by increasing the number of primary histories, type B uncertainties (due to uncertainties in the cross sections, nuclear models, particle transport, geometry, etc.) are more difficult to estimate. The results of this work could be used to estimate (an upper limit to) the type B uncertainty in the f_Q/f_{Q_0} ratios calculated with PENH, FLUKA, and GEANT4/TOPAS, due to the uncertainty in cross-section data, nuclear models, and particle transport. Figure 3(c) shows that the differences in f_Q/f_{Q_0} ratios are well within three (type A) standard uncertainties of the data points calculated with FLUKA. Thus, it could be concluded that an upper limit to the type B uncertainty in the f_Q/f_{Q_0} ratios (due to the uncertainty in cross-section data, nuclear models, and particle transport) is the type A uncertainty in the f_Q/f_{Q_0} ratios calculated with FLUKA. That is, $u_B \leq 0.3\%$.

5. CONCLUSION

The Monte Carlo codes PENH , FLUKA, GEANT4/TOPAS, and EGSNRC were investigated and used to calculate the absorbed dose in a simple water-filled reference volume and two air-filled volumes representing simplified ionization chambers for the irradiation with 1.25 MeV photons representing a ^{60}Co beam and with 150 MeV protons — EGSNRC was used only for the photon beam calculations. The absorbed doses to medium (per primary particle) agreed within 1.4% or better for the photon field among all codes. For the irradiation with 150 MeV protons, the absorbed doses to medium (per primary particle) agreed within 1.0% or better among the three codes capable of transporting protons (PENH, FLUKA, and TOPAS/Geant4). It was shown that by choosing appropriate transport settings which were reported in detail, the results for the f_Q/f_{Q_0} ratios agreed within 0.7%. In other words, PENH, FLUKA, and TOPAS/Geant4 are all suitable to calculate f_{Q_0}, f_Q, and k_{Q,Q_0} factors in proton beams.

ACKNOWLEDGMENTS

This work is part of the RTNORM research project, funded by the European Metrology Programme for Innovation and Research (EMPIR), grant number 16NRM03, an initiative co-funded by the European Union's Horizon 2020 research and innovation programme and the EMPIR Participating States. We thank the TOPAS forum and especially Joseph Perl for fruitful discussions. CG is also grateful to Edmond Sterpin for his insight on PENH nuclear models. Part of the computational resources and services used in this work were provided by the VSC (Flemish Supercomputer Center), funded by the Research Foundation - Flanders (FWO) and the Flemish Government Department EWI.

APPENDIX A

PHYSICS LIST IN TOPAS FOR PHOTON AND PROTON FIELDS

As described in Section 2.C, we used the physics list *g4em-standard_opt3* for both the photon and proton simulations for the Monte Carlo code GEANT4/TOPAS. We also tested the physics list *g4em-standard_opt4* for both the photon and proton simulations. In Fig. 8, the absorbed doses for the three cavities calculated with PENH and GEANT4/TOPAS for the two physics lists as well as the deviations relative to PENH are shown on the left side for photons [panels (a) and (b)]. The absorbed dose in the water-filled reference volume is $\sim$0.5% smaller and the absorbed dose in the air-filled cavities is $\sim$2% smaller when replacing the physics list *g4em-standard_opt3* by *g4em-standard_opt4*. Hence, the deviations relative to PENH are up to $-$1.5% instead of 0.5%. In Fig. 8 in panel (c), the resulting f_{Q_0} factors for photons are shown: when using the physics list *g4em-standard_opt4*, the f_{Q_0} factor is $\sim$1.141 instead of $\sim$1.125 and hence 1.4% greater and does not agree with the Spencer–Attix water to air mass stopping power ratio $s_{w,air}$ anymore.

In panels (d) and (e), the absorbed doses for the three cavities calculated with PENH and GEANT4/TOPAS for the two physics lists as well as the deviations relative to PENH are shown for protons. The difference in the absorbed dose is <0.1% for the water-filled reference volume and <0.36% for the air-filled cavities when replacing the physics list *g4em-standard_opt3* by *g4em-standard_opt4*. For the resulting f_Q factors, the differences are smaller than 0.4% for the different physics lists. The maximum deviation between PENH and GEANT4/TOPAS rises from 0.5% for the physics list *g4em-standard_opt3* to 0.8% for the physics list *g4em-standard_opt4*.

Since the multiple scattering models used in the physics lists *g4em-standard_opt3* and *g4em-standard_opt4* are not the only differences we cannot clarify whether these scattering models are responsible for the different results.

In conclusion: for the proton simulations, both the physics lists *g4em-standard_opt3* and *g4em-standard_opt4* can be used whereas for the photon simulations, the physics list *g4em-standard_opt4* does not lead to reasonable results. Additionally, one has to keep in mind that the physics lists provided by Geant4 may vary with the versions of the code. Hence, the physics lists used in this work may lead to different results in the future when changed in new versions of Geant4.

APPENDIX B

SCORING THE SPECTRAL FLUENCE IN TOPAS

As mentioned in Section 2.C, we used a self-programmed scorer in TOPAS to score the spectral fluence in the water cavity. The reason is that the scorer *fluence* provided by TOPAS is not designed to score a **spectral** fluence. Although the fluence can be binned by energy, this energy binning is not based on the particle's energy when the scoring hit is generated. The scorer *fluence* bins the fluence of the particle to the energy the particle had when the particle was incident on the scoring volume (i.e., when entering the scoring volume). However, this so-scored energy-binned fluence does not correspond to the spectral fluence of a particle. In the case that a particle is produced within the scoring volume, the difference between the result of the energy-binned scorer *fluence* and the spectral fluence becomes clear: The scorer *fluence* provided by TOPAS connects the fluence of this particle created within the scoring volume to the energy its predecessor had when entering the scoring volume and not to the energy of the scored particle it had when the hit was generated — as it is the case when scoring the spectral fluence.

In Fig. 9, the fluences of electrons at 5 cm water depth in a 1.25 MeV photon beam are shown: In the first scenario, the fluence is binned by the energy the particle had when entering the scoring volume (as it is done in the scorer *fluence* provided by TOPAS). In the second scenario, the fluence is

binned by the energy the particle had when generating the scoring hit (this corresponds to the spectral fluence and is the scoring method used in this study).

As can be seen, the fluence scored with the scorer *fluence* provided by TOPAS shows electrons with an energy of 1.25 MeV. These electrons were produced within the scoring volume, and hence, TOPAS bins the fluence of these electrons by the energy their predecessor (in this case a 1.25 MeV photon) had when entering the scoring volume. In contrast, the scorer used in this study for the TOPAS simulations does not show this peak since the fluence is binned by the energy of the particle itself that was created in the scoring volume. Correspondingly, differences in the fluence of low-energy electrons can be seen: Since the scorer *fluence* provided by TOPAS bins the fluence of low-energy electrons that are created within the scoring volume by the energy of their predecessors, the fluence of low-energy electrons is smaller compared to the spectral fluence scored with the self-programmed scorer which bins the fluence by the energy of the electron itself that was produced in the scoring volume. The spectral fluence scored with the self-programmed scorer was already shown in Fig. 4 and proven to agree with the results from the Monte Carlo codes PENH, FLUKA, and EGSNRC.

To avoid confusion when using the scorer *fluence* provided by TOPAS, several scoring options are now included in the new TOPAS version 3.2.

[a]Author to whom correspondence should be addressed. Electronic mail: kilian-simon.baumann@staff.uni-marburg.de

REFERENCES

1. Almond PR, Bniggs PJ, Coursey BM, Hanson WF, Huq MS, Nath R. AAPM's TG-51 protocol for clinical reference dosimetry of high-energy photon and electron beams. *Med Phys*. 1999;26:1847–1870.
2. Andreo P, Burns DT, Hohlfeld K, et al. Absorbed Dose Determination in External Beam Radiotherapy: An International Code of Practice for Dosimetry based on Standards of Absorbed Dose to Water. Technical Report Series TRS-398 (International Atomic Energy Agenca, Vienna); 2000.
3. Deutsches Institut für Normung (DIN 6800-2), Dosismessverfahren nach der Sondenmethode für Photonen- und Elektronenstrahlung - Teil 2: Dosimetrie hochenergetischer Photonen- und Elektronenstrahlung mit Ionisationskammern. DIN 6800-2; 2006.
4. Vatnitsky SM, Siebers JV, Miller DW. Calorimetric determination of the absorbed dose–to–water beam quality correction factor kQ for high-energy photon beams. *Med Phys*. 1995;22:1749–1752.
5. Medin J, Ross CK, Klassen NV, Palmans H, Grussel E, Grindborg J-E. Experimental determination of beam quality factors, k_Q, for two types of Farmer chamber in a 10 MV photon and a 175 MeV proton beam. *Phys Med Biol*. 2006;51:1503.
6. Krauss A, Kapsch R-P. Calorimetric determination of k_Q factors for NE 2561 and NE 2571 ionization chambers in 5 cm × 5 cm and 10 cm × 10 cm radiotherapy beams of 8 MV and 16 MV photon. *Phys Med Biol*. 2007;52:6243–6259.
7. Seuntjens JP, Ross CK, Shortt KR, Rogers DW. Absorbed-dose beam quality conversion factors for cylindrical chambers in high energy photon beams. *Med Phys*. 2000;27:2763–2779.
8. Palmans H, Mondelaers W, Theriens H. Absorbed dose beam quality correction factors k_Q for the NE2571 chamber in a 5 MV and a 10 MV photon beam. *Phys Med Biol*. 1999;44:647–663.
9. Radiotherapy Normative, "Ionizing radiation dosimetry for radiotherapy", EURAMET/EMPIR research project (2017–2019) 2018; http://www.rtnorm.eu/
10. Zink K, Wulff J. Beam quality corrections for parallel-plate ion chambers in electron reference dosimetry. *Phys Med Biol*. 2012;57:1831–1854.
11. Muir BR, Rogers DWO. Monte carlo calculations of k_Q, the beam quality conversion factor. *Med Phys*. 2010;37:5939–5950.
12. Sempau J, Andreo P, Aldana J, Mazurier J, Salvat F. Electron beam quality correction factors for plane-parallel ionization chambers: Monte Carlo calculations using the PENELOPE system. *Phys Med Biol*. 2004;49:4427–4444.
13. Erazo F, Lallena AM. Calculation of beam quality correction factors for various thimble ionization chambers using the Monte Carlo code PENELOPE. *Phys Med*. 2013;29:163–170.
14. Panettierei V, Sempau J, Andreo P. Chamber-quality factors in ^{60}Co for three plane-parallel chambers for the dosimetry of electrons, protons and heavier charged particles: PENELOPE Monte Carlo simulations. *Phys Med Biol*. 2008;53:5917–5926.
15. Gomà, C, Andreo P, Sempau J. Monte Carlo calculation of beam quality correction factors in proton beams using detailed simulation of ionization chambers. *Phys Med Biol*. 2016;61:2389–2406.
16. Wulff J, Baumann K-S, Verbeek N, Bäumer C, Timmermann B, Zink K. TOPAS/Geant4 configuration for ionization chamber calculations in proton beams. *Phys Med Biol*. 2018;63:115013.
17. ICRU. Key Data For Ionizing-Radiation Dosimetry (ICRU Report 90 vol 14). Bethesda, Maryland, USA: International Commission on Radiation Units and Measurements; 2014.
18. Muir BR, McEwen MR, Rogers DWO. Measured and Monte Carlo calculated k_Q factors: accuracy and comparison. *Med Phys*. 2011;38:4600–4609.
19. Renner F, Wulff J, Kapsch R-P, Zink K. Uncertainties in Monte Carlo-based absorbed dose calculations for an experimental benchmark. *Phys Med Biol*. 2015;60:7637–7653.
20. Rogers DWO, Bazalova-Carter M, Bloch WE. et al. RECORDS: improved reporting of Monte Carlo Radiation transport studies: report of the AAPM Research Committee Task Group 268. *Med Phys*. 2018;45:e1.
21. Palm A, Mattsson O, Andreo P. Calibration of plane-parallel chambers and determination of p_{wall} for the NACP and Roos chambers for ^{60}Co gamma-ray beams. *Phys Med Biol*. 2000;45:971–981.
22. Low DA, Parikh P, Dempsey JF, Wahab S. Huq S. Ionization chamber volume averaging effects in dynamic intensity modulated radiation therapy beams. *Med Phys*. 2003;30:1706–1711.
23. Schardt D, Steidl P, Krmer M, Weber U, Parodi K, Brons S. Precision Bragg-Curve Measurements for Light-Ion Beams in Water. GSI Scientific Report; 2007:page 373.
24. Gillin MT, Sahoo N, Bues M, et al. Commissioning of the discrete spot scanning proton beam delivery system at the University of Texas M.D. Anderson Cancer Center, Proton Therapy Center, Houston. *Med Phys*. 2010;37:154–163.
25. Gomà C, Lorentini S, Meer D, Safai S. Proton beam monitor chamber calibration. *Phys Med Biol*. 2014;59:4961–4971.
26. Andreo P, Wulff J, Burns DT, Palmans H. Consistency in reference radiotherapy dosimetry: resolution of an apparent conundrum when (60) Co is the reference quality for charged-particle and photon beams. *Phys Med Biol*. 2013;58:6593–6621.
27. Pfuhl T, Horst F, Schuy C, Weber U. Dose build-up effects induced by delta electrons and target fragments in proton Bragg curve-measurements and simulations. *Phys Med Biol*. 2018;63:175002.
28. Salvat F. A generic algorithm for Monte Carlo simulation of proton transport. *Nucl Instr Meth Phys Res B*. 2013;316:144–159.
29. Salvat F. *PENELOPE-2014: A code System for Monte Carlo Simulation of Electron and Photon Transport*. Paris: Nuclear Energy Agency; 2014.
30. Sterpin E, Sorriaux J, Vynckier S. Extension of PENELOPE to protons: simulation of nuclear reactions and benchmark with Geant4. *Med Phys*. 2013;40:111705.
31. Sempau J, Andreo P. Configuration of the electron transport algorithm of PENELOPE to simulate ion chambers. *Phys Med Biol*. 2006;51:3533–3548.
32. Berger MJ. Monte Carlo calculation of the penetration and diffusion of fast charged particles. In: Alder B, Fernbach S, Rotenberg M, eds.

Methods in Computational Physics, vol. 1. New York: Academic Press; 1963:135–215.
33. Sterpin E, Sorriaux J, Souris K, Vynckier S, Bouchard H. A Fano cavity test for Monte Carlo proton transport algorithms. *Med Phys*. 2014;41:11706.
34. Sempau J, Badal A, Brualla L. A PENELOPE-based system for the automated Monte Carlo simulation of clinacs and voxelized geometries—application to far-from-axis fields. *Med Phys*. 2011;38:5887–5895.
35. Battistoni G, Boehlen T, Cerutti F, et al. Overview of the FLUKA code. *Ann Nucl Energy*. 2015;82:10–18.
36. Ferrari A, Sala PR, Fasso A, Ranft J. FLUKA: a multi-particle transport code. Tech. Report: CERN-2005-10; 2005, INFN/TC_05/11, SLAC-R-773.
37. Battistoni G, Bauer J, Boehlen TT, et al. The FLUKA code: an accurate simulation tool for particle therapy. *Front Oncol*. 2016;6:116.
38. Böhlen TT, Cerutti F, Chin MPW, et al. The FLUKA code: developments and challenges for high energy and medical applications. *Nucl Data Sheets*. 2014;120:221–214.
39. Böhlen TT, Cerutti F, Dosanjh M, et al. Benchmarking nuclear models of FLUKA and GEANT4 for carbon ion therapy. *Phys Med Biol*. 2010;55:5833–5847.
40. Robert C, Dedes G, Battistoni G, et al. Distributions of secondary particles in proton and carbon-ion therapy: a comparison between GATE/Geant4 and FLUKA Monte Carlo codes. *Phys Med Biol*. 2013;58:2879–2899.
41. Lourenco A, Bouchard H, Galer S, Royle G, Palmans H. The influence of nuclear interactions on ionization chamber perturbation factors in proton beams: FLUKA simulations supported by a Fano test. *Med Phys*. 2019;46:885–891.
42. Perl J, Shin J, Schuemann J, Faddegon B, Paganetti H. TOPAS: an innovative proton Monte Carlo platform for research and clinical applications. *Med Phys*. 2012;39:6818–6837.
43. Agostinella S, Allison J, Amako K, et al. Geant4 - a simulation toolkit. *Nucl Instrum Methods Phys Res A*. 2003;506:250–303.
44. Testa M, Schuemann J, Lu H-M, et al. Experimental validation of the TOPAS Monte Carlo system for passive scattering proton therapy. *Med Phys*. 2013;40:1–16.
45. Geant4 Collaboration. GEANT4: Physics Reference Manual Geant4 10.3 (8 December 2017); 2016. https://indico.cern.ch/event/679723/contributions/2792554/attachments/1559217/2454299/Physic sReferenceManual.pdf (last called on April, 17th)
46. Urban L. *Multiple scattering Model in GEANT4*. Budapest: Research Institute for Particle and Nuclear Physics; 2002.
47. O'Brien DJ, Roberts DA, Ibbot GS, Sawakuchi GO. Reference dosimetry in magnetic fields: formalism and ionization chamber correction factors. *Med Phys*. 2016;43:4915–4927.
48. Ivanchenko VN, Kadri O, Maire M, Urban L. Geant4 models for simulation of multiple scattering. *J Phys*. 2010;219:32045.
49. Goudsmit S, Saunderson JL. Multiple scattering of electrons. *Phys Rev*. 1940;57:24.
50. Goudsmit S, Saunderson JL. Multiple scattering of Electrons II. *Phys Rev*. 1940;58:36–42.
51. Makarova A, Gottschalk B, Sauerwein W. Comparison of Geant4 multiple Coulomb scattering models with theory for radiotherapy protons. *Phys Med Biol*. 2017;62:5959–5974.
52. O'Brien DJ, Sawakuchi GO. TU-D-205-4: Evaluation of the Electron Condensed History Algorithms in Geant4 for Radiotherapy Simulations. 59th Annual Meeting of the AAPM, Denver, USE; 2017.
53. Klein O, Nishina Y. Über die Streuung von Strahlung durch freie Elektronen nach der neuen relativistischen Quantendynamik von Dirac. *Zeitschrift für Physik*. 1929;52:853–868.
54. ICRU. *Stopping of Ions Heavier than Helium (ICRU Report 73)*. Bethesda, Maryland: International Comission on Radiation Units and Measurements; 2005.
55. Folger G, Ivanchenko VN, Wellisch JP. The binary cascade. *Eur Phys J*. 2004;21:407–417.
56. Bielajew A. Fundamentals of the Monte Carlo method for neutral and charged particle transport. The University of Michigan, Department of Nuclear Engineering and Radiological Sciences; 2016.
57. Kawrakow I, Mainegra-Hing E, Rogers DWO, Tessier F, Walter BRB. The EGSnrc code system: Monte Carlo simulation of electron and photon transport. Report PIRS-701 (National Research Council of Canada; 2010.
58. Kawrakow I. Accurate condensed history Monte Carlo simulation of electron transport: I. EGSnrc, the new EGS4 version. *Med Phys*. 2000;27:485–498.
59. Kawrakow I. Accurate condensed history Monte Carlo simulation of electron transport: II. Application to ion chamber response simulations. *Med Phys*. 2000;27:499–513.
60. Wulff J, Zink K, Kawrakow I. Efficiency improvements for ion chamber calculations in high energy photon beams. *Med Phys*. 2008;35:1328–1336.
61. Kawrakow I, Mainegra-Hing E, Tessier F, Walter BRB. The EGSnrc C++ class library. NRC Report PIRS-898 (rev A) Ottawa, Canada; 2009.
62. Rogers DWO, Kawrakow I, Seuntjens JP, Walter BRB, Mainegra-Hing E. User Codes for EGSnrc. NRC Report PIRS-702 (rev C) Ottawa, Canada; 2015.
63. Walter BRB, Kawrakow I, Rogers DWO. History by history statistical estimators in the BEAM code system. *Med Phys*. 2002;29:2745–2752.
64. Kraft G, Scholz M, Bechthold U. Tumor therapy and track structure. *Radiat Environ Bioph*. 1999;38:229–237.
65. Andreo P, Brahme A. Stopping power data for high-energy photon beams. *Phys Med Biol*. 1986;31:839–858.
66. Czarnecki D, Poppe B, Zink K. Impact of new ICRU Report 90 recommendations on calculated correction factors for reference dosimetry. *Phys Med Biol*. 2018;63:155015.
67. Gomà, C, Andreo P, Sempau J. Spencer–Attix water/medium stopping-power ratios for the dosimetry of proton pencil beams. *Phys Med Biol*. 2013;58:2509–2522.
68. Tilley DR, Weller HR, Cheves CM. Energy levels of light nuclei A = 16-17. *Nucl Phys A*. 1993;564:1-183.
69. Yang Z, Tsai P, Lee S, Liu Y, Chen C, Sato T, Sheu R. Inter-comparison of Dose Distributions Calculated by FLUKA, GEANT4, MCNP, and PHITS for Proton Therapy. EPJ Web Conf. Volume 153, Article Number 04011;2017.
70. Parodi K, Mairani A, Brons S, et al. Monte Carlo simulations to support start-up andtreatment planning of scanned proton and carbon ion therapy at a synchrotron-based facility. *Phys Med Biol*. 2012;57:3759–3784.
71. Parodi K, Mairani A, Sommerer F. Monte Carlo-based parametrization of the lateral dose spread for clinical treatment planning of scanned proton and carbon ion beams. *J Radiat Res*. 2013;54:i91–i96.

IOP Publishing Phys. Med. Biol. 65 (2020) 055015 (17pp) https://doi.org/10.1088/1361-6560/ab6e53

Physics in Medicine & Biology

IPEM Institute of Physics and Engineering in Medicine

OPEN ACCESS

PAPER

Monte Carlo calculation of beam quality correction factors in proton beams using TOPAS/GEANT4

Kilian-Simon Baumann[1,2], **Sina Kaupa**[2], **Constantin Bach**[2], **Rita Engenhart-Cabillic**[1,3] **and Klemens Zink**[1,2,3,4]

[1] Department of Radiotherapy and Radiooncology, University Medical Center Giessen-Marburg, Marburg, Germany
[2] Institute of Medical Physics and Radiation Protection, University of Applied Sciences, Giessen, Germany
[3] Marburg Ion-Beam Therapy Center (MIT), Marburg, Germany
[4] FIAS—Frankfurt Institute for Advanced Studies, Frankfurt, Germany

E-mail: kilian-simon.baumann@staff.uni-marburg.de

Keywords: proton dosimetry, proton therapy, beam quality correction factors, IAEA TRS-398 CoP, Monte Carlo, TOPAS, Geant4

RECEIVED
31 October 2019

REVISED
9 January 2020

ACCEPTED FOR PUBLICATION
21 January 2020

PUBLISHED
6 March 2020

Abstract

To provide Monte Carlo calculated beam quality correction factors (k_Q) for monoenergetic proton beams using TOPAS, a toolkit based on the Monte Carlo code GEANT4.

Monte Carlo simulations of six plane-parallel and four cylindrical ionization chambers were carried out. The latest ICRU 90 recommendations on key data for ionizing-radiation dosimetry were used to calculate the electronic stopping powers and to select the mean energy necessary to create an ion pair in air (W_{air}).

f_{Q_0} factors were calculated for a ^{60}Co spectrum at a depth of 5 g cm^{-2}. f_Q factors and f_Q/f_{Q_0} ratios as well as k_Q factors were calculated at the entrance region of monoenergetic proton beams with energies between 60 MeV and 250 MeV.

Additionally, perturbation correction factors for the Exradin A1SL ionization chamber at an energy of 250 MeV were calculated.

f_{Q_0} factors agreed within 0.7% or better, f_Q factors within 1.7% or better and f_Q/f_{Q_0} ratios within 2.2% or better with Monte Carlo calculated values provided in the literature. Furthermore, k_Q factors calculated in this work were found to agree within 1% or better with experimentally determined k_Q factors provided in the literature, with only two exceptions with deviations of 1.4% and 2.4%.

The total perturbation correction factor for the Exradin A1SL chamber was 0.969(7) and hence significantly different than unity in contrast to the assumption from the IAEA TRS-398 code of practice (CoP).

TOPAS/GEANT4 can be used to calculate k_Q factors in clinical proton beams. k_Q factors for six plane-parallel and four cylindrical ionization chambers were calculated and provided for the upcoming update of the IAEA TRS-398 CoP.

1. Introduction

The IAEA TRS-398 CoP for reference dosimetry in external radiotherapy beams (Andreo *et al* 2000) is currently being updated. The updated TRS-398 CoP will be based on the new ICRU 90 (Seltzer *et al* 2016) recommendations on key data for ionizing-radiation dosimetry. The RTNORM project (RTNORM 2019) is supporting the IAEA with fully Monte Carlo calculated k_Q factors for different ionization chambers and various radiotherapy beams that will be provided in the updated TRS-398 CoP. Furthermore, k_Q factors for monoenergetic proton beams will be provided which is not the case in the current TRS-398 CoP. Hence, there is a need for Monte Carlo calculated k_Q factors in monoenergetic proton beams. Please note that f_Q/f_{Q_0} ratios, which are the basis of Monte Carlo calculated k_Q factors, are the only part of k_Q factors that can be calculated using the Monte Carlo method. When using the term 'Monte Carlo calculated k_Q factors' we mean the Monte Carlo calculation of f_Q/f_{Q_0} ratios and subsequent derivation of k_Q factors by using the $W_{air,Q}$ values.

For ion beams the data of Monte Carlo calculated k_Q factors is scarce. Gomà *et al* (2016) used PENH (Salvat 2013) to calculate k_Q factors in monoenergetic proton beams for nine plane-parallel and three cylindrical ionization chambers. In the version of PENH that was used in that study no proton nuclear interactions were included and hence no secondary particles originating from non-elastic nuclear interactions were transported. Therefore, GAMOS (Arce *et al* 2014) a toolkit based on GEANT4 (Agostinelli *et al* 2003) was used to generate a phase space file in water directly in front of the ionization chamber while proton nuclear interactions were considered. This phase space file was subsequently used in PENH to calculate the dose absorbed in water in a reference volume and the dose absorbed in air in the sensitive volume of the ionization chambers. The so-calculated k_Q factors were compared to experimentally determined values from the literature and found to agree within 1%.

In a study by Gomà and Sterpin (2019) PENH was used to calculate k_Q factors in monoenergetic and modulated proton beams for nine plane-parallel and six cylindrical ionization chambers. In the version of PENH that was used in that study the simulation of proton nuclear interactions (and prompt-gamma emission) for all ICRU 63 (Barschall *et al* 2000) isotopes was included. The k_Q factors agreed with experimentally determined values on the 1% level. The f_Q factors calculated by Gomà and Sterpin (2019) were compared to f_Q factors calculated by Gomà *et al* (2016) for three chambers. Especially for high energies the results from both studies differed. Thus, the authors concluded that proton nuclear interactions should be included in the Monte Carlo calculation of k_Q factors, especially for high energies.

To the best of our knowledge, no other Monte Carlo code than PENH has been used for the calculation of k_Q factors in clinical proton beams so far. However, other Monte Carlo codes like TOPAS (Perl *et al* 2012) a toolkit based on GEANT4 as well as FLUKA (Ferrari *et al* 2005, Böhlen *et al* 2014) have been used for ionization chamber calculations in clinical proton beams: Wulff *et al* (2018) used TOPAS/GEANT4 to calculate f_Q factors for the IBA NACP-02 and Farmer NE 2571 ionization chamber in monoenergetic proton beams with energies between 70 MeV and 250 MeV. Two different nuclear interaction models were used and compared: binary cascade (BIC) and Bertini cascade (BERT). The f_Q factors calculated in that study agreed with those calculated by Gomà *et al* (2016) within 0.6% or better. The difference in f_Q factors for the different nuclear interaction models was 0.3% at maximum. Lourenço *et al* (2019) used FLUKA to calculate perturbation correction factors for three different PTW chambers. In the studies by Wulff *et al* (2018) and Lourenço *et al* (2019) only clinical proton beams and no photon beams (which are needed for the calculation of f_{Q_0} factors) have been investigated.

Hence, in a study by Baumann *et al* (2019) f_{Q_0} factors, f_Q factors and f_Q/f_{Q_0} ratios were calculated in a 1.25 MeV monoenergetic photon and a 150 MeV monoenergetic proton beam for simple air-filled cavities placed in a water phantom. The Monte Carlo codes PENH, FLUKA and TOPAS/GEANT4 were used. The resulting f_Q/f_{Q_0} ratios agreed within 0.7% or better between the codes. Since Gomà *et al* (2016) used PENH to calculate k_Q factors in monoenergetic proton beams in agreement with experimental data within 1%, the authors concluded that both FLUKA and TOPAS/GEANT4 can also be used for the calculation of k_Q factors in clinical proton beams. However, no k_Q factors for ionization chambers were calculated in that study.

Hence, the aim of this study is to calculate k_Q factors for six plane-parallel and four cylindrical ionization chambers in monoenergetic proton beams using the Monte Carlo code TOPAS/GEANT4. These k_Q factors shall be compared to experimentally determined k_Q factors provided in the literature. Furthermore, by providing k_Q factors calculated with a Monte Carlo code different than PENH we add important value, since for ion beams the data of Monte Carlo calculated k_Q factors is scarce and all Monte Carlo calculated k_Q factors for clinical proton beams provided in the literature have been derived using PENH.

Furthermore, the perturbation correction factor p_Q of ionization chambers is assumed to be 1 for proton beams in the IAEA TRS-398 CoP (Andreo *et al* 2000). Gomà and Sterpin (2019) calculated f_Q factors and water to air stopping power ratios $s_{w,air}$ in monoenergetic proton beams and hence were able to derive perturbation correction factors. The authors concluded that the perturbation correction factors of some ionization chambers might be significantly different than unity for proton beams. Hence, perturbation correction factors for one exemplary cylindrical ionization chamber shall be calculated in this study to clarify whether the assumption from the IAEA TRS-398 CoP is sufficiently accurate or not.

2. Materials and methods

2.1. Calculation of k_{Q,Q_0} factors

Monte Carlo k_{Q,Q_0} factors were calculated as (Andreo *et al* 2013):

$$k_{Q,Q_0} = \frac{f_Q}{f_{Q_0}} \frac{W_{\mathrm{air},Q}}{W_{\mathrm{air},Q_0}} = \frac{(D_w/\bar{D}_{\mathrm{air}})_Q}{(D_w/\bar{D}_{\mathrm{air}})_{Q_0}} \frac{W_{\mathrm{air},Q}}{W_{\mathrm{air},Q_0}} \quad (1)$$

Q denotes the user beam quality and Q_0 the reference beam quality. Note that, when ^{60}Co gamma radiation is the reference beam quality, the subscript Q_0 is typically omitted and k_Q is used instead of k_{Q,Q_0}. The factor f is both

chamber-specific and beam quality-dependent and gives the proportionality between the absorbed dose to water at the reference point when the chamber is absent (D_w) and the average absorbed dose to air in the cavity of the air-filled ionization chamber ($\bar{D}_{air}$) (Sempau *et al* 2004). $W_{air,Q}$ is the mean energy necessary to create an ion pair in air depending on the beam quality Q.

The dose values D_w and $\bar{D}_{air}$ were calculated using Monte Carlo simulations. The values for $W_{air,Q}$ were taken from the ICRU 90 (Seltzer *et al* 2016) (33.97 $\pm$ 0.12 eV for electrons, 34.44 $\pm$ 0.14 eV for protons).

2.2. Calculation of perturbation correction factors p_Q

Exemplary perturbation correction factors were calculated as described by Wulff *et al* (2008) for the cylindrical ionization chamber Exradin A1SL and a monoenergetic proton beam of 250 MeV. We calculated the following perturbation factors: p_{cel} that accounts for the central electrode in a cylindrical ionization chamber; p_{stem} that takes into account perturbations produced by the chamber stem; p_{wall} that considers that the material of the wall is different than water; the product of $p_{dis} \cdot p_{cav}$ that accounts for the effective point of measurement and the fact that the dose deposited in the cavity is an average dose deposited in a finite volume. From these perturbation correction factors we calculated the total perturbation correction factor p_Q as (Wulff *et al* 2008):

$$p_Q = p_{cel} \cdot p_{stem} \cdot p_{wall} \cdot p_{dis} \cdot p_{cav} \quad (2)$$

2.3. Possible influence of the death volume for ionization chambers

In a recent study by Pojtinger *et al* (2019) it was shown that the collecting volume of ionization chambers is not necessarily equal to the cavity of the ionization chamber. If a guard ring is present the resulting electric field lines can lead to a death volume in the vicinity of the guard ring inside the cavity. The resulting sensitive volume of the chamber is the cavity minus the death volume since charges produced in this death volume are not collected by the electrodes.

In this study we calculated the dose in the whole cavity of each chamber disregarding the potential death volume. Since the dose deposited in the sensitive volume might be different than the dose deposited in the complete cavity, this might have an effect on the calculated k_Q factors. In order to estimate the potential influence of this death volume on calculated k_Q factors, we calculated the dose deposited in the cavity of the Exradin A1SL chamber in a 250 MeV monoenergetic proton beam while the cavity was divided into 10 thin slabs (thickness of 0.4445 mm each). By investigating the space-resolved dose deposition we can derive the possible effect of the death volume.

2.4. Chamber geometries and materials

We investigated six plane-parallel ionization chambers (PTW Roos, PTW Markus, PTW Advanced Markus, IBA NACP-02, IBA PPC-05 and IBA PPC-40) and four cylindrical ionization chambers (NE 2571, PTW 30013, IBA FC65-G and Exradin A1SL). In table 1 the geometry and material compositions for the plane-parallel ionization chambers are summarized. For graphite the physical density ρ_g is shown since it varies between the manufacturers. The geometries of the cylindrical ionization chambers are too complex to be summarized in a table, hence, in figure 1 cross sections of the cylindrical ionization chambers are shown.

In table 2 all materials used in this study and their physical densities as well as the mean ionization potentials I used to calculate the electronic stopping powers are shown. For air and water we used the physical densities and I-values and for graphite the I-value as given in the ICRU 90.

2.5. Beam qualities and reference conditions

As reference beam quality Q_0 we used a ^{60}Co source. We used the energy spectrum as described by Mora *et al* (1999). The beam was uniform and parallel and impinging perpendicular on the water phantom surface. The field size was $10 \times 10\,cm^2$. The beam was transported through vacuum between the source and the water phantom. Typically, a divergent source is used for high-energy photon simulations that develops a rectangular field at a certain depth in water at a certain distance to the source (see for instance (Wulff *et al* 2008, Zink and Wulff 2012, Gomà and Sterpin 2019)). However, such a source is not implemented in TOPAS/GEANT4 by default. Hence, we used an uniform and parallel beam.

As proton source we took an uniform and parallel beam of $10 \times 10\,cm^2$ impinging perpendicular on the water phantom surface. We investigated eight different monoenergetic beams (60, 70, 80, 100, 150, 160, 200 and 250 MeV). The beam was transported through vacuum between the source and the water phantom.

For the simulations with the ^{60}Co spectrum we followed the IAEA TRS-398 CoP (Andreo *et al* 2000). That is, the reference depth z_{ref} was $5\,g\,cm^{-2}$. For the monoenergetic proton beams we used reference depths z_{ref} of $1\,g\,cm^{-2}$ for low proton energies (60 and 70 MeV) and $2\,g\,cm^{-2}$ for higher energies ($E \geqslant 80$ MeV). Beam quality correction factors k_Q for the cylindrical ionization chambers were only calculated for high energies ($E \geqslant 150$ MeV).

Table 1. Dimensions and materials of the plane-parallel chambers as investigated in this study. ρ_g denotes the physical density of the graphite used in each chamber.

Ionization chamber	Thickness of entrance window	Electrode spacing (mm)	Radius of sensitive volume (mm)	Thickness of collecting electrode
IBA				
NACP-02	0.1 mm PET 0.5 mm graphite $(\rho_g = 1.82\ g\ cm^{-3})$	2	5	50 μm graphite $(\rho_g = 1.82\ g\ cm^{-3})$ 0.25 mm PMMA
PPC-05	0.95 mm C552 50 μm graphite $(\rho_g = 1.82\ g\ cm^{-3})$	0.6	5	50 μm graphite $(\rho_g = 1.82\ g\ cm^{-3})$ 0.45 mm PPE
PPC-40	0.9 mm PMMA 0.1 mm graphite $(\rho_g = 0.93\ g\ cm^{-3})$	2	8	0.1 mm graphite $(\rho_g = 0.93\ g\ cm^{-3})$ 1 mm PMMA
PTW				
Advanced Markus	0.87 mm PMMA 0.3 mm PE	1	2.5	20 μm graphite $(\rho_g = 0.82\ g\ cm^{-3})$
Markus	0.87 mm PMMA 0.4 mm Air 30 μm PE	2	2.65	20 μm graphite $(\rho_g = 1.72\ g\ cm^{-3})$
Roos	1.1 mm PMMA 20 μm graphite $(\rho_g = 0.82\ g\ cm^{-3})$	2	7.5	20 μm graphite $(\rho_g = 0.82\ g\ cm^{-3})$

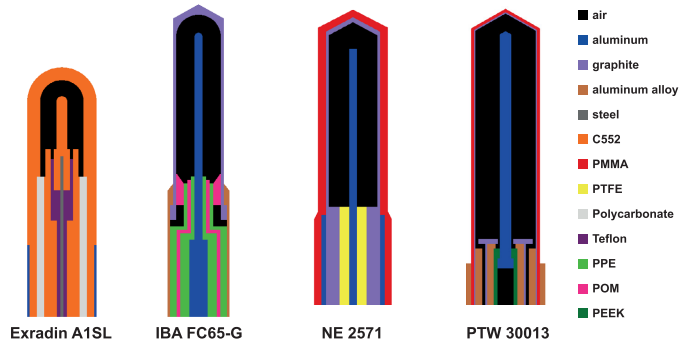

Figure 1. Cross sections of the chamber geometries for the cylindrical ionization chambers investigated in this study. The legend on the right connects the used colours to the corresponding materials. The chambers are not printed true to scale.

The absorbed dose to water D_w was calculated in a disc of 1 cm of radius and 250 μm of height. This disk was centered at z_{ref} in a water phantom of $20 \times 20 \times 20\,cm^3$ for the photon simulations and $20 \times 20 \times 5\,cm^3$ for the proton simulations. We chose to take a smaller water phantom for the proton simulations in order to reduce computing time and since proton backscatter can be considered negligible (Salvat 2013, Gomà *et al* 2016).

To calculate the average absorbed dose to air $\bar{D}_{air}$ in the cavity of the ionization chambers, each ionization chamber was positioned with its reference point at z_{ref}. For plane-parallel chambers, the reference point is at the center of the inner surface of the chamber's entrance window. For cylindrical chambers the reference point corresponds to the center of the cavity on the symmetry axis.

2.6. TOPAS/GEANT4

We used TOPAS (TOol for PArticle Simulation) version 3.1.p1 (Perl *et al* 2012), a toolkit based on the Monte Carlo code GEANT4 (GEometry And Tracking) version geant4-10-03-patch-01 (Agostinelli *et al* 2003). Since TOPAS is based on GEANT4, it uses the same physics models, processes, and interaction models. TOPAS

Table 2. Mass densities ρ and mean excitation energies I of the different materials as used in this study in alphabetical order.

Material	ρ (g cm^{-3})	I (eV)
Air	0.0012	85.7
Aluminum	2.70	166.0
Aluminum alloy	2.70	166.4
C552 (shonka)	1.76	86.8
Graphite	0.82–1.82	81.0
Polycarbonate	1.20	73.1
Polyether ether ketone (PEEK)	1.31	74.1
Polyether methacrylate (PMMA)	1.19	74.0
Polyethylene (PE)	0.93	56.5
Polyethylene terephthalate (PET)	1.50	78.7
Polyoxymethylene (POM)	1.43	77.4
Polyphenyl ether (PPE)	1.06	64.0
Polystyrene	1.05	68.7
Polytetrafluoroethylene (PTFE/Teflon)	2.25	99.1
Silicone	1.10	88.0
Steel	8.06	317.7
Water	0.9982	78.0

has been tested extensively against experimental data (Perl *et al* 2012, Testa *et al* 2013). TOPAS is capable of transporting various kinds of particles including photons, electrons, positrons, neutrons, protons, and heavy ions. In GEANT4, electro-magnetic (EM) interactions of the charged particles are grouped in the condensed history (CH) approach. A multiple scattering (MSC) algorithm is used to calculate the angular deflection of all soft collisions at the end of a given step. O'Brien *et al* (2016) and Wulff *et al* (2018) showed that TOPAS passes the Fano test within 0.1% for photons and 0.1%–0.2% for protons (depending on the beam geometry) as long as the appropriate physics lists are used and as long as these physics lists are tuned to calculate the radiation transport accurately enough. In another study by Simiele and DeWerd (2018) different transport parameters, multiple scattering algorithms and versions of GEANT4 were investigated with the conclusion that depending on the multiple scattering algorithm used, the step size has to be limited in order to pass the Fano test within less than 0.5%. Based on the findings by O'Brien *et al* (2016) and Wulff *et al* (2018), Baumann *et al* (2019) showed that TOPAS/GEANT4 can be used to calculate f_Q/f_{Q_0} ratios (which are the basis of Monte Carlo calculated k_Q factors, compare equation (1)) in clinical proton beams for simple air-filled cavities placed in a water phantom. Hence, in this study we used the same physics lists and settings as used by Baumann *et al* (2019). For the photon simulations we used the physics list **g4em-standard_opt3** that makes use of the *G4UrbanMscModel* (Urban 2002) to describe the multiple scattering of all charged particles. For the proton simulations we used the physics list **g4em-standard_opt4** which makes use of the models *WentzelVI* (Ivanchenko *et al* 2010) and *Goudsmit–Saunderson* (Goudsmit and Saunderson 1940a, 1940b) for the multiple scattering of charged particles: for electrons and positrons with energies below 100 MeV, the *Goudsmit–Saunderson* model is used. For electrons and positrons with an energy above 100 MeV and for protons with energies below 500 MeV, the *WentzelVI* model is used. The multiple scattering models used in this study are summarized in table 3. Please note that the Goudsmit–Saunderson model is not implemented by default in the version geant4-10-03-patch-01 which is used in this study but has been implemented by us.

We used the physics list **g4h-phy_QGSP_BIC_HP** to manage the simulation of non-elastic nuclear interactions. The *Binary Cascade* model (Folger *et al* 2004) is used in this list for inelastic nucleon-nucleus processes. Furthermore, we used the default physics lists **g4ion-binarycascade**, **g4decay**, **g4h-elastic_HP** and **g4stopping**.

To control the length of a step in the CH, the parameter *dRoverR* is used in GEANT4. This parameter describes the maximum length of a step in relation to the residual range of the particle. For the photon simulations we set *dRoverR* to 0.003, for the proton simulation to 0.05. While losing energy, the maximum length of a step in the CH decreases until it gets smaller than the *finalRange*, below which the particle is ranged out in a single step. For the photon simulations we set *finalRange* to 1 nm, for the proton simulations to 100 nm. The parameter controlling the production of secondaries is given in units of length in GEANT4. Secondary particles with a *continuous slowing down approximation* range (R_{CSDA}) lower than this production cut are absorbed on the spot. The default production cut in the whole geometry was set to 500 μm, corresponding to $\sim$200 keV electrons in water. Within the ionization chamber and a surrounding envelope, the production cut was set to 1 μm (corresponding to $<$10 keV electrons in water). Note that in the study by Baumann *et al* (2019) a production cut of 0.065 μm was used (which corresponds to $\sim$1 keV electrons in water). In order to save computing time, we increased this value. We checked that this larger production cut has no significant influence on the calculation of f_{Q_0} and f_Q factors. This

Table 3. Multiple scattering models used in TOPAS/GEANT4 for the photon and proton simulations.

Radiation field	Multiple scattering model for e^+/e^-	Multiple scattering model for primaries
^{60}Co spectrum	Urban model	/
Monoenergetic protons	Goudsmit–Saunderson (E $\leqslant$ 100 MeV) Wentzel VI (E $>$ 100 MeV)	Wentzel VI (E $\leqslant$ 500 MeV)

Table 4. Production cuts and transport simulation parameters used in TOPAS/GEANT4 for the photon and proton simulations.

		dRoverR		*finalRange* (nm)	
Region	Production cut (μm)	Photon-sim.	Proton-sim.	Photon-sim.	Proton-sim.
Scoring volume and envelope	1	0.003	0.05	1	100
Water phantom	500	0.003	0.05	1	100

has also been investigated for f_Q factors in proton beams by Wulff *et al* (2018) with the same result. To ensure that the secondary particle fluence in the ionization chamber is not affected by the higher production cut in the water phantom, we used an envelope surrounding the ionization chamber with a thickness equal to the production cut applied in the water phantom (500 μm) multiplied by a safety factor of 1.2. The safety factor of 1.2 is applied to account for the possibility that an electron may travel a distance larger than R_{CSDA} due to energy-loss straggling (Sempau and Andreo 2006). Since the lowest energy GEANT4 can handle is 990 eV by default, the production cut is automatically adapted in materials where the production cut of 1 μm corresponds to an energy $<$990 eV. For example, the production cut in air is set to 47.2 μm, which is the maximum range of 990 eV electrons in air. All production cuts and transport simulation parameters are summarized in table 4.

No variance reduction techniques were used. The statistical uncertainties were estimated by combining the uncertainties from independent runs performed with different random seeds as described in Bielajew (2016).

3. Results and discussion

3.1. f_{Q_0} factors for the ^{60}Co spectrum

In table 5 the Monte Carlo calculated f_{Q_0} factors for the ^{60}Co spectrum for all ionization chambers investigated in this study are shown. The values within parenthesis correspond to one standard uncertainty in the last digit. Furthermore, combined data for $f_{Q_0} = (s_{w,air})_{Q_0} \cdot p_{Q_0}$ as provided by the upcoming revision of the TRS-398 CoP (Andreo *et al* 2019) is shown. The given values are the average of 16 different f_{Q_0} factors all calculated with Monte Carlo codes (EGS*nrc*, PENH, PENELOPE, and TOPAS/GEANT4, while the TOPAS/GEANT4 results are those from this study). Chambers were modeled using blue prints or geometries published in former studies.

For all chambers the f_{Q_0} factors calculated in this study agree within one standard uncertainty with the values provided by Andreo *et al* (2019).

In figures 2 and 3 in the upper panels the f_{Q_0} factors for the plane-parallel and cylindrical ionization chambers are shown along with various values published in the literature. In the bottom panel the relative deviations between the values from this study and the values from the literature are shown. The values published in the literature were derived using different Monte Carlo codes and partly different sets of *I*-values. An overview of these characteristics is given in table 6.

For each chamber the deviation between the f_{Q_0} factor calculated in this study using TOPAS/GEANT4 and the factors published in the literature is smaller than 0.7% (independently on the choice of *I*-values). For almost each chamber the f_{Q_0} factor calculated in this study agrees with each published value within two standard deviations or better. The only exceptions are for the PTW Roos chamber and the results from Zink and Wulff (2012) as well as the IBA PPC-40 chamber and the results from Gomà *et al* (2016). Taking into account the variance between the f_{Q_0} factors published in the literature using different Monte Carlo codes and sets of *I*-values, TOPAS/GEANT4 can be used equivalently for the calculation of f_{Q_0} factors for both plane-parallel and cylindrical ionization chambers in ^{60}Co beams as long as the physics settings are adapted accordingly. Note that the variance between f_{Q_0} factors published in the literature is larger for plane-parallel ionization chambers compared to cylindrical chambers.

Table 5. Monte Carlo calculated f_{Q_0} factors for ^{60}Co radiation for different plane-parallel and cylindrical ionization chambers. The values within parenthesis correspond to one standard uncertainty in the last digit.

Chamber	f_{Q_0} this study	f_{Q_0} Andreo *et al* (2019)
PTW Roos	1.143(3)	1.142(5)
PTW Markus	1.149(4)	1.143(5)
PTW Adv. Markus	1.142(4)	1.143(5)
IBA NACP-02	1.158(3)	1.154(5)
IBA PPC-05	1.144(4)	1.141(5)
IBA PPC-40	1.148(2)	1.142(5)
NE 2571	1.110(3)	1.108(4)
PTW 30013	1.112(3)	1.109(4)
IBA FC65-G	1.111(3)	1.108(4)
Exradin A1SL	1.102(5)	1.103(4)

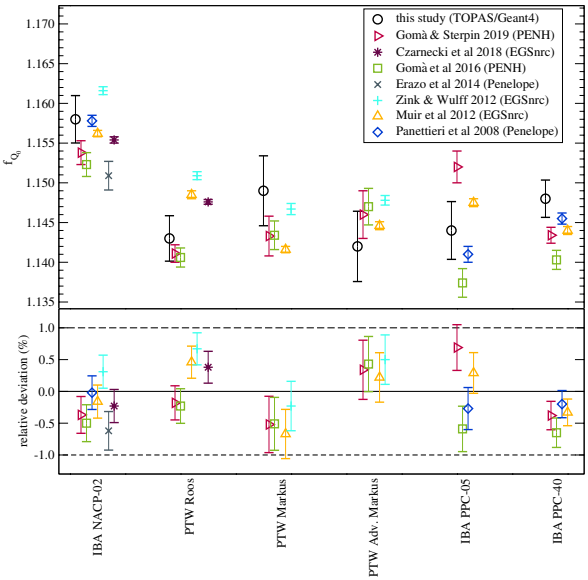

Figure 2. In the upper graph Monte Carlo calculated f_{Q_0} factors for ^{60}Co radiation for different plane-parallel chambers and comparison with values from the literature are shown (see table 6 for further explanation). In the bottom graph the relative deviations between the values from this study and the values from the literature are shown. For better clarity, the 0% deviation is marked with a solid line and the ±1% deviations are marked with dashed lines. The error bars correspond to one standard uncertainty.

3.2. f_Q factors for monoenergetic proton beams

In table 7 the f_Q factors for all ionization chambers investigated in this study are shown as a function of the initial energy of the monoenergetic proton beams. The depth z_{ref} at which the chambers were positioned is depicted as well. The values within parenthesis correspond to one standard uncertainty in the last digit(s).

Furthermore, the water to air stopping power ratios $s_{w,air}$ as calculated by Gomà and Sterpin (2019) are given for the different beam qualities in order to estimate perturbation correction factors as done in section 3.3.

Figures 4 and 5 show the f_Q factors from this study along with f_Q factors published in the literature. Some of the values published in the literature were derived using different Monte Carlo codes. An overview of the corresponding characteristics is given in table 8.

For the IBA NACP-02 the f_Q factors agree within one standard deviation for energies up to 150 MeV. For higher energies the differences are up to 1.2% between this study and Gomà and Sterpin (2019), 0.9% between

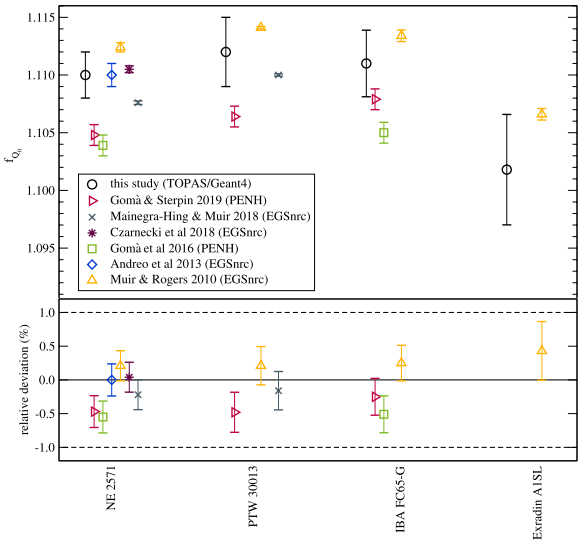

Figure 3. In the upper graph Monte Carlo calculated f_{Q_0} factors for ^{60}Co radiation for different cylindrical chambers and comparison with values from the literature are shown (see table 6 for further explanation). In the bottom graph the relative deviations between the values from this study and the values from the literature are shown. For better clarity, the 0% deviation is marked with a solid line and the $\pm 1\%$ deviations are marked with dashed lines. The error bars correspond to one standard uncertainty.

this study and Gomà *et al* (2016) and 0.5% between this study and Wulff *et al* (2018). The reason for the difference in f_Q factors between this study and Wulff *et al* (2018) is that in this study the geometry of the IBA NACP-02 is slightly different and a smaller value for *dRoverR* and *finalRange* has been taken.

For the PTW Roos chamber the differences between the f_Q factors calculated in this study and the values from Gomà and Sterpin (2019) are significant for both low and high energies. The maximum deviation is -1% for an energy of 250 MeV while the deviation for low energies is about 0.4%. Differences between the f_Q factors calculated in this study and the values from Lourenço *et al* (2019) are $\sim$0.1% for the energies 60 MeV and 250 MeV while the deviation for an energy of 150 MeV is 0.4%.

For all plane-parallel chambers it can be seen that the f_Q factors agree within two standard uncertainties or better between this study and the studies by Gomà and Sterpin (2019) and Gomà *et al* (2016) for low energies and begin to diverge for higher energies. Only for the PTW Roos chamber as already mentioned and the PTW Adv. Markus chamber significant differences in the f_Q factors between the studies can be seen for low energies. Note that Gomà *et al* (2016) used a different geometry for the IBA PPC-05 chamber, hence the deviations of the f_Q factors relative to this study are quite large. The largest deviation of f_Q factors between this study and the values published in the literature is 1.7% and can be seen for the PTW Markus chamber at an energy of 250 MeV.

For the f_Q factors for cylindrical ionization chambers as shown in figure 5 the factors calculated in this study agree within $<$0.1% with those calculated by Wulff *et al* (2018) for 150 MeV and 200 MeV. For 250 MeV a deviation of $\sim$0.5% is visible. In contrast to the calculation of the IBA NACP-02 chamber, the geometry of the NE 2571 chamber used in this study is exactly the same as used by Wulff *et al* (2018). The only remaining difference between these two studies is that in this study a smaller value for *dRoverR* and *finalRange* has been taken.

For all cylindrical chambers the f_Q factors calculated in this study agree within one standard uncertainty with the factors calculated by Gomà *et al* (2016). Again, the values calculated by Gomà and Sterpin (2019) agree with the factors from this study only for low energies (e.g. 150 MeV) within one standard uncertainty. For higher energies the values do not agree within two standard uncertainties. The largest deviation of 1.3% can be seen for the NE 2571 chamber at an energy of 250 MeV.

In general, the agreement between the values from this study and the values from Gomà *et al* (2016) is better than the agreement between this study and the values from Gomà and Sterpin (2019). The difference between these two studies (Gomà and Sterpin (2019) and Gomà *et al* (2016)) is that in the study from 2019 proton nuclear

Table 6. Description of the values for f_{Q_0} from the literature in chronological order.

Study	Monte Carlo code	I_w (eV)	I_g (eV)	Comments
Gomà and Sterpin (2019)	PENH	78	81.1	—
Czarnecki *et al* (2018)	EGS*nrc*	78	81.1	Values provided in private communication
Mainegra-Hing and Muir (2018)	EGS*nrc*	78	81.1	Values provided in Gomà and Sterpin (2019)
Gomà *et al* (2016)	PENH	78	81.1	—
Erazo *et al* (2014)	PENELOPE-2011	75	78	Values provided in Gomà *et al* (2016)
Andreo *et al* (2013)	EGS*nrc*	78	81.1	—
Zink and Wulff (2012)	EGS*nrc*	75	78	Calculated perturbation correction factors p_{Q_0}: $f_{Q_0} = p_{Q_0} \cdot s_{w,\mathrm{air}}$ ($s_{w,\mathrm{air}} = 1.133$)
Muir *et al* (2012)	EGS*nrc*	75	78	Values provided in Gomà *et al* (2016)
Muir and Rogers (2010)	EGS*nrc*	75	78	Values provided in private communication
Panettieri *et al* (2008)	PENELOPE-2006	75	78	Used three different ^{60}Co sources: we used the weighted mean of the corresponding f_{Q_0} factors

Table 7. Monte Carlo calculated f_Q factors for monoenergetic proton beams as a function of initial proton energy and the depth z_{ref} at which the chambers were positioned. The values within parenthesis correspond to one standard uncertainty in the last digit(s).

Q	60 MeV	70 MeV	80 MeV	100 MeV	150 MeV	160 MeV	200 MeV	250 MeV
z_{ref} (g cm^{-2})	1	1	2	2	2	2	2	2
$s_{w,air}$	1.130	1.130	1.130	1.130	1.129	1.129	1.129	1.129
PTW Roos	1.1219(5)	1.1237(6)	1.1235(6)	1.1239(7)	1.1242(8)	1.1247(9)	1.1220(11)	1.1177(12)
PTW Markus	1.1344(15)	1.1341(15)	1.1318(14)	1.1353(17)	1.1318(23)	1.1321(21)	1.1291(27)	1.1226(34)
PTW Adv. Markus	1.1365(12)	1.1345(15)	1.1348(15)	1.1343(16)	1.1329(22)	1.1331(23)	1.1315(25)	1.1252(28)
IBA NACP-02	1.1177(7)	1.1198(8)	1.1196(7)	1.1209(10)	1.1213(12)	1.1201(12)	1.1211(14)	1.1141(15)
IBA PPC-05	1.1139(8)	1.1157(10)	1.1162(9)	1.1181(12)	1.1200(14)	1.1169(19)	1.1156(28)	1.1122(20)
IBA PPC-40	1.1210(5)	1.1229(5)	1.1215(5)	1.1225(6)	1.1206(8)	1.1212(9)	1.1196(10)	1.1157(11)
NE 2571					1.1232(9)	1.1225(9)	1.1185(11)	1.1115(12)
PTW 30013					1.1257(9)	1.1244(9)	1.1211(11)	1.1168(11)
IBA FC65-G					1.1237(10)	1.1223(10)	1.1192(11)	1.1137(12)
Exradin A1SL					1.1073(23)	1.1036(26)	1.1035(30)	1.0938(34)

Table 8. Description of the values for f_Q from the literature in chronological order.

Study	Monte Carlo code	I_w (eV)	I_g (eV)	Comments
Gomà and Sterpin (2019)	PENH	78	81.1	Chamber positioned at same depths as in this study
Lourenço *et al* (2019)	FLUKA	78	81.1	Calculated perturbation correction factors and stopping power ratios Values provided in private communication Used a slightly different (∼180 μm) depth No transport of electrons
Wulff *et al* (2018)	TOPAS/GEANT4	78	81.1	We used the values derived using the BIC model Values for 70 MeV not considered since a different depth has been used
Gomà *et al* (2016)	PENH	78	81.1	Values for 70 MeV not considered since a different depth has been used

interactions have been activated in PENH. In the study from 2016 no proton nuclear interactions have been included in PENH. However, the simulations were combined with simulations performed with GAMOS (Arce *et al* 2014) a toolkit based on GEANT4 where nuclear interactions were included, which might explain the better agreement between this study and the study by Gomà *et al* (2016). Furthermore, Gomà and Sterpin (2019) discussed that the differences in f_Q factors for higher energies might be due to differences in the nuclear interaction models. To investigate this statement, we recalculated the f_Q values for the IBA NACP-02 and NE 2571 for an energy of 250 MeV without the use of nuclear interaction models (n.i.m.) by deactivating the physics list **g4h-phy_QGSP_BIC_HP**. The results are shown in figure 6: PENH with n.i.m. corresponds to the values from Gomà and Sterpin (2019) while PENH with n.i.m. from GEANT4 corresponds to the values from Gomà *et al* (2016). The f_Q factors calculated with TOPAS/GEANT4 increase by roughly 1.5% when deactivating the nuclear interaction model. For PENH it is the other way round: the f_Q factors are larger when nuclear interaction models are activated. Interestingly, the values calculated with TOPAS/GEANT4 without the activation of nuclear interaction models agree with those calculated with PENH when these models are activated. However, it is not possible to identify the role of nuclear interaction models for the calculation of f_Q factors in proton beams from these results. This remains an issue to be solved in further investigations.

3.3. Perturbation correction factors for monoenergetic proton beams

From the f_Q factors and water to air stopping power ratios $s_{w,air}$ as shown in table 7 the total perturbation correction factors p_Q can be derived as $p_Q = f_Q/(s_{w,air})_Q$. It can be seen that for some chambers and energies the perturbation correction factors are significantly different than unity in contrast to the assumption from the IAEA TRS-398 CoP (Andreo *et al* 2000). To investigate which part of the chamber might lead to this difference we calculated the perturbation correction factors for the Exradin A1SL chamber at 250 MeV. The results are shown in table 9. The perturbation factor with the largest influence is p_{wall} which accounts for the influence of the chamber wall. The total perturbation correction factor p_Q is 0.969(7). Hence, it can be concluded that the assumption of the IAEA TRS-398 CoP (that all perturbation correction factors in proton beams are 1 for all

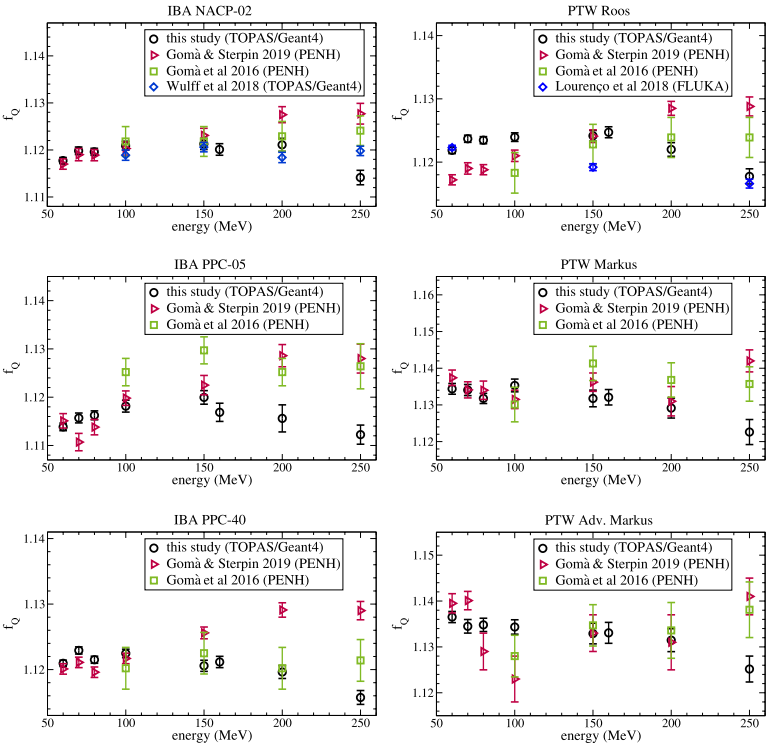

Figure 4. Monte Carlo calculated f_Q factors for monoenergetic proton beams as a function of initial proton energy for different plane-parallel chambers and comparison with values from the literature. The error bars correspond to one standard uncertainty.

ionization chambers) might not be sufficiently accurate for all chambers and proton energies—especially in the case for the factor p_{wall}.

3.4. k_Q factors for monoenergetic proton beams

In table 10 the k_Q factors for all ionization chambers investigated in this study are shown as a function of the initial energy of the monoenergetic proton beams. The depth z_{ref} at which the chambers were positioned is depicted as well. The values within parenthesis correspond to one standard uncertainty in the last digit(s).

To compare the results from this study with Monte Carlo calculated values published in the literature, we decided not to compare the k_Q factors itself but the f_Q/f_{Q_0} ratios which are the basis of Monte Carlo calculated k_Q factors. In figures 7 and 8 f_Q/f_{Q_0} ratios from this study along with f_Q/f_{Q_0} ratios published in the literature are shown. Note that both Gomà and Sterpin (2019) and Gomà *et al* (2016) used the same $W_{\text{air},Q}$ values as in this study.

For the plane-parallel chambers the f_Q/f_{Q_0} ratios between this study and Gomà and Sterpin (2019) agree within two standard uncertainties or better for low energies, except for the IBA PPC-05. For high energies the difference in f_Q/f_{Q_0} ratios increases up to 2.2%. The agreement between this study and Gomà *et al* (2016) is better compared to the agreement with Gomà and Sterpin (2019) except for the IBA PPC-05. However, the chamber model used by Gomà *et al* (2016) is different from that used in this study as discussed by Gomà and Sterpin (2019).

The same can be seen for the cylindrical chambers: while the maximum difference between this study and Gomà and Sterpin (2019) is 1.8% for the NE 2571, the maximum difference between this study and Gomà *et al* (2016) is 0.8%.

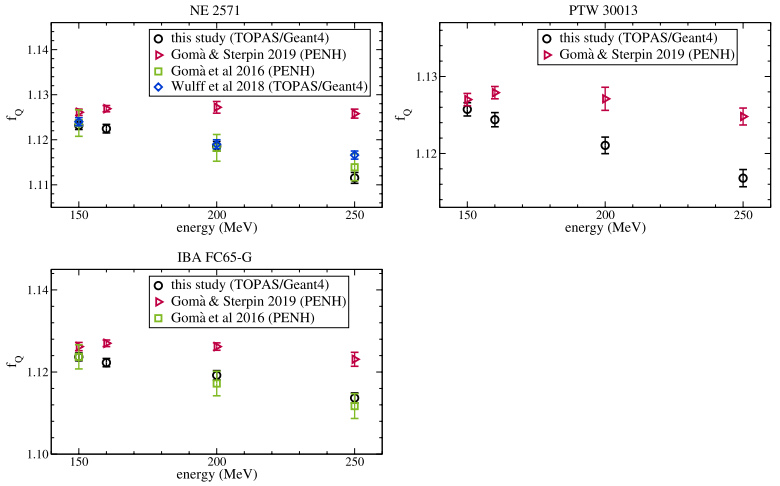

Figure 5. Monte Carlo calculated f_Q factors for monoenergetic proton beams as a function of initial proton energy for different cylindrical chambers and comparison with values from the literature. The error bars correspond to one standard uncertainty.

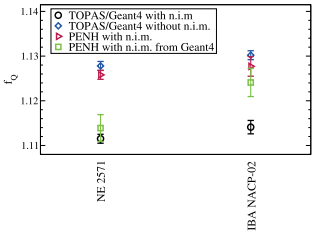

Figure 6. Monte Carlo calculated f_Q factors for the IBA NACP-02 and NE 2571 at an energy of 250 MeV with and without the use of nuclear interactions models (n.i.m.) calculated with TOPAS/GEANT4 and the f_Q factors calculated with PENH taken from Gomà and Sterpin (2019) and Gomà *et al* (2016). The uncertainties represented by error bars correspond to one standard uncertainty.

Table 9. Perturbation correction factors for the Exradin A1SL chamber at a proton energy of 250 MeV. The values within parenthesis correspond to one standard uncertainty in the last digit.

Perturbation correction factor	Value
p_{cel}	0.996(4)
p_{stem}	0.995(4)
p_{wall}	0.970(3)
$p_{dis} \cdot p_{cav}$	1.007(3)
p_Q	0.969(7)

In general, the agreement for low energies is better than for higher energies. The differences for high energies might be due to differences in the nuclear interaction models used in the different Monte Carlo codes as discussed above and by Gomà *et al* (2016) and in parts by Baumann *et al* (2019). Of course, the differences in f_Q/f_{Q_0} ratios might also be due to slight differences in the geometry of the chamber models and the materials used between this study and Gomà and Sterpin (2019) and Gomà *et al* (2016). Note that Gomà and Sterpin (2019) provided the physical densities and mean excitation energies of the materials used in their study which are approximately the same values as used in this study, except for small differences in some plastics. Gomà *et al* (2016) did not provide these values. Furthermore, in a study by Baumann *et al* (2019) f_Q/f_{Q_0} ratios were calculated for simple

Table 10. Monte Carlo calculated k_Q factors for monoenergetic proton beams as a function of initial proton energy and the depth z_{ref} at which the chambers were positioned. The values within parenthesis correspond to one standard uncertainty in the last digit.

Q	60 MeV	70 MeV	80 MeV	100 MeV	150 MeV	160 MeV	200 MeV	250 MeV
z_{ref} (g cm^{-2})	1	1	2	2	2	2	2	2
PTW Roos	0.995(6)	0.997(6)	0.996(6)	0.997(6)	0.997(6)	0.997(6)	0.995(6)	0.991(6)
PTW Markus	1.001(7)	1.000(7)	0.998(7)	1.001(7)	0.998(7)	0.999(7)	0.996(7)	0.990(7)
PTW Adv. Markus	1.009(7)	1.007(7)	1.007(7)	1.007(7)	1.006(7)	1.006(7)	1.004(7)	0.999(7)
IBA NACP-02	0.979(6)	0.980(6)	0.980(6)	0.981(6)	0.982(6)	0.981(6)	0.981(6)	0.975(6)
IBA PPC-05	0.987(6)	0.989(6)	0.989(6)	0.991(6)	0.992(6)	0.990(6)	0.989(6)	0.986(6)
IBA PPC-40	0.990(6)	0.992(6)	0.991(6)	0.991(6)	0.990(6)	0.990(6)	0.989(6)	0.986(6)
NE 2571					1.026(6)	1.025(6)	1.022(6)	1.015(6)
PTW 30013					1.027(6)	1.025(6)	1.022(6)	1.018(6)
IBA FC65-G					1.026(6)	1.024(6)	1.022(6)	1.017(6)
Exradin A1SL					1.019(7)	1.015(7)	1.015(7)	1.006(8)

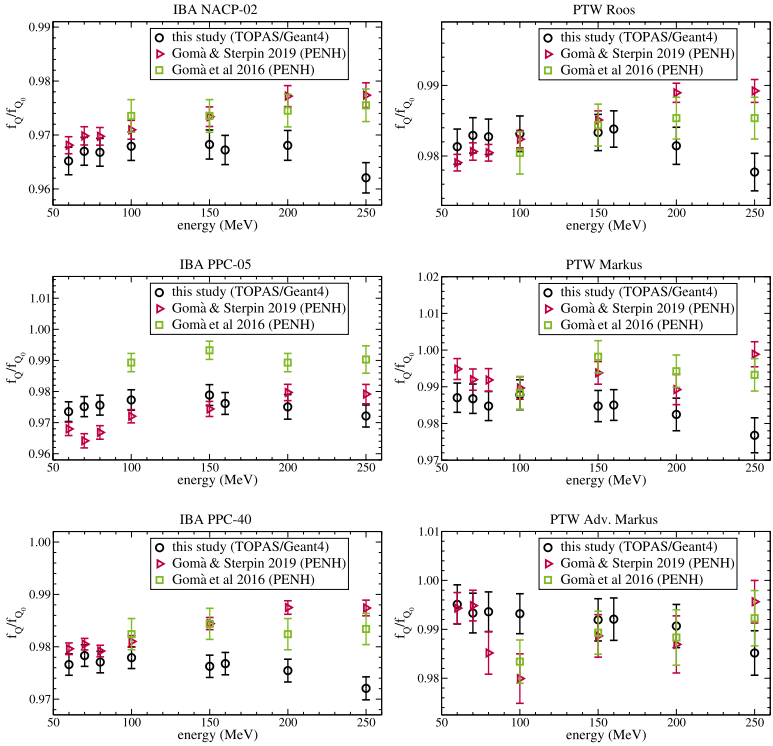

Figure 7. Monte Carlo calculated f_Q/f_{Q_0} ratios for monoenergetic proton beams as a function of initial proton energy for different plane-parallel chambers and comparison with values from the literature. The error bars correspond to one standard uncertainty.

air-filled cavities as representatives of plane-parallel and cylindrical ionization chambers with different Monte Carlo codes (PENH, FLUKA and TOPAS/GEANT4). A monoenergetic 150 MeV proton beam has been used and the cavities were positioned at a depth of 2 g cm^{-2}. The maximum deviation of the f_Q/f_{Q_0} ratios between the codes was 0.7%. The maximum difference of f_Q/f_{Q_0} ratios found in this study for an energy of 150 MeV for the plane-parallel chambers is 1.4%. For the cylindrical chambers and an energy of 150 MeV it is 0.8%. Hence, the

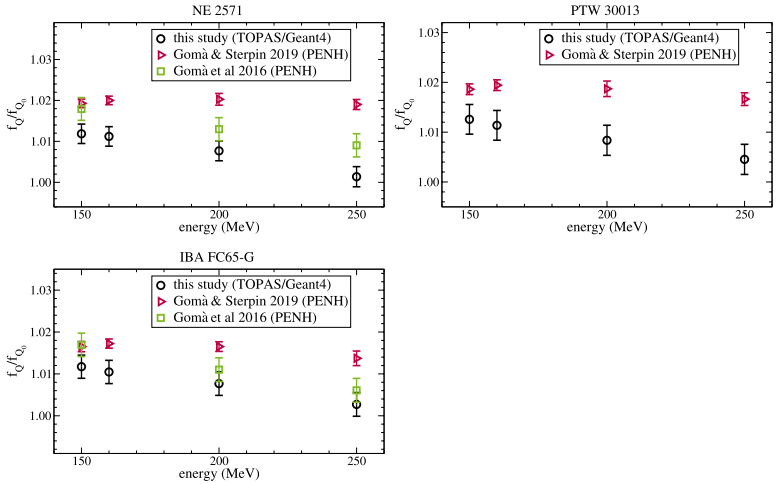

Figure 8. Monte Carlo calculated f_Q/f_{Q_0} ratios for monoenergetic proton beams as a function of initial proton energy for different cylindrical chambers and comparison with values from the literature. The error bars correspond to one standard uncertainty.

Table 11. Ratios of k_Q factors in a 70 MeV monoenergetic proton beam, at a reference depth of 2 g cm^{-2}, for different ionization chambers studied in this study and comparison with experimental values in the literature for non-modulated beams. The values within parenthesis correspond to one standard uncertainty in the last digit. In the right column the relative deviations between the values from this study and the values from the literature are given.

Ionization chambers	This study	Palmans *et al* (2001)	Palmans *et al* (2002)	Deviation (%)
IBA FC65-G/NE 2571	1.000(4)	0.997(3)		0.3
IBA NACP-02/NE 2571	0.920(3)		0.930(3)	−1.0
PTW Markus/NE 2571	0.942(4)		0.940(3)	0.2
PTW Roos/NE 2571	0.935(2)		0.937(3)	−0.2
R_{res} (g cm^{-2})	2.10	2.65	2.65	

deviations of f_Q/f_{Q_0} ratios for real ionization chambers are in the order of the deviations for simple air-filled cavities, although the geometries are more complex.

To validate whether the nuclear interaction models lead to larger deviations between the Monte Carlo codes independent on the chamber geometry, we re-calculated the simulations for simple air-filled cavities as done by Baumann *et al* (2019) for an energy of 250 MeV. We used exactly the same geometries, physics lists and source parameters. The largest difference between TOPAS/GEANT4 and PENH for an energy of 250 MeV was 0.6% and hence comparable to the differences observed for an energy of 150 MeV. Interestingly, the difference between the codes does not increase with energy for simple air-filled cavities as it is the case for the ionization chambers. Hence, it might be that differences between the codes occur because of the materials and/or complexity of the chamber geometries.

In order to further validate the k_Q factors calculated with TOPAS/GEANT4 in this study, in table 11 the ratios of k_Q factors are shown for some of the ionization chambers and compared to experimental data. Palmans *et al* (2001) and Palmans *et al* (2002) determined experimentally the ratios of k_Q factors between different chambers and the NE 2571 as a reference chamber. A non-modulated proton beam with $R_{res} = 2.65$ cm has been used. Hence, we re-calculated the corresponding chambers (NE 2571, IBA FC65-G, IBA NACP-02, PTW Markus and PTW Adv. Markus) in a 70 MeV monoenergetic proton beam ($R_{res} = 4.10$ cm) at a depth of 2 g cm^{-2}. In the studies by Palmans *et al* (2001) and Palmans *et al* (2002) the ratios of k_Q factors were not reported explicitly but can be found in Gomà *et al* (2016). For all four ratios of k_Q factors the deviation between the ratios calculated in this study and the experimentally determined values are 1% at maximum.

In table 12 ratios of k_Q factors are shown for several ionization chambers that were determined by Gomà *et al* (2015). For the comparison we took the values determined in a non-modulated proton beam with $R_{res} \approx 6$ cm. This corresponds to an initial proton energy of 100 MeV and a chamber depth of 2 g cm^{-2}. Hence, we calculated the k_Q factors for the IBA FC65-G and PTW 30013 in a 100 MeV proton beam at that depth. For the IBA NACP-02,

Table 12. Ratios of k_Q factors in a 100 MeV monoenergetic proton beam, at a reference depth of 2 g cm^{-2}, for different ionization chambers studied in this study and comparison with experimental values in the literature for non-modulated beams. The values within parenthesis correspond to one standard uncertainty in the last digit. In the right column the relative deviations between the values from this study and the values from the literature are given.

Ionization chambers	This study	Gomà *et al* (2015)	Deviation (%)
IBA NACP-02/FC65-G	0.947(4)	0.943(4)	0.4
PTW Adv. Markus/FC65-G	0.972(5)	0.949(4)	2.4
PTW Markus/FC65-G	0.967(5)	0.953(4)	1.4
PTW Roos/FC65-G	0.962(4)	0.960(4)	0.2
PTW 30013/FC65-G	0.999(4)	1.002(4)	−0.3
R_{res} (g cm^{-2})	5.76	5.93	

Table 13. Monte Carlo calculated k_Q factors in monoenergetic proton beams for different ionization chambers studied in this study and comparison with experimental values in the literature for non-modulated beams. The values within parenthesis correspond to one standard uncertainty in the last digit(s). In the right column the relative deviations between the values from this study and the values from the literature are given.

Ionization chamber	Energy (MeV)	This study	Medin *et al* (2006)	Medin (2010)	Deviation (%)
IBA FC65-G	150	1.026(6)	1.021(7)		0.5
NE 2571	150	1.026(6)	1.021(7)		0.5
NE 2571	160	1.025(6)		1.032(13)	−0.7

PTW Roos and PTW 30013 the deviations of the ratios of k_Q factors calculated in this study are smaller than 0.5% compared to the experimentally determined ratios. For the PTW Markus chamber the deviation is 1.4% and for the PTW Adv. Markus it is 2.4%. Note that the deviation for the ratio of k_Q factors including the PTW Markus chamber is only 0.2% compared to the experimentally determined ratio of k_Q factors from Palmans *et al* (2002) (see table 11).

At last, Medin (2010) experimentally determined the k_Q factor for the NE 2571 in a proton beam with $R_{res} = 16.5$ cm. Correspondingly, we took the k_Q factor calculated for an initial energy of 160 MeV at a depth of 2 g cm^{-2} ($R_{res} = 15.74$ g cm^{-2}). Medin *et al* (2006) experimentally determined the k_Q factors for the NE 2571 and the IBA FC65-G and a proton beam with $R_{res} = 14.7$ cm. Correspondingly, we took the k_Q factors calculated for an initial energy of 150 MeV at a depth of 2 g cm^{-2} ($R_{res} = 13.85$ g cm^{-2}). The k_Q factors calculated in this study as well as the experimentally determined values by Medin (2010) and Medin *et al* (2006) are shown in table 13. The maximum deviation between the k_Q factors calculated in this study relative to the k_Q factors determined experimentally is 0.7%.

In conclusion, the comparison of k_Q factors and ratios of k_Q factors calculated in this study using the Monte Carlo code TOPAS/GEANT4 with experimental values shows good agreement on the 1% level with only two exceptions for the PTW Adv. Markus chamber (2.4%) and the PTW Markus chamber (1.4%). However, for the PTW Markus chamber we also found good agreement (deviation of only 0.2%) when the ratio of k_Q factors was compared to the experimentally determined values from Palmans *et al* (2002).

3.5. Possible influence of the death volume for ionization chambers

In figure 9 the dose deposited in the Exradin A1SL chamber irradiated with a 250 MeV monoenergetic proton beam is shown. The cavity was divided into the tip and 10 slabs each 0.4445 mm thick. Slab 1 is next to the tip, slab 10 next to the chamber stem. In red the dose deposited in the tip and each of the slabs. In green the cumulated dose: the cumulated dose for slab i averages the doses deposited in the tip and in the slabs 1 to i. It can be seen that the dose deposited in the different slabs varies by up to 0.25% at maximum while the dose increases towards the chamber stem. The larger dose deposited in the slabs in the vicinity of the chamber stem might be due to secondary particles (e.g. electrons) produced in the stem that are being scattered into the cavity. However, due to the short range of these secondary particles, the influence on the dose in the complete cavity is small which is in agreement with the finding that the perturbation correction factor for the chamber stem is 0.995(3) and hence roughly 1. The cumulated dose is quasi-constant over the complete cavity while the maximum deviation between any two cumulated dose values is 0.04%, which is not significant (one standard deviation is ∼0.05% for each cumulated dose value). Following the study by Pojtinger *et al* (2019), the death volume is located in the vicinity of the guard ring and hence the chamber stem. Since the cumulated dose is quasi-constant over the complete cavity, it does not matter how large the sensitive volume is: for example, if the sensitive volume is restricted to the tip, the dose measured with the chamber would not be significantly different from the dose measured if the sensitive volume was consisting of the tip and any number of slabs. Hence, the influence of the death volume on the dose deposited in the cavity is negligible for this investigated chamber and does not influence the calculation of k_Q factors significantly. Since the other cylindrical

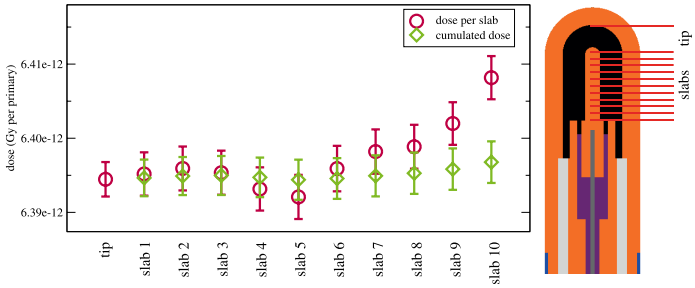

Figure 9. Dose deposited in the Exradin A1SL chamber irradiated with a 250 MeV monoenergetic proton beam. The cavity was divided into the tip and 10 slabs each 0.4445 mm thick. Slab 1 is next to the tip, slab 10 next to the chamber stem. In red the dose deposited in the tip and each of the slabs. In green the cumulated dose inculing the dose deposited in the tip and subsequently including slab per slab the dose deposited in each slab. The error bars correspond to one standard uncertainty.

ionization chambers investigated in this study have a larger cavity compared to the Exradin A1SL, the results from this investigation should be applicable to the other cylindrical chambers, as well.

4. Conclusion

The Monte Carlo code TOPAS/GEANT4 was used to calculate f_{Q_0} factors in a ^{60}Co spectrum and f_Q factors in monoenergetic proton beams for six plane-parallel and four cylindrical ionization chambers. From these factors k_Q factors were derived. The comparison of k_Q factors calculated in this study with experimentally determined k_Q factors and ratios of k_Q factors showed good agreement on the 1% level. Hence, TOPAS/GEANT4 can be used to calculate k_Q factors for ionization chambers in monoenergetic proton beams. The comparison with other Monte Carlo calculated f_Q/f_{Q_0} ratios showed that the role of nuclear interaction models has to be investigated further for high proton energies.

Additionally, perturbation correction factors for the Exradin A1SL chamber in a 250 MeV monoenergetic proton beam were calculated. It can be concluded that the assumption of the IAEA TRS-398 CoP (that all perturbation correction factors in proton beams are 1 for all ionization chambers) might not be sufficiently accurate for all chambers and proton energies—especially in the case for the factor p_{wall}.

Acknowledgments

This work is part of the RTNORM research project, funded by the European Metrology Programme for Innovation and Research (EMPIR), Grant No. 16NRM03, an initiative co-funded by the European Union's Horizon 2020 research and innovation programme and the EMPIR Participating States.

We thank the TOPAS forum and especially Joseph Perl for fruitful discussions. We would like to thank A Lourenço for providing values for the perturbation factors. We would like to thank B Muir and D Czarnecki for providing values for the f_{Q_0} factors. We would like to thank C Gomà for the simulations of simple air-filled cavities for 250 MeV protons.

ORCID iDs

Kilian-Simon Baumann https://orcid.org/0000-0003-1223-523X
Klemens Zink https://orcid.org/0000-0001-5785-4101

References

Agostinelli S *et al* 2003 Geant4—a simulation toolkit *Nucl. Instrum. Methods Phys. Res.* A **506** 250–303

Andreo P *et al* 2019 Determinatin of consensus k_Q mean values for megavoltage photon beams for the update of IAEA TRS-398 *Phys. Med. Biol.* (submitted)

Andreo P, Burns D T, Hohlfeld K, Huq M S, Kanai T, Laitano F, Smyth V and Vynicker S 2000 Absorbed dose determination in external beam radiotherapy: an international code of practice for dosimetry based on standards of absorbed dose to water *Technical Report* Technical Report Series TRS-398 (Vienna: International Atomic Energy Agency) (http://www-naweb.iaea.org/nahu/DMRP/documents/CoP_V12_2006-06-05.pdf)

Andreo P, Wulff J, Burns D T and Palmans H 2013 Consistency in reference radiotherapy dosimetry: resolution of an apparent conundrum when ^{60}Co is the reference quality for charged-particle and photon beams *Phys. Med. Biol.* **58** 6593–621
Arce P *et al* 2014 Gamos: a framework to do GEANT4 simulations in different physics fields with an user-friendly interface *Nucl. Instrum. Methods Phys. Res.* A **735** 304–13
Barschall H H, Chadwick M B, Jones D L T, Meulders J P, Schuhmacher H and Young P G 2000 Nuclear data for neutron and proton radiotherapy and for radiation protection *ICRU Report* 63 International Commission on Radiation Units and Measurements (https://inis.iaea.org/collection/NCLCollectionStore/_Public/32/048/32048887.pdf)
Baumann K S, Horst F, Zink K and Gomà C 2019 Comparison of PENH, FLUKA, and GEANT4/TOPAS for absorbed dose calculations in air cavities representing ionization chambers in high-energy photon and proton beams *Med. Phys.* **46** 4639–53
Bielajew A 2016 Fundamentals of the Monte Carlo method for neutral and charged particle transport The University of Michigan, Department of Nuclear Engineering and Radiological Sciences (http://www.umich.edu/~nersb590/CourseLibrary/MCbook.pdf)
Böhlen T T, Cerutti F, Chin M P W, Fassò A, Ferrari A, Ortega P G, Mairani A, Sala P R, Smirnov D and Vlachoudis V 2014 The FLUKA code: developments and challenges for high energy and medical applications *Nucl. Data Sheets* **120** 211–4
Czarnecki D, Poppe B and Zink K 2018 Impact of new ICRU report 90 recommendations on calculated correction factors for reference dosimetry *Phys. Med. Biol.* **63** 155015
Erazo F, Brualla L and Lallena A M 2014 Electron beam qualitykQ, q0factors for various ionization chambers: a Monte Carlo investigation with penelope *Phys. Med. Biol.* **59** 6673–91
Ferrari A, Sala P R, Fasso A and Ranft J 2005 FLUKA: a multi-particle transport code *Technical Report* CERN-2005-10, INFN/TC 05/11, SLAC R-773 (Geneva: CERN) (https://doi.org/10.2172/877507)
Folger G, Ivanchenko V N and Wellisch J P 2004 The binary cascade *Eur. Phys. J.* A **21** 407–17
Gomà C and Sterpin E 2019 Monte Carlo calculation of beam quality correction factors in proton beams using PENH *Phys. Med. Biol.* **64** 185009
Gomà C, Andreo P and Sempau J 2016 Monte Carlo calculation of beam quality correction factors in proton beams using detailed simulation of ionization chambers *Phys. Med. Biol.* **61** 2389–406
Gomà C, Hofstetter-Boillat B, Safai S and Vörös S 2015 Experimental validation of beam quality correction factors for proton beams *Phys. Med. Biol.* **60** 3207–16
Goudsmit S and Saunderson J L 1940a Multiple scattering of electrons *Phys. Rev.* **57** 552
Goudsmit S and Saunderson J L 1940b Multiple scattering of electrons II *Phys. Rev.* **58** 36
Ivanchenko V N, Kadri O, Maire M and Urban L 2010 Geant4 models for simulation of multiple scattering *J. Phys.: Conf. Ser.* **219** 032045
Lourenço A, Bouchard H, Galer S, Royle G and Palmans H 2019 The influence of nuclear interactions on ionization chamber perturbation factors in proton beams: FLUKA simulations supported by a Fano test *Med. Phys.* **46** 885–91
Mainegra-Hing E and Muir B R 2018 On the impact of ICRU report 90 recommendations on kQ factors for high-energy photon beams *Med. Phys.* **45** 3904–8
Medin J 2010 Implementation of water calorimetry in a 180 MeV scanned pulsed proton beam including an experimental determination of kQ for a farmer chamber *Phys. Med. Biol.* **55** 3287–98
Medin J, Ross C K, Klassen N V, Palmans H, Grusell E and Grindborg J E 2006 Experimental determination of beam quality factors, kQ, for two types of farmer chamber in a 10 MV photon and a 175 MeV proton beam *Phys. Med. Biol.* **51** 1503–21
Mora G M, Maio A and Rogers D W O 1999 Monte carlo simulation of a typical Co-60 therapy source *Med. Phys.* **26** 2494–502
Muir B R and Rogers D W O 2010 Monte Carlo calculations of, the beam quality conversion factor *Med. Phys.* **37** 5939–50
Muir B R, McEwen M R and Rogers D W O 2012 Beam quality conversion factors for parallel-plate ionization chambers in MV photon beams *Med. Phys.* **39** 1618–31
O'Brien D J, Roberts D A, Ibbot G S and Sawakuchi G O 2016 Reference dosimetry in magnetic fileds: formalism and ionization chamber correction factors *Med. Phys.* **43** 4915–27
Palmans H, Verhaegen F, Denis J M and Vynckier S 2002 Dosimetry using plane-parallel ionization chambers in a 75 MeV clinical proton beam *Phys. Med. Biol.* **47** 2895–905
Palmans H, Verhaegen F, Denis J M, Vynckier S and Thierens H 2001 Experimental p_{wall} and p_{cel} correction factors for ionization chambers in low-energy clinical proton beams *Phys. Med. Biol.* **46** 1187–204
Panettieri V, Sempau J and Andreo P 2008 Chamber-quality factors in60co for three plane-parallel chambers for the dosimetry of electrons, protons and heavier charged particles: PENELOPE Monte Carlo simulations *Phys. Med. Biol.* **53** 5917–26
Perl J, Shin J, Schuemann J, Faddegon B and Paganetti H 2012 TOPAS: an innovative proton Monte Carlo platform for research and clinical applications *Med. Phys.* **39** 6818–37
Pojtinger S, Kapsch R P, Dohm O S and Thorwarth D 2019 A finite element method for the determination of the relative response of ionization chambers in MR-linacs: simulation and experimental validation up to 1.5 T *Phys. Med. Biol.* **64** 135011
RTNORM 2019 Radiotherapy normative, 'ionizing radiation dosimetry for radiotherapy', euramet/empir research project (2017–2019) (Accessed: 5 February 2020) (www.rtnorm.eu)
Salvat F 2013 A generic algorithm for Monte Carlo simulation of proton transport *Nucl. Instrum. Methods Phys. Res.* B **316** 144–59
Seltzer S M, Fernández-Verea J M, Andreo P, Bergstrom P M, Burns D T, Krajcar Bronić I, Ross C K and Salvat F 2016 Key data for ionizing-radiation dosimetry: measurement standards and applications. ICRU Report 90 *J. ICRU* **14** 1–110
Sempau J and Andreo P 2006 Configuration of the electron transport algorithm of penelope to simulate ion chambers *Phys. Med. Biol.* **51** 3533–48
Sempau J, Andreo P, Aldana J, Mazurier J and Salvat F 2004 Electron beam quality correction factors for plane-parallel ionization chambers: Monte Carlo calculations using the PENELOPE system *Phys. Med. Biol.* **49** 4427–44
Simiele E and DeWerd L 2018 On the accuracy and efficiency of condensed history transport in magnetic fields in GEANT4 *Phys. Med. Biol.* **63** 235012
Testa M, Schuemann J, Lu H M, Shin J, Faddegon B, Perl J and Paganetti H 2013 Experimental validation of the TOPAS Monte Carlo system for passive scattering proton therapy *Med. Phys.* **40** 121719
Urban L 2002 Multiple scattering model in GEANT4 *Report No. CERN-OPEN-2002-070* (Geneva: CERN) (https://cds.cern.ch/record/592633)
Wulff J, Baumann K S, Verbeek N, Bäumer C, Timmermann B and Zink K 2018 TOPAS/GEANT4 configuration for ionization chamber calculations in proton beams *Phys. Med. Biol.* **63** 115013
Wulff J, Heverhagen J T and Zink K 2008 Monte-Carlo-based perturbation and beam quality correction factors for thimble ionization chambers in high-energy photon beams *Phys. Med. Biol.* **53** 2823–36
Zink K and Wulff J 2012 Beam quality corrections for parallel-plate ion chambers in electron reference dosimetry *Phys. Med. Biol.* **57** 1831–54

Appendix

Academic Faculty

Here is listed all personnel who has been directly or indirectly (for example by teaching prior to this dissertation) of assistance:

In Munich:

Walter Assmann
Ilka Brunner
Thomas Franosch
Hermann Gaub
Martin Gersch
Martin Kerscher
Roland Kersting
Harald Lesch
Viatcheslav Mukhanov
Katia Parodi
Lode Pollet
Christian Römelsberger
Hartmut Ruhl
Dorothee Schaile
Ulrich Schollwöck
Thomas Udem
Harald Weinfurter
Heribert Zenk
Wolfgang Zinth

In Lund:

Melvyn B. Davis
Peter Christiansen
Ingemar Lundström
Anders Mikkelsen
Dirk Rudolph

In Gießen

Joachim Breckow
Martin Fiebich
Volker Groß
Jürgen Koch
Thomas Schanze
Klemens Zink

At GSI:

Uli Weber

In Marburg:

Rita Engenhart-Cabillic

Acknowledgments

First of all I would like to thank my supervisors for making this thesis possible. I thank Prof. Dr. Rita Engenhart-Cabillic and Prof. Dr. Klemens Zink for all their ideas and of course the time they spent to answer questions and to help me solving problems of both scientific and bureaucratic nature. Special thanks for making it possible to attend so many national and international conferences and for motivating me to contribute to these conferences with several talks and posters.
Very special thanks to Dr. Uli Weber from GSI who contributed essentially to this thesis with his many excellent ideas and his widely diversified knowledge. It was - and is - a pleasure working with him and I hope that our collaboration will go on for a long time.
I also thank Dr. Jörg Wulff from WPE Essen for sharing his experience and knowledge concerning Monte Carlo codes and for his readiness to help with and establish several Monte Carlo-based projects. Again, I hope that this collaboration will go on for a long time.
Many thanks to all clinical staff -physicists and physicians- from the University Hospital Center Gießen-Marburg and my colleagues from the Institute of Medical Physics and Radiation Protection in Gießen who were always at hand when help was needed. Special thanks to Veronika Flatten who contributed to this thesis with both her clinical and physical knowledge.
I am also thankful for the great collaboration between physicists and physicians at the University Hospital Center Gießen-Marburg that was essential for the execution of this thesis.
I acknowledge the TOPAS discussion forum and especially Joseph Perl for helping with TOPAS-related problems and for fruitful discussions.
I also acknowledge the financial support from Strategischer Forschungsfonds der THM and Marburg International Doctorate that made possible some of my conference attendances.